A NOVEL CFD-BASED APPROACH FOR OPTIMISATION OF THE DIRECTIONAL SOLIDIFICATION PROCESS

By

Steven Dale

A Thesis Submitted To
The University of Birmingham
For The Degree Of
Engineering Doctorate

School of Metallurgy and
Materials
The University of Birmingham
Edgbaston
Birmingham
B15 2TT
United Kingdom

UNIVERSITY OF
BIRMINGHAM

University of Birmingham Research Archive

e-theses repository

This unpublished thesis/dissertation is copyright of the author and/or third parties. The intellectual property rights of the author or third parties in respect of this work are as defined by The Copyright Designs and Patents Act 1988 or as modified by any successor legislation.

Any use made of information contained in this thesis/dissertation must be in accordance with that legislation and must be properly acknowledged. Further distribution or reproduction in any format is prohibited without the permission of the copyright holder.

ABSTRACT

The directional solidification process is used to produce single crystal turbine blades for modern aero engines. The spacing of primary dendrites (PDAS) within the microstructure are an indication of the thermal gradient attained during solidification; process optimisation is being driven by the desire to refine the single crystal microstructure and maximise the thermal gradient which can reduce the propensity for defects, such as freckles, forming during solidification.

Optimisation of the casting process also allows experimental materials to be investigated such as eutectic alloys, which require more stringent process conditions.

A CFD-based method has been used in order to predict the thermal field within a ‘single shot’ Bridgman furnace and validated experimentally. The CFD model has been used to design an optimised heating element with the aim of increasing the thermal gradient achievable when casting single crystal alloys.

Dendrite arm spacing has been measured from alloys cast using both heating element designs, with the concept experimental heating element showing a reduction in PDAS of up to 30% compared to the standard design for the same furnace conditions.

The viability of casting eutectic alloys with such a furnace has also been assessed both experimentally and analytically using a CFD approach.

The most beautiful thing we can experience is the mysterious. It is the source of all true art and all science. He to whom this emotion is a stranger, who can no longer pause to wonder and stand rapt in awe, is as good as dead: his eyes are closed.

Albert Einstein

ACKNOWLEDGEMENTS

Nine years ago I thought my life was fulfilled, I had a job and a car but there was an underlying feeling that I hadn't achieved what I thought I could. One day I made a decision; I was going to go to university. I sold my car and moved away from all of the people that I was closest to. A special person gave me the courage to do that, and I will always be grateful.

My undergraduate degree was at Sheffield Hallam University to study Mechanical Engineering; there I met one of my closest friends, Andy; so thank you for the beers.

During my study at the University of Birmingham I have met many more friends who have supported me more than they realise; thank you Chris, Alex, Nick, Rebecca, Katie and Andrew. On a practical note I am hugely indebted to Peter Cranmer for operation of the Bridgman furnace, and Adrian Caden for guidance within the foundry.

Special thanks go to Dr Dmytro Shevchenko for help with CFX modelling, Dr Jean-Christophe Gebelin for advice about everything, Dr Robert Broomfield for help with casting and Professor Roger Reed for practical advice and guidance. My supervisors Dr Mark Ward, Dr Paul Withey, Mr Paul Brown and Dr Neil Jones have helped enormously and this wouldn't have been achievable without them.

Special thanks go to Nick Green, Paul Bowen and Paul Brown for being so supportive of me through the difficult times; and Rolls-Royce Plc, who have shown unfaltering faith in me as an individual. Thank you.

Finally; thank you to Sheena for her love and support. I am incredibly lucky she is part of my life.

TABLE OF CONTENTS

CHAPTER 1 INTRODUCTION 1

CHAPTER 2 LITERATURE REVIEW 6

2.1 Turbine blade operating conditions 6

2.2 Move to directional solidification 7

2.3 Interest in eutectic alloys 12

2.4 Survey of selected nickel based superalloys 16

2.4.1 CMSX-4 16

2.4.2 γ-γ'-δ 20

2.4.3 COTAC 23

2.4.4 γ-γ'-α 28

2.4.5 NiTaC 30

2.5 Creep rupture life and the Larson-Miller Parameter 32

2.6 Solidification of alloys and the plane front stability criterion 42

2.6.1 Dendrite arm spacing 50

2.6.2 Eutectic phase spacing 52

2.7 Freckle defect formation 54

2.8 The current and future role of Re and Ru in nickel based superalloys 59

2.9 Practice of directional solidification 60

2.9.1 Process Development 66

2.10 Finite element modelling 77
2.10.1 ProCAST Furnace Model 81
2.11 Summary 84
CHAPTER 3 EXPERIMENTAL PROCEDURE 86
3.1 Production of single crystal components 86
3.1.1 Wax geometry & investment shell production 87
3.1.2 Casting and single crystal selection 91
3.2 Casting of eutectic alloys 92
3.2.1 The use of pre-formed sintered alumina tubes 92
3.3 Microstructure modification of Nickel based alloys 93
3.4 Assessment of microstructure by metallographic analysis 98
3.4.1 Preparation 98
3.4.2 Measurement 100
3.5 Furnace centreline temperature measurement using a moving thermocouple 104
3.6 Measurement of furnace electrical properties during heating cycles 109
3.7 Computer Modelling 111
CHAPTER 4 BRIDGMAN FURNACE 113
4.1 Background 113
4.1.1 Hot zone temperature control 117
4.1.2 Bridgman furnace power input and experimental readings 121
CHAPTER 5 CFX FURNACE MODEL 129

5.1 Introduction 129

5.1.1 DC Current approximation 130

5.2 Electrical current flow 133

5.2.1 CFX benchmark calculation 134

5.2.2 Mesh sensitivity study 137

5.3 Electrical resistance 149

5.3.1 Resistors in series 150

5.3.2 Resistors in parallel 151

5.3.3 Calculation of furnace heating element electrical resistance 153

5.4 Electrical resistive (Joule) heating 163

5.4.1 CFX benchmark calculation of Joule heating in an amorphous wire with uniform heat loss 163

5.5 Radiation heat transfer 167

5.6 Construction of CFX furnace model 170

5.6.1 Materials 176

5.6.2 Meshing 181

5.6.3 Boundary conditions 182

5.6.4 Run Parameters 183

5.6.5 CFX model 20 x 10^{-3} m ID baffle 184

5.6.6 CFX model 110 x 10^{-3} m ID baffle 190

5.6.7 Discrete transfer model ray comparison 191

5.7 Validation of CFX models using furnace centreline temperature 193

5.7.1 Comparison with thermal data for 110 x 10^{-3} m by 30 x 10^{-3} m slotted baffle, 1843.15 K 198

5.7.2 Comparison with thermal data for 110 x 10^{-3} m diameter baffle 1803.15 K 199

5.8 Comparison of CFX thermal profiles with ProCAST model validated using instrumented mould 200

5.9 Preliminary Conclusions 208

5.10 Baffle effect on heater thermal profile 209

5.10.1 Effect of baffle diameter on heater thermal profile 209

5.10.2 Effect of baffle thickness on heater thermal profile 211

5.10.3 Discussion 213

5.11 Effect of mould position and transient view factors on heater thermal profile .. 215

5.12 Experimental heater design 219

5.12.1 Design methodology 219

5.12.2 Manufacture 225

5.12.3 Electrical resistance 227

5.12.4 CFX results for experimental heater incorporated in Bridgman furnace with 20 x 10^{-3} m ID baffle and 110 x 10^{-3} m ID baffle 227

5.13 Validation of experimental heater model using furnace centreline temperatures 230

5.14 Comparison of standard heater and experimental heater thermal profiles 233

5.14.1 20 x 10^{-3} m ID baffle 233

5.14.2 110 x 10^{-3} m ID baffle 237

5.15 Conclusions 245

5.15.1 Furnace model development 245

5.15.2 Experimental heater design 247

CHAPTER 6 MICROSTRUCTURE MODIFICATION OF NICKEL BASED ALLOYS 248

6.1 Introduction 248

6.2 Results and analysis 248

6.2.1 Multiple-component mould – an analogy of industrial casting conditions . 248

6.2.2 Single component mould with use of extensive radiation baffling 260

6.2.3 Eutectic alloy casting 268

6.2.4 VeriCAST2 validation geometry 289

6.3 Conclusions 309

6.3.1 PDAS modification 309

6.3.2 Eutectic alloys 312

CHAPTER 7 CONCLUSIONS 313

7.1 Furnace model development 313

7.2 Experimental heater design and PDAS modification 314

7.3 Eutectic alloys 316

CHAPTER 8 FUTURE WORK 317

REFERENCES 319

APPENDIX 329

Material Data 329

Alumina (Alsint) 329

Calcarb 331

COTAC 744 332

γ-γ’-δ 333

Graphite 335

Copper 336

Sigraflex 337

Stainless Steel 338

Zircar 340

Experimental heater manufacturing drawing 341

LIST OF FIGURES

Figure 2-1: Creep strain evolution with time for conventionally cast (equiaxed), directionally solidified (columnar) and single crystal specimens of Mar-M200 subjected to a stress of 206 MPa at 982°C (Kear and Piearcey, 1967) 8

Figure 2-2: a) Spiral single crystal selector (Pig tail) design, b) Bottom run seeded mould design, c) Top run seeded mould design. Both seeded moulds showing single crystal seed adjacent to the chill (Goulette et al., 1984) 9

Figure 2-3: Turbine entry temperature of Rolls-Royce civil engines, 1940-2006. Figure obtained from (Reed, 2006) adapted from (Cumpsty, 1997). 11

Figure 2-4: Binary eutectic phase diagram highlighting eutectic temperature, eutectic point and eutectic composition (Stohr and Khan, 1980). 12

Figure 2-5: Coupled zone (shaded region) on eutectic phase diagram. a) Symmetric and probable normal microstructure. b) Skewed and probable abnormal microstructure (Davis, 1996) 14

Figure 2-6: Both [211] twinning and (010) slip deformation modes exhibited in the Ni^3Nb phase after 5% total strain in room temperature tensile test (Lemkey, 1973) 22

Figure 2-7: Dislocation pile-ups against a tantalum carbide fibre in the COTAC 3 composite during an in-situ tensile test (Stohr and Khan, 1980) 25

Figure 2-8: Typical microstructure of directionally solidified $\gamma - \gamma' - \alpha$. a) Solidified at 5.6 mm hr^{-1} b) Solidified at 17 mm hr^{-1}(Whittenberger and Wirth, 1982) 29

Figure 2-9: a) Larson-Miller plot of the alloys DS CM 247 LC, CM 186 LC, CMSX-4 and CMSX 10 (Erickson, 1996) b) Rupture life in hours plotted against applied stress for varying temperature intervals for CMSX-4 (Broomfield et al., 1998). 36

Figure 2-10: A representation of creep-rupture results for COTAC 744 plotted as log σ – log tr (Stohr and Khan, 1980) 38

Figure 2-11: Log stress v Log time to rupture plot of Ni-base eutectic alloys and Ni-base single crystal superalloys under a range of constant temperature conditions. Data was extrapolated from the following sources; COTAC 744 - (Stohr and Khan, 1980), COTAC 784 - (Damerval, 1987), NiTaC 13 - (Woodford, 1977), NiTaC 14B - (Henry et al., 2005), $\gamma - \gamma' - \delta$ (Lemkey, 1973), CMSX-4 (Broomfield et al., 1998), CMSX-10 (Erickson, 1996) and $\gamma - \gamma' - \alpha$ (Whittenberger and Wirth, 1982) 40

Figure 2-12: Log stress v Log time to rupture plot of Ni-base single crystal superalloys and Ni-base eutectic alloys under a range of constant temperature conditions. Ni-base eutectic alloys are plotted as (time to rupture/2) which is equivalent to the creep potential of a single crystal superalloy Data extrapolated from the same sources as in Figure 2-11. 41

Figure 2-13: Concentration profile ahead of a planar solidification front (Stohr and Khan, 1980) 45

Figure 2-14: Equilibrium phase diagram of binary eutectic alloy (Stohr and Khan, 1980) 46

Figure 2-15: Morphologies of directionally solidified nickel based superalloys plotted as log V versus log G (where V is the growth rate and G the thermal gradient). The solid lines shown are contours of constant G/V ratios. Unfilled circles represent

alligned planar growth, unfilled squares, diamonds, triangles and ovals represent cellular growth, filled shapes represent dendritic growth (Quested and McLean, 1984). 48

Figure 2-16: G/V solidification requirements for various alloy systems. Data extrapolated from (Lemkey, 1973, Stohr and Khan, 1980, Whittenberger and Wirth, 1982, Woodford, 1977). 49

Figure 2-17: Influence of Ta content on freckle chain formation in Ni-base superalloy specimens (Pollock et al., 1992) 56

Figure 2-18: Calculated Ra number based on directional solidification castings investigating grain defects in the single crystal alloy SX-1 calculated as a function of the thermal parameter G and solidification parameter R (Pollock and Murphy, 1996). The thermal gradient G has been determined empirically from the relationship between PDAS, G and V and the critical Ra number is plotted against this (Beckermann et al., 2000) 58

Figure 2-19: The dependence of freckle formation on the primary dendrite arm spacing showing no freckles at a spacing of $320\mu m$ at a cooling rate of 0.1 °C.s^{-1} (Pollock et al., 1992)..... 58

Figure 2-20: Sectional view of a standard Rolls-Royce DS furnace (Goulette et al., 1984) 62

Figure 2-21: Idealised model of steady state heat flow for an infinitely long thin rod moving at a velocity, V from a furnace at temperature, Tf into a cooling zone of temperature, Tc. Adapted from (Reed, 2006). 63

Figure 2-22: Schematic showing (a) longitudinal cross section of furnace and (b) transverse. Detailing concentric heating elements and mould located within the furnace (Piwonka, 1974) 68

Figure 2-23: Illustration of proposed laser heating apparatus in which heat can either be applied by scanning to a whole mould or applied selectively to part of the mould surface (Schlienger and French, 2008)..... 68

Figure 2-24: SEM micrographs of dendrite morphology in a nickel based superalloy sectioned parallel to the growth direction. a) 2.5 mm/min, Bridgman b) 2.5 mm/min, LMC (Reed, 2006) 70

Figure 2-25: Schematic showing furnace with coolant spray nozzle directed towards the outer surface of the casting mould (Brinegar, 2003)..... 71

Figure 2-26: Primary dendrite arm spacing for different casting processes in the upper and lower aerofoil of a pseudo blade geometry (Konter et al., 2000) 72

Figure 2-27: a) Directional solidification furnace showing moveable baffle, b) Plan view of furnace showing mechanism proposed to move baffle into varying positions(Lallement, 1989) 74

Figure 2-28: Diagram of directional solidification furnace showing the position of moveable baffles during operation (Brinegar et al., 2000) 74

Figure 2-29: a-c) Sectional view of furnace showing mould in various positions during the withdrawal process and the interaction with the flexible baffle d) Plan view of one flexible baffle configuration (Brokloff et al., 1990) 75

Figure 2-30: Illustration of furnace with centrally located baffle (Hugo and Betz, 1997).. 76

Figure 2-31: View of floating baffle material and its use in a furnace incorporating liquid metal cooling (Klug, 2002) 77

Figure 3-1: Illustration of stages in the investment casting process. a) Wax pattern b) Wax pattern with 1st stage shell c) Fully shelled mould d) Single crystal component exactly replicating wax starter geometry. 90

Figure 3-2: Graphical representation of test bar cluster mould including spiral seed selectors surrounding radiation baffle geometry. A 90^{o} segment has been omitted from view for clarity. 95

Figure 3-3: Graphical representation of single test bar consisting of alumina tube and supporting base including radiation baffle. A 90^{o} segment has been omitted from view for clarity. 96

Figure 3-4: Graphical representation of VeriCAST test geometry and surrounding radiation baffle. A 90^{o} segment has been omitted from view for clarity. 97

Figure 3-5: Example of measured PDAS values displayed in histogram format taken from work by (Warnken and Reed, 2011). 101

Figure 3-6: Successive steps of image processing in to count phase spacing of a rod-like eutectic alloy. a) Original microscope image, b) Adjusted image to transform phases into flat white with flat black matrix, c) Processed image showing counted image overlays and omitted phases lying on the border of the image. 103

Figure 3-7: Sintered alumina tubes and was mould used to produce thermocouple housing

assembly. 105

Figure 3-8: Images showing position of thermocouple assembly within furnace hot zone. 106

Figure 3-9: Image showing the extent at which the base of the thermocouple assembly and chill resided out of the furnace hot zone. 108

Figure 3-10: Image showing electrical current sensor loop connected to one of the 3 phase supply cables. 110

Figure 4-1: Schematic view of heater insulation assembly; dimensions in mm. 114

Figure 4-2: Photograph showing ‘single shot’ Bridgman furnace vacuum chamber; including induction melting unit, hot zone insulation surrounding heating element, input electrodes to supply power, control thermocouples and chill spool which forms part of the cold zone. 115

Figure 4-3: View of furnace hot zone, looking down from position occupied by induction melt unit, with VeriCAST mould in place and top insulation removed. This view highlights the space constraints within the single shot furnace hot zone particularly with reference to a susceptor which is not incorporated in this furnace configuration. Control thermocouples can also be seen. 117

Figure 4-4: Comparison of programmed furnace heat up profile and control thermocouple temperature, comprising heat-up to 1823.15 K and soak period. 120

Figure 4-5: Typical electrical current and voltage measurements taken over a 5400s period with the furnace hot zone set to heat up to 1823.15 K and maintain temperature. The

furnace configuration used a 20 x 10^{-3}m ID baffle and standard graphite heating element. 122

Figure 4-6: Measured electrical current voltage taken over a 5400s period with the furnace hot zone set to heat up to 1823.15K and maintain temperature. The furnace configurations shown use a 20 x 10^{-3} m ID and 110 x 10^{-3} m ID baffle and standard graphite heating element. 123

Figure 4-7: Experimentally determined voltage measurements for three furnace configurations, using the standard graphite heating element. 127

Figure 4-8: Experimentally determined electrical current measurements for three furnace configurations using the standard graphite heating element. 127

Figure 4-9: Estimate of furnace power for three configurations calculated from experimentally determined current and voltage measurements. 128

Figure 5-1: a) Geometry of graphite heating element used in the single shot furnace b) Photograph of heating element showing contrasting shades of graphite indicating areas of preferential electrical current flow 134

Figure 5-2: Right angle bend in geometry showing coordinate points and subscripts..... 135

Figure 5-3: Illustration of mesh node spacing as used in the mesh dependency study 138

Figure 5-4: % error between analytical solution and CFX results for maximum current density at apex of 90° turn, calculated using fixed node spacing in the x and y legs of the geometry and varying node spacing around the apex 140

Figure 5-5: % error between analytical solution and CFX results for maximum current

density at apex of 90° turn, calculated using fixed node spacing of 2.5 x 10^{-4} m at apex of turn and varying node spacing in x and y legs of geometry..... 140

Figure 5-6: Comparison of analytical solution and CFX calculation for uniform electrical current density in the x and y legs of the geometry and maximum current density around the apex of the 90° turn. The radius of the turn varied between 1 x 10^{-3} m and 10 x 10^{-3} m. 142

Figure 5-7: Error % between analytical solution and CFX calculations for electrical current density in x and y legs of the geometry and around the apex of the 90° turn. 142

Figure 5-8: CFX calculations of electrical current density showing maximum value around apex of turn for varying radii; a) 1 x 10^{-3} m, b) 2.5 x 10^{-3} m, c) 5 x 10^{-3} m, d) 7.5 x 10^{-3} m, e) 10 x 10^{-3} m. 143

Figure 5-9: Annotation of strip width measurement from reference point D. 144

Figure 5-10: Comparison of CFX calculation with analytical solution for distance from reference point D in which electrical current density falls within a specified uniformity range. a) 1% b) 2%. Black line indicates analytical solution distance, green contour is specified uniformity range, red contour is specified uniformity range + f and blue contour is specified uniformity range – f. 146

Figure 5-11: Comparison of CFX calculation with analytical solution for distance from reference point D in which electrical current density falls within a specified uniformity range. c) 5% d) 10%. Black line indicates analytical solution distance, green contour is specified uniformity range, red contour is specified uniformity range + f and blue contour is specified uniformity range – f. 147

Figure 5-12: An example of optimised meshing of the furnace heating element in which element size is scaled proportionally from the apex of the radius. 148

Figure 5-13: Example of N series resistors which are equivalent to a single resistor, adapted from (Rizzoni, 2003). 150

Figure 5-14: Example of N number of resistors in parallel which are equivalent to a single resistor by use of a defined relationship, figure adapted from (Rizzoni, 2003). 152

Figure 5-15: Geometry of graphite heating element a) Full heating element as used in practice b) Representation of heating as two parallel resistors, lines emanating from points A & B indicate the terminals are shared between resistors R_1 and R_2. 154

Figure 5-16: a) Isometric view of half heating element split into component series resistors. b) Labelled series resistors representing half heating element, R1 in Figure 5-15. . 156

Figure 5-17: View of split heating element showing dimensions X*, Y*, g, h and l. 157

Figure 5-18: Plot of experimentally determined voltage and current values for all experimental trials resulting in a total of 40387 data points. 160

Figure 5-19: Plot of experimentally determined voltage and current values corrected using correction factor. 162

Figure 5-20: Electrical resistance of graphite heater element calculated using an analytical approximation, using CFX and determined experimentally. Error bar on experimental results show the calculated error. 162

Figure 5-21: Comparison between theoretically calculated values for wire core temperature with those calculated using CFX. 166

Figure 5-22: Comparison between theoretically calculated values for wire radial temperature difference with those calculated using CFX. 166

Figure 5-23: Component parts of the CFX furnace model. 170

Figure 5-24: Illustration of 'Vacuum' domain in which radiation heat transfer calculations take place. 171

Figure 5-25: Geometry of furnace model showing incorporation of thermocouple protruding into furnace hot zone through the outer and inner insulation. 172

Figure 5-26: Illustration of baffle geometry variation used in the CFX calculations. a) 20 x 10^{-3} m Ø, b) 20 x 10^{-3} m Ø double thickness. 173

Figure 5-27: Illustration of baffle geometry variation used in the CFX calculations. a) 110 x 10^{-3} m Ø, b) 110 x 10^{-3} m by 30 x 10^{-3} m slotted baffle 174

Figure 5-28: Half of the graphite heating element showing positions of electrical input. 175

Figure 5-29: CFX model of Bridgman furnace incorporating single layer radiation baffle with 20 x 10^{-3} m diameter cut-out heated to a set hot zone temperature of 1823.15 K. Contour plots show heating element surface temperature and control thermocouple surface temperature. 185

Figure 5-30: CFX model of Bridgman furnace incorporating single layer radiation baffle with 20 x 10^{-3} m diameter cut-out heated to a set hot zone temperature of 1823.15 K. Contour plots show electrical current density with an applied current of 482 A. 186

Figure 5-31: Electrical current density contours on heating element with a potential difference of 14.6V. 188

Figure 5-32: CFX model of Bridgman furnace incorporating single layer radiation baffle with 20 x 10^{-3} m diameter cut-out heated to a set hot zone temperature of 1923.15 K. Contour plots show a) Heating element surface temperature and control thermocouple surface temperature b) Electrical current density with an applied current of 528 A. 189

Figure 5-33: CFX model of Bridgman furnace incorporating single layer radiation baffle with 110 x 10^{-3} m diameter cut-out heated to a set hot zone temperature of 1823.15 K. Contour plots show heating element surface temperature and control thermocouple surface temperature. 190

Figure 5-34: Discrete transfer radiation heat transfer results for; a) 12 rays, net heat transfer 233.37 W m^{-2}, b) 32 rays, net heat transfer 230.37 W m^{-2}..... 192

Figure 5-35: Experimental thermocouple temperature data and modelled temperature data of temperature along Z-axis of furnace for a hot zone temperature of 1823.15 K with a 110 x 10^{-3} m diameter baffle. (Graph shows approximate position of furnace hot zone, baffle location and cold zone for clarity)..... 195

Figure 5-36: Experimental thermocouple temperature data and modelled temperature data of temperature along Z-axis of furnace for a hot zone temperature of 1823.15 K with a 20 x 10^{-3} m diameter baffle. (Graph shows approximate position of furnace hot zone, baffle location and cold zone for clarity)..... 196

Figure 5-37: Experimental thermocouple temperature data and modelled temperature data of temperature along Z-axis of furnace for a hot zone temperature of 1923.15 K with a 20 x 10^{-3} m diameter baffle. (Graph shows approximate position of furnace hot zone, baffle location and cold zone for clarity)..... 197

Figure 5-38: Furnace centreline thermocouple data measured by (Newell, 2009) for a hot zone temperature of 1843.15 K with a slotted radiation baffle compared with results from a CFX model. 198

Figure 5-39: Furnace centreline thermocouple data for a hot zone temperature of 1803.15 K with a 110 x 10^{-3} m diameter baffle compared with CFX model results. Experimental data obtained from (Newell, 2009). 199

Figure 5-40: Transient thermocouple temperature data for point 3 in VeriCAST2 validation mould. Data obtained from (Newell, 2009). 201

Figure 5-41: Comparison of ProCAST split heater temperature with calculated split heater temperature using CFX. Furnace comprises 110 x 10^{-3} m diameter baffle with set hot zone temperature of 1803.15 K. Full temperature contour of heater surface temperature calculated using CFX is also plotted for reference. Temperature contour of heating element highlights blue areas in which the heater temperature falls below that of the control thermocouple temperature, highlighting the similarity between the ProCAST and CFX models. 202

Figure 5-42: Comparison of ProCAST split heater temperature with calculated split heater temperature using CFX. Furnace comprises 110 x 10-3 m by 30 x 10-3 m slotted baffle with set hot zone temperature of 1843.15 K. Full temperature contour of heater surface temperature calculated using CFX shown for comparison. 204

Figure 5-43: Comparison of ProCAST split heater temperature with modified CFX split heater temperature. 205

Figure 5-44: Two experimentally determined temperature readings taken using a furnace

with a set temperature of 1843.15 K with a 110 x 10^{-3} by 30 x 10^{-3} slotted baffle. Figures show measured temperature data, that calculated using a constant temperature ProCAST model and that with a split heater model. For comparison, calculated lower heater temperature data from ProCAST and CFX models are shown. Experimental data obtained from (Newell, 2009). 206

Figure 5-45: Experimentally determined thermocouple data with ProCAST lower heater temperature and revised CFX lower heater temperature shown. Experimental data obtained from (Newell, 2009). 207

Figure 5-46: Area average heater temperature at discrete positions along the z-axis calculated using CFX model. The graph shows the heater surface temperature for the same prescribed hot zone temperature of 1823.15 K and two baffle configurations. 210

Figure 5-47: Area average heater temperature at discrete positions along the z-axis calculated using CFX model. The graph shows the heater surface temperature for the same prescribed hot zone temperature of 1823.15 K and two baffle configurations. 212

Figure 5-48: Area average heater temperature at discrete positions along the z-axis calculated using CFX model. The graph shows the heater surface temperature for the same prescribed hot zone temperature of 1823.15 K with three baffle configurations with the ability to block successive levels of radiant heat from leaving the hot zone. 214

Figure 5-49: Experimentally determined electrical input, and mould position while casting CMSX-4 using a VeriCAST2 mould using a 110 x 10^{-3} m ID radiation baffle and a

furnace set temperature of 1803.15 K. 215

Figure 5-50: Positions of VeriCAST2 mould relating to measured furnace energy input levels. a) 0mm, b) 25mm, c) 150mm and d) 250mm. 0mm is the mould starting position and relates to a position just below the radiation baffle 216

Figure 5-51: Area average heater temperature at discrete positions along the z-axis calculated using CFX model. The graph shows the heater surface temperature for the same prescribed hot zone temperature of 1803.15 K and 110 x 10-3 m ID baffle for four VeriCAST2 mould positions. 218

Figure 5-52: a) Geometry of single turn on standard heating element b) CFX calculation of current density in single turn for a given electrical input c) CFX calculated temperature in a single turn, given an electrical input and radiation heat loss to ambient surroundings. 221

Figure 5-53: Modified geometry to reduce the distance between the apex of turn and bottom of heating element showing electrical current and temperature hot spot. ... 222

Figure 5-54: Further design iteration comprising narrow channels at the base of the heating element in order to produce a high current density and localised temperature variation..... 222

Figure 5-55: Final design of proposed experimental graphite heating element. 224

Figure 5-56: Illustration of CNC milling operation used to manufacture the graphite heating elements. 225

Figure 5-57: Photograph showing experimental graphite heating element due to be

installed in the Bridgman furnace heating assembly..... 226

Figure 5-58: CFX model of experimental Bridgman furnace incorporating single layer radiation baffle with 20 x 10^{-3} m diameter cut-out heated to a set hot zone temperature of 1923.15 K. Contour plots show a) Heating element surface temperature and control thermocouple surface temperature b) Electrical current density with an applied current of 331 A. 228

Figure 5-59: CFX model of experimental Bridgman furnace incorporating single layer radiation baffle with 110 x 10^{-3} m diameter cut-out heated to a set hot zone temperature of 1823.15 K. Contour plots show a) Heating element surface temperature and control thermocouple surface temperature b) Electrical current density with an applied current of 402 A. 229

Figure 5-60: Experimental thermocouple temperature data and modelled temperature data of temperature along Z-axis of experimental furnace for a hot zone temperature of 1923.15 K with a 20 x 10^{-3} m diameter baffle. (Graph shows approximate position of furnace hot zone, baffle location and cold zone for clarity) 231

Figure 5-61: Experimental thermocouple temperature data and modelled temperature data of temperature along Z-axis of experimental furnace for a hot zone temperature of 1823.15 K with a 110 x 10^{-3} m diameter baffle. (Graph shows approximate position of furnace hot zone, baffle location and cold zone for clarity) 232

Figure 5-62: Comparison of the experimentally measured temperature data along the Z-axis of the furnace for the standard and experimental heating element with a 20 x 10^{-3} ID baffle and a set hot zone temperature of 1923.15 K. 234

Figure 5-63: Area average heater temperature at discrete positions along the z-axis calculated using CFX model. The graph shows the heater surface temperature for the same prescribed hot zone temperature of 1923.15 K and 20 x 10^{-3} m ID baffle with the standard and experimental heaters. '0' references the bottom of the heating element, '0.325' the top. For illustration, the surface temperature +/- 10K either side of the TC temperature (which equates to +/- 0.5%) is shown to highlight the variation in position of the set temperature between a) standard heater and b) experimental heater. 235

Figure 5-64: An alternative representation of experimentally determined data shown in Figure 5-62 showing the temperature transmitted by radiant heat along the Z-axis of the furnace for a prescribed hot zone temperature of 1923.15 K and 20 x 10^{-3} m ID baffle with the standard and experimental heaters. '0' references the bottom of the heating element, '0.325' the top. 236

Figure 5-65: Comparison of the experimentally measured temperature data along the Z-axis of the furnace for the standard and experimental heating element with a 110 x 10^{-3} m ID baffle and a set hot zone temperature of 1823.15 K. 238

Figure 5-66: An alternative representation of experimentally determined data shown in Figure 1 58 showing the temperature transmitted by radiant heat along the Z-axis of the furnace for a prescribed hot zone temperature of 1823.15 K and 110 x 10^{-3} m ID baffle with the standard and experimental heaters. '0' references the bottom of the heating element, '0.325' the top. 239

Figure 5-67: Area average heater temperature at discrete positions along the z-axis calculated using CFX model. The graph shows the heater surface temperature for a

prescribed hot zone temperature of 1823.15 K and 110 x 10-3 m ID baffle with the standard and experimental heaters. ‘0’ references the bottom of the heating element, ‘0.325’ the top. For illustration, the surface temperature +/- 10K either side of the TC temperature (which equates to +/- 0.5%) is shown to highlight the variation in position of the set temperature between a) standard heater and b) experimental heater. 241

Figure 5-68: Comparison of the experimentally measured temperature data along the Z-axis of the furnace for the standard and experimental heating element with a set hot zone temperature of 1823.15 K and experimental heater with hot zone temperature of 1923.15K. All configurations with a 110 x 10^{-3} m ID baffle. 243

Figure 6-1: Macro image of cross-section (a) and micrograph (taken using a polarized filter in order to highlight dendrite centres) (b) showing primary dendrites in CMSX-4 with a mean spacing of 321.36 x 10^{-6} m. Taken at 60 x 10^{-3} m above spiral seed selector and cast using standard heating element, a hot zone reference temperature of 1823.15 K and a withdrawal velocity of 6.36 x 10^{-5} ms^{-1}. The mould comprised four 12 x 10^{-3} m diameter bars each with a spiral seed selector located on a bayonet fitting equally spaced at the four quadrants on a circle of approximate diameter ~60 x 10^{-3} m (See Chapter 3). The baffle comprised a 110 x 10^{-3} m ID orifice and a nominal thickness of 3.8 x 10^{-3} m. 250

Figure 6-2: Macro image of cross-section (a) and micrograph (taken using a polarized filter in order to highlight dendrite centres) (b) showing primary dendrites in CMSX-4 with a mean spacing of 246.96 x 10^{-6} m. Taken at 60 x 10^{-3} m above spiral seed selector and cast using experimental heating element, a hot zone reference

temperature of 1823.15 K and a withdrawal velocity of 6.36 x 10^{-5} ms^{-1}. The mould comprised four 12 x 10^{-3} m diameter bars each with a spiral seed selector located on a bayonet fitting equally spaced at the four quadrants on a circle of approximate diameter ~60 x 10^{-3} m (See Chapter 3). The baffle comprised a 110 x 10^{-3} m ID orifice and a nominal thickness of 3.8 x 10^{-3} m. 251

Figure 6-3: Box plot representation of primary dendrite arm spacing averaged over a distance between 20 x 10^{-3} and 120 x 10^{-3} m above the restriction showing the effect of heater design and withdrawal speed on the microstructure. 255

Figure 6-4: Variation in PDAS as a function of height within the test bar i.e. axial distance from the seed selector, where the seed selector = 0. The furnace parameters were a hot zone reference temperature of 1823.15 K, a 110 x 10^{-3} m ID baffle and a withdrawal velocity of 6.36 x 10^{-5} $m.s^{-1}$. 257

Figure 6-5: Variation in PDAS as a function of height within the test bar i.e. axial distance from the seed selector, where the seed selector = 0. The furnace parameters were a hot zone reference temperature of 1823.15 K, a 110 x 10^{-3} m ID baffle and a withdrawal velocity of 10.67 x 10^{-5} $m.s^{-1}$. 257

Figure 6-6: Derived thermal gradient as a function of height within the test bars for all experimental conditions. The constant furnace parameters were a hot zone reference temperature of 1823.15 K and 110 x 10^{-3} m ID baffle. 259

Figure 6-7: Micrographs, taken using a polarising filter in order to highlight dendrite centres, of a cross section of the single crystal alloy CMSX-4 taken at a distance of 60 x 10^{-3} m above the chill, cast at a withdrawal velocity of 10.67 x 10^{-5} $m.s^{-1}$ with a radiation baffle comprising a 20 x 10^{-3} m ID orifice and a nominal thickness of 3.8 x

10^{-3} m. The mould comprised an alumina tube with nominal wall thickness of 2 x 10^{-3} m supported on the chill by a copper stand. The micrographs represent a combination of heater geometry and temperature; a) Standard heating element 1823.15 K, mean PDAS 169.12 x 10^{-3} m. b) Experimental heating element 1823.15 K, mean PDAS 165.63 x 10^{-3} m. c) Standard heating element, 1923.15 K, mean PDAS 153.17 x 10^{-3} m. and d) Experimental heating element, 1923.15 K, mean PDAS 154.47 x 10^{-3} m. 261

Figure 6-8: Box plot representation of primary dendrite arm spacing averaged over a distance between 60 x 10-3 and 140 x 10-3 m above the restriction showing the effect of heater design and hot zone reference temperature on the microstructure. 264

Figure 6-9: Variation in PDAS as a function of height within the test bar i.e. axial distance from the seed selector, where the seed selector = 0. The furnace parameters were a withdrawal velocity of 10.67 x 10^{-5} m.s^{-1}, 20 x 10^{-3} m ID baffle and hot zone reference temperature of 1823.15 K or 1923.15 K. 265

Figure 6-10: Derived thermal gradient as a function of height within the test bars for all experimental conditions. The constant furnace parameters were a withdrawal rate of 10.67 x 10^{-5} m.s^{-1} and 20 x 10^{-3} m ID baffle. 266

Figure 6-11: CFX model results for COTAC 744 cast in a 13 x 10^{-3} m ID alsint tube. The furnace parameters were a hot zone reference temperature of 1823.15 K using the standard heating element and a double layer 20 x 10^{-3} m ID baffle. Shown in main view is the heating element temperature contour; enlarged is the liquidus and solidus temperature range of the alloy (red liquid, blue solid). 271

Figure 6-12: CFX model results for COTAC 744 cast in a 13 x 10^{-3} m ID alsint tube. The

furnace parameters were a hot zone reference temperature of 1823.15 K using the experimental heating element and a double layer 20 x 10^{-3} m ID baffle. Shown in main view is the heating element temperature contour; enlarged is the liquidus and solidus temperature range of the alloy (red liquid, blue solid). 272

Figure 6-13: CFX model results for COTAC 744 cast in a 13 x 10^{-3} m ID alsint tube. The furnace parameters were a hot zone reference temperature of 1923.15 K using the standard heating element and a double layer 20 x 10^{-3} m ID baffle. Shown in main view is the heating element temperature contour; enlarged is the liquidus and solidus temperature range of the alloy (red liquid, blue solid). 273

Figure 6-14: CFX model results for COTAC 744 cast in a 13 x 10^{-3} m ID alsint tube. The furnace parameters were a hot zone reference temperature of 1923.15 K using the experimental heating element and a double layer 20 x 10^{-3} m ID baffle. Shown in main view is the heating element temperature contour; enlarged is the liquidus and solidus temperature range of the alloy (red liquid, blue solid). 274

Figure 6-15: $\gamma - \gamma' - \delta$ eutectic alloy calculated using the experimental heating element (top) and standard heating element (bottom). The furnace parameters were a set hot zone temperature of 1923.15 K and comprised a 20 x 10^{-3} m ID double layer baffle. 276

Figure 6-16: Micrograph of longitudinal section of COTAC 744; a) View of entire cross section of 12 x 10^{-3} m diameter test bar. b) Enlarged view of section showing aligned to dendritic transition 279

Figure 6-17: a) magnified longitudinal view showing strengthening fibres within Ni matrix. b) SEM image showing precipitate strengthening phase within the matrix and

strengthening fibres 280

Figure 6-18: Micrographs showing transverse sections of eutectic alloy COTAC 744 cast at varying withdrawal velocities, assumed to be equivalent to solidification velocity; a) 9.48 x 10^{-3} m/hr 50x magnification, b) 9.48 x 10^{-3} m/hr 100x magnification c) 10.43 x 10^{-3} m/hr 50x magnification d) 10.43 x 10^{-3} m/hr 100x magnification. 281

Figure 6-19: Micrographs showing transverse sections of eutectic alloy COTAC 744 cast at varying withdrawal velocities, assumed to be equivalent to solidification velocity; e) 11.38 x 10^{-3} m/hr 50x magnification, f) 11.38 x 10^{-3} m/hr 100x magnification g) 12.26 x 10^{-3} m/hr 50x magnification h) 12.26 x 10^{-3} m/hr 100x magnification. 282

Figure 6-20: Variation in phase spacing for rate of solidification (assumed to be equivalent to withdrawal velocity) when casting COTAC 744. 283

Figure 6-21: Longitudinal, a) & c), and transverse, b) & d,) sections of the $\gamma - \gamma' - \delta$ alloy, cast at a withdrawal velocity of 8 x 10^{-3} m hr^{-1}. 284

Figure 6-22: Longitudinal section view of the eutectic alloy $\gamma - \gamma' - \delta$ annotated to show the matrix and precipitate phase and the Ni_3Nb strengthening phase. 285

Figure 6-23: Micrograph showing interface shape of $\gamma - \gamma' - \delta$ alloy when cast using the standard heater, hot zone reference temperature of 1923.15 K and then 'quenched' in the cold zone to induce an aligned to dendritic transition. This can be compared with the solid liquid interface shape calculated using the CFX furnace model for identical conditions. The furnace baffle comprised of a two layer Sigraflex material with a 20 x 10^{-3} m ID. 287

Figure 6-24: Micrograph showing interface shape of COTAC 744 alloy when cast using

the standard heater, hot zone reference temperature of 1923.15 K and then 'quenched' in the cold zone to induce an aligned to dendritic transition. This can be compared with the solid liquid interface shape calculated using the CFX furnace model for identical conditions. The furnace baffle comprised of a two layer Sigraflex material with a 20 x 10^{-3} m ID. 288

Figure 6-25: VeriCAST geometry showing positions of sections taken for metallographic analysis in work conducted by (Jennings, 1996).Dimensions shown in mm (1 x 10^{-3} m). 290

Figure 6-26: Positions of in-situ TC measurements taken by (Newell, 2009). Metallographic analysis conducted at 110mm, 135mm and 'top' (not shown). Dimensions in mm (1 x 10^{-3} m). 291

Figure 6-27: Section positions to be taken from VeriCAST test piece for this work. Section A_A corresponds to Newell TC point 7 and Jennings position A, Section B_B corresponds to Newell TC points 5 & 6 and Jennings position B, ‘Bottom’ section corresponds to Newell TC point 4 and Jennings position C, ‘Middle’ section corresponds to Newell TC point 3 and Jennings position D, ‘Top’ section taken from Jennings position F, and section C_C corresponds to Newell TC points 2 & 1 and Jennings position G. 293

Figure 6-28: VeriCAST geometry showing positions of metallographic analysis along aerofoil. 295

Figure 6-29: Cross-sectional illustration of aerofoil showing two locations of analysis .. 296

Figure 6-30: Macro images and micro images (inset) of VeriCAST aerofoil section cast

using the experimental heating element. a) Bottom, b) Middle, c) Top. 298

Figure 6-31: Plot showing PDAS values obtained from sections at top, middle and bottom of aerofoil from casting produced at the CRDF and at Birmingham using the standard heating element and from this work using the experimental heating element; CRDF and Newell values obtained from (Newell, 2009). The furnace parameters were a hot zone reference temperature of 1803.15 K, a withdrawal velocity of 6.36 x 10^{-5} ms^{-1} and a 110 x 10^{-3} m ID radiation baffle. 299

Figure 6-32: Section A_A which coincides with section A from (Jennings, 1996) and TC position 7 from (Newell, 2009). 300

Figure 6-33: Section B_B which coincides with section B from (Jennings, 1996) and TC positions 5 & 6 from (Newell, 2009). 301

Figure 6-34: Section C_C which coincides with section G from (Jennings, 1996) and TC positions 1 & 2 from (Newell, 2009). 302

Figure 6-35: Experimentally measured PDAS for six sections of the VeriCAST test geometry. Data presented by (Jennings, 1996) was cast using an assembly of four VeriCAST moulds with a hot zone reference temperature of 1798.15 K (1525^{o}C) and a withdrawal velocity of 9"hr^{-1} (6.35 x 10^{-5} ms^{-1}). Data from (Newell, 2009) and this work was cast with a hot zone reference temperature of 1803.15 K (1530^{o}C) and a withdrawal velocity of 6.36 x 10^{-5} ms^{-1}. All casts used the largest aperture 'standard' baffle, 110 x 10^{-3} m ID for the single shot Bridgman furnace. 304

Figure 6-36: Micrographs showing structure of CMSX-4 at discrete locations corresponding to thermocouple locations used in ProCAST validation work by

(Newell, 2009). The cast was produced using the experimental heating element with a hot zone reference temperature of 1803.15 K, a withdrawal velocity of 6.36 x 10^{-5} ms^{-1} and a 110 x 10^{-3} m ID baffle. 306

Figure 6-37: Estimated thermal gradient achieved when casting VeriCAST geometry using experimental heater, plotted against thermal gradient calculated by ProCAST model for identical conditions and those measured during validation work by (Newell, 2009). The furnace parameters were a hot zone reference temperature of 1803.15 K, a withdrawal velocity of 6.36 x 10^{-5} ms-1 and a 110 x 10^{-3} m ID baffle. 308

Figure 6-38: Comparison of PDAS values measured during this study for a number number of experimental conditions and heater configurations. Data obtained from work by (Jennings, 1996, Newell, 2009) also shown for comparison. Red horizontal line on graph shows minimum PDAS value below which freckling was not observed (Pollock et al., 1992). 311

Figure A-1: Alumina thermal conductivity. 329

Figure A-2: Alumina specific heat capacity. 330

Figure A-3: Alumina emissivity. 330

Figure A-4: Calcarb specific heat capacity. 331

Figure A-5: Calcarb thermal conductivity. 331

Figure A-6: COTAC 744 density 332

Figure A-7:COTAC 744 specific heat capacity. 332

Figure A-8: COTAC 744 Thermal conductivity. 333

Figure A-9: γ-γ'-δ density. 333

Figure A-10: γ-γ'-δ specific heat capacity. 334

Figure A-11: γ-γ'-δ thermal conductivity. 334

Figure A-12: Graphite specific heat capacity. 335

Figure A-13: Graphite thermal conductivity. 335

Figure A-14: Copper specific heat capacity. 336

Figure A-15: Copper thermal conductivity. 336

Figure A-16: Sigraflex specific heat capacity. 337

Figure A-17: Sigraflex thermal conductivity. 337

Figure A-18: Sigraflex emissivity. 338

Figure A-19: Stainless steel specific heat capacity. 338

Figure A-20: Stainless steel thermal conductivity. 339

Figure A-21: Zircar thermal conductivity. 340

LIST OF TABLES

Table 2-1: Comparison of turbine entry temperature, specific fuel consumption and specific weight of gas turbine engines through the years 1945-1985 (Pratt, 1986). The specific fuel consumption is calculated as the mass fuel flow rate delivered to the engine as a function of the thrust mass produced by the engine. A lower number means the engine id more fuel efficient. 11

Table 2-2: Composition in weight % of the second generation superalloy CMSX-4(Erickson, 1996) 16

Table 2-3: Reported equilibrium liquidus and solidus temperatures for CMSX-4 16

Table 2-4: Composition in weight % of two experimental eutectic alloy systems(Lemkey, 1973) 21

Table 2-5: Composition in weight % of modified eutectic alloy composition (Lemkey, 1973) 21

Table 2-6: Compositions of early NiTaC composite and successive generations of COTAC composites, (1) (Rabinovitch et al., 1983),(2) (Khan and Stohr, 1980), (3) (Damerval, 1987) 26

Table 2-7: Nominal composition of experimental alloy $\gamma - \gamma' - \alpha$ (Whittenberger and Wirth, 1982) 29

Table 2-8: Nominal compositions of several NiTaC eutectic alloys, 1) (Rabinovitch et al., 1983), 2)(Woodford, 1977), 3) (Henry et al., 2005) 30

Table 2-9: Critical G/V ratio for various alloy systems, above which plane front growth breaks down 49

Table 2-10: Selected alloys studied by (Hobbs et al., 2005) showing rank, castabiity and relative density inversion. Also highlighted are alloying elements thought to have a positive or negative effect in the formation of the freckle defect. 55

Table 3-1: Recipe for shell system and method for producing moulds for investment casting 89

Table 3-2: Grinding and polishing stages used in preparation for metallographic analysis. 99

Table 4-1: Comparison of control thermocouple temperature, in bold, and secondary thermocouple temperatures during the steady state soak period for a number of experimental trials. 119

Table 4-2: Comparison of electrical current measured using one of three input cables and measured over all three input cables. The data set includes various hot zone temperatures. 126

Table 5-1: Dimensions of parameters shown in Figure 5-2 used for the mesh sensitivity study 137

Table 5-2: Theoretical calculations for distance from reference point D to achieve a desired degree of uniformity of electrical current density in the x and y legs of the geometry 145

Table 5-3: Parameters used to calculate electrical resistance of furnace heating element. 158

Table 5-4: Furnace components, materials and material references as used in the CFX model. 176

Table 5-5: Thermal gradient for experimental furnace configurations calculated using centreline thermocouple experimental thermocouple readings. 244

Table 6-1: Mean dendrite arm spacing for a range of test bars produced using the standard and experimental heaters at a set hot zone temperature of 1823.15 K while the withdrawal velocity was varied from 6.36 – 10.67 x 10^{-5} ms^{-1}. The baffle geometry used was 110 x 10^{-3} m ID Sigraflex. The standard error is an estimation of the amount the sample mean deviates from the actual mean of a population and is estimated as s/√n, where s is the sample standard deviation and n is the number of observations. The 95% confidence interval is calculated as $x \pm 1.96 \times standard\ error$. The value of 1.96 is the normal distribution value for 95% confidence taken from normal distribution tables. 253

Table 6-2:Thermal gradients derived from mean PDAS measurements taken for all experimental casts produced with test bar cluster. 259

Table 6-3: Mean dendrite arm spacing for a range of test bars produced using the standard and experimental heaters at a set withdrawal velocity of 10.67 x 10^{-5} $ms^{-1}$with a varying hot zone temperature of 1823.15 K or 1923.15 K. The baffle geometry used was 20 x 10^{-3} m ID Sigraflex. The standard error is an estimation of the amount the sample mean deviates from the actual mean of a population and is estimated as s/√n, where s is the sample standard deviation and n is the number of observations. The 95% confidence interval is calculated as $x \pm 1.96 \times standard\ error$. The value of 1.96 is the normal distribution value for 95% confidence taken from normal

distribution tables. 262

Table 6-4: Thermal gradient measurements derived from mean PDAS measurements for all experimental conditions. The constant furnace parameters were a withdrawal rate of 10.67 x 10^{-5} m.s^{-1} and 20 x 10^{-3} m ID baffle. 267

Table 6-5: Estimated thermal gradient achieved using standard and experimental heating elements for two eutectic alloys. The furnace parameters used were a double layer 20 x 10^{-3}m ID sigraflex baffle and hot zone reference temperatures of 1823.15 K and 1923.15 K. Calculations were made using CFX model with additional domain geometry to represent alloy, mould, chill and ram. Eutectic material data was calculated using JMatPro. 270

Table 6-6: Summary of withdrawal velocity and G/V ratio on the microstructure of COTAC 744 alloy 278

Table 6-7: Results of PDAS evaluation for two locations at the bottom, middle and top of the VeriCAST aerofoil section. CRDF and SS002-10 data obtained from (Newell, 2009), results using the experimental heater from this work. All casts we carried out using the same nominal furnace conditions; hot zone reference temperature of 1803.15 K, 110 x 10^{-3} m ID radiation baffle and a withdrawal velocity of 6.36 x 10^{-5} ms^{-1}. 297

Table 6-8: PDAS values measured during this study at discrete locations in the VeriCAST test geometry. 303

Table 6-9: Measured PDAS values at various points in a cast using the VeriCAST using the experimental heater with a hot zone reference temperature of 1803.15 K, a

withdrawal velocity of 6.36 x 10^{-5} ms^{-1} and a 110 x 10^{-3} m ID baffle. Positions reflect in-situ thermocouple measurements made by (Newell, 2009). 305

FREQUENTLY USED ABBREVIATIONS AND SYMBOLS

TET	Turbine Entry Temperature
TBC	Thermal Barrier Coating
DS	Directional Solidification
TCP	Topologically Close Packed
FCC	Face Centred Cubic
PDAS	Primary Dendrite Arm Spacing
DAS	Dendrite Arm Spacing
ZIO	Zone Intensified Overheating
LMC	Liquid Metal Cooling
CFD	Computational Fluid Dynamics
FEA	Finite Element Analysis
UTC	University Technology Centre
CRDF	Company Research and Development Facility
HPC	High Performance Computing
GCC	Gas Cooling Casting
A	Area
G	Thermal Gradient
V	Velocity
λ_1	Primary Dendrite Arm Spacing
N	Number (of)

CHAPTER 1 INTRODUCTION

The modern gas turbine is arguably one of the most remarkable engineering achievements of the last century.

The birth of the modern aero engine is often attributed to Sir Frank Whittle although others also deserve credit for technological contributions to the field. Maxime Guillaume patented an idea for an axial jet engine in 1922; Hans von Ohain proposed a turbojet with both an axial and centrifugal compressor and was the first jet engine to fly in 1939. However it was Frank Whittle's patent for a turbojet proposed in 1928 that became the most widely available and studied.

In 1943 Rolls-Royce took over development of the Whittle W.2B engine and 1 year later was in active service powering the Gloster Meteor which was the only allied jet aircraft to see active service in World War II (Rolls-Royce, 1986).

Interest in jet engines at the time was naturally geared towards military applications where speed was the most critical characteristic; however during post-war years the use of jet engines for civilian applications became of significant interest where speed was of less concern and the need for more efficient engines would become the driving force. Today efficiency is the selling point of many modern engines such as the Trent 1000 and Trent XWB.

Despite the significant evolution in materials used for construction of modern civil or military jet engines the fundamental principles have remained unchanged. The modern turbofan engine is a derivative of the turbojet engine which bears the most resemblance to the original concept.

A modern turbojet engine contains an axial compressor comprising rows of blades which act to slow and squeeze air entering the engine and subsequently increase the air pressure. The air is then fed into a combustor where it is mixed with vaporised fuel and ignited. The ignition of the fuel air mixture causes a rapid pressure and velocity change and the expanding gas is forced out of the combustor through a turbine as its pressure drops towards atmospheric. The turbine acts to extract mechanical energy out of the expanding gas stream which subsequently leaves the back of the engine driving the aircraft forward.

The energy captured by the turbine is transmitted to the compressor via a central shaft and a reciprocal cycle is set up given that fuel energy is continually added in the combustor.

In a modern turbofan engine a large fan is added at the start of the compressor stage which acts to force a large volume of air to bypass the core of the engine at a relatively low velocity; this maximises the propulsive efficiency of the engine, reducing specific fuel consumption but at the cost of speed.

The increased complexity of additional fans and optimal rotational velocity of compressor and turbine stages has led manufacturers to increase the number of shafts transmitting mechanical energy from the turbine stages to the compressor stages.

Rolls-Royce large civil engines have a three shaft configuration; the HP compressor connects to the HP turbine, both are immediately next to the combustion chamber, the IP compressor connects to the IP turbine, and finally the LP compressor, also known as the fan, connects to the LP turbine.

The primary stage in extracting mechanical energy form the gas stream is that of the HP turbine and the evolution of turbine blade technology has been necessitated by the requirement to raise the turbine entry temperature (TET) to achieve optimal engine

efficiency and reduce specific fuel consumption.

The developments in turbine blade technology have been realised by a number of means;

- The change from wrought to cast blades (Reed, 2006). This also prompted the move towards net-shape manufacturing by allowing more intricate geometries to be produced.

- The introduction of blade cooling technologies

- Elongated crystals orientated such that the elastically soft [001] crystallographic direction is coincident with the direction of maximum load.

- The removal of grain boundaries and grain boundary strengthening elements by producing single crystal (SX) components

Further increase in the TET is difficult and relies heavily on process optimisation of current SX casting techniques or new alloy development such as eutectic alloys.

Nickel based single crystal blades are produced using the Bridgman method, the name derived from the Bridgman-Stockbarger crystal growing technique. The industrial variant of this is often called the high rate solidification process (McLean, 1983) and is used by Rolls-Royce to cast single crystal turbine blades (Goulette et al., 1984).

All furnaces rely on a process in which a mould is held in the mould chamber (hot zone) at a temperature above the liquidus temperature of the alloy and withdrawn through an interface into a cooling chamber (cold zone) in which heat is extracted by radiation. The

interface between the hot and cold zones should be as close to adiabatic as practically possible with respect to radiation heat transfer and is often achieved with radiation baffling.

Furnace designs are based on the requirement to produce multiple components for a given cycle; the small bore furnace is a Rolls-Royce experimental furnace capable of casting multiple component geometry (Jennings, 1996) whereas the single shot furnace located at the University of Birmingham is restricted to single components, however the benefits of this type of furnace is the potential to offer significantly higher thermal gradients than industrial scale units.

Current methods of increasing the thermal gradient are fairly intuitive; modifying the heat input in the hot zone, maximising the effectiveness of the interface region or increasing the rate of heat extraction in the cold zone.

Research carried out thus far (Newell, 2009) has experimented with optimised radiation baffling while simultaneously developing a process model using the ProCAST software. The research showed that extensive radiation baffling could increase the thermal gradient.

The process model was validated using two baffle configurations, and results highlighted that the furnace hot zone was not constant but was dependent on the baffle configuration used and as such two separate thermal profiles were used in order to validate the ProCAST model. The understanding of the furnace hot zone temperature profile is currently limited to these validated conditions.

Methods to increase the rate of heat extraction in the cold zone include liquid metal cooling (LMC) and in this context optimisation of the hot zone temperature profile are becoming increasingly relevant as developments in the technology, such as Zone

Intensified Overheating Liquid Metal Cooling (Liu et al., 2008, Liu et al., 2010) demand increased local superheats in order to stabilise the solidification front. Should LMC or an equivalent technology be used on an industrial scale, optimisation of the hot zone temperature profile will be equally as relevant.

Increasing the thermal gradient has multiple benefits; firstly in single crystal alloys the propensity for freckle formation will be reduced by minimising the segregation of elements (Pollock and Murphy, 1996, Pollock et al., 1992) and heat treatments used to homogenise the microstructure due to such segregation can be optimised. Secondly, alternative alloys such as eutectics can be proposed as future materials given assessment of the casting capability.

The aim of this work therefore will be as follows:

- Assess the effect that baffle configurations have on the hot zone temperature profile using a fully validated CFD based method in order to further the understanding of the current ProCAST model.

- Use the understanding gained to develop a method of improving the thermal gradient in conditions where extensive radiation baffling is limited.

- Assess the mechanical properties of candidate eutectic alloy systems with respect to current single crystal alloys using historical data.

- Use modelling and experimental techniques to assess the capability of the single shot furnace to cast such alloys.

CHAPTER 2 LITERATURE REVIEW

2.1 Turbine blade operating conditions

The main factors determining the operating conditions under which the turbine blade of a modern gas turbine engine are subjected are the Turbine Entry Temperature (TET), pressure, gas flow composition and the resultant centrifugal stresses (Tamarin, 2002); all of which will vary cyclically during a typical flight.

During takeoff, TET can be in excess of 1500 °C (Cumpsty, 1997) at which point the blade metal temperature would typically be in the region of 1050–1120 °C (Fullagar et al., 1996). The temperature then gradually decreases through cruise and flight idle stages until landing and reverse thrust, at which point the TET is again raised significantly. Even so, during the least intensive stages of a flight cycle, the blade metal temperature will still be above 550 °C (Fullagar et al., 1996) in which case Ni-base alloys are exclusively used (Williams and Starke, 2003). It has been shown for aircraft systems that about 20% of the flaws developed in operation are as a result of this cyclic temperature variation (Tamarin, 2002).

The life of a turbine blade is limited by creep, oxidation resistance or by thermal fatigue (Cumpsty, 1997), and as the peak TET gas temperature is in excess of the alloy melting temperature the use of advanced Thermal Barrier Coatings (TBC's) and internal cooling channels are required to retain structural integrity (Rolls-Royce, 1986). For this reason, single crystal Ni-base alloys, which are predominantly used for turbine components, are not only developed for high temperature creep resistance, of which only a few percent creep strain can be tolerated, but also for compatibility with thermal barrier coatings.

2.2 Move to directional solidification

Development of alloys and processing techniques has progressed markedly since the invention of the gas turbine; early metallurgical improvements can be attributed to the introduction and optimisation of solid solution and γ'strengthened nickel-base superalloys (McLean, 1983), and a combination of metallurgical, processing and design improvements in subsequent years.

Early turbine blades were produced in either wrought or cast form with negligible difference in performance between the two processes, however with the introduction of vacuum induction casting technologies in the 1950's the quality and cleanliness of the alloys were improved dramatically by removing unwanted alloy constituents (Reed, 2006), vastly improving the quality of both wrought and cast blades.

The process of casting turbine blades has several advantages however; firstly, casting components allows the incorporation of air cooling channels, in which air from the compressor is diverted through the turbine blade to offer additional cooling. Secondly, casting allows an increase in the volume fraction of the γ'precipitates and the temperature in which they dissolve in the γ matrix (McLean, 1983). On the contrary, wrought superalloys could only be produced with limited amounts of γ'precipitates due to temperature constraints during the processing (McLean, 1983).

Turbine blades were initially cast with an equiaxed microstructure in which crystals of a random orientation are nucleated in an undercooled isothermal melt i.e. the local growth direction and heat flux proceeds in all directions. This results in a polycrystalline solid composed of randomly orientated grains with a dendritic morphology (Kurz and Fisher, 1989).

It was further noted that the grains grow along preferred crystallographic directions <001> and with an applied directional heat flux will grow in a preferred direction. Due to the higher growth rate of these grains, they dominate the solid/liquid interface morphology, and so overgrow the randomly orientated outer equiaxed grains which will initially form on the mould walls, therefore leading to a columnar grain structure (Kurz and Fisher, 1989).

This technique, often called Directional Solidification (DS), was applied to the processing of turbine blade alloys with the aim of reducing grain boundaries that were transverse to the applied stress as it was shown that mechanical properties were greatly improved when grains were produced parallel to the stress axis. The improvement was as a result of inhibited grain boundary fracture (Vernsnyde and Guard, 1960) which was also attributed to alloying additions such as B, Zr and Hf (Williams and Starke, 2003).

It was a natural progression to remove grain boundaries, longitudinal or otherwise, completely and produce single crystal structures which give the best creep performance due to the fact that grain boundary deformation would not take place and failure mechanisms would be limited to dislocation climb and glide, Figure 2-1.

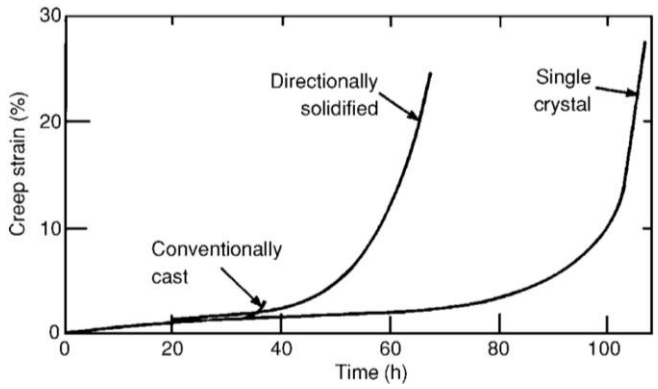


Figure 2-1: Creep strain evolution with time for conventionally cast (equiaxed), directionally solidified (columnar) and single crystal specimens of Mar-M200 subjected to a stress of 206 MPa at 982°C (Kear and Piearcey, 1967)

Production of single crystal components could use existing DS furnace technology and only required changes in mould design to ensure growth of a single crystal. The simplest method to achieve this being the use of a crystal selector shown in Figure 2-2 a) which is based upon competitive dendritic growth through a restrictive passage and takes advantage of the $< 001 >$ growth direction of cubic crystals (Goulette et al., 1984), this also allowed the minimisation of cyclic stresses as the crystal is orientated parallel to the maximum load (McLean, 1983).

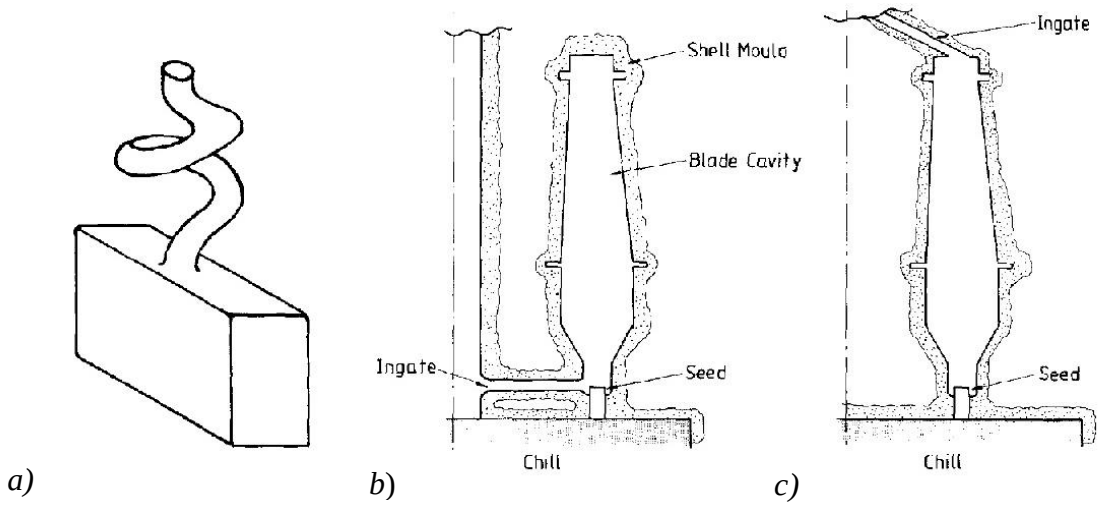


Figure 2-2: a) Spiral single crystal selector (Pig tail) design, b) Bottom run seeded mould design, c) Top run seeded mould design. Both seeded moulds showing single crystal seed adjacent to the chill (Goulette et al., 1984)

The use of spiral crystal selectors however can result in fragile mould assemblies and great care must be taken to ensure the longitudinal orientation of the crystal lies with a tolerable range. A more technically difficult approach is that of component seeding, in which a seed crystal is inserted into a prepared mould in order to initiate single crystal growth as shown in Figure 2-2 b) & c).

The advantage of a seeded mould is that the precise orientation of the crystal can be set before solidification of the main component, something not possible with a spiral selector.

Even with the superior mechanical properties offered by advancements in alloy chemistry and processing, the incipient melting temperature of an alloy system represents a limit to the temperature that can be withstood and as such the TET increases have only been possible due to the introduction of Thermal Barrier Coatings (TBC's). The use of advanced coatings results in a reduction in the metal surface temperature (and hence a greater temperature differential when compared to the TET) and also offers greater oxidation resistance (Miller, 1987, Miller, 1997).

The TBC generally consists of bond coat, which is typically $MCrAlY$ (where $M \equiv Ni, Co\ or\ NiCo$) which provides a bond between the alloy surface and subsequent ceramic layer and is intended to mitigate spallation due to difference in thermal expansion between the two (Miller, 1987, Reed, 2006). From the bond coat a thermally grown layer of Al_2O_3 is formed during thermal cycling and prevents oxidation of the alloy substrate and on top of this layer the $ZrO_2 - (6\% - 8\%)Y_2O_3$ ceramic layer is applied to provide thermal protection due to its low thermal conductivity.

Owing to the combined efforts of improved alloy chemistry, optimised processing conditions and use of surface engineering techniques; over a 50 year period there has been a significant increase in the TET of civil gas turbine engines, Figure 2-3.

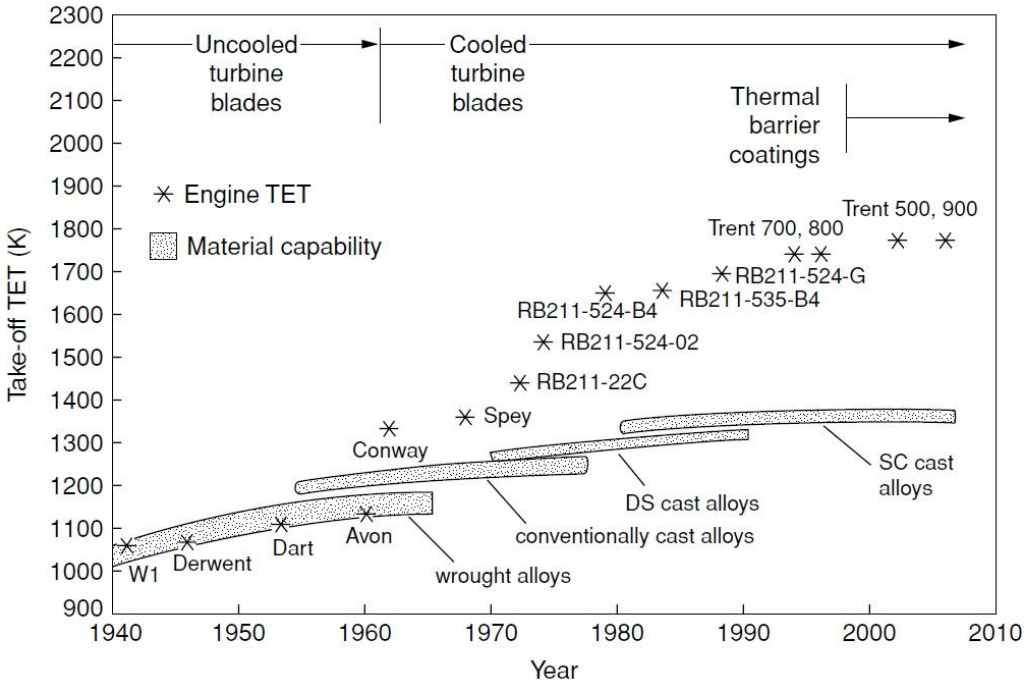


Figure 2-3: Turbine entry temperature of Rolls-Royce civil engines, 1940-2006. Figure obtained from (Reed, 2006) adapted from (Cumpsty, 1997).

Increasing the TET allows engines to run more efficiently by reducing specific fuel consumption while increasing the maximum thrust capability. As shown in Table 2-1, during the 40 years spanning 1945-1985 the TET of gas turbine engines increased by around 70%, while specific fuel consumption and specific weight decreased markedly, highlighting the importance of TET on the combustion process.

Table 2-1: Comparison of turbine entry temperature, specific fuel consumption and specific weight of gas turbine engines through the years 1945-1985 (Pratt, 1986). The specific fuel consumption is calculated as the mass fuel flow rate delivered to the engine as a function of the thrust mass produced by the engine. A lower number means the engine id more fuel efficient.

Year	Turbine entry temperature, °C	Specific fuel consumption, (kg/hr)/kg	Specific weight, kg/kg
1945	800	0.854	0.8
1985	1350	0.4	0.2

2.3 Interest in eutectic alloys

The evolution of the directional solidification process allowed metallurgists to understand how to produce microstructure that contributed to the mechanical strength of the alloy. In the 1960's it was proposed that the technique of directional solidification could be applied to alloys that solidified to produce two or more solid phases, by eutectic reaction, and a new class of material was developed (McLean, 1983). The word eutectic is a literal translation of the Greek word 'eutektos' meaning easily melted.

Using this processing method a composite material is produced; generally with a strong reinforcing phase and a more ductile matrix. The composite microstructure is produced 'in-situ' as one process so this class of material is often referred to as 'in-situ composites'

A eutectic system is a mixture of elements; know as a eutectic composition, in such a proportion that the mixture solidifies at the lowest temperature, known as the eutectic temperature, than any other mixture of the same elements. The intersection of these lines on the phase diagram is known as the eutectic point as shown in Figure 2-4.

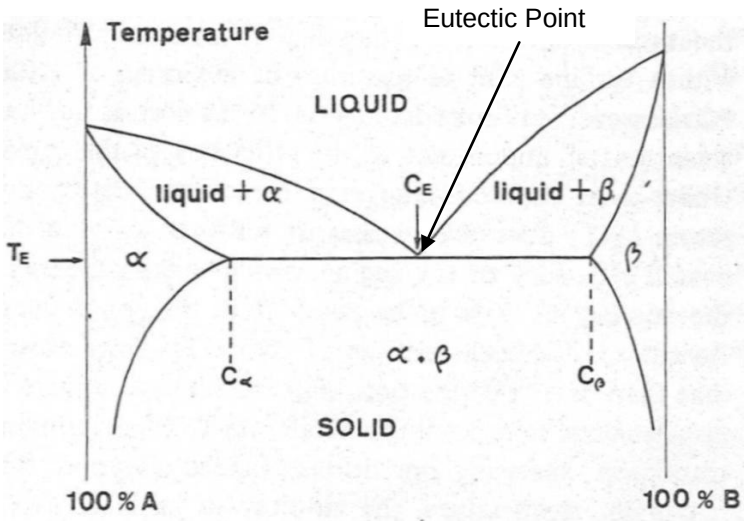


Figure 2-4: Binary eutectic phase diagram highlighting eutectic temperature, eutectic point and eutectic composition (Stohr and Khan, 1980).

In the case of a binary eutectic; when a liquid of eutectic composition is solidified under a positive thermal gradient, two phases grow simultaneously and perpendicular to the solidification front. To obtain a composition with a regular microstructure, the melting isotherm needs to remain planar and the solidification speed constant (Stohr and Khan, 1980).

Many eutectics when solidified possess fine, uniform, rod or lamellar structures; although other structures described as broken lamellar, globular and acicular have also been reported (Flemings, 1974). However for many eutectic alloys of engineering interest, lamellar or rod microstructures are preferred due to the desire to obtain alloys with regular morphology and a continuous strengthening phase.

A great deal of work was carried out in the 1930's to summarise the main features of eutectic microstructures and, as such, two broad classifications were defined; normal and abnormal eutectic microstructures (Hogan et al., 1971).

Normal microstructures mainly comprise the lamellar or rod microstructures and are formed by the simultaneous growth of two solid phases at an equal growth velocity, whereas abnormal microstructures are formed when the two solid phases are prevented from growing at an equal linear velocity, in which case rod or lamellar growth is not possible.

A number of observations have been made to account for the fact that two microstructures are able to form; a common feature being that the phases present in a lower volume fraction grows at a higher velocity and creates a pseudo-dendritic pattern in the melt (Hogan et al., 1971).

A concept defined to assess the probability of obtaining a normal or abnormal

microstructure is that of the coupled zone. The concept merely states that when a normal structure is formed it is usually found that the two solid phases are present in more or less equal proportion by volume, whereas when the liquidus lines are skewed, an abnormal microstructure will be formed (Davis, 1996).

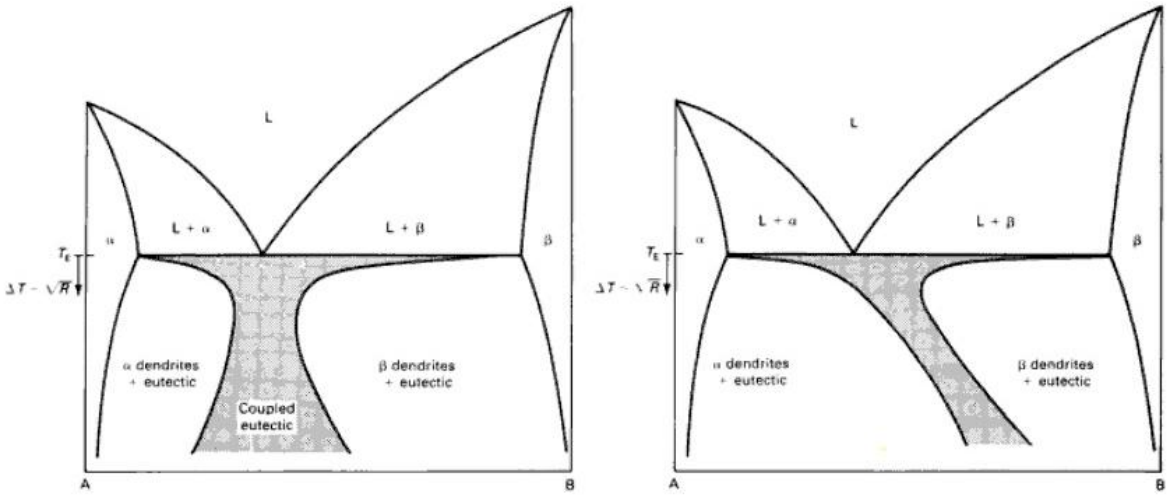


Figure 2-5: Coupled zone (shaded region) on eutectic phase diagram. a) Symmetric and probable normal microstructure. b) Skewed and probable abnormal microstructure (Davis, 1996)

A more detailed approach was presented by (Jackson and Hunt, 1966), relating eutectic microstructure to the morphology of the individual phases. Two phases were defined; non-faceted and faceted phases. Non faceted phases solidify via an atomically rough solid/liquid interface and are isotropic in terms of crystal growth direction, whereas faceted phases arise from an atomically smooth solid/liquid interface and grow in a preferential crystallographic direction (McLean, 1983). This in turn led to three general combinations of morphology to be proposed;

- Non-faceted/non-faceted in which either rod or lamellar can be obtained depending on the relative volume fractions in the melt. This type of combination is the most adequately defined by theoretical work and is entirely determined by diffusion in

the liquid.

- Faceted/non-faceted is a category in which most composites of industrial importance fall. The faceted phase usually accounts for the smaller volume fraction strengthening phase and given sufficient solidification conditions, such as low solidification velocity and sufficient thermal gradient, is very similar to the non-faceted/non-faceted case and theoretical comparisons can apply.
- Faceted/faceted is a combination that is unlikely to produce a microstructure that is consistent enough to be used as a composite material.

The need for composite materials, eutectic or otherwise, was self-evident at the time as the precipitation strengthened superalloys had reached a plateau in thermo-mechanical performance. The prospect of producing composite materials, by eutectic reaction, was particularly attractive; well understood directional solidification technology could be used and the single stage process produces composite materials that are relatively thermodynamically stable (McLean, 1983).

From the late 1960's to the 1980's significant research was carried out in the development of eutectic alloys as the potential mechanical properties matched or exceeded those of superalloys of the time. Research soon dwindled however once the beneficial effects of Rhenium (Re) were understood and utilised in single crystal alloys. That said, since the incorporation of Re in present day superalloys, there have been developments involving Re incorporation into eutectic alloy systems such as later developments in the COTAC series with COTAC 784 and the NiTaC series with NiTaC 13 and 14B.

2.4 Survey of selected nickel based superalloys

This section will provide a summary of the metallurgical aspects of a range of single crystal and eutectic alloys.

2.4.1 CMSX-4

CMSX-4 (Harris et al., 1992, Harris and Erickson, 1987) is a second generation nickel based superalloy patented by the Canon Muskegon Corporation and has received co-operative development, notably by companies such as Rolls-Royce, as the use of the alloy has grown (Harris and Wahl, 2004). The commercially available composition is shown in table Table 2-2.

Table 2-2: Composition in weight % of the second generation superalloy CMSX-4(Erickson, 1996)

Alloy	Cr	Co	Mo	W	Ta	Re	Nb	Al	Ti	Hf	Ni	Density ($g.cm^{-3}$)
CMSX-4	6.5	9.0	0.6	6.0	6.5	3.0	-	5.6	1.0	0.1	Bal.	8.70

The non-equilibrium liquidus and solidus temperatures of CMSX-4 are open to dispute; predominantly due to the complex nature of the solidification process and local compositional variations due to phase changes during cooling. However a range of values has been established and used in previous work as shown in Table 2-3.

Table 2-3: Reported equilibrium liquidus and solidus temperatures for CMSX-4

Alloy	$T_{Liquidus}$ (°C)	$T_{Solidus}$ (°C)	Reference
	1360	1270	(Carter et al., 2000)
CMSX-4	1385	1314	(Hooper, 2001)
	1381	1329	(Elliott and Pollock, 2007)

Further alloy development by Cannon Muskegon Corporation led to the development of CMSX-10 (Erickson, 1994) which has been studied collaboratively with Rolls-Royce (D'Souza and Dong, 2007, D'Souza and Dong, 2008); also known as, or a variant of, RR3000 (Hooper, 2002). This alloy is similar in metallurgy to CMSX-4 so will not be discussed at length here, other than to note that with modifications to the alloy composition, notably the increased weight % of alloying elements such as Re, CMSX-10 exhibits superior creep performance in relation to CMSX-4 (Erickson, 1996).

A point that is relevant for this work is that CMSX-10 has an increased susceptibility to freckling when compared to CMSX-4 (Hobbs et al., 2005) and will be discussed in the relevant section.

The as cast microstructure of the alloy exhibits a dendritic morphology (given the correct processing conditions) and can be broadly thought to compose of a mixture of Ni-rich gamma (γ) interspersed with gamma prime dendrites (γ') and interdendritic ($\gamma - \gamma'$) eutectic.

In practice however the as-cast microstructure is highly segregated due to the complex nature of the alloy and the behaviour upon solidification. During the initial stages of solidification the first solid to form is enriched with higher melting point elements such as W and Re, forming the dendrites; subsequently the liquid in the 'mushy zone' (transient region between solid and liquid) becomes depleted of these elements and instead becomes enriched with lower melting point element such as Al, Ta and Ti forming the interdenritic region (Walter et al., 2005). Due to this compositional gradient a great degree of microstrucural anisotropy is present in the as-cast material.

Due to this as cast heterogeneous nature of the material, solution heat treatment is required in order to homogenise the microstructure; with the fully heat-treated microstructure consisting of a γ base phase containing ordered cuboidal γ' precipitates of the $L1_2$ structure to a maximum volume fraction of around 70% (Zambaldi et al., 2007). The γ'phase is based on Ni_3Al in the form $(Ni, Co)_3(Al, Ti, Ta, Nb)$ and dissolved Cr, W and Ti (Reed, 2006).

A determining factor of the mechanical properties of Ni-base superalloys is the volume fraction and morphology of the γ' phase (Sims, 1984), particularly in creep resistance. The reason for this is that creep deformation is limited to the channels in the γ matrix between the γ' precipitates; therefore in order to increase the creep strength of the alloy it is logical to increase the volume fraction of the γ' phase in order to reduce the area in the γ matrix and inhibit creep propagation.

The favourable mechanical properties obtained by volume fraction additions of the γ' phase reached a plateau of around 70%. This is no coincidence. Some strengthening is attributed to the $\gamma - \gamma'$ interface rather than just dispersed hard precipitates and above a γ' volume fraction of around 70% the creep strength diminishes (Murakumo et al., 2004). A high volume fraction of γ' is achieved by introducing high levels of γ' hardening elements such as Al and in particular Ta which also acts to reduce the susceptibility to freckle formation.

In order to maintain the mechanical strength of such an alloy, coarsening of the γ' phase must be restricted which can be achieved in a number of ways; firstly, it has been shown that reducing the lattice misfit (δ) minimises the $\gamma - \gamma'$ interfacial energy ensuring that γ' coarsening is restricted (Ford and Arthey, 1986, Kuhn et al., 1991, Reed, 2006), where δ is

defined as (Reed, 2006);

$$\delta = 2 \times \left[\frac{a_{\gamma'} - a_{\gamma}}{a_{\gamma'} + a_{\gamma}}\right] \qquad 2.1$$

where a is the lattice parameter measure in nanometres (nm).

In the case of CMSX-4 the lattice misfit has been defined as -0.6782×10^{-3} and -1.8107×10^{-3} at 25°C and 1100°C respectively (Pyczak et al., 2004) and will result in compressive stresses in the γ matrix thus countering any applied tensile stress and reducing the overall operating stress in the γ channels. The misfit has been shown to become more negative with temperature (Bruno and Pinto, 2004, Pyczak et al., 2004).

Secondly; it has been shown that the addition of Re helps stabilise the γ' phase, as during solidification Re is rejected due to its slow diffusion rate in nickel and builds up at the $\gamma - \gamma'$ interface (Broomfield et al., 1998). It has been proposed that the most effective strengthening elements are those that diffuse slowest in nickel; such as Re, W and Ta (Reed, 2006).

High levels of these elements however can lead to precipitation of Topologically Close-Packed (TCP) phases and have been shown to be detrimental to the creep life of an alloy as strengthening elements are constrained in the TCP phase. It has been shown that the addition of Ruthenium (Ru) can alleviate this effect by so-called "reverse partitioning" causing many of the refractory elements to partition more strongly to the γ' phase thus allowing more refractory elements to be added to improve strength (Walston et al., 2004), although this effect is still not fully understood (Reed, 2006).

Levels of Re in CMSX-4 and CMSX-10 are 3.0 and 6.0 weight % respectively.

2.4.2 γ-γ'-δ

Various alloy systems from the $Ni - Al - Nb$ ternary system have been comprehensively examined in various works. The $Ni - Al - Nb$ system has two binary eutectics; $Ni - Ni_3Al$ and $Ni - Ni_3Nb$ and a pseudo-binary eutectic $Ni_3Al - Ni_3Nb$. Monovariant troughs from these eutectics converge at the ternary eutectic $Ni - Ni_3Al - Ni_3Nb$ (Lemkey, 1973, Rabinovitch et al., 1983). All variations of this alloy produce an intermetallic strengthening phase within a ductile matrix, where the volume ratio of the strengthening phase to matrix is sufficiently high to produce a lamellar structure.

The pseudo-binary eutectic $Ni_3Al - Ni_3Nb$ and ternary eutectic $Ni - Ni_3Al - Ni_3Nb$ attracted significant interest from researchers in the 1970's investigating the alloys mechanical properties for its potential application in high temperature environments (Gangloff and Hertzberg, 1973, Kraft and Thompson, 1973, Thompson et al., 1972), and also the alloy potential use as high temperature fasteners for use in the space programme as at the time the alloy was the strongest nickel based alloy known (George, 1972).

However the pseudo-binary eutectic $Ni_3Al - Ni_3Nb$ suffered from poor low temperature ductility which could be improved as long as the microstructure had a low fault density and the lamellar spacing was not decreased by increased solidification rate, however the ternary eutectic $Ni - Ni_3Al - Ni_3Nb$ had an inherently greater ductility (Kraft and Thompson, 1973).

It was noted that improvements in the alloy oxidation resistance would benefit its utility as a high temperature turbine components and would be permissible as Cr and Al are both soluble in nickel. Based on studies made of the high ductility of the $Ni - Ni_3Nb$ system, a study of the $Ni - Nb - Cr - Al$ system was undertaken and subsequently the addition of

Cr was made to selected compositions (Lemkey, 1973).

Two quaternary alloys were studied of varying compositions were studied as shown in Table 2-4. The phases of these alloys generally being a Cr enriched γ matrix strengthened by γ' precipitates of Ni_3Al and reinforced by lamellae of the δ phase Ni_3Nb.

Table 2-4: Composition in weight % of two experimental eutectic alloy systems(Lemkey, 1973)

Alloy	Ni	Nb	Cr	Al
1	Bal.	19.7	9.0	1.0
2	Bal.	20.0	6.0	2.5

When investigating the mechanical behaviour of the composites, a slight reduction in the Nb content was made to the lower Cr composition in order to improve the low temperature ductility and an improved composition was developed as shown in Table 2-5. However more stringent growth conditions were required than for the pseudo-binary $\gamma' - \delta$ alloy which has a critical G/V ratio of $< 0.23\ °C\ hr\ mm^{-2}$ compared to $1.50\ °C\ hr\ mm^{-2}$ for the quaternary alloy.

Table 2-5: Composition in weight % of modified eutectic alloy composition (Lemkey, 1973)

Alloy	Ni	Nb	Cr	Al
3	Bal.	19.7	6.0	2.5

Selected area diffraction indicated the preferred growth was $[1\bar{1}0]\gamma \| [100]\delta$, the interface plane was parallel to $(111)\gamma$ and $(010)\delta$. The structure and chemical homogeneity of the alloy was found to be uniform along a section 150 mm in length, grown at 30 mm hr^{-1} in a high temperature gradient water cooled furnace (Lemkey, 1973).

The failure mechanisms observed for the alloy under longitudinal tensile conditions was by twinning and slip; when tensile stress was applied parallel to the $[100]\delta$ direction, the Ni_3Nb phase plastically deformed by twinning on the (211) planes and slip on the (010) plane up to a temperature of approximately 1000 °C, Figure 2-6. Above 1100 °C other twin planes were operable and broader twins were observed.

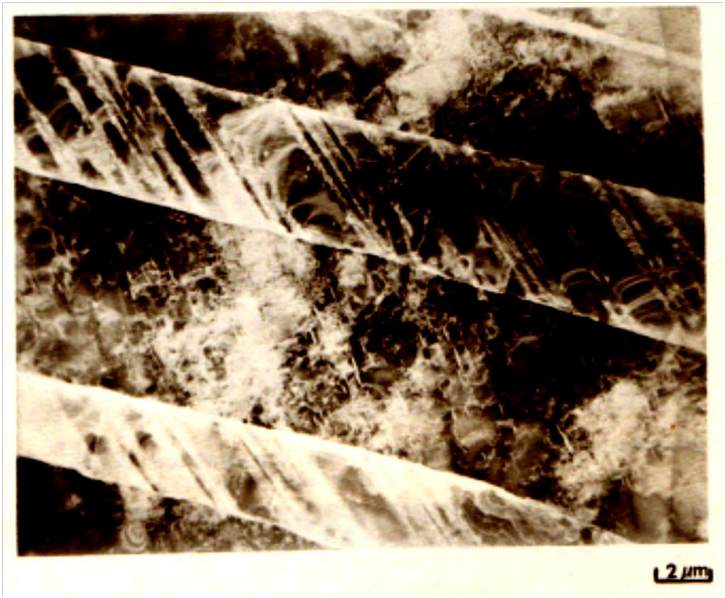


Figure 2-6: Both [211] twinning and (010) slip deformation modes exhibited in the Ni^3Nb phase after 5% total strain in room temperature tensile test (Lemkey, 1973)

Ductility of the alloy was good when loaded parallel to the $[100]\delta$ plane at all temperature intervals from room temperature up to 1235 °C, however under transverse conditions the alloy exhibits virtually no transverse ductility due to the nature of the reinforcement mechanism.

Perhaps one of the most detrimental shortcomings of this alloy is the intrinsic lack of shear creep resistance, due to delamination of the lamellae structure (Stohr and Khan, 1980). As turbine blades are fixed to the turbine disk using a 'fir tree root' that would be parallel to the direction of the strengthening phase; shear stress arising from centrifugal forces could

lead to premature failure of the blade in an operational environment.

The alloy exhibits an inherent resistance to oxidation and hot corrosion due to the high Cr content however, as with current single crystal alloys, it was recommended that thermal barrier coatings should be used in order to protect against thermal fatigue and maximise oxidation protection. The pack aluminide coatings $NiCrAlY$ and $NiCrAlY/Pt$ were applied to $\gamma - \gamma' - \delta$ test pieces for oxidation and thermal fatigue testing at cycles between 1088-316 °C with no apparent coating failures for all but one test piece over 7500 cycles and a low weight loss of between 0.07 to 0.34%, (Hill and Humphreys, 1977). The single test piece failure was attributed to longitudinal cracking initiating from the mounting fixture and may be an indication of sensitivity to the mechanical fixation method. Neither coating adversely affected the fatigue resistance.

2.4.3 COTAC

The study of composites containing γ-metal carbides or $\gamma - \gamma'$ metal carbides began at ONERA (*Office National d'Etudes et Recherches Aérospatiales*) in the late 1960's with the research of pseudo-binary eutectics of Co, Ni or Fe containing mono-carbides of the transition metals TaC, NbC and TiC (Rabinovitch et al., 1983).

The first alloys of note were named COTAC 3 and NiTaC 5 and could be considered γ-metal carbides. The names associated with these alloys were given as a consequence of the alloy composition; COTAC 3 consisted of a cobalt base and tantalum carbide strengthening phase and NiTaC, a nickel base and a tantalum carbide strengthening phase.

The resistance of COTAC 3 to creep was encouraging; however the alloy exhibited low strength in the temperature range 700-800 °C in comparison to γ'-strengthened nickel base

superalloys. This limitation was overcome by heat treating the alloy, thus producing an exceptionally high strength up to 1100 °C and hence COTAC 33 was developed.

A problem with both alloys was their intrinsic instability during thermal cycling which resulted in fibre degradation. Two mechanisms were observed for this phenomenon; if the maximum cycling temperature was rather low, the thermal expansion mismatch between the phases would cause plastic deformation and fibre rupture may take place due to this mechanical effect. Conversely if the maximum cyclic temperature was high plastic deformation would also help the diffusion controlled degradation of the reinforcing phase through the formation of serrations (Bibring et al., 1976).

One failure mechanism observed, that was associated with fibre failure, during an in-situ tensile test were shear planes originating in the matrix. It was surmised that the probable mechanism was the formation of dislocation pile-ups adjacent to the strengthening fibre resulting in local stress concentrations. Under such conditions the local stress becomes sufficiently high to propagate cracks in the monocrystaline carbide fibre; the cracks can then propagate under the influence of the applied stress and lead to failure as shown in Figure 2-7.



Figure 2-7: Dislocation pile-ups against a tantalum carbide fibre in the COTAC 3 composite during an in-situ tensile test (Stohr and Khan, 1980)

It was recognised that the essential component in optimising the allot performance during thermal cycling and isothermal creep was the hardening of the matrix in order to limit plastic strain. In the case of COTAC 3 which consisted of a Co matrix, this was achieved by a fine and homogenous precipitation of Ta carbide and was further refined in COTAC 33 with solid solution hardening by the addition of 5 weight % of tungsten. However a plateau in performance was achieved with the Co matrix and this led to the abandonment of a Co matrix in favour of Ni.

The advantage of a Ni-matrix is that it could be efficiently hardened by the precipitation of the γ' phase in solid solution by the addition of W and Mo (Stohr and Khan, 1980) and for this reason the association of alloy name to composition ended shortly after COTAC 33,

and subsequent alloys in the COTAC series were Ni based as shown in Table 2-6.

Table 2-6: Compositions of early NiTaC composite and successive generations of COTAC composites, (1) (Rabinovitch et al., 1983),(2) (Khan and Stohr, 1980), (3) (Damerval, 1987)

Alloy	Cr	Co	Mo	W	Al	Y	Ta	Re	Nb	B	C	Ni
COTAC 3 [(1)]	20.0	Bal.	---	---	---	---	12.8	---	---	---	0.78	10.0
NiTaC 5 [(1)]	10.0	20.0	---	10.0	3.0	---	9.0	---	---	---	0.4	Bal.
COTAC 74 [(2)]	10.0	20.0	---	10.0	4.0	---	---	---	4.9	---	0.6	Bal.
COTAC 744 [(2)]	4.0	10.0	2.0	10.0	6.0	---	---	---	3.8	---	0.47	Bal.
COTAC 784 [(3)]	4.0	10.0	2.0	4.0	6.5	0.2	---	4.0	4.0	100ppm	0.4	Bal.

The evolution of the COTAC series resulted in COTAC 74 and incorporated a Ni precipitation strengthened matrix and the replacement of $Ta - C$ with $Nb - C$, allowing an increase in the volume fraction of reinforcement fibres and a decrease in density. The weak point of COTAC 74 was its creep performance under high stress in the medium temperature range and also the intrinsic sensitivity to fibre degradation during thermal-cyclic-creep. Tests were conducted to examine the alloy under aero engine operating conditions and at 1070 °C under a stress of 120 MPa the life was in the order of 500 hours which was deemed acceptable; however when conducted at 1250 °C for only a matter of minutes, the fibres were badly damaged.

This weakness necessitated the hardening of the matrix further through γ' phase precipitation by increasing the Al content and with the addition of 2% molybdenum; subsequently the alloy COTAC 744 was developed, the nominal composition shown in Table 2-6.

This alloy possessed a high γ' volume fraction ~ 58% and good stability in all temperature

ranges. The volume fraction of the strengthening fibres is approximately 6-8% depending on the composition and within each grain the lattice and fibres are both FCC and are parallel with the epitaxy relations $[001]matrix \parallel [001]fibre$; in all compositions where the growth direction is $[001]$ the matrix contains at least 2% Cr (Stohr and Khan, 1980).

It has been reported that COTAC 744 is practically insensitive to thermal cycling in the operational temperature range of 20-1070 °C, showed no signs of fibre degredation and offered a life double that of COTAC 74. Further to this, estimations were made of the conditions required for detrimental fibre coarsening and it was determined that at 1100 °C a 10% reduction in the number of fibres per unit area would require 1800 hours of holding time which is significantly greater than the time a turbine blade in operation stays at its maximum temperature, around 300 hours for current generation superalloys (Reed, 2006).

The effect of shear creep was tested on samples of COTAC 74 in conditions of 700 °C at 400 MPa, the time to rupture was found to be around 100 hours, which was deemed acceptable for use in the fir tree root of a turbine blade (Rabinovitch et al., 1983). Given the data obtained for COTAC 74, it is expected that COTAC 744 should perform equally as well.

COTAC 744 has good oxidation and corrosion resistance and solidification of near net shape components are good, except for some small solidification defects near the surface of less than 100 micrometers, although these defects will disappear during high-temperature corrosion and oxidation protection treatments generally carried out on turbine blades (Stohr and Khan, 1980).

The creep resistance of the alloy exceeded superalloys at the time and owing to combined properties, such as creep, thermal and mechanical fatigue etc, could provide a temperature

gain of ~80 °C when compared to current superalloys (Stohr and Khan, 1980). As the Ni matrix of the alloy is similar to that of traditional single crystal alloys and relies heavily on precipitation strengthening, it was recognised that with increased levels of Al to 6.5 weight % and the replacement of W with the stabilising effect of Re to 4.0 weight % and Mo to 2.0 weight %, the creep resistance of the alloy could be further improved. Y was also added in order to improve corrosion resistance and minor additions of B (100 ppm) to improve transverse ductility (Damerval, 1987); this alloy was designated COTAC 784.

On the basis of alloy compositions, no particular compatibility issues would be anticipated for this range of alloys.

2.4.4 γ-γ'-α

This material has a $\gamma - \gamma'$ matrix reinforced by ductile $\alpha - Mo$ fibres and possesses the nominal compositions as shown in Table 2-7. A key difference of the alloy in comparison with other eutectic systems, in which the strengthening phase consists of either a brittle intermetallic or carbide, is the nature of the strengthening.

The Mo fibres are formed in a $Ni - Al$ base matrix as shown in Figure 2-8 and as both the fibre and matrix are ductile it was surmised that the allowable plastic deformation before failure should be greater than that of alloys with a brittle second phase, (Whittenberger and Wirth, 1982).

The alloy exhibits good tensile ductility and strength in all temperature ranges up to 1100 °C and the primary reason for investigation was to improve the alloys creep rupture life and oxidation resistance.

Table 2-7: Nominal composition of experimental alloy $\gamma - \gamma' - \alpha$ (Whittenberger and Wirth, 1982)

Alloy	Ni	Mo	Al
$\gamma - \gamma' - \alpha$	Bal.	32.0	6.0

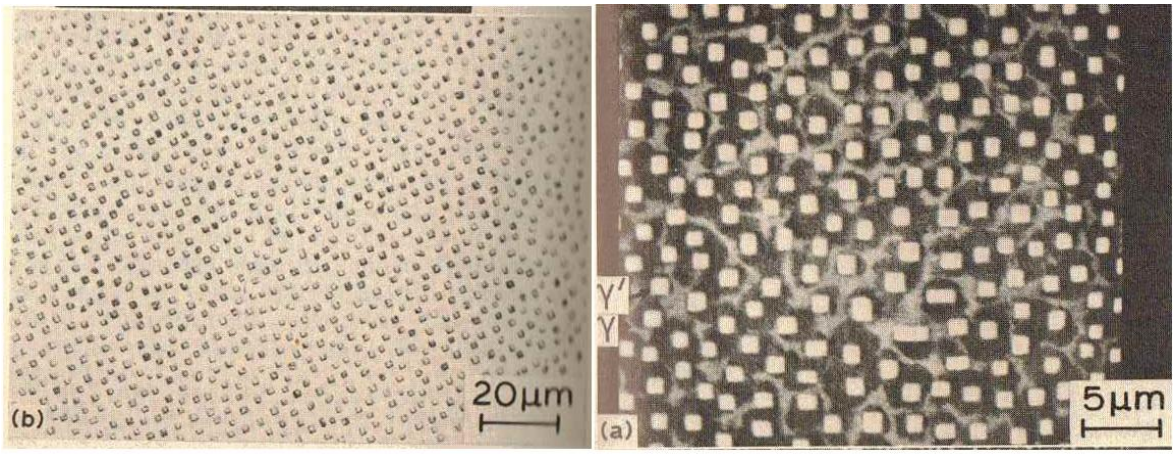


Figure 2-8: Typical microstructure of directionally solidified $\gamma - \gamma' - \alpha$. a) Solidified at 5.6 mm hr^{-1} b) Solidified at 17 mm hr^{-1}(Whittenberger and Wirth, 1982)

As such, many studies were carried out on compositions of varying complexity which were in turn solidified at varying velocities. It was subsequently noted that creep strength was not influenced by the solute concentration, nor was the strength improved by small additions of Re or V. The only effective strengthening technique was to decrease the inter-fibre spacing by increasing the solidification velocity (Whittenberger and Wirth, 1982).

Creep properties were comparable with other eutectic systems up to ~1000 °C however above this temperature other eutectics surpassed it; however a point of interest with this alloy system was that the G/V requirement was the lowest of any of the euetectics under serious consideration at the time.

2.4.5 NiTaC

The NiTaC series of alloys was developed by the General Electric Company Aero Engine Business Group (AEBG) in the 1960's and are nickel based fibre strengthened alloys. An early development in the series was the alloy NiTaC-5 as discussed previously, and the development followed a similar path to that of the COTAC alloys in that the volume fraction of the precipitation strengthening in matrix was successively increased with the addition of further Al. Two of the most recently developed and perhaps the most studied are the alloys NiTaC-13, (Woodford, 1977) and NiTaC-14B, (Menzies et al., 1988); the nominal compositions are shown in Table 2-8.

Table 2-8: Nominal compositions of several NiTaC eutectic alloys, 1) (Rabinovitch et al., 1983), 2)(Woodford, 1977), 3) (Henry et al., 2005)

Alloy	Al	B	C	Co	Cr	Mo	Re	Ta	V	W	Ni
NiTaC-5 (1)	3.0	---	0.4	20.0	10.0	---	---	9.0	---	10.0	Bal.
NiTaC-13 (2)	5.4	---	0.54	3.3	4.4	---	6.2	8.1	5.6	3.1	Bal.
NiTaC-14B (3)	5.3	0.015	0.43	3.8	3.8	3.0	6.4	11.4	---	4.3	Bal.

NiTaC-13 has successfully completed engine trials in use as an un-cooled IP (Intermediate Pressure) turbine blade, the monocarbide fibres $(Ta,V)C$ are typically $1\,\mu m$ in cross-section and occupy about 2-4% of the microstructure. The Face Centre Cubic (FCC) fibre and γ have a common growth axis [100] and $[110]TaC \| [110]\gamma \| \gamma - TaC$ interface, (Jackson et al., 1974).

The matrix contains around 60 volume % of γ' the $F.C.C$ ordered structure based on Ni_3Al which is attributed to the increased levels of Re additions that have been made which have allowed increased solid solution strengthening of the matrix.

The alloy attracted significant interest due to its good performance in creep tests in the medium to high temperature range; tensile properties were also on a par with other eutectic systems - COTAC, $\gamma - \gamma' \delta$ at medium temperature ranges and significantly better at high temperatures.

NiTaC-14B was a further development in the NiTaC family of alloys which resulted in strength improvements over NiTaC-13 while retaining a balance of ductility, toughness and environmental resistance (Menzies et al., 1988). As such, this alloy was investigated as a candidate for cooled HP (High Pressure) turbine blades which yielded interesting findings;

- Blades were cast "upside down" i.e. the tip and aerofoil was cast first and the root section cast later. This was due to chemical segregation throughout the length of the casting, (Gigliotti and Henry, 1976) which reduced rupture strength towards the top. Therefore, blades were cast in the tip-down configuration in order to ensure the best rupture properties are achieved in the aerofoil.
- Due to surface defects such as carbides forming during the casting process, blades were cast oversize in order to provide sufficient stock for their removal by machining.

It was found that the NiTaC-14B was a good candidate material for such an application although processing was still fairy rigorous and time consuming.

Due to the low Cr content of the alloy system (in relation to single crystal superalloys such as CMSX-4) the inherent corrosion resistance of the alloys is poor and it was determined that oxidation resistant coatings would inevitably be required in a service environment. An extensive study was carried out on the NiTaC-13 alloy and its compatibility with NiCrAlY

type coatings and during cyclic burner rig tests both performed satisfactorily (Jackson et al., 1974).

2.5 Creep rupture life and the Larson-Miller Parameter

The creep life of an alloy is a particularly important parameter, especially in the case of turbine blades as they are operating under high temperatures and stresses. During alloy development there are two predominant tests that can be conducted in order to assess the mechanical characteristics of potential alloy compositions.

One such test is to determine the stress-rupture life of a material and involves a tensile specimen being tested under variable load and constant temperature until failure occurs, hence the time to rupture, t_r of an alloy can be determined. This test is generally carried out under higher stresses and temperatures than that of a creep test and is useful for determining alloy compositions for applications where some strain can be tolerated but failure must be avoided. This type of test is also shorter in time and requires less complex instrumentation and therefore best suited to alloys that are under development (Pope, 1996).

In the case of turbine alloys where tolerable strain is limited due to the intrinsic geometry constraints within the machinery, the life of a component is usually categorised by a percentage of creep in a set time period i.e. 1% creep strain in 1000 hours. This type of test takes longer to carry out as it involves lower stresses and temperatures and also requires more sophisticated equipment to record the results such as inductance gauges to measure creep rate. In general this type of data is generally obtained once the viability of an alloy has been fully established (Pope, 1996).

In order to quantify the creep resistance of an alloy there are several methods that can be used to represent experimental data. Generally all creep and stress-rupture data is analysed in terms of three variables; time, stress and temperature. Perhaps the most important parameter for many materials under loading conditions that are invariant with time is that of steady-state creep rate, $\dot{\epsilon}_{ss}$. Its dependence in stress can be expressed as:

$$\dot{\epsilon}_{ss} = K_1 \sigma^n \qquad 2.2$$

Its dependence in stress and temperature can be expressed as:

$$\dot{\epsilon}_{ss} = K_2 \sigma^n exp\left(-\frac{Q}{RT}\right) \qquad 2.3$$

where σ is the applied stress, n is the stress exponent, K2 is a constant, Q is the activation energy, R is the universal gas constant and T is the absolute temperature (Reed, 2006).

When considering the time to rupture, t_r the Monkman-Grant relationship must be satisfied.

$$t_r \times \dot{\epsilon}_{ss}^M = K_3 \qquad 2.4$$

When considering elevated temperature tensile creep experiments the product of the time-to-rupture and steady-state creep rate raised to the power M can be considered an approximation of a constant for many materials (Davies, 1997). The constant $K3$ is numerically equal to the creep ductility of the material (Reed, 2006).

At a constant stress the following expressions can be written;

$$t_r exp\left[-\frac{Q}{RT}\right] = K_4 \qquad 2.5$$

Or

$$\log_{10} t_r - 0.4343 \frac{Q}{RT} = K_5 \qquad 2.6$$

Where, K_4 and K_5 are constants, equation 2.6 can be written;

$$LMP = T(C + \log_{10} t_r) \qquad 2.7$$

Where; LMP is the Larson-Miller parameter, T is the absolute temperature and C is the Larson-Miller constant which varies between 15 and 25 for many alloys and is commonly assumed to be 20 for superalloys (Reed, 2006).

The temperatures and stresses which a turbine blade is subjected occur cyclically at varying stages during a flight, resulting in accumulated creep strains during these cycles. To mitigate this risk, one could incorporate a margin of safety to account for any condition; however this would lead to a compromise in weight of the aero engine. An alternative approach is called the life fraction rule, similar to Miner's Law in fatigue, and states that rupture occurs when the sum of all the fractions of the rupture life at different stress/temperature combinations becomes equal to unity.

When using an extrapolation approach such as this to predict long-term creep behaviour it is important to remember the following assumptions:

1. The mechanism of creep is considered to remain the same in the range of interest.
2. The microstructure remains essentially unaltered.

Generally the Larson-Miller parameter is an adequate method of representing the lifetime of a material, based upon applied stress and temperature, using a correlative approach based on the Arrhenius rate equation.

This allows a representation of experimentally obtained creep test data to be plotted on a single curve extrapolated from a few short creep tests, Figure 2-9 a) and can give designers a means of estimating the service life of components within a wide range of temperature and stresses.

Most importantly, once the Larson-Miller curve has been plotted, the life of an alloy can be estimated; for example, based upon the applied stresses at a constant temperature, Figure 2-9 b).

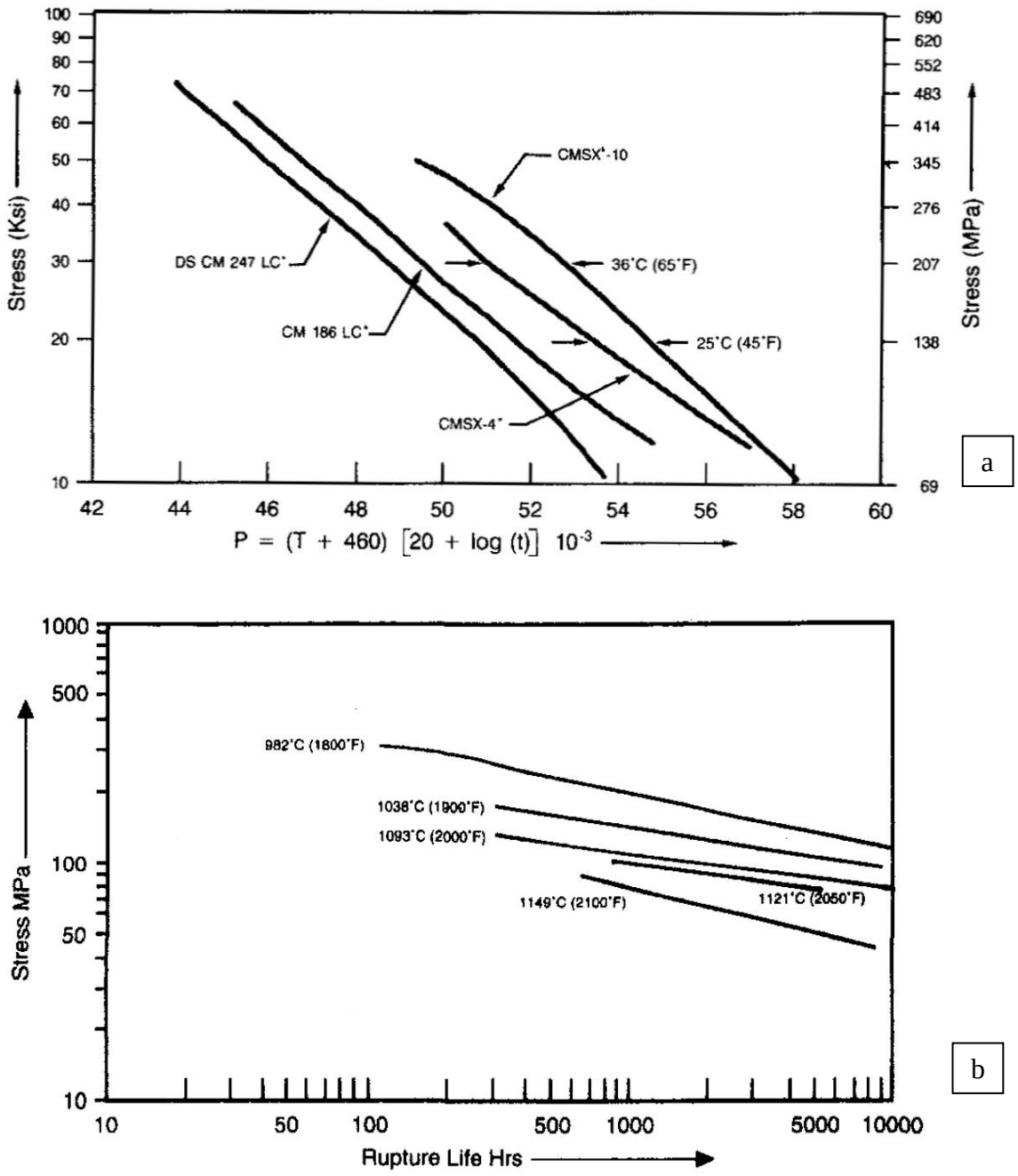


Figure 2-9: a) Larson-Miller plot of the alloys DS CM 247 LC, CM 186 LC, CMSX-4 and CMSX 10 (Erickson, 1996) b) Rupture life in hours plotted against applied stress for varying temperature intervals for CMSX-4 (Broomfield et al., 1998).

It was noted for certain eutectic composites, particularly the COTAC and NiTaC type, the extrapolation of short term data by means of the Larson-Miller parameter leads to an underestimation of the long term creep potential of the alloys.

This lies in the fact that for superalloys an elongation of 1% equates to almost all of the useful creep potential of the alloys, whereas with eutectic alloys the rupture occurs between 1.5-2% elongation owing to the combined strengthening effect of the fibres and matrix (Stohr and Khan, 1980).

To adequately represent the creep potential of the COTAC 744 composite an equation was proposed in the form;

$$\sigma = A{t_r}^{-m} \qquad 2.8$$

where; A is a constant, t_r is the time to rupture and m is a time exponent (Stohr and Khan, 1980).

The value of the representation presented lies in the fact that the exponent of time appears to be independent of temperature (Stohr and Khan, 1980), however the representation in equation 2.8 shows good agreement with experimental data shown in Figure 2-10, allowing long term creep estimations to be made.

Similarly, when investigating the creep-rupture data for NiTaC 13 it was discovered that the Larson-Miller constant, C is highly dependent on the applied stress imposed and based upon experimental observations the Larson-Miller parameter was modified to incorporate a stress dependent time/temperature parameter, equation 2.9, and showed good agreement with the experimental data (Woodford, 1977).

$$LMP = T\left[\frac{2000}{\sigma} + logt_r\right] \qquad 2.9$$

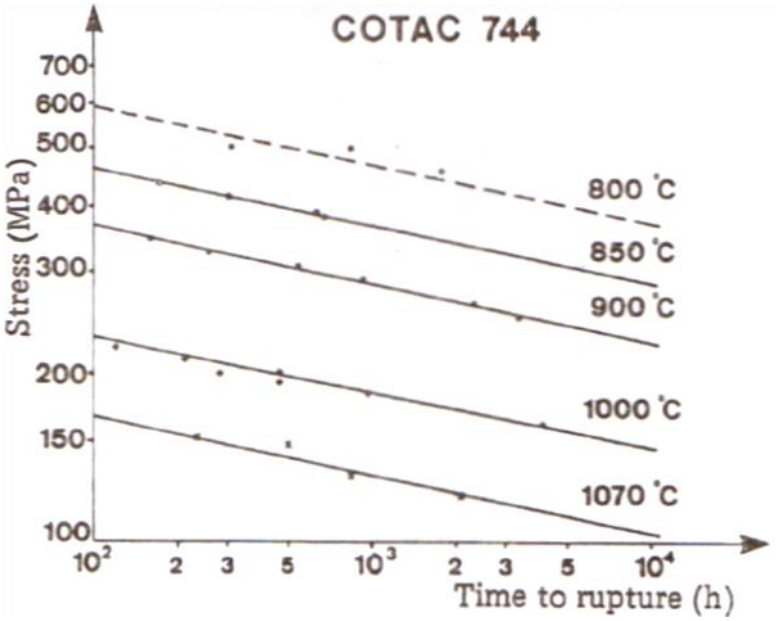


Figure 2-10: A representation of creep-rupture results for COTAC 744 plotted as log σ – log t_r (Stohr and Khan, 1980)

Given that the Larson-Miller plots of $\gamma - \gamma' - \delta$ alloys, $\gamma - \gamma' - \alpha$ alloys, CMSX-4 and CMSX-10 have been obtained and a representation of the creep performance of the COTAC and NiTaC alloys are available, a comparative assessment of the creep potential can be made by predicting the relative performance at a predetermined constant temperature under varying stress levels. The data has been plotted on a $\log \sigma$ v $\log t_r$ graph

for a number of eutectic alloys and Ni-base superalloys as shown in Figure 2-11.

As mentioned, due to the nature of the strengthening, eutectic alloys show creep resistance up to around 2% elongation a property that is generally not attributed to single crystal superalloys of interest and can be as much as double the creep potential of these alloys. Therefore, in order to make a representative comparison, perhaps it is prudent to plot the eutectic alloys as $(Time\ to\ rupture/2)$ whereas the single crystal alloys are plotted as time to rupture. This is shown in Figure 2-12.

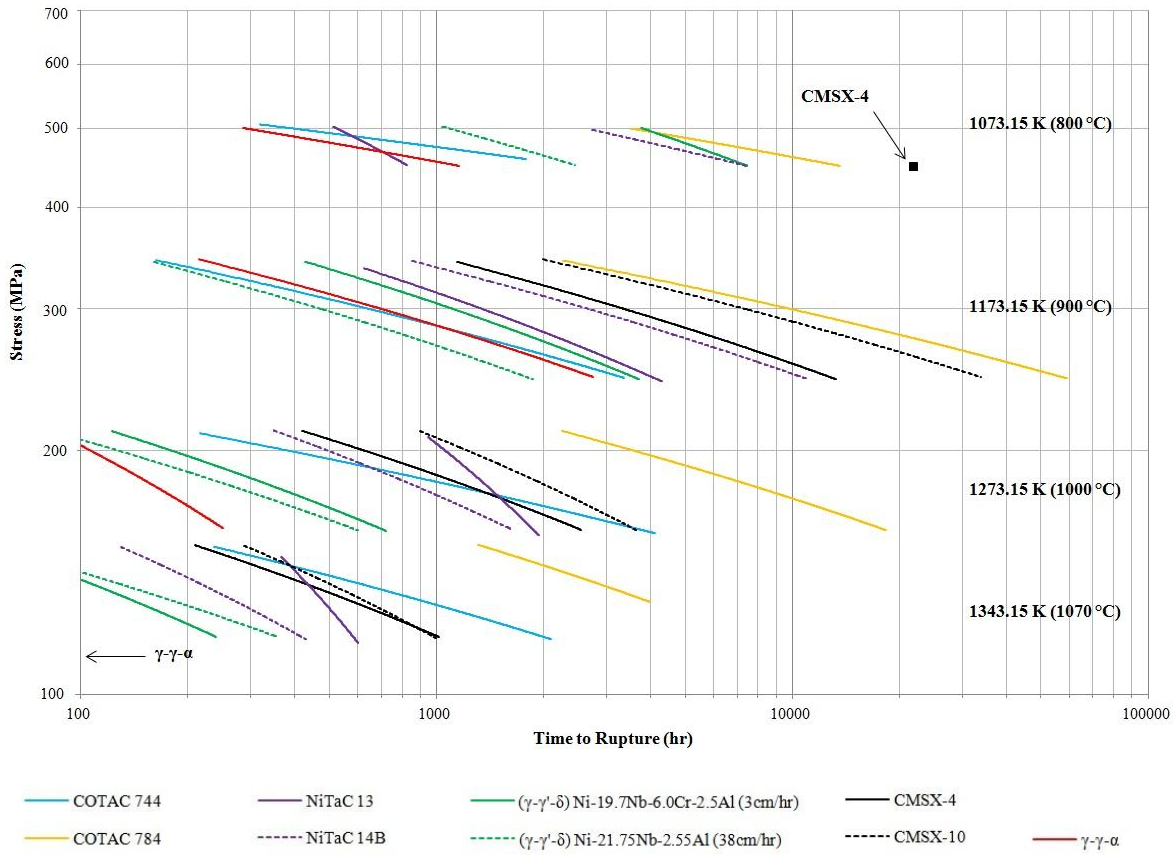


Figure 2-11: Log stress v Log time to rupture plot of Ni-base eutectic alloys and Ni-base single crystal superalloys under a range of constant temperature conditions. Data was extrapolated from the following sources; COTAC 744 - (Stohr and Khan, 1980), COTAC 784 - (Damerval, 1987), NiTaC 13 - (Woodford, 1977), NiTaC 14B - (Henry et al., 2005), $\gamma - \gamma' - \delta$ (Lemkey, 1973), CMSX-4 (Broomfield et al., 1998), CMSX-10 (Erickson, 1996) and $\gamma - \gamma' - \alpha$ (Whittenberger and Wirth, 1982)

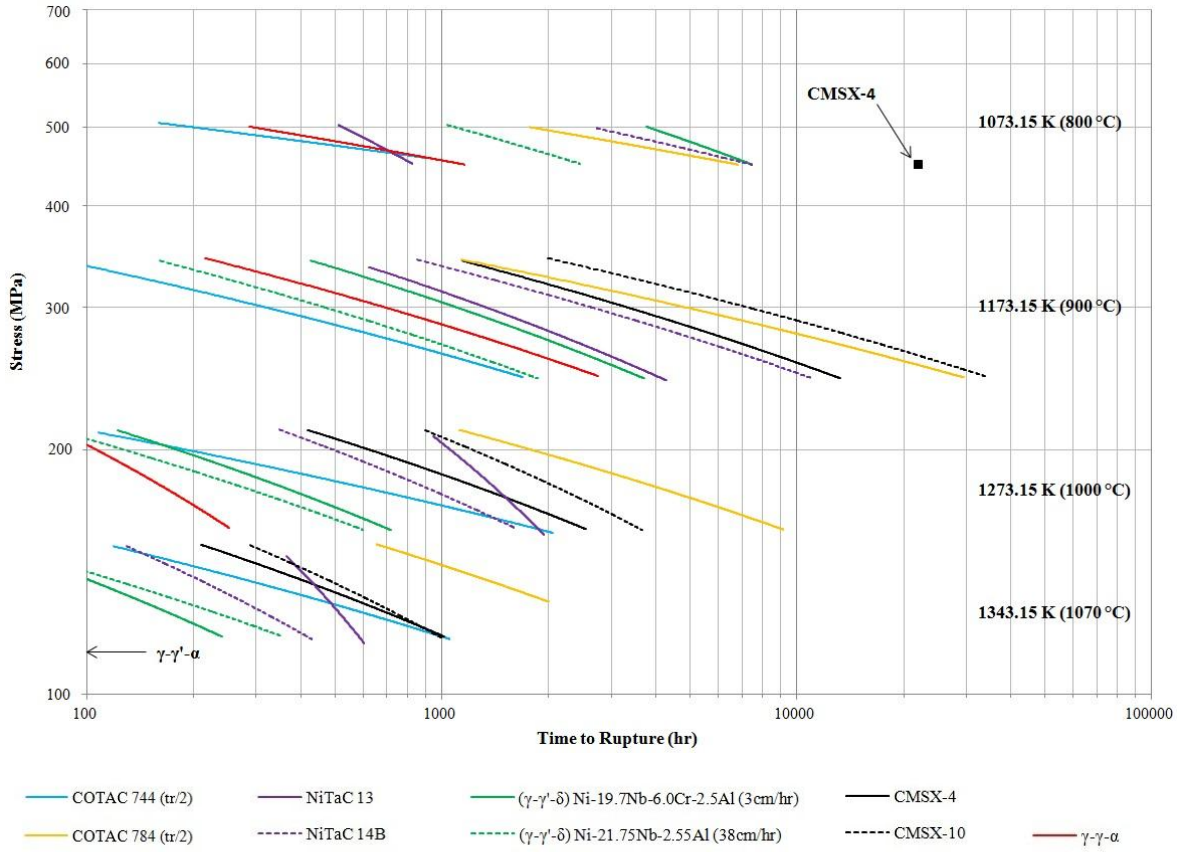


Figure 2-12: Log stress v Log time to rupture plot of Ni-base single crystal superalloys and Ni-base eutectic alloys under a range of constant temperature conditions. Ni-base eutectic alloys are plotted as (time to rupture/2) which is equivalent to the creep potential of a single crystal superalloy Data extrapolated from the same sources as in Figure 2-11.

When examining Figure 2-11 and Figure 2-12 it can be seen that the Re containing eutectic COTAC 784 is superior in creep performance to that of CMSX-4 and CMSX-10 in the low stress/high temperature ranges when taking into account the full creep potential of the alloy. Even so, when taking the creep potential $tr/2$ as discussed previously, the alloy is still superior up to 200 MPa at 1273.15 K.

The non Re containing alloy COTAC 744 is comparable to CMSX-4 and CMSX-10 in both cases at high temperature/low stress cases.

The $\gamma - \gamma' - \delta$ type alloys fall short in creep potential when compared to the 2nd and 3rd generation single crystals; however the $\gamma - \gamma' - \delta$ systems in question have not benefited from the enhanced solid solution strengthening offered by the addition of Re.

2.6 Solidification of alloys and the plane front stability criterion

As the solidification of a pure metal is rarely encountered, it is useful to investigate the redistribution and partitioning of solute at an advancing solidification front.

Equilibrium solidification is the assumption that crystal growth is slow enough to allow complete diffusion in the liquid state and complete diffusion in the solid state, the relative amounts of solid and liquid at any temperature given by the Lever rule (Flemings, 1974).

Even though early stages of solidification are driven by nucleation, later stages are dominated by growth kinetics and even if the system as a whole is not in thermodynamic equilibrium, since the kinetic undercooling is small this can be assumed to apply at the interface.

For a given interfacial temperature the composition of solid, C_s, and liquid, C_l at the interface can be obtained from the phase diagram. In most alloys the solute preferentially partitions to the liquid and the partitioning coefficient, k is given as a ratio of these compositions;

$$k = \frac{C_s}{C_l} \qquad 2.10$$

Therefore the solute will be expelled from the solid into the liquid when $k < 1$ as in most engineering alloys.

In most cases of directional solidification, diffusion in the solid is very limited and diffusion in the liquid is too slow to allow equilibrium solute concentrations to be maintained in the melt; therefore equilibrium solute concentrations are only maintained at the solid-liquid interface (McLean, 1983).

In early stages of solidification an initial solid will form of composition, kC_0 as solute is rejected into an enriched zone in the liquid ahead of the solid-liquid interface where C_0 is the composition of the alloy during the subsequent solidification. The next layer will be slightly richer than the previous and subsequently the solid that forms will be of a higher solute concentration at later stages of the solidification (Porter et al., 2009).

This can be examined by making the following assumptions (Rabinovitch et al., 1983):

1. The solidus and liquidus are considered to be straight lines and the partition coefficient is constant.

2. There is no convection in the liquid and diffusion is the only mechanism for the redistribution of the excess solute ahead of the front.

3. Referring to the phase diagram shown in Figure 2-14, elements A and B are considered to be pure with no present impurities.

4. The solidification is carried out with a planar front, under a constant thermal gradient and a constant solidification front velocity V.

If the crystal is long enough a steady state is approached, that of alloy C_0, and the distribution in the boundary layer is given by;

$$D_l \frac{d^2 C_l}{dx'^2} + V \frac{dC_l}{dx} = 0 \qquad 2.11$$

Where x is the distance from the interface, D_l the liquid diffusion coefficient, C_l the liquidus composition and V the growth velocity; boundary conditions are $C_l = \frac{C_o}{k}$ at $x \geq 0$ and $C_l = C_o$ at $x = \infty$ (Flemings, 1974).

A solution to equation 2.11 can now be found (Tiller et al., 1953), to describe the concentration profile ahead of a planar interface moving through a binary alloy and it can be shown that the concentration profile in the liquid for steady-state conditions is given by the relationship:

$$C_l(x) = C_o\left[1 + \left(\frac{1-k}{k}\right)exp\left(-\frac{V}{D_l}x\right)\right] \qquad 2.12$$

The distribution of the solute concentration from C_l to C_0 over a characteristic distance is:

$x = \frac{D_L}{kV}$

A graphical representation of this is shown in Figure 2-13.

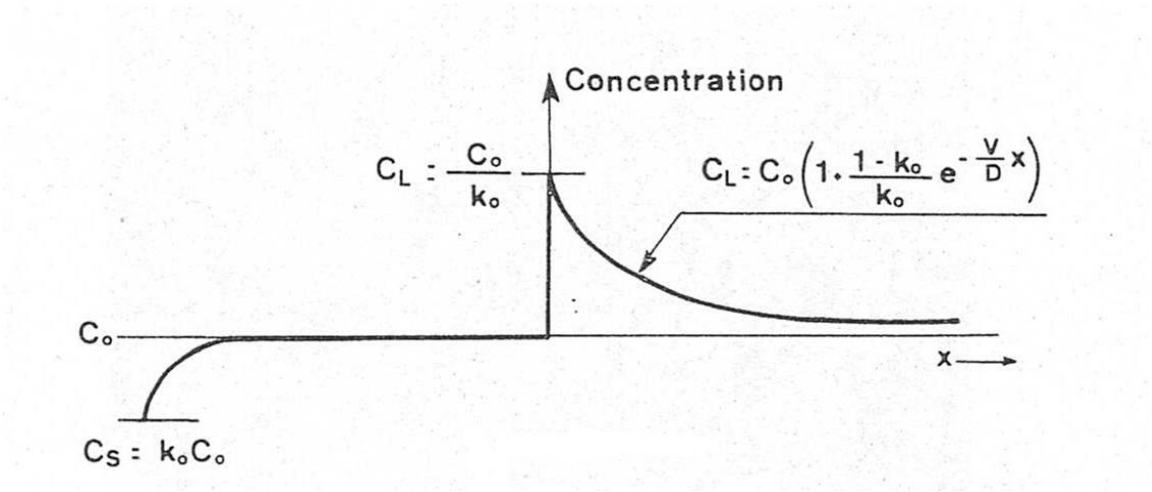


Figure 2-13: Concentration profile ahead of a planar solidification front (Stohr and Khan, 1980)

Constitutional undercooling will occur when the real temperature in the liquid at each point is lower than the temperature T_E given by the equilibrium phase diagram shown in Figure 2-14.

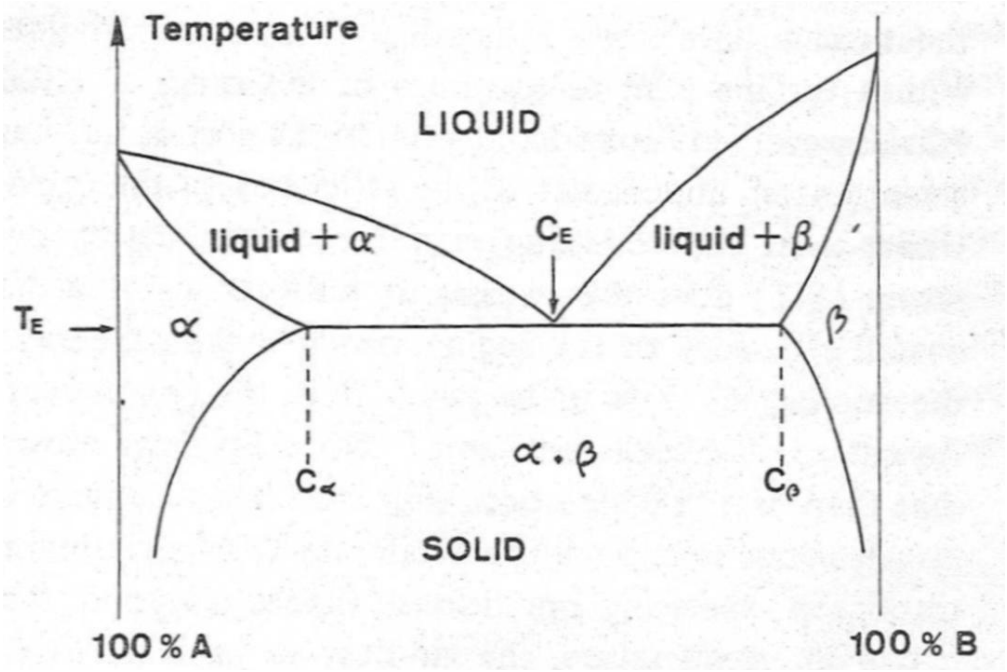


Figure 2-14: Equilibrium phase diagram of binary eutectic alloy (Stohr and Khan, 1980)

The equilibrium temperature of the liquid is given by;

$$T_l(x) = T_o - mC_l \qquad 2.13$$

Where; $T_o$is the melting temperature of the pure metal, m is the slope of the liquidus line and C_l is the equilibrium concentration of the liquid, or can also be written (Stohr and Khan, 1980);

$$T_l(x) = T_o - mC_o\left[1 + \left(\frac{1-k}{k}\right)exp\left(-\frac{V}{D_l}x\right)\right] \qquad 2.14$$

So if G is the thermal gradient imposed in the vicinity of the liquid-solid interface defined by the temperature, T_i the real temperature ahead of the front is:

$$T_l^r = T_i + Gx = T_o - m\frac{C_o}{k} + Gx \qquad 2.15$$

Equations 2.13-2.15 can be used to calculate the length of the undercooled zone for various growth rates. There will be no undercooling if the slope of the real temperature of the liquid is greater than the slope at the origin representing the equilibrium temperature (Stohr and Khan, 1980).

When considering true binary eutectics, there is no undercooling as the eutectic liquid and solid have exactly the same composition, however when considering an alloy of near eutectic composition, as is the case with most eutectic alloys of engineering importance or indeed alloys for single crystal application, it has been shown that a planar front can occur given the following relationship (Flemings, 1974);

$$\frac{G}{V} \geq -\frac{mC_o(1-k)}{kD_l} \qquad 2.16$$

Which when simplified can be written as;

$$\frac{G}{V} \geq -m\frac{C_E - C_o}{D_l} \qquad 2.17$$

Where C_E and C_o are the compositions of the eutectic and composition of the alloy respectively and m the slope of the liquidus line; and as $m(C_E - C_o)$ is the melting range of the alloy ΔT then the equation can be written;

$$\frac{G}{V} \geq \frac{\Delta T}{D_l} \qquad 2.18$$

i.e. the ratio of temperature gradient to solidification velocity must be greater than or equal to the ratio of compositional solidification range to diffusion coefficient.

In alloys where a constitutional undercooling occurs, any morphological instability will

result in the morphology changing from planar to cellular to dendritic and is dependent on the G/V ratio. The solidification morphology for several nickel based superalloys has been defined as a function of solidification velocity and thermal gradient as shown in Figure 2-15.

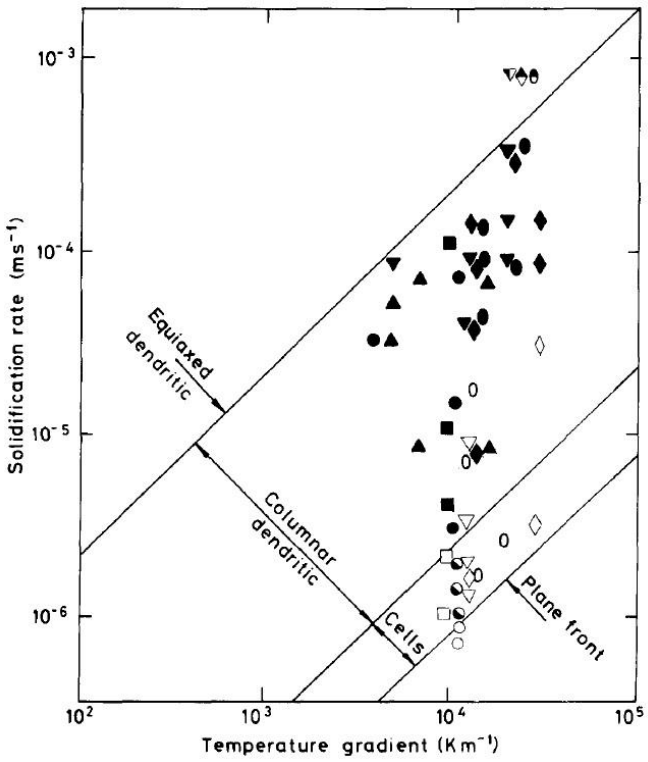


Figure 2-15: Morphologies of directionally solidified nickel based superalloys plotted as log V versus log G (where V is the growth rate and G the thermal gradient). The solid lines shown are contours of constant G/V ratios. Unfilled circles represent alligned planar growth, unfilled squares, diamonds, triangles and ovals represent cellular growth, filled shapes represent dendritic growth (Quested and McLean, 1984).

As described by the plane front stability criterion, each alloy system has an intrinsic critical G/V ratio that must be met in order to achieve a desired microstructure during casting. Table 2-9 summarises the critical G/V ratios reported for various alloy systems of interest with the corresponding solidification velocity plotted as a function of temperature gradient in Figure 2-16.

Table 2-9: Critical G/V ratio for various alloy systems, above which plane front growth breaks down

	COTAC 744	**NiTaC 13**	$\boldsymbol{\gamma - \gamma' - \delta}$	$\boldsymbol{\gamma - \gamma' - \alpha}$
Critical G/V (°C.hr.mm^{-2})	1.25	1.0	1.5	0.5

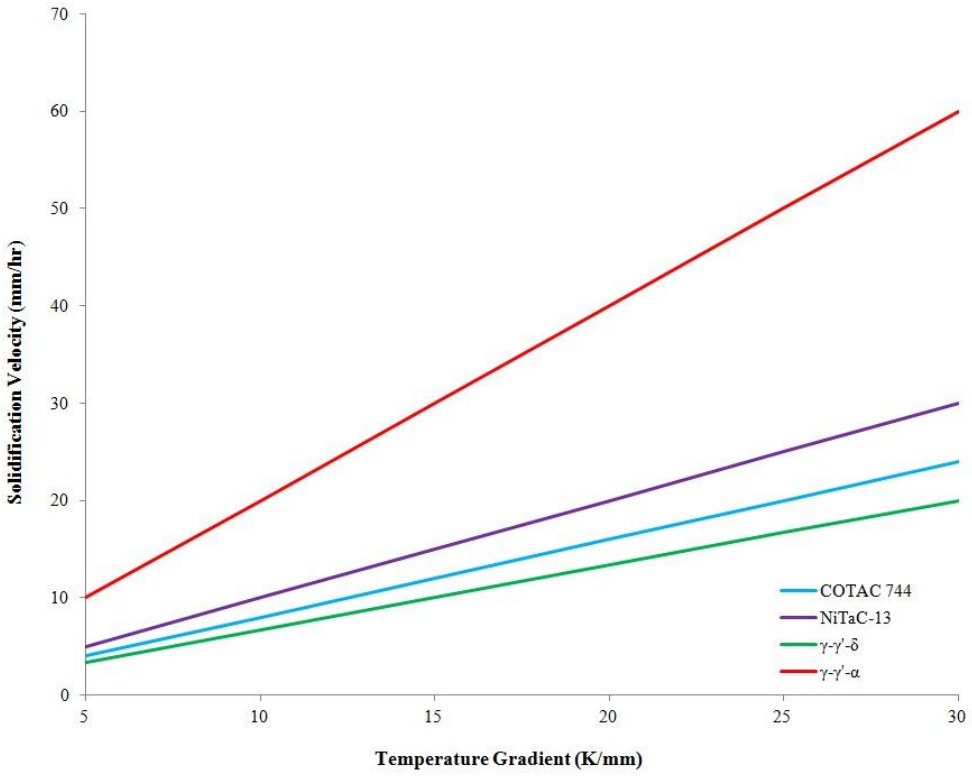


Figure 2-16: G/V solidification requirements for various alloy systems. Data extrapolated from (Lemkey, 1973, Stohr and Khan, 1980, Whittenberger and Wirth, 1982, Woodford, 1977).

2.6.1 Dendrite arm spacing

In single crystal alloys, where a planar front is rarely encountered due to the need to maintain the economics of the casting process, a dendritic morphology is the most commonly observed and can be characterised by dendrite tip radius R_{tip}, the Primary Dendrite Arm Spacing (PDAS) λ_1 and the secondary dendrite spacing, λ_2.

The growth rate and dendrite morphology are predominantly dependent on the kinetics at the dendrite tip region; the geometry of which is generally assumed to be a paraboloid of revolution. The problem of diffusion in this context has been solved by Ivanstov (Ivantsov, 1985, Ivantsov, 1947) and also by Horvay and Cahn (Horvay and Cahn, 1961).

The work by Ivantsov relates the dendrite tip radius to the dendrite tip velocity as a ratio and therefore one can deduce that the dendrite can have a large tip radius and grow slowly or have a small tip radius and grow faster. It is therefore necessary to establish a criterion to determine the dendrite tip radius. The solvability criterion (Langer, 1988) is the most widely accepted presently and is of the same form as the marginal stability criterion (Langer and Müller-Krumbhaar, 1978a, Langer and Müller-Krumbhaar, 1978b) with both giving similar results in most cases.

In a similar manner to eutectic phase formation in planar growth, dendrites also reject solute during solidification and during this an array of parallel growing dendrites form which grow favourably along <001> directions in the F.C.C system. The characteristic distance between the dendrites is the PDAS and determining the dendrite tip radius is required to further predict the PDAS with regard to G and V. A relationship according to (Hunt, 1979, Kurz and Fisher, 1989) is given by;

$$\lambda_1 = \frac{4.3(\Delta T_o D_l \Gamma)^{1/4}}{k^{1/4} V^{1/4} G^{1/2}} \qquad 2.19$$

Where λ_1 is the primary dendrite arm spacing, ΔT_o is the equilibrium freezing range and Γ the Gibbs-Thomson coefficient.

Re-arranging equation 2.19 yields:

$$\lambda_1 = 4.3 \left(\frac{\Delta T_o D \Gamma}{k}\right)^{1/4} G^{-1/2} V^{-1/4} \qquad 2.20$$

Observations of Equation 2.20 indicate that the PDAS is a function of the thermal gradient, G and the solidification velocity, V and scales inversely with both components. A further simplification leads to a rule that is most predominantly used;

$$\lambda_1 = c * G^{-1/2} V^{-1/4} \qquad 2.21$$

where c is a material dependent constant.

This parameter given in Equation 2.21 gives a reasonable estimate of the average primary dendrite arm spacing one would expect given necessary process conditions, however it is recognised that a range of stable dendrite spacing's exist (Ding et al., 1996, Han and Trivedi, 1994, Wang et al., 2003, Weidong et al., 1993) and the theoretical model should only be used qualitatively.

Other relationships have been derived to quantify primary dendrite arm spacing with process parameters (Beckermann et al., 2000, Ma and Sahm, 1998); however the model in the form of equation 2.21 is the most widely used.

The constant, C used in equation 2.21 is known to fall within a range of values for nickel based superalloys; the values are in the order of ~1344-1819.2 ^{o}C (Kermanpur et al., 2000,

Krug, 1998, Newell, 2009, Horrocks, 1990a), Brown, 2013).

When the growth rate and PDAS are known it is possible to make qualitative estimates of the thermal gradient (McLean, 1983), the relationship is utilised in this work in order to make such observations; and as such the constant, $c = 1819.2$ will be used as this has been experimentally determined with respect to the alloy CMSX-4 (Brown, 2013, Newell, 2009). An example of dendrite morphology is shown in Figure 2-24.

2.6.2 Eutectic phase spacing

The stability criterion shown in Equation 2.18, although approximate, can be used to determine the process requirements for given alloys, provided they possess a composition close to that of a eutectic. Experimental observations for various alloy systems yield a critical G/V ratio that must be fulfilled during processing in order to obtain a composite with an aligned microstructure.

The solidification of eutectic alloys is a subject that has been extensively studied; continued growth is controlled by the laws of diffusion in the liquid and by the form of the liquid-solid interface (Li and Zhou, 2005).

A model proposed by (Jackson and Hunt, 1966) derived the relationship between the undercooling ΔT at the interface and the interlamellar or interfibre spacing, λ as:

$$\Delta T = K_1 \lambda V + K_2/\lambda \qquad 2.22$$

Where K_1 and K_2 are constant parameters for a given system.

So, using the extremum condition where the eutectic grows at the minimum undercooling, the following equation can be derived;

$$\lambda^2 V = \frac{K_2}{K_1} \qquad 2.23$$

So;

$$\lambda^2 V = constant \qquad 2.24$$

The approximate relationship given in equation 2.24 is the most commonly used to the interlamellar/interfibre parameter, λ with the solidification velocity, V. At particularly high solidification velocities however it was noted that the standard approximation described does not hold true as, the Peclet number varies under such conditions (Trivedi et al., 1987).

The Peclet number is a dimensionless number and is a ratio of the rate of advection of a flow to its rate of diffusion and is defined as:

$$P_e = \frac{LV}{D_l} \qquad 2.25$$

Where L is the characteristic diffusion length.

In the theoretical model, L is defined as half the interlamellar spacing ($i.e. L = \lambda/2$) so the peclet number is defined as:

$$P_e = \frac{V\lambda}{2D_l} \qquad 2.26$$

By extending the Jackson and Hunt analysis to conditions encountered during rapid solidification it is found that the parameter, K_1 in equation 2.22 is no longer constant but rather it is dependent on the Peclet number; hence equation 2.23 can be written:

$$\lambda^2 V = f(P_e) \qquad 2.27$$

2.7 Freckle defect formation

The freckling defect, first studied by (Giamei and Kear, 1970), is one of the most common defects that can occur during solidification. As such the phenomenon has received extensive attention primarily because it has been shown that the propensity of freckle defects is related to the composition of the alloy and those that are rich in elements such as *Re* and *W* are particularly prone to the defect (Tin et al., 2001).

Freckles appear as small chains of equiaxed grains which are randomly orientated and aligned parallel to the solidification direction (Pollock and Murphy, 1996) and are created as a result of convective instabilities in the solidification front as a result of micro-segregation of individual alloying elements.

It has been shown that Re and W segregate to the dendrite core and Al, Ti and Ta partition to the interdendritic region (Karunaratne et al., 2001); this becomes self-evident when examining the composition of the freckle chains as they differ from that of the base alloy and instead are richer in the elements that partition to the interdendritic region (Pollock and Tin, 2006).

As a result of this micro-segregation the interdendritic region becomes less dense than the surrounding liquid and a density inversion is set up (Beckermann et al., 2000). Once the buoyancy of the interdendritic liquid overcomes the viscous drag forces which have been preventing it from rising, thermosolutal convection currents can occur; also known as "freckle plumes". The density inversion and subsequent thermosolutal convection current phenomenon has been directly observed by (Copley et al., 1970) in ingots of a transparent pseudo-metallic $NH_4Cl : H_2O$ system.

These freckle plumes cause fragmentation of a surrounding primary or secondary dendrite arm which are then carried into the liquid above the mushy zone, and if sufficiently large, remain without being re-melted and nucleate to form equiaxed grains (Gu et al., 1997).

It is clear that the propensity for freckle formation is a factor of alloy composition and this has been shown in a number of studies (Pollock and Murphy, 1996, Pollock et al., 1992) and the varying severity of the density inversion is a direct result of the weight % variation of alloying elements such as Re and W.

A comprehensive study has been undertaken by (Hobbs et al., 2005) in which a range of alloys were ranked according to the relative density inversion $\Delta\rho/\rho_0$ a selection of alloys studied are shown in Table 2-10.

Table 2-10: Selected alloys studied by (Hobbs et al., 2005) showing rank, castabiity and relative density inversion. Also highlighted are alloying elements thought to have a positive or negative effect in the formation of the freckle defect.

Alloy	Ni	Al	Cr	Co	Mo	Ti	Nb	Ta	W	Re	Ru	Hf	Rank	Castability	$\Delta\rho/\rho_0$
SRR300I		5.8	**5.5**	8.0	**2.0**	-	-	**7.5**	**4.0**	**5.3**	-	0.1	1	Good	0.01047
CMSX-4		5.6	**6.5**	9.0	**0.6**	1.0	-	**6.5**	**6.0**	**3.0**	-	0.1	18	Moderate	0.02455
UCSX6		6.3	-	4.0	-	-	-	**6.0**	**8.0**	**6.8**	3.0	-	37	Poor	0.05426

The conclusions of this study were that the introduction of Cr and Mo reduce the degree to which the Re and W partition to the dendrite core and the use of Re and W should be minimised to improve the amenability of Ni-base alloys (Hobbs et al., 2005), this proposal is in conflict with published research indicating the benefitial effects of such elements for creep resistance so a balance must obviously be struck.

The use of Ta is shown to reduce the density inversion (Pollock et al., 1992), as even though a relatively heavy element, it partitions to the interdendritic liquid region and

neutralises the buoyancy force of the less dense elements in the interdendritic liquid. A range of alloy compositions with different Ta content is shown in Figure 2-17.

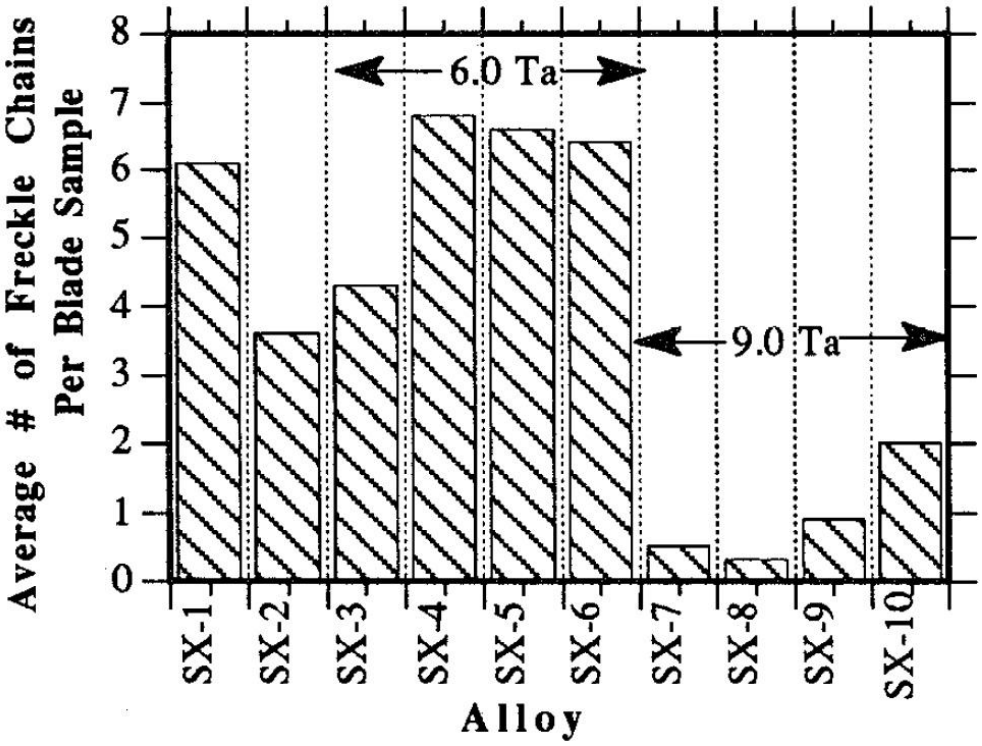


Figure 2-17: Influence of Ta content on freckle chain formation in Ni-base superalloy specimens (Pollock et al., 1992)

Carbon additions have also shown to be beneficial in reducing the susceptibility for freckling (Al-Jarba and Fuchs, 2004, Tin et al., 2000, Tin et al., 2001) by the formation of carbides around the liquidus (Reed, 2006).

The density inversion and the likelihood of freckle formation can be directly linked to the Rayleigh number which is a measure of the ratio of the buoyancy force to the retarding frictional force in the mushy zone (Pollock and Murphy, 1996). The form of the Rayleigh number has varied in a number of studies (Auburtin et al., 2000, Beckermann et al., 2000, Pollock and Murphy, 1996), however the most widely used is given by (Beckermann et al., 2000, Worster, 1992) as;

$$Ra_h = \frac{(\Delta\rho/\rho_o) g \bar{K} h}{\alpha v}$$

Where; the subscript h associated with the Rayleigh number denotes that it is a mean value over a distance h which is the height of the mush, α and v are the thermal diffusivity and kinematic viscosity respectively and $\bar{K}$ is the mean permeability corresponding to the average solid fraction $\bar{\varepsilon}_s$ and is given as:

$$\bar{K} = K_o \frac{(1-\bar{\varepsilon}_s)^3}{\bar{\varepsilon}_s^2}$$

K_o is $6 \times 10^{-4} \lambda_1^2$ (Schneider et al., 1997).

A critical Ra number of 0.25 has been defined by (Beckermann et al., 2000) under which no freckle chains were observed in experimental casts with the maximum Ra number occurring at a solid fraction of 0.1; Figure 2-18

It has been observed experimentally that the scale of the dendrite morphology will affect the propensity for freckle formation and a finer PDAS will inhibit the formation of freckles, potentially due to narrowing of the interdendritic channels which serves to reduce the thermosolutal convection currents. It has been shown by (Pollock et al., 1992) that there is a minimum PDAS in which freckles have not been observed in Ni-base superalloys, shown in Figure 2-19 ; around $320\ \mu m$. As the scale of the microstructure is linked to the solidification parameters G and V there is a threshold cooling rate below which freckles are likely to form (Copley et al., 1970), the PDAS threshold observed relates to a cooling rate of $0.1\ °C.s^{-1}$.

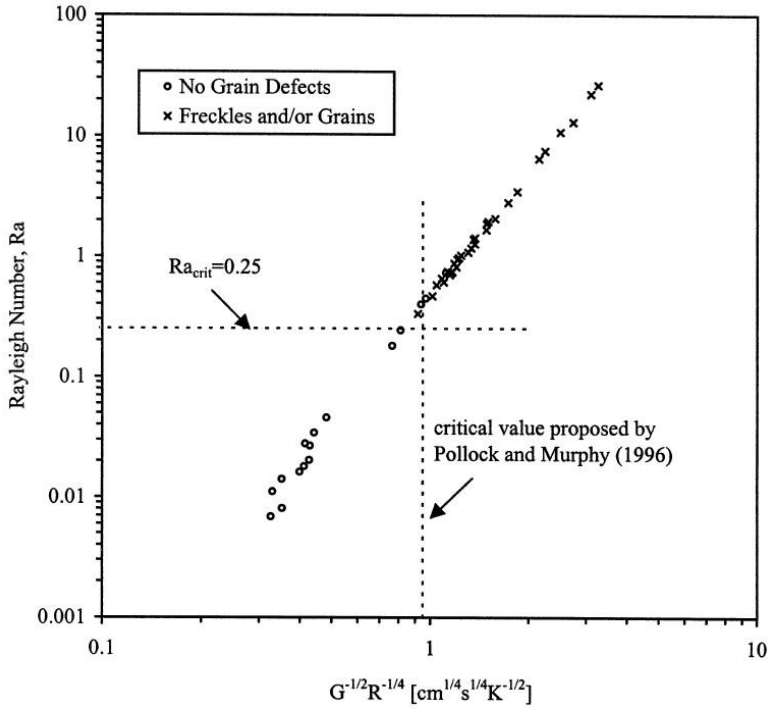


Figure 2-18: Calculated Ra number based on directional solidification castings investigating grain defects in the single crystal alloy SX-1 calculated as a function of the thermal parameter G and solidification parameter R (Pollock and Murphy, 1996). The thermal gradient G has been determined empirically from the relationship between PDAS, G and V and the critical Ra number is plotted against this (Beckermann et al., 2000)

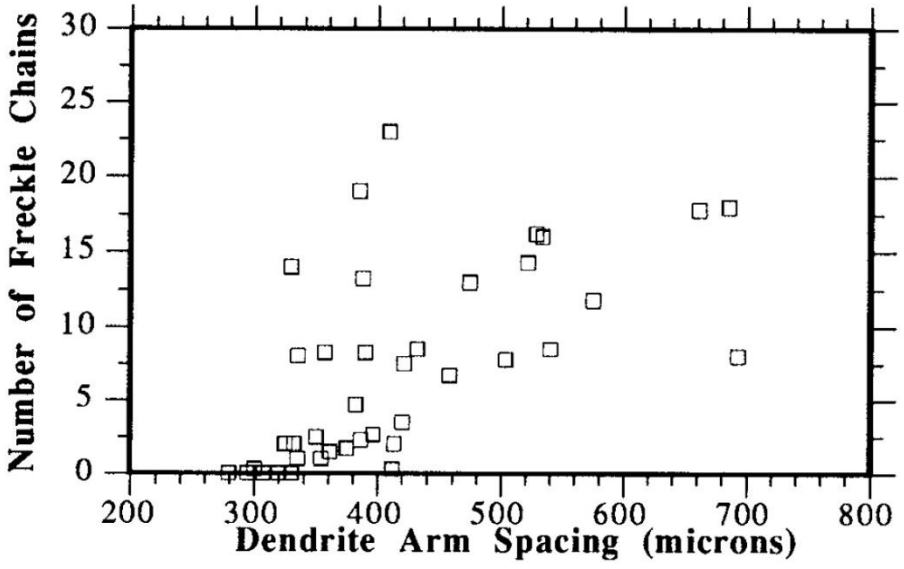


Figure 2-19: The dependence of freckle formation on the primary dendrite arm spacing showing no freckles at a spacing of $320\mu m$ *at a cooling rate of 0.1 °C.s^{-1} (Pollock et al., 1992)*

It is clear that the probability of freckle formation when casting Ni-base superalloys is intrinsically linked with alloy chemistry and the solidification process.

Improvements to the casting process is one way in which defects can be inhibited in order to improve the efficiency of the industrial process.

2.8 The current and future role of Re and Ru in nickel based superalloys

As discussed in section 2.4 a significant aspect of superalloy development has been the addition of Re and Ru; Re to strengthen the γ matrix by solid solution means and also by retarding the γ' coarsening process which increased the creep performance at elevated temperatures and Ru to inhibit the formation of detrimental TCP formation.

Re has been increasingly used as an addition to Ni based superalloys and is also used as a petroleum-reforming catalyst in the production of lead free petrol; representing an estimated 70% and 20% of use respectively (Polyak, 2013). Other applications of Re, primarily as $W-Re$ and $Mo-Re$ alloys are more diverse and include thermocouples, x-ray tubes and flashbulbs to name but some (Polyak, 2011).

Re exists in extremely small quantities throughout nature, however not as a separate mineral, but is instead extracted as a by-product of the copper mining industry when trace elements of *Re* and *Mo* are extracted from copper. Re is deposited mostly in Chile, the United States, Poland, Uzbekistan and Kazakhstan (Polyak, 2013)

As of 2008 net import reliance in the US was 85% of apparent consumption and strategies were considered in which rhenium supplies could be bolstered, through more efficient

processing techniques or the introduction of recycling programs. This prompted GE aviation to introduce The Rhenium Reduction Strategy, which included four paths; revert, recycle, recover and reduce. Two significant stages of this program are recycling and reducing.

Recycling entails recovery of Re containing superalloys from fielded hardware as it reaches the end of useful service life. In March 2008, aviation industry news reported that Turkish Airlines was the first customer to participate in GE Aviation's reclamation programme in which customers returns their scrap HP turbine blades to GE for cleaning and melting for recycling.

In conjunction with this, alloys with reduced Re or zero Re content are being developed such as Rene N515 (1.5 wt % Re) and Rene N500 (no Re), with the desire to retain as much mechanical performance as possible and ideally match the mechanical properties exhibited by 2nd generation single crystal alloys.

It was proposed that DS Eutectic alloys could offer a solution for the replacement of Rhenium containing superalloys, providing issues relating to the processing of such alloys are resolved.

2.9 Practice of directional solidification

The simplest method of imposing directional freezing is to cast into a mould that has sufficient heat extraction at one end and good thermal insulation elsewhere (McLean, 1983). Initial attempts at directional solidification used this methodology with the mould placed onto a heat sink whilst the other sides were insulated with exothermic compounds (Vernsnyde and Guard, 1960).

The power down technique was a natural extension of the preceding method; the introduction of power control via a furnace that was external to the casting allowed the rate of heat input to be carefully controlled therefore giving a steady solidification rate, this process is described in a patent application by (Sink, 1965). The power down process suffered however from a relatively low temperature gradient and also a reduction in the gradient over the length of the casting as the solidifying front moved further away from the source of heat extraction.

An improvement over the power down technique was the high rate solidification process (Tingquist and Laux, 1974) which is a modification of the Bridgman-Stockbarger crystal growing technique (McLean, 1983); hence the furnaces used for this application are commonly referred to as Bridgman furnaces.

This method is the most widely used to produce turbine blade components and in-house development of the technique at Rolls-Royce began in 1968 (Goulette et al., 1984); as such the high rate solidification process is often referred to as directional solidification (DS). The directional solidification furnace can be broadly split into three distinct zones; the hot zone (comprising the heating element), the baffle region (which is intended to ideally form an adiabatic barrier to radiation) and the cold zone (which in the standard process is a heat sink for radiation from the mould). An illustration of a single zone furnace for directional solidification is shown in Figure 2-20.

In the directional solidification method a mould is located on a water cooled chill plate, usually made of copper, and initially positioned within the heating chamber (hot zone) of the furnace. The hot zone is set to a pre-determined temperature; the temperature being monitored by in-situ thermocouples in conjunction with a proportional-integral-derivative

controller (PID).

The mould is removed at a controlled withdrawal rate from the hot zone of the furnace via means of a linear actuator, into a cooling chamber (cold zone) whilst the furnace hot zone is maintained at a set temperature (McLean, 1983). The initial process of heat extraction is by conduction through the copper chill plate; however as the process continues and conduction through the solid alloy becomes less effective the process becomes dominated by radiation heat loss.

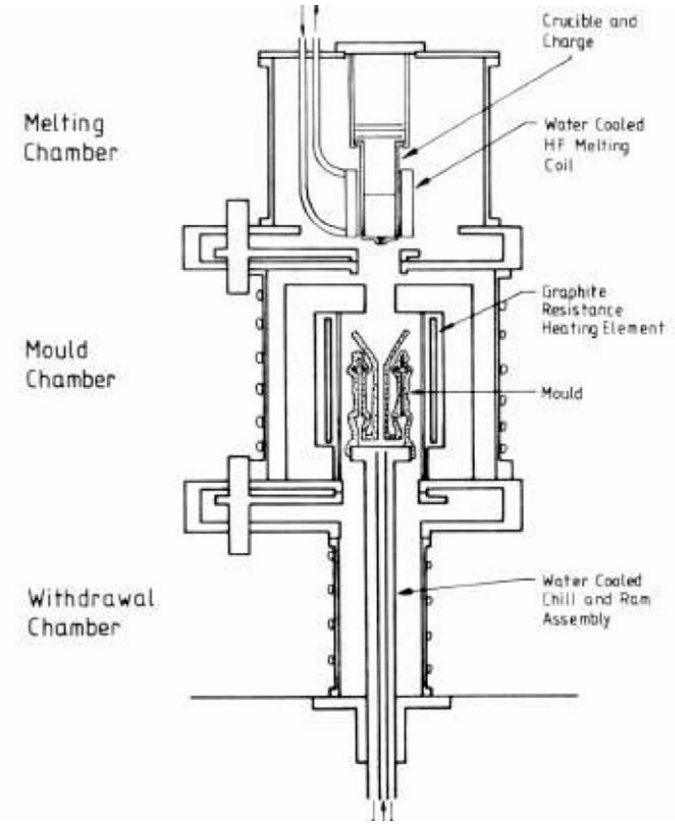


Figure 2-20: Sectional view of a standard Rolls-Royce DS furnace (Goulette et al., 1984)

The conditions within the cooling zone are maintained by means of furnace radiation baffles, which minimise radiant heat loss from the furnace into the cooling zone (McLean, 1983). The radiation baffles are located between the heating chamber and the cooling zone and contain sufficient openings in order to allow the mould to pass through during the

directional solidification process. Ideally for efficient design the baffle opening should be as minimal as possible, or at least the baffle should contain the smallest opening compatible with the casting geometry.

The impetus for the use of radiation baffles can be assessed analytically;

The directional solidification process requires a controlled rate of heat input, heat extraction and withdrawal velocity in order to satisfy steady-state heat flow boundary conditions in the liquid and solid parts of the component. An approximation of the process is shown in Figure 2-21, where an infinitely long cylindrical rod of radius, r, moves at a uniform rate, V, from a furnace of temperature, T_f into a cooling medium, T_c.

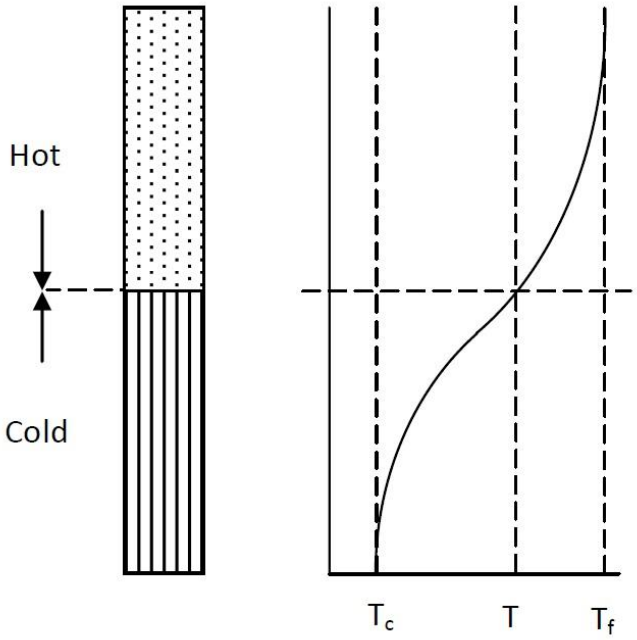


Figure 2-21: Idealised model of steady state heat flow for an infinitely long thin rod moving at a velocity, V from a furnace at temperature, Tf into a cooling zone of temperature, Tc. Adapted from (Reed, 2006).

Assuming heat flow only occurs in the x direction, the following heat flow equation must be satisfied;

$$k\frac{\partial^2 T}{\partial x^2} + vc\frac{\partial T}{\partial x} + \dot{Q} = 0 \qquad 2.28$$

Where k is the thermal conductivity, c is the volumetric specific heat capacity and $\dot{Q}$ is the volumetric heat flow rate (+/-)

At the melting temperature of the alloy, $(T = T_m)$, latent heat occurs at the solid liquid interface which must also be considered (McLean, 1983, Reed, 2006).

$$\left[k_s\frac{\partial T}{\partial x}\right]_s = \left[k_l\frac{\partial T}{\partial x}\right]_l + Lv \qquad 2.29$$

As the component emerges into the cooling zone, $x < 0$, heat extraction can be described by the Newtonian heat transfer law in which a combined heat transfer coefficient, h, is used to satisfy the equation;

$$q = h(T - T_c) \qquad 2.30$$

For varying casting processes, h can be defined accordingly, and for the HRS Bridgman process has been approximated to be in the order of $46\ W/(m^2K)$ (Konter et al., 2000).

The standard differential equations to describe the heat field in a moving solid can therefore be described (Livingston et al., 1970) for $x < 0$, Equation 2.31 $x > 0$, Equation 2.32 assuming the region between hot and cold zones is a perfect adiabatic interface.

$$T[x] = T_c + (T_m - T_c)\exp\left[\beta_s x\right] \qquad 2.31$$

$$T[x] = T_f - \left(T_f - T_m\right)\exp\left[-\beta_l x\right] \qquad 2.32$$

The coefficients β_s and β_l are defined as;

$$\left[\beta_s = \frac{2h}{k_s r} + \left(\frac{vc}{2k_s}\right)^2\right]^{\frac{1}{2}} - \frac{vc}{k_s}$$

And;

$$\beta_l = \frac{vc}{k_l}$$

Manipulation of these equations, described elsewhere (McLean, 1983, Reed, 2006), enables calculation of the thermal gradient, G and also the maximum velocity that a component could be withdrawn in a theoretical furnace before the solid liquid interface breaks down and radial heat flow is introduced.

In practise the heat analysis models that have been described will only give an approximation of the temperature field within a component for various reasons;

- The assumption of a perfectly adiabatic transition region between the hot and cold zones is not possible thermodynamically.
- In many cases when casting components using the HRS Bridgman process the use of radiation baffles is limited due to size and geometry of the components.

One assumption that perhaps will introduce error in the analytical models is that of an isothermal furnace hot zone temperature (T_f in Equation 2.32). This assumption is generally not valid (especially when casting large gas turbine blades) as there will intrinsically be some heat transfer between zones. The consequences of changes in the heater temperature close to the hot/cold transition in relation to the reference hot zone temperature are shown to be movement of the solid/liquid interface as the cooling efficiency exceeds the heating capability for the given conditions (Elliott et al., 2004b).

Economic necessity has led to the casting of multiple components, generally an array of components in a ‘cluster’ so this has mitigated the effectiveness of the radiation baffles in an industrial context (Goulette et al., 1984). Perhaps this is one reason why it has been shown that the use of increased superheat in this furnace configuration can lead to an increase in the resultant thermal gradient and hence a lower PDAS for given geometry (Horrocks, 1990a)).

2.9.1 Process Development

There have been a multitude of process developments in the search for improvements in the achievable thermal gradient, not only to improve the castability of eutectic alloys but also to optimise current single crystal alloys by the means of PDAS reduction, which can reduce homogenisation heat treatment time, reduce interdendritic segregation and reduce the susceptibility of freckle formation in difficult to cast alloys.

Perhaps it is most useful to subdivide the methods into three distinct categories in a similar way that the geometry of the directional solidification furnace is often referred. They are optimisation of heat input (hot zone), the use of enhanced cooling methods (cold zone) and optimisation of baffle design (adiabatic barrier).

2.9.1.1 Optimisation of heat input

Previous studies of the industrial casting process have highlighted the requirement for careful control of the hot zone of the furnace in the directional solidification process; specifically that a high hot zone temperature will increase the thermal gradient by pushing the solidification front further down towards the cold zone, hence compressing the solid-liquid interface and reducing the PDAS for a given cast (Horrocks, 1990a)). This however

is limited by the cooling effectiveness of the cold zone and the inability to effectively remove excess heat energy will have a negative effect on the thermal gradient.

Referring back to the theory of directional solidification as shown in Figure 2-21, it is intuitive to think that conditions within the hot zone could be refined further by increasing the temperature closer to the baffle region. Indeed this methodology is current used with a twin zone heater configuration in which the hot zone is heated by two separate heaters, with the lower heater having a higher set temperature than the one above. The drawbacks to this approach are that the use of separate heaters and power supplies are required which is a complication to the process.

Methods to increase the hot zone temperature in the baffle region have also been proposed in furnaces which make use of induction coils and hot zone susceptors. The proposed ideas make use of slots cut into chosen areas of the susceptor which will interfere with the eddy current motion therefore creating local heat variations with the intention of creating the highest temperature near the baffle region (Gigliotti and Sawyer, 1980, Taylor, 1983a).

Another approach is the introduction of a centrally located heating element in conjunction with the existing surrounding heater (Piwonka, 1974) as shown in Figure 2-22.

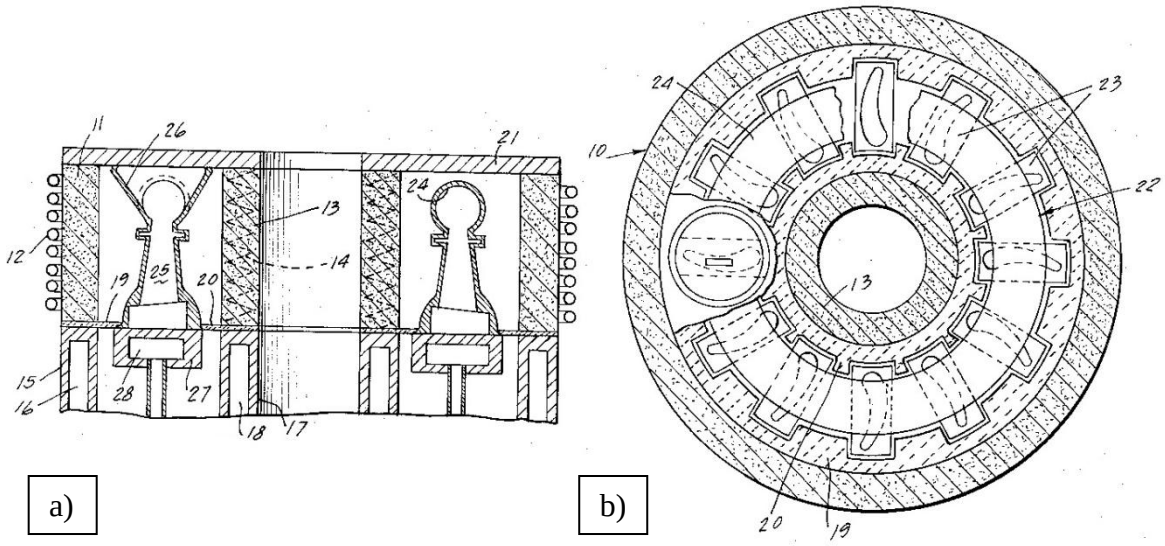


Figure 2-22: Schematic showing (a) longitudinal cross section of furnace and (b) transverse. Detailing concentric heating elements and mould located within the furnace (Piwonka, 1974)

A more radical approach is that of localised heating directly onto the mould surface by the means of focused laser energy (Schlienger and French, 2008), as shown in Figure 2-23.

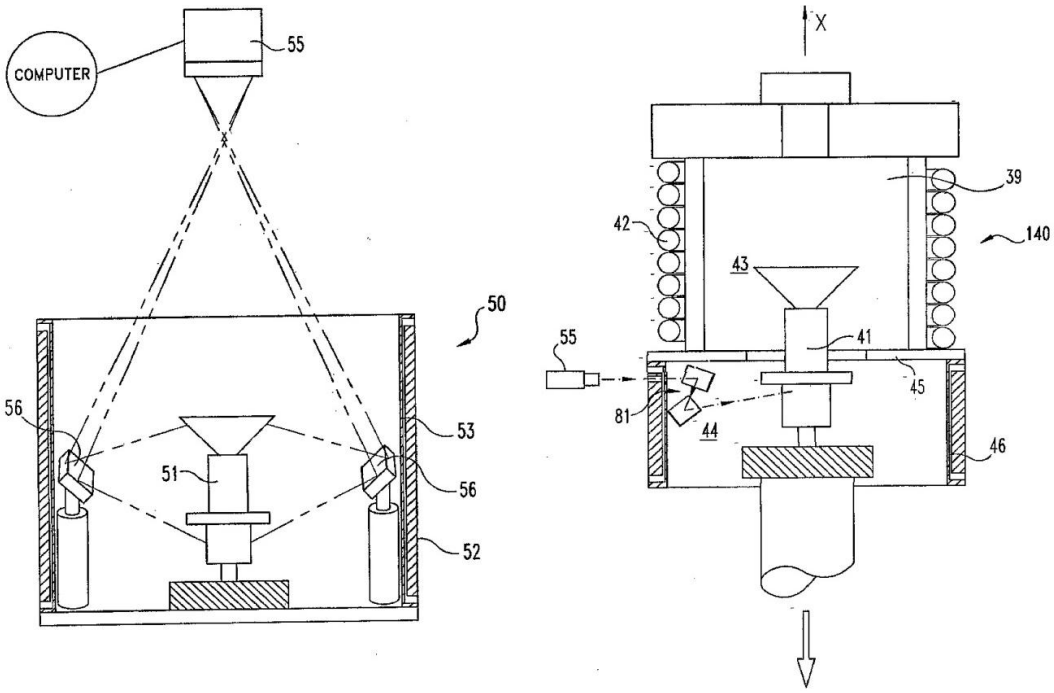


Figure 2-23: Illustration of proposed laser heating apparatus in which heat can either be applied by scanning to a whole mould or applied selectively to part of the mould surface (Schlienger and French, 2008)

In practise the laser heating method would require more than one laser diode; realistically a circular array of mounted diodes would be required possibly in conjunction with some sort of redirection apparatus in the form of moveable mirrors. Therefore this method would require significant investment to be implemented.

Other methods have been devised to optimise the heat input within the furnace hot zone. Zone Intensified Overheating (ZIO) has arisen from the investigation of accelerated cooling techniques such as liquid metal cooling and is a derivative of the twin zone heater concept. Liquid Metal Cooling (LMC), which will be discussed shortly, enhances the cooling effect within the cold zone and therefore results in the movement of the solid liquid interface into the hot zone. This can be prevented by adding additional superheat via small heaters located above the baffle region in order to confine the liquid solid interface (Liu et al., 2008, Liu et al., 2010).

2.9.1.2 Enhanced cooling methods

A number of methods have been proposed with the aim of increasing the rate of heat extraction from the mould surface in the cold zone of the furnace; as the traditional directional solidification relies on radiation heat transfer alone for heat extraction it is intuitive to introduce another heat transfer mechanism in the form of conduction in order to improve the efficiency of the process.

The most prevalent of these methods is that of LMC in which the mould is extracted from the furnace and submerged into a bath of liquid metal, usually tin or aluminium, which have much lower melting temperatures (~300 °C-660 °C) than the nickel superalloys that are cast.

The LMC method is shown to increase the thermal gradient and hence result in a refinement of the dendrite structure for nominally identical conditions in comparison to the Bridgman method, Figure 2-24.

The use of an intermediate baffle layer in the form of floating alumina beads, as mentioned previously, is still required in order to protect the liquid metal bath from radiant heat emanating from the hot zone.

Due to the enhanced conduction cooling of the LMC method, which can result in movement of the solid-liquid interface and curvature of the solidification front (Elliott et al., 2004b), localised heaters near the vicinity of the solid-liquid interface have been used successfully (Liu et al., 2008, Liu et al., 2010).

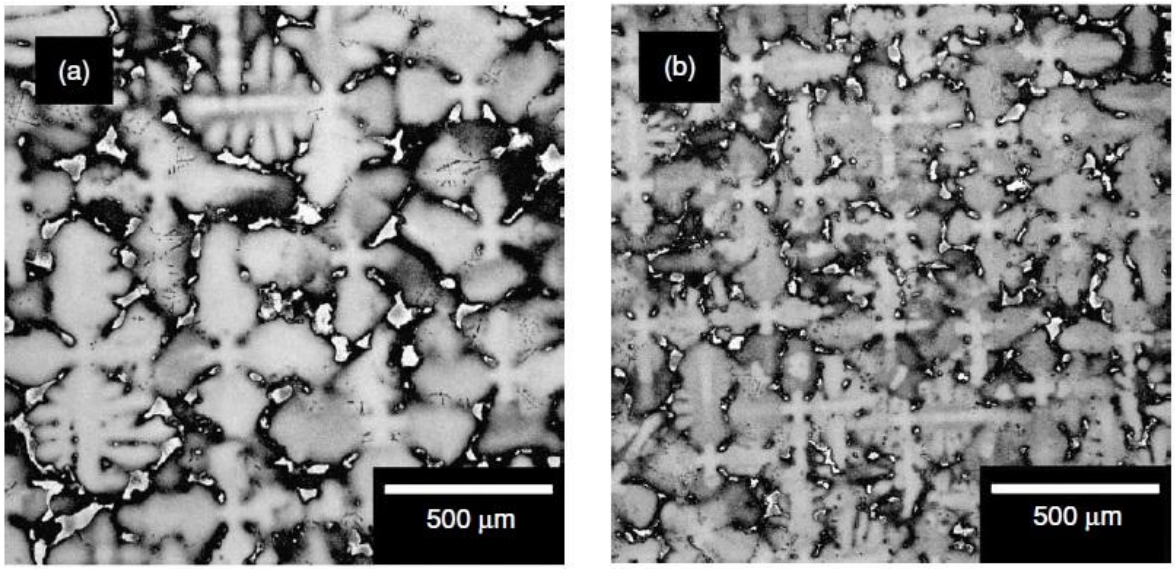


Figure 2-24: SEM micrographs of dendrite morphology in a nickel based superalloy sectioned parallel to the growth direction. a) 2.5 mm/min, Bridgman b) 2.5 mm/min, LMC (Reed, 2006)

Other methods to increase the rate of heat extraction by the introduction of conductive cooling include the application of a liquid coolant directly onto the mould surface in the form of a spray (Brinegar, 2003, Lemkey, 1973) as shown in Figure 2-25.

This method has been utilised on an experimental level during the investigation of the $\gamma - \gamma' - \delta$ composite in which sample bars were solidified by the direct application of water as a cooling medium (Lemkey, 1973).

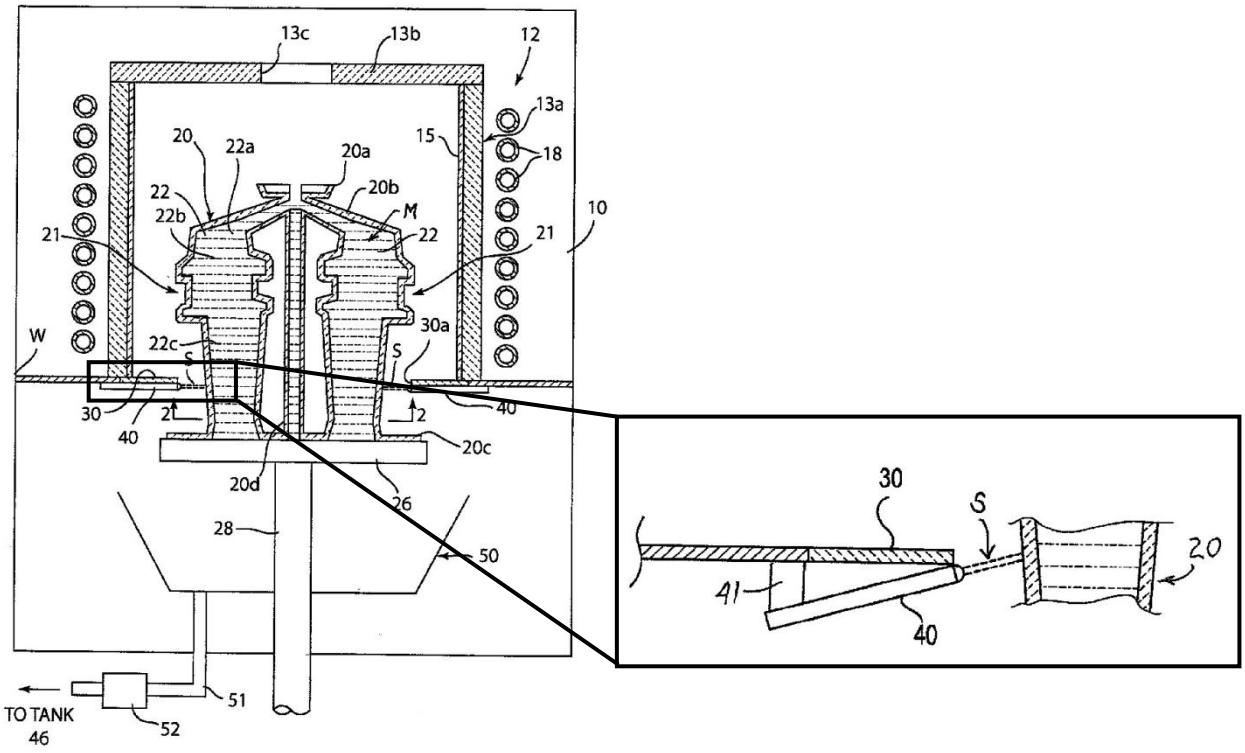


Figure 2-25: Schematic showing furnace with coolant spray nozzle directed towards the outer surface of the casting mould (Brinegar, 2003)

The use of a fluidised bed quenching has also been developed in which the mould is withdrawn into a heat sink comprising fine powders, of alumina for example, suspended in an inert gas such as He, Ar or N_2 under low pressure (Quested and Northwood, 1980). A broadly similar method has also been proposed in which loose ceramic beads are used to form a pseudo-liquid heat sink and extract heat by conduction due to their close contact with the mould (Thomas, 1976).

A method which theoretically produces higher thermal gradients than that of LMC is the method of Gas Cooling Casting (GCC) in which cooling gasses are directed at the surface

of the mould in the cold zone of the furnace (Konter et al., 2000). The increased thermal gradients in comparison to the LMC process are attributed by the author to the impingement on the mould by the high velocity gas layer which is said to bridge the gap between the solidified alloy and the mould material; an area of which is still dominated by radiation heat transfer in the LMC process.

Figure 2-26 shows a comparison of the measured PDAS in aerofoil geometry for the GCC, LMC and Bridgman process.

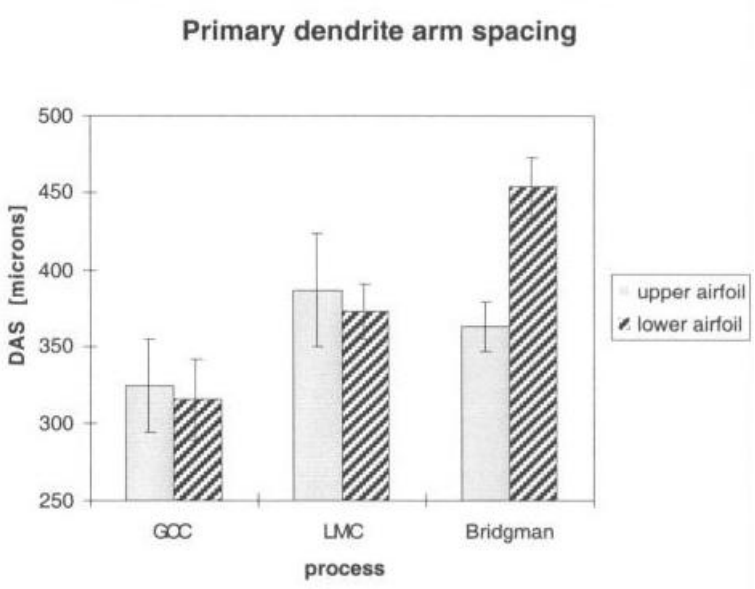


Figure 2-26: Primary dendrite arm spacing for different casting processes in the upper and lower aerofoil of a pseudo blade geometry (Konter et al., 2000)

A drawback of the GCC process however is the introduction of the cooling gas and the effect this may have on the heat distribution within the furnace due to possible convection; also any increase in vapour pressure within the furnace may have a detrimental effect on the life of the resistive heating element. The process of gas layer impingement attributed to the GCC processes would also require further clarification as in many instances a seal coat is applied to the mould in order to prevent moisture absorption during storage which could

inhibit the effectiveness of the process.

2.9.1.3 Optimisation of baffle design

The search for optimised processing techniques using the directional solidification process has highlighted the necessity for efficient baffle design in order to maintain the integrity of the cooling zone in the furnace.

It is clear that efficient barriers to block heat transfer, in the form of furnace baffles, are critical in order to increase thermal gradients during casting. As discussed previously, an extra level of complexity to the heat transfer between hot zone, mould and cold zone is introduced when multi-component geometry such as turbine blade clusters are to be cast. Various solutions to this have been proposed in order to try and retain a sufficient mechanical barrier to heat transfer.

One solution incorporates a pair of semi-circular baffles opposing one another with the ability to vary the aperture size of the baffle by movement in the horizontal direction (Lallement, 1989) as shown in Figure 2-27.

Other design configurations use multiple baffles with varying internal profiles that can move vertically with the mould in order to maintain a constant gap between baffle and mould (Brinegar et al., 2000, Graham, 2004, Soderstrom et al., 2005, Terkelsen, 1973) a design of which is shown in Figure 2-28.

Another method proposed is the application of a flexible baffle (Atkinson and Walsh, 1995) and the configuration in which a flexible baffle may be applied (Brokloff et al., 1990), Figure 2-29.

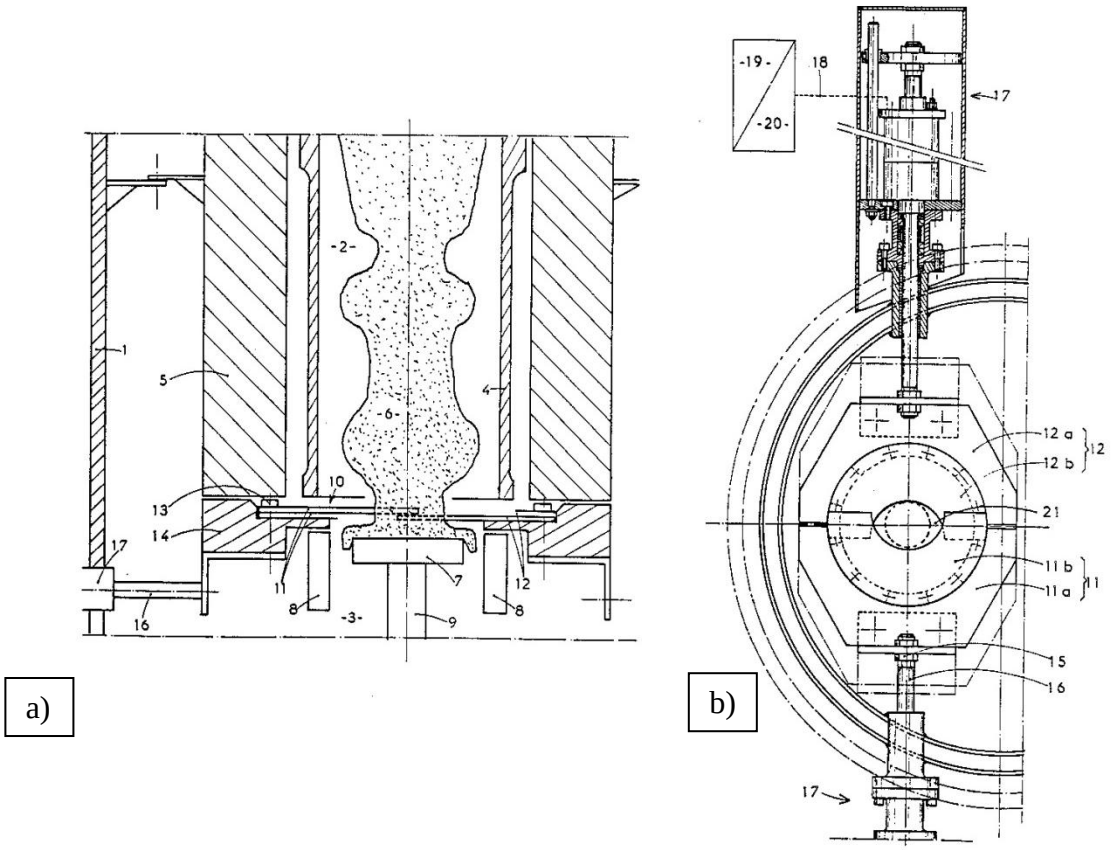


Figure 2-27: a) Directional solidification furnace showing moveable baffle, b) Plan view of furnace showing mechanism proposed to move baffle into varying positions(Lallement, 1989)

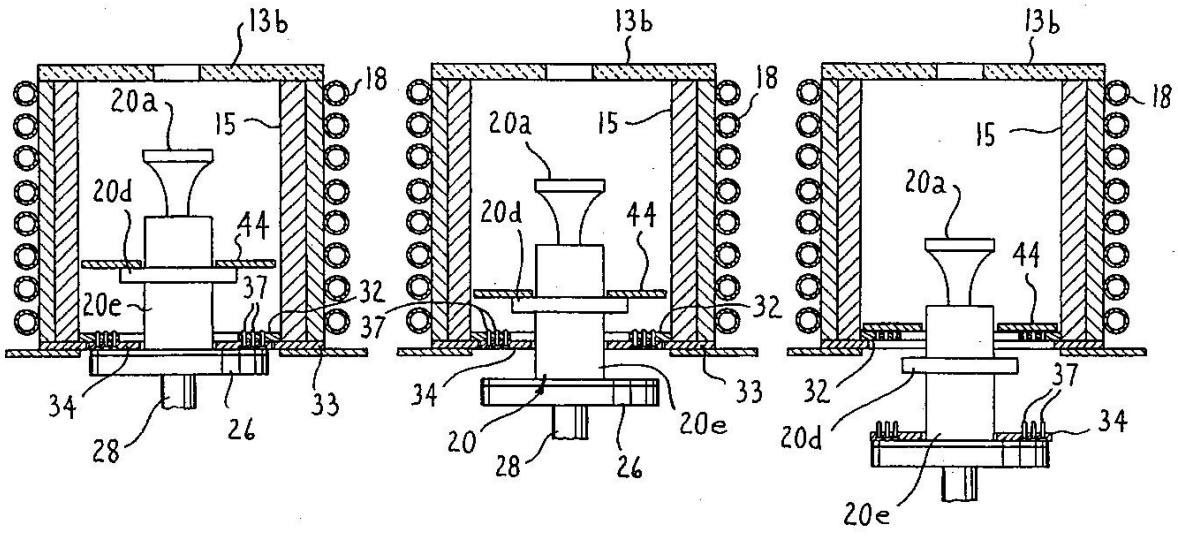


Figure 2-28: Diagram of directional solidification furnace showing the position of moveable baffles during operation (Brinegar et al., 2000)

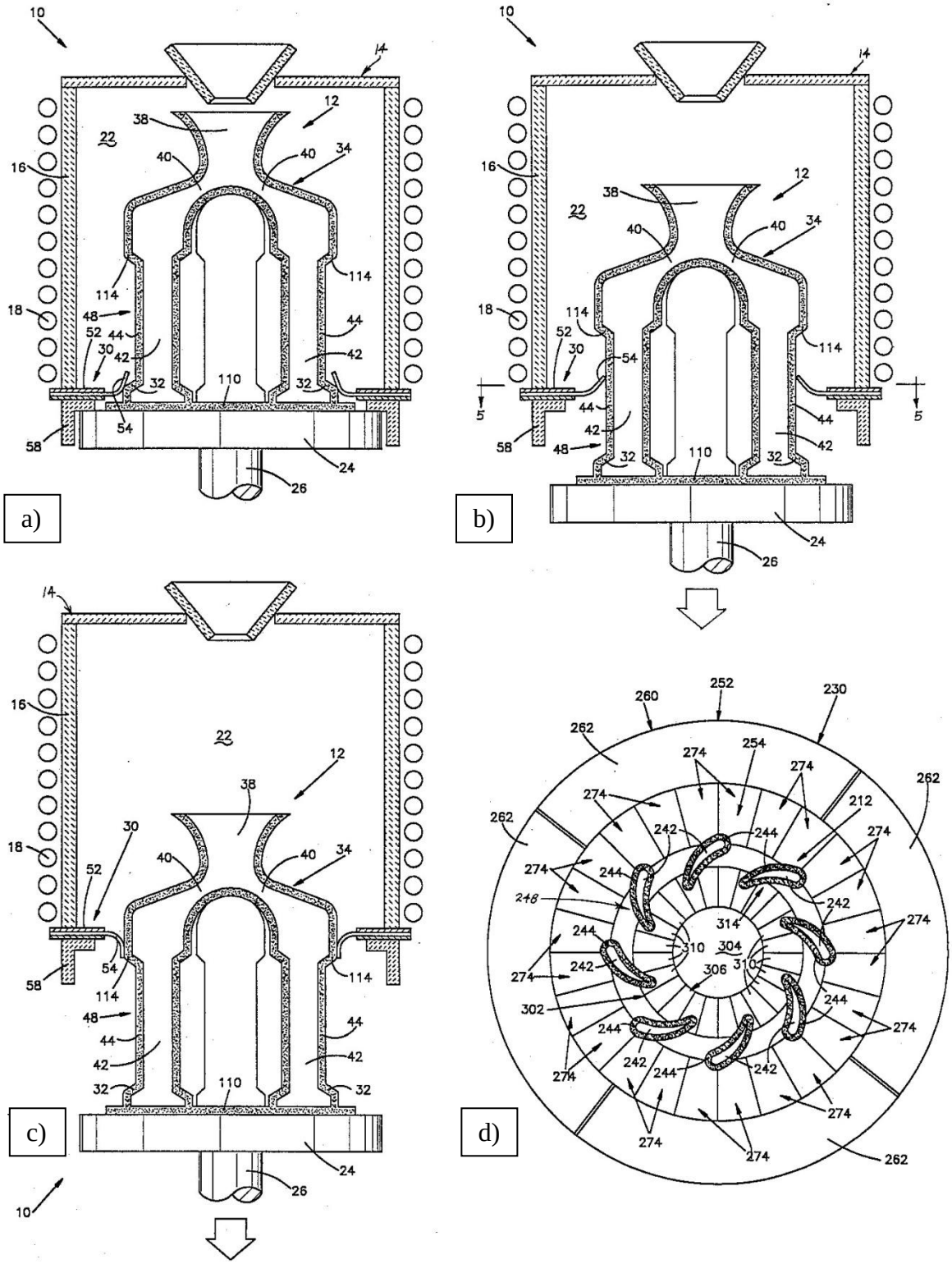


Figure 2-29: a-c) Sectional view of furnace showing mould in various positions during the withdrawal process and the interaction with the flexible baffle d) Plan view of one flexible baffle configuration (Brokloff et al., 1990)

When considering the casting of multiple components, the use of a centrally located baffle has been suggested in the previously mentioned flexible baffle and has also been proposed for use with rigid radiation baffles (Hugo and Betz, 1997), Figure 2-30.

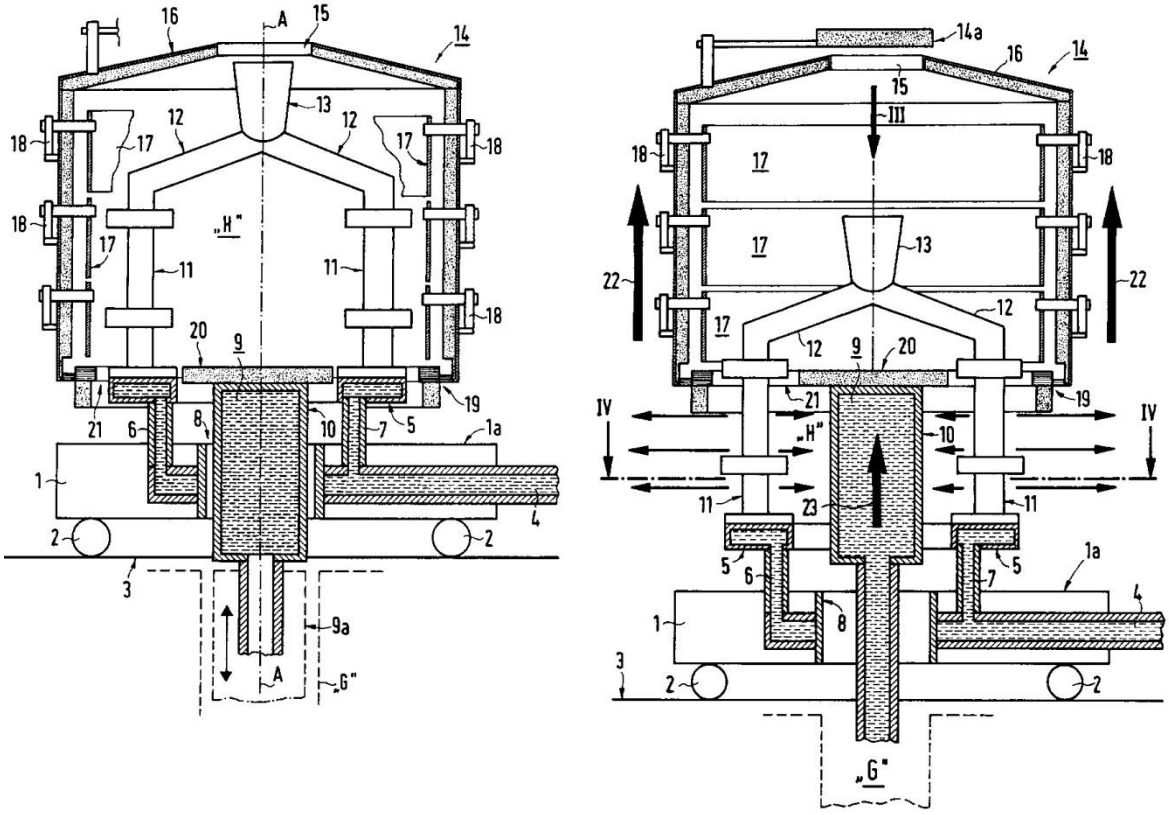


Figure 2-30: Illustration of furnace with centrally located baffle (Hugo and Betz, 1997)

Liquid metal cooling is one proposed method to increase the rate of heat extraction within the furnace cold zone however the efficiency of this process also suffers as a result of the liquid alloy being heated by radiation from the furnace hot zone (Elliott et al., 2004a).

To alleviate this the use of novel baffle methods have been proposed; one such method involves the use of floating insulation baffles resting on the surface of the molten cooling alloy which act to block radiant heat flow from the heater to the liquid bath (Klug, 2002) as shown in Figure 2-31.

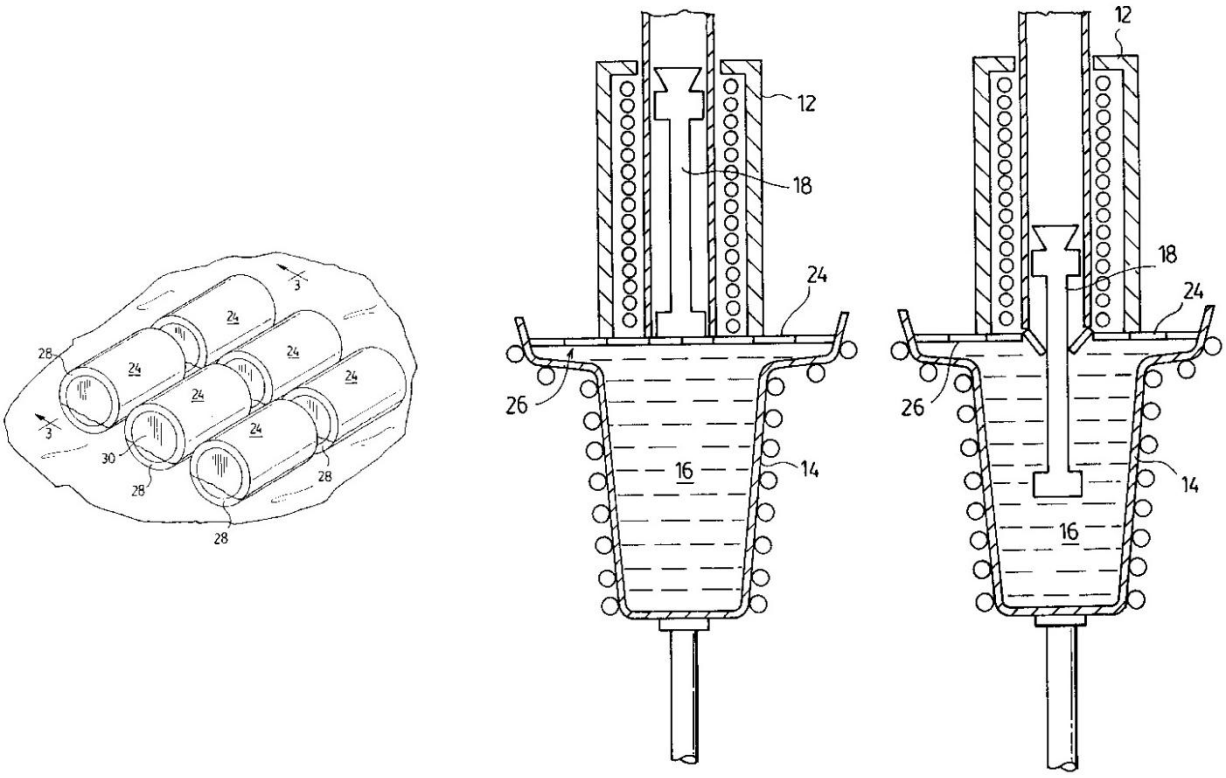


Figure 2-31: View of floating baffle material and its use in a furnace incorporating liquid metal cooling (Klug, 2002)

2.10 Finite element modelling

The practise of mathematical modelling has been known of and used for many years and is now routinely used to predict the physics of a process or experiment for a given set of parameters. The term Computational Fluid Dynamics (CFD) was coined by (Harlow and Fromm, 1965).

The terms Finite Element Analysis (FEA) and CFD perhaps carry different connotations for engineers; FEA is most commonly associated with traditional stress-type analysis and CFD, logically, associated with fluid flow/heat transfer problems. Both approaches are equally valid and differ by the underlying physical problems that are to be solved; Newton's laws of motion, Maxwell's equations, Navier-Stokes equations etc and use

similar methods to reach an outcome, however a number of discretisation methods exists.

To solve a complex real world problem there a number of steps that can be taken in order to reach a solution. Firstly, it is useful to simplify the problem and produce some sort of idealised model, perhaps by the use of boundary conditions that are known to the user, in order to eradicate a level of uncertainty or variation. The problem is then ready to be solved by mathematical models using a number pre-determined theories discussed earlier, depending on what it is you are attempting to solve; be it fluid flow, stress or electrical current flow. At this point it is not unreasonable to sub-divide the part, generally called a domain, into a number of smaller entities, called elements, in order to simplify the mathematics. When this is carried out we have a discretised domain, i.e. the problem is mathematically discrete and the physics at element level are ready to be calculated iteratively.

One of the first methods to use this technique in order to solve a complex problem was called the Finite Difference Method (FDM) and was first used by (Richardson, 1911) to calculate stresses in a masonry dam. This method discretises a domain spatially into structured grid points and is tied to a coordinate system e.g. Cartesian, cylindrical; hence this is called a structured mesh. This discretisation method is mathematically easy to implement and allows the use of local Taylor expansion to approximate differential equations; however is limited to relatively simple geometry due to the nature of the discretisation process.

The Finite Element Method/Analysis (FEM/FEA) derived from simple calculations of the force and deflection of building frames and trusses (Cheung et al., 1996) and the process developed into the framework method in which a plane elastic medium was represented as

a collection of bars and beams (Hrennikoff, 1941).

The discretisation method, as many engineers may recognise it, derived from the work by (Courant, 1943) with the introduction of triangular sub-regions, and was further refined in the 60's and 70's with (Clough, 1960) associating the name FEA to the technique. The method discretises a domain into finite elements consisting of corner nodes to represent a flat surface or 4-8 node quadratic elements to represent a curved surface (Cheung et al., 1996)

Advantages of the technique are that the material properties of adjoining elements do not have to be the same i.e. multi-domain/material cases can be solved and irregular shaped domains can be calculated due to the fact that the discretisation does not need to follow the coordinates of a regular grid hence the mesh is 'unstructured'.

The Finite Volume Method (FVM) is similar in many respects to that of the FDM in that the domain is discretised into control volumes with bounding nodes, however rather than calculating with respect to these, the solution is calculated at a computational node at the centre of each element volume; essentially at the centre of gravity for each element.

Both FEA and FVM are suitable for unstructured complex geometry; the FEA discretisation is said to be easier to implement however the FVM method is favoured for CFD flow based problems. Perhaps for these reasons software such as CFX® and ProCAST® use an unstructured finite element based finite volume method, where the finite element base comes from the use of a shape function to describe the way in which a variable changes across an element however the numerical approximation is based at the element vertex or volume centre as in the finite volume method (Cross et al., 2006).

Finite element modelling is used extensively in a number of areas as an investigative tool

to aid the development of new processing techniques by the simulation of a number of process variables which can save time and cost without the need to commit to experimental trials.

On such area, and one which will be discussed at length in the body of the thesis, is the casting of components using the Bridgman method; commonly referred to as directional solidification.

Before the common use of finite element modelling the temperature field within a furnace was often measured experimentally, generally using an array of static thermocouples or moving thermocouples which were withdrawn along the furnace centreline. Further to this, the measurement of temperature gradients within a casting was often measured by in-situ thermocouples within a mould which adds significant expense to the process. Computer modelling of the process allows a greater range of process variables to be predicted on the basis of model validated using a limited number of experimental trials.

Accurate thermal models are intrinsic to the process especially when increasing the complexity of the calculations carried out. Recent applications of the finite element modelling method are able to predict stress and strain evolution within the cast geometry as solidification occurs (Panwisawas et al., 2011). Further to this, the propensity for recrystallisation can be predicted within the casting based on plastic strain calculations (Panwisawas et al., 2012).

Another area in which process modelling using the finite element method is becoming increasingly important is in the production of turbine disk components; or more generically the forging process. During forging recrystallisation is promoted by heating and mechanically working the component which results in the introduction of plastic strain.

Computer modelling is often used in order to calculate the strain energy within a component with the desire of predicting the microstructure evolution.

The use of computer modelling to make complex predictions of phenomena such as stress/strain relies on a sound understanding of the driving forces, in the case of the directional solidification process, the temperature field within the furnace. This is discussed in the following section.

2.10.1 ProCAST Furnace Model

The ProCAST modelling method is an application in which the casting process can be simulated in order to calculate any number of characteristics that may be important part of the as-cast geometry. This may be calculation of the thermal gradient, estimations of the expected dendrite morphology or residual stress accumulated through component mould interaction upon cooling.

ProCAST furnace models and their application by Rolls-Royce to simulate the Bridgman casting process have been well established (Jennings, 1996), in order to calculate the thermal history of a cast component during a casting cycle and relate this to the thermal gradient and microstructure. To do this, moulds instrumented with thermocouples were used to record the transient temperature history at discrete points within the components and then compare this with calculations made within the software.

Standard mould geometry was used for validation purposes, called a VeriCAST mould, and was intended to represent turbine blade geometry including the root section which poses significant cross-sectional area changes.

Prior to the availability of such software, furnace efficiency was measured by assessing as-

cast microstructure in relation to casting velocity (Horrocks, 1990b)) and by quantifying changes made to the process such as flow rate of cooling water in the cold zone and modification to baffle geometry (Horrocks, 1990a)).

The experimental 'single shot' Bridgman furnace was relocated from a casting facility in Bristol (CRDF) to the University of Birmingham (UTC) around the year 2000 and was intended to be used as an experimental casting facility.

A significant part of the Bridgman furnace pre and post-move validation from the CRDM to the UTC which was conducted by (Newell, 2009) involved the casting of VeriCAST geometry and analysis of the resultant microstructure, predominantly from the aerofoil section; this is discussed further in Chapters 5 & 6.

In a manner similar to standard practices, a VeriCAST mould was instrumented with thermocouples at discrete positions and during a casting cycle with a hot zone reference temperature of 1803.15 K a withdrawal velocity of 6.36×10^{-5} ms^{-1} and a radiation baffle comprising a 110×10^{-3} m ID orifice.

A further mould geometry of a straight test bar with a 12×10^{-3} m ID was also instrumented and cast by (Newell, 2009) with furnace parameters consisting of a hot zone reference temperature of 1843.15 K a withdrawal velocity of 6.36×10^{-5} ms^{-1} and a radiation baffle comprising a 110×10^{-3} m by 30×10^{-3} m rectangular orifice.

A ProCAST model was developed and, at the time, represented the furnace heating element in the hot zone as a cylinder of constant temperature. However in order to match with experimental temperature measurements it was recognised that the heating element temperature must be split with the lower portion at a temperature below the hot zone reference temperature and the upper portion above; a split of around 90 K. This method

continued to be used.

Comparisons of experimental results with the ProCAST predictions of thermal gradient for the VeriCAST geometry were reasonably good with an error of between 4 - 7% for the lower portion of the blade closest to the chill however errors increased towards the top section as withdrawal continued into the cold zone.

Errors between measured and predicted for the test bar geometry with the more restrictive baffle were less favourable; at two discrete points which resided close to the chill in the lower portion of the hot zone, errors were shown to be in the region of 16 - 17%, which in real terms of thermal gradient represented a discrepancy of $1.59 – 1.74 \times 10^3$ K m^{-1}.

This magnitude of error is not ideal however, and although it may not pose such a significant problem when casting single crystal alloys due to the less stringent casting conditions, if casting eutectic alloys an error such as this may result in a cellular or dendritic microstructure when casting close to the limits of the G/V ratio.

The current ProCAST model is a useful tool for validating pre-existing furnace configurations; however if wishing to explore new concepts, especially those involving enhanced heating in the hot zone, which has been shown to be beneficial in an industrial content (Horrocks, 1990b)) and also when using accelerated cooling techniques (Liu et al., 2008, Liu et al., 2010), then a greater understanding of the furnace thermal characteristics and hot zone temperature is required.

2.11 Summary

Single crystal alloys are currently used in high pressure turbine blade applications due to their relatively high melting temperature and resistance to creep deformation. Refinement of the microstructure, namely the dendrite arm spacing and resistance to freckle formation, can both be achieved by optimising the casting process and increasing the thermal gradient.

Eutectic alloys are potential successor materials to single crystal nickel alloys due to their intrinsic creep resistance as a result of the microstructure; however an aligned microstructure requires plane front solidification during the casting process which in turn requires a steep thermal gradient.

Process modelling is being increasingly used in order to predict parameters as a result of the casting process such as the thermal gradient, microstructure and propensity for freckle formation and is applicable to the simulation of both single crystal casting and eutectic alloy casting; however this relies on a sound understanding of the thermal field within the Bridgman furnace.

Based on information presented in the literature review the remaining challenges for this work are as follows:

- Assess the effects that baffle configurations have on the hot zone temperature profile using a fully validated CFD based method in order to further the understanding of the current ProCAST model.

- Use the understanding gained to develop a method of improving the thermal gradient in conditions where extensive radiation baffling is limited.

- Use modelling and experimental techniques to assess the capability of the single shot furnace to cast eutectic alloys.

- Assess potential refinements made to the microstructure of single crystal alloys as a result of process improvements made.

CHAPTER 3 EXPERIMENTAL PROCEDURE

This section will detail a number of experimental and observational techniques used throughout this study.

The production of single crystal components when casting the single crystal alloy CMSX-4 will be described which details the single crystal selection methods used, along with standard wax pattern production and investment shell manufacture. The casting of eutectic alloys will also be described, along with the rationale for casting techniques used.

The assessment of as-cast microstructure by metallographic examination will also be described along with chemical etchants used to reveal microstructure and relevant techniques and software used for analysis.

Furnace temperature measurements have been carried out, along with transient power measurements during casting trials. Finally a brief overview of the computer modelling software will be detailed along with relevant system information.

3.1 Production of single crystal components

As described previously, the manufacture of turbine blades for aero engines has changed radically since the first wrought blades were produced. Following this, subsequent iterations of the casting process took place until the casting of single crystals became commonplace.

The modern casting method is often referred to as the high rate solidification process and the furnace used called a Bridgman furnace. There are a number of types of such furnace;

the small bore furnace, the twin zone furnace, in which the hot zone can be set to two different temperatures and are controlled independently of one another, and the ‘single shot’ development furnace.

The single shot Bridgman furnace has been used exclusively throughout this work, in its standard configuration and experimental configuration, which will be described in a later section.

3.1.1 Wax geometry & investment shell production

3.1.1.1 History

The investment casting method, which can also be referred to as the lost wax process (Pattnaik et al., 2012), has been utilised for centuries to produce precision net-shape components from a number of metallic materials. In fact the process can be dated back to as early as 5000BC when the method was used to make basic tools and weaponry such as arrow heads (Taylor, 1983b).

As the name suggests, the process relies on was replicas of the part to be produced. Early methods no doubt employed natural occurring wax materials, however modern wax is a mixture of complex compounds containing natural and synthetic wax and resins.

The jewellery making industry found significant use for the lost was/investment casting process (Jones and Yuan, 2003), due to the good surface finish and relatively low volume of components made.

However a significant driving force for interest in the technique on an industrial scale was the onset of the 2nd world war due to the requirement of complex components with precision geometry (Pattnaik et al., 2012).

3.1.1.2 Manufacture

Wax patterns were produced using a semi-automated wax injection machine which injects standard moulds, normally manufactured out of aluminium or low carbon steel with a cavity insert for a threaded hanger; with molten wax at high temperature and pressure. The wax patterns are then removed from the mould and a manipulator handle is inserted. The wax patterns are then dipped into a degreaser for 45s and then allowed to dry.

The investment casting process relies on a ceramic shell which will retain structural integrity at temperatures of the molten alloy (~ 1573 – 1673 K) and often above, especially when superheat is used to maximize the thermal gradient.

This is generally achieved by dipping the wax pattern into ceramic slurry formed of mixtures of zircon ($Z_rS_iO_4$), silica (S_iO_2) and alumina (Al_2O_3), (Reed, 2006) followed by stuccoing with progressively larger particles of the same materials; fine particles for the first coat followed by strengthening coats.

The shell system used is one adopted form Rolls-Royce but comprises a secondary EHT coat which acts to reduce the amount of secondary coats used from around 10 to 6.

The primary slurry coat was applied along with the primary stucco coat which is a fine powder to ensure a good surface finish, this was then dried overnight. This was followed by 6 successive coats of secondary slurry and stucco followed by a final seal coat.

Stucco coats were applied by hand with a sieve in order to ensure an even coat, during which a breathing mask was worn to filter fine airborne particulates. It is also worth noting that after dipping in slurry, excess should be left to drip off the pattern, during which the pattern should be orientated by 180^o through successive coats. This prevented excess

thinning of the shell wall at the top of the component near the hanger, due to gravity.

The recipe for the shell system used and key process requirements are detailed in Table 3-1, B5 and B4 refer to the British Standard viscosity measurement cups (BSI, 1977).

Table 3-1: Recipe for shell system and method for producing moulds for investment casting

	Slurry Manufacture	
	Primary Coat / PDS 62	**Secondary Coat / PDS 262 (EHT Secondary Slurry)**
Binder	1 litre, Morrisol	1 kg, EHT
Filler	4.8 kg, Zircosil 200M	3.75 kg, Zircosil 200M
Antifoam	5.15 ml, Octanol	
Wetting Agent	10.3 ml, SynperonicNX	
Flow time / Initial mix	28–31 s (B5)	60–70 s (B4)
Flow time / 24 hrs		55 s (B4)
Flow time / in use		52 s (B4)
	Shell build up	
Application method	Dip / Fine brush	Dip
Stucco	Al 80	Al 28/48
Dry time	24 hrs	1.5-2 hrs
Temperature	294.15 K (21^{o}C)	294.15 K (21^{o}C)
Air speed / Relative humidity	0.1ms-1 / 10%	3ms-1 / 50%
	Build sequence	
Primary coat	1	
Secondary coats		6
Seal coat		1 (Dry overnight)

Moulds were then de-waxed in a boiler clave by flash melting of the wax in order to avoid expansion and possible cracking of the shell; this was carried out at 9 Bar / 453-553 K. The mould was then sintered at 1173.15 K for 3600s to increase the mechanical strength of the mould; this process also acts to burn off any remaining wax.

The operational stages from wax to cast single crystal component are shown in Figure 3-1.



Figure 3-1: Illustration of stages in the investment casting process. a) Wax pattern b) Wax pattern with 1st stage shell c) Fully shelled mould d) Single crystal component exactly replicating wax starter geometry.

3.1.2 Casting and single crystal selection

The casting of single crystal alloys has already been discussed in detail in Chapter 2 so only the salient points will be discussed here.

There are two main techniques for single crystal selection; the use of a spiral seed selector, commonly referred to as a 'pig tail' selector, and a single crystal seed used in conjunction with a restriction within the mould.

In this study both techniques have been used; the spiral seed selector when casting multiple test bars in a cluster, as shown in Figure 3-1 and described in section 3.3, and the seed crystal and restriction when casting the VeriCAST mould geometry and single test bars with close fitting radiation baffles. Of the two techniques, the use of a spiral seed selector appears to be the most effective.

When casting the VeriCAST test piece and test bar cluster, a bayonet fitting was included as part of the build-up which enables firm attachment of the mould to the chill of the Bridgman furnace.

When casting single test bar geometry a different approach was utilised; under normal circumstances alloy ingots are induction melted above the hot zone of the furnace and then poured into the mould below. This poses problems when casting single test bars, predominantly due to the risk of alloy splash when pouring.

There is also a compatibility issue with the induction melting unit as the minimum volume of alloy that can be melted is greater than the volume of a single 12-13 x 10^{-3} m ID test bar.

In order to mitigate this, pre-cast single crystal bars, produced using the moulds shown in Figure 3-1, were inserted into pre-sintered alumina tubes. The end of the pre-cast geometry

was machined to ensure good contact with the chill of the furnace. Under casting conditions the single crystal bar is then melted in-situ within the furnace hot zone before withdrawal is commenced.

One potential drawback to this approach is the inability to inhibit re-crystallisation during the withdrawal process, which is indeed the case; however experience has shown that due to the dominant single crystal existing in the un-melted section any grains will tend to form at the inner wall of the test bar mould.

Given that the object of this exercise is to evaluate the PDAS and ensuring that any measurements do not traverse grain boundaries, this is a reasonable approach.

3.2 Casting of eutectic alloys

Two selected eutectic alloys were chosen to be cast as part of this study, COTAC 744 and $\gamma - \gamma' - \delta$. As noted by (McLean, 1983) when casting eutectic alloys the issue of melt containment has arisen which has precluded the use of *Si, Zr* shell systems and limited experimentation to Al_2O_3 based moulds which have been used successfully with high superheats and high thermal gradients (Lemkey, 1973).

3.2.1 The use of pre-formed sintered alumina tubes

The scope of this work it to assess the viability of casting eutectic alloys using industrial type methods or at least methods that could be integrated within current casting practices. As no net-shape components are to be cast, and only test bar type geometry required, then pre-formed sintered Al_2O_3 tubes have been used throughout.

To mitigate the risks described in section 3.1.2 samples of eutectic alloy were pre-cast

using a mould of similar geometry to that shown in Figure 3-1, without the seed selector, at a constant withdrawal rate.

Bars were then cut into sections and inserted into an alumina test bar mould, ensuring good contact between the pre-formed alloy and the chill.

3.3 Microstructure modification of Nickel based alloys

Numerous methods have been devised with the aim of increasing the thermal gradient and decrease PDAS by various means and it has been shown that an increase in hot zone temperature will increase the thermal gradient and show a decrease in PDAS (Horrocks, 1990a)). Increasing the withdrawal velocity, assumed to be equivalent to the solidification velocity, will also reduce PDAS. These two variables however are not independent, and an increase in the withdrawal velocity will reduce the thermal gradient (Horrocks, 1990a)).

The most prevalent method of increasing the thermal gradient and modify the microstructure is to use extensive radiation baffling (Newell, 2009), this option is limited however when casting multiple geometry moulds or clusters' with complex geometry. In this instance large diameter 'standard' baffles are the only viable option and optimisation is limited to hot zone temperature or withdrawal velocity.

The aim of this work is to assess the effects on thermal gradient and resultant microstructure by modifying the hot zone temperature profile which will be explained in detail in Chapters 5 & 6. As such, a selected number of casting conditions were chosen;

- A number of multiple component mould containing four 12 x 10^{-3} m diameter bars with spiral selectors shall be cast using a 110 x 10^{-3} m diameter radiation baffle with a set hot zone temperature of 1823.15 K a shown in Figure 3-2. The hot zone set temperature will remain constant however the hot zone temperature profile will be altered; the withdrawal rate altered from a speed of 6.36 x 10^{-5} ms^{-1} to 10.67 x 10^{-5} ms^{-1}. This is intended to quantify the effect of modifications to the hot zone temperature profile.

- A further series of casts will use a single 13 x 10^{-3} m ID test bar mould in conjunction with an extensive 20 x 10^{-3} m ID radiation baffle, as shown in Figure 3-3, which would be expected to give the largest thermal gradient. Under these conditions the hot zone temperature will vary from 1823.15 K to 1923.15 K for both a standard and modified hot zone temperature profile while the withdrawal rate is constant and set to 10.67 x 10^{-5} ms^{-1}. This is intended to determine the maximum achievable thermal gradient using the single shot Bridgman furnace and produce the smallest PDAS in the alloy.

- Selected eutectic alloys will be cast using the furnace condition described above using a 13 x 10^{-3} m ID test bar mould in order to utilize the maximum thermal gradient configuration. The withdrawal rate will be varied depending on the alloy G/V ratio in order to produce an aligned microstructure and validate the G/V ratio/ furnace thermal gradient.

- Finally a VeriCAST mould, shown in Figure 3-4, will be cast using a hot zone temperature of 1803.15 K, a 110 x 10^{-3} m ID baffle and a withdrawal velocity of 6.36 x 10^{-5} ms^{-1}. This is intended to quantify modifications made to the hot zone with data obtained from literature.

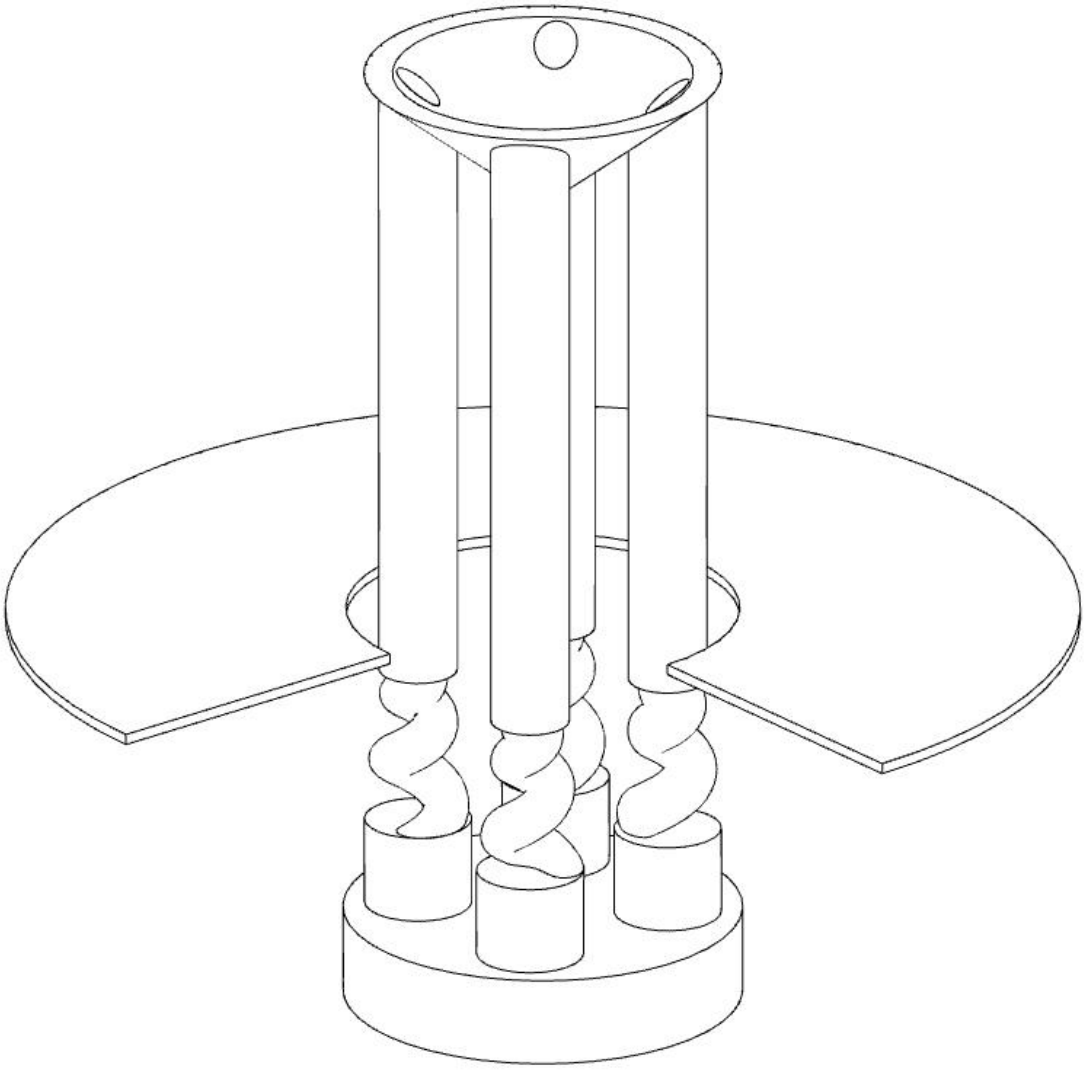


Figure 3-2: Graphical representation of test bar cluster mould including spiral seed selectors surrounding radiation baffle geometry. A 90^{o} segment has been omitted from view for clarity.

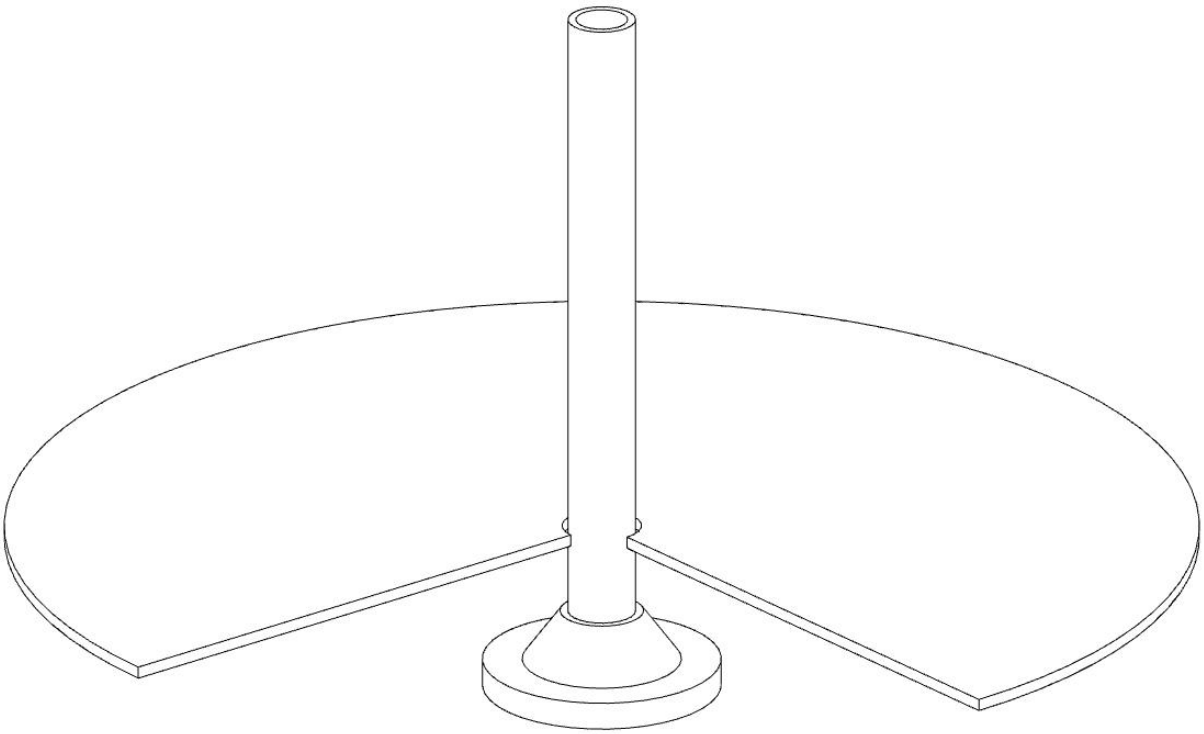


Figure 3-3: Graphical representation of single test bar consisting of alumina tube and supporting base including radiation baffle. A 90^{o} segment has been omitted from view for clarity.

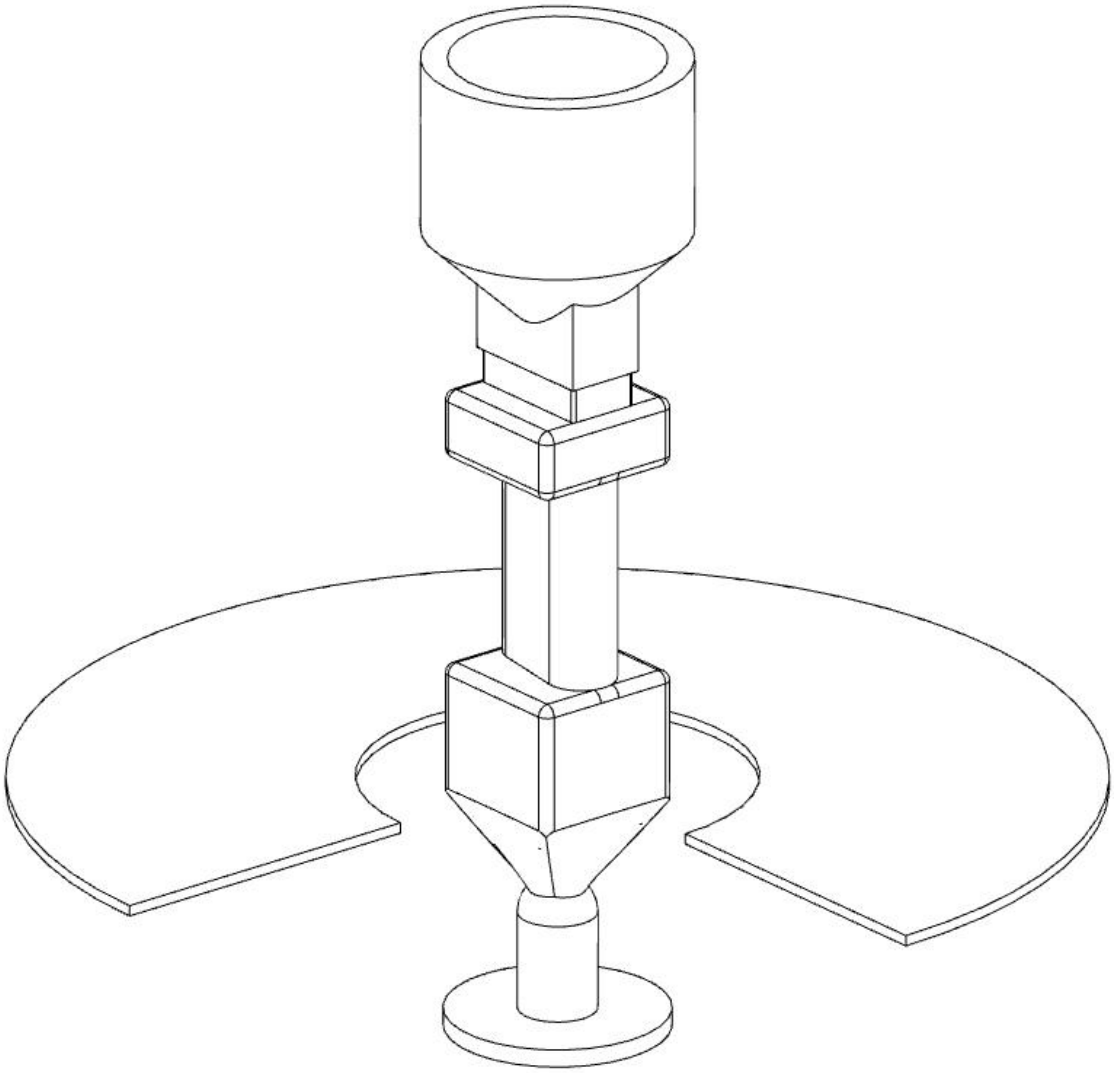


Figure 3-4: Graphical representation of VeriCAST test geometry and surrounding radiation baffle. A 90^{o} segment has been omitted from view for clarity.

3.4 Assessment of microstructure by metallographic analysis

3.4.1 Preparation

In order to facilitate the analysis of alloy microstructure a smooth, flat highly polished surface is imperative. This surface can then be chemically etched in order to preferentially attack sites of interest, revealing the microstructure.

The choice of grinding and polishing routine is largely decided by the alloy to be analysed and personal preference; the initial route followed used fairly sparse grinding and longer polishing stages however this often led to inconsistent results. Due to this a more comprehensive routine was established which incorporated more grinding stages and reduced the grit particle size incrementally. An outline of the procedure is shown in Table 3-2.

A standard etchant used for superalloys is Kalling's No2 made up of 5g Copper Chloride ($CuCl_2$) diluted with 100ml of Hydrochloric Acid (HCl) and 100ml of Ethanol (C_2H_60) which is swapped over the polished sample, or the sample immersed, at 293.15 K; the $\gamma - \gamma' - \delta$ eutectic alloy was also etched using this method.

Due to the extremely fine strengthening phase possessed by the COTAC 744 eutectic alloy standard etchant used to attack the Ni matrix would not expose the strengthening fibres sufficiently. After experimentation with other mixtures, the etchant Murakami's Reagent was used with good results. This etchant is made up of 10g Potassium Ferricyanide (K3[Fe(CN)6], 10g Potassium Hydroxide (KOH) diluted with 100ml water, and shown to highlight carbides, particularly in steels (Vort et al.), and proved to highlight the NbC strengthening phase within the Ni matrix of the COTAC alloy successfully.

Table 3-2: Grinding and polishing stages used in preparation for metallographic analysis.

Stage	Medium [1)]Rigid Disk [2)]Paper	Standard ANSI Grit	Median Particle Diameter / x 10^{-6} m	Disk Velocity / RPM	Pressure / N	Lubricant	Application Time / s
1	[1)] PIANO 80	80	180	250	15	Water	120
2	[1)] PIANO 120	120	106	250	15	Water	120
3	[1)] PIANO 220	220	60 [*Estimate]	250	15	Water	300
4	[2)] 400 GRIT	400	25.8	250	15	Water	300
5	[2)] 800 GRIT	800	6.5	150	15	Water	300
6	[1)] DAC	N/A	3	150	15	3µm Suspended Diamond	300
7	[1)] NAP	N/A	1	150	7.5	1µm Suspended Diamond	120 / 180

3.4.2 Measurement

3.4.2.1 Single crystal alloys

In directionally solidified dendritic structures the primary dendrite arm spacing is one of the most useful characteristics to determine, and once known can be used to derive the thermal gradient or solidification velocity of the component using a relatively simple relationship.

In order to measure the PDAS from experimental samples, a statistical method was used, proposed by (Warnken and Reed, 2011, Warnken and Reed, 2012) where a full description is provided.

In this method the software PlotDigitizer is used as a tool to identify and mark dendrite cores with respect to their x and y coordinates on a cross sectional macro image of known size. The results of this operation are then exported as a table of all identified dendrite coordinates.

An algorithm is then used in the software program, R, to characterise the distribution and spacing of nearest neighbours for each of the primary dendrites by a pair-wise relation. This results in a value pertaining to the spacing of the primary dendrite arms and also a measure of the number of nearest neighbours for each dendrite.

The advantages of this method are that a macro image containing a large number of dendrites can be evaluated with little operator effort and additional characteristics are also provided, such as a frequency distribution of the spacing, an example of which is shown in Figure 3-5 taken from (Warnken and Reed, 2011), and coordination number which is quantitative indicator of the morphology of the lattice.

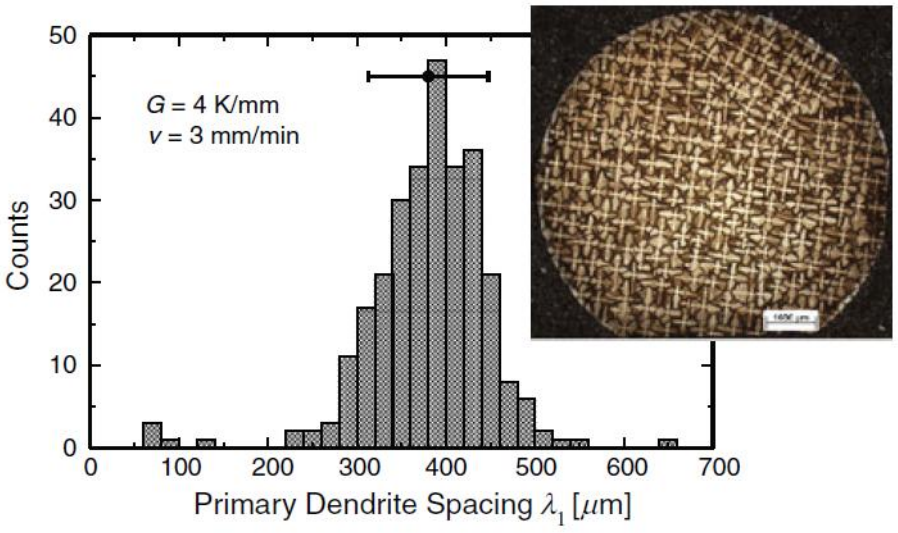


Figure 3-5: Example of measured PDAS values displayed in histogram format taken from work by (Warnken and Reed, 2011).

3.4.2.2 Eutectic alloys

A characteristic of the microstructure of eutectic systems is that of the phase spacing. This can be related to the solidification conditions in a relation proposed by (Jackson and Hunt, 1966), which has been experimentally determined by others (Lemkey, 1973, Thompson et al., 1972) and can be directly related to mechanical properties of the alloy.

Analysis of lamellar phase spacing is generally straight forward and involves the analysis of longitudinal sections where the line intercept method can be used to derive the average spacing. Measurement of the phase spacing of rod like structures is more arduous, especially when the rod diameter is likely to be only a few microns and a microscope image with reasonable magnification is still likely to contain tens of hundreds of sites present.

In order to conduct this work the image analysis software ImageJ was used to facilitate a fairly simple process.

The first stage is to obtain a micrograph image of a potential site for analysis and note the x, y dimensions in the measurement unit of choice in order to calculate the area of the measured site.

The first step is to adjust the image using the 'adjust - threshold' command which will transform the microscope image, shown in Figure 3-6 a) into a flat two-tone version with a single colour tone representing the phases to be counted, Figure 3-6 b).

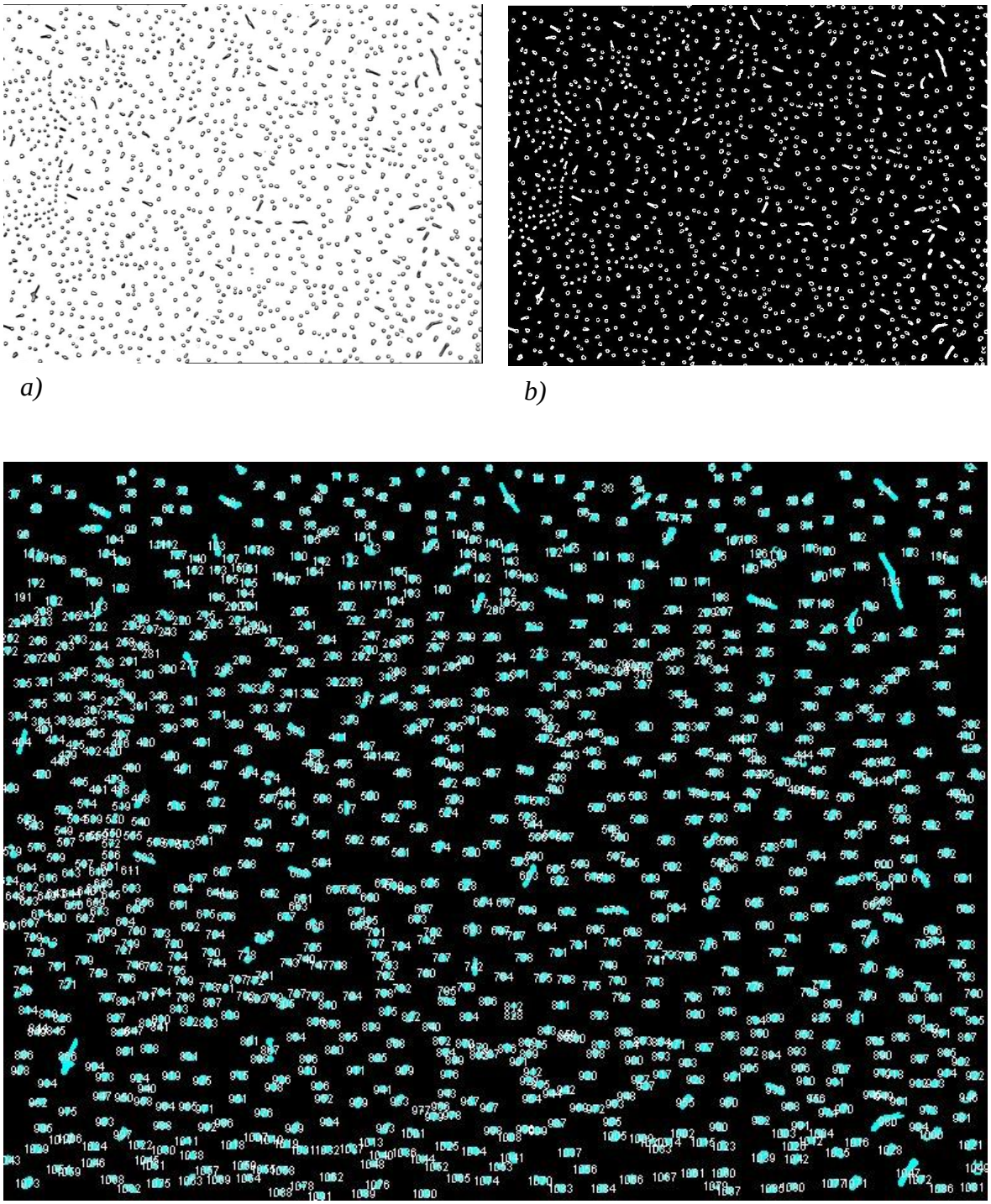
The next step is to use the 'analyse – particles' command with the option to 'show overlays' and 'omit on edges' selected. The latter command will not count any phases that do not fall fully within the bounds of the counting frame.

The programme then proceeds to count all phases present and overlay the sites counted onto the image in view for verification, Figure 3-6 c).

The standard equation to determine the phase spacing, λ_1, can then be used in the form:

$$\lambda_1 = \sqrt{\frac{A}{N}} \qquad 3.1$$

where A is the area of the measured frame and N is the number of instances counted.



a) *b)*

c)

Figure 3-6: Successive steps of image processing in to count phase spacing of a rod-like eutectic alloy. a) Original microscope image, b) Adjusted image to transform phases into flat white with flat black matrix, c) Processed image showing counted image overlays and omitted phases lying on the border of the image.

3.5 Furnace centreline temperature measurement using a moving thermocouple

In order to fully characterise the temperature profile within the Bridgman furnace a technique was used in which a thermocouple was positioned vertically on the chill, so as to maintain colinearity with the Z-axis of the furnace. The position of the chill can then be altered in a similar manner to when withdrawing a cast so the thermocouple can record a temperature history of the furnace thermal profile; this is a standard validation technique used in Rolls-Royce (Jennings, 1996, Brown, 2012).

The thermocouple of choice was a Type 'B' (Pt-30%Rh / Pt-6%Rh) with an alumina sheath nominally 5×10^{-4} m in thickness to ensure wire separation. Calibration was carried out by Rolls-Royce at the PCF in accordance with set standards; the nominal error is expected to be in the order of ±0.25%. The thermocouple was further insulated by an alumina tube of 4×10^{-3} m ID and 6×10^{-3} m OD which was incorporated into the thermocouple assembly.

The assembly housing was constructed using sintered alumina tubes joined using a wax mould in order to form a base that could be clamped to the chill as shown in Figure 3-7. The cavity formed by the wax mould was then filled with alumina slurry and allowed to air dry. The wax was then removed using standard means and the assembly sintered at 1173.15 K for 3600 s.

The axial extent of temperature measurement covered a distance of 0.5 m and was initiated when the top of the thermocouple was in line with the top of the heating element a shown in Figure 3-8 a), the position of the thermocouple within the assembly was confirmed by

x-ray as shown in Figure 3-8 c).

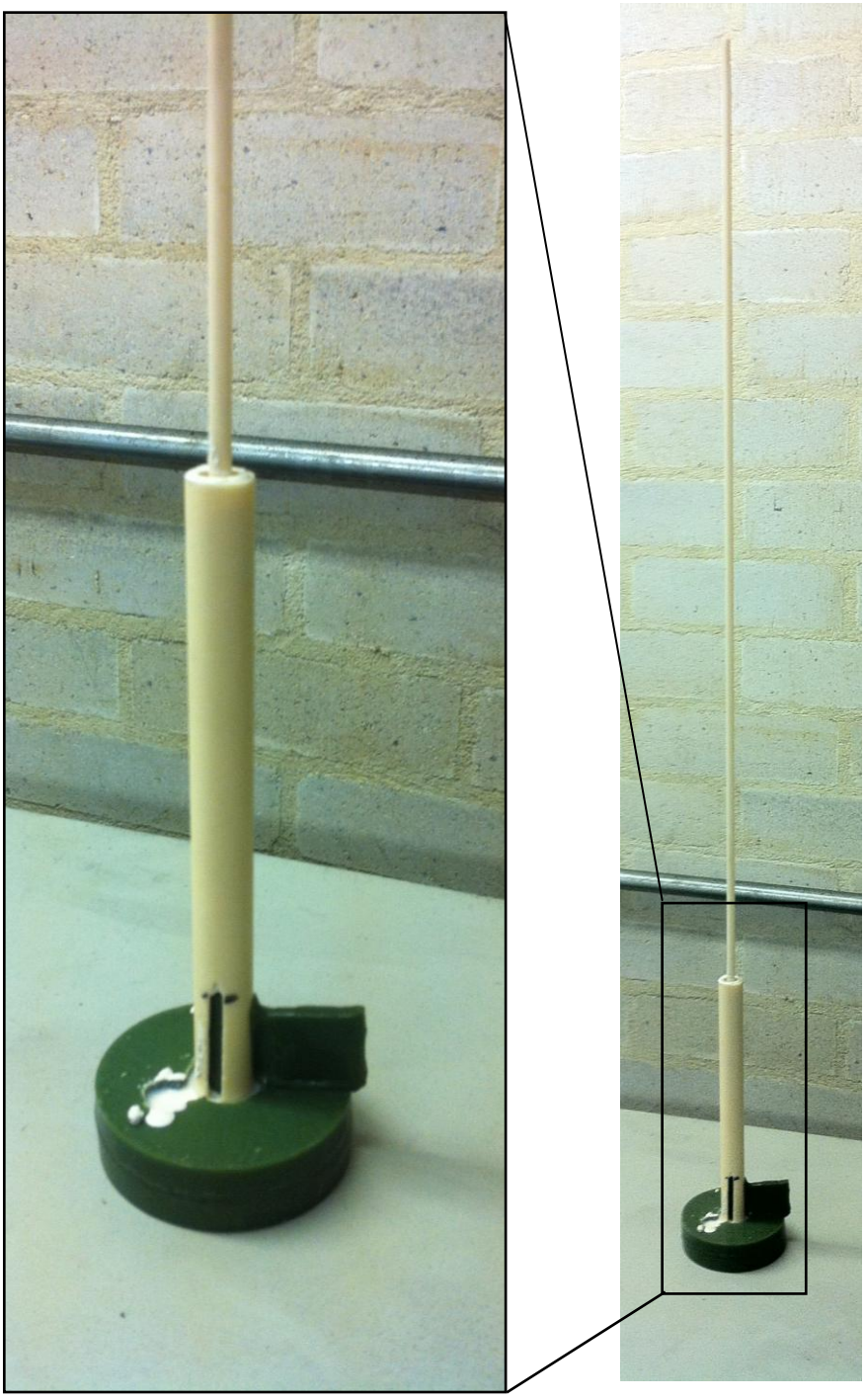


Figure 3-7: Sintered alumina tubes and was mould used to produce thermocouple housing assembly.

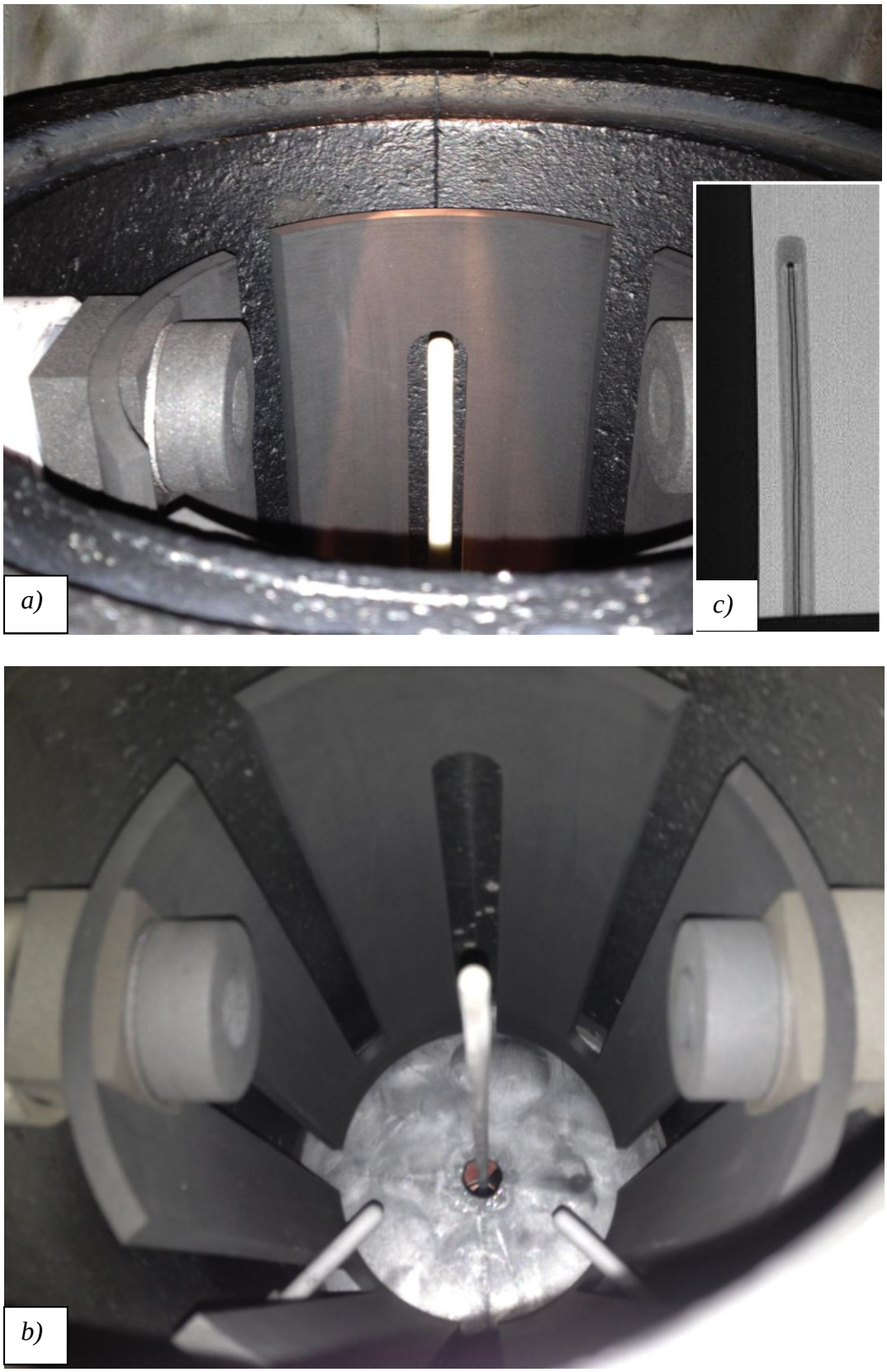


Figure 3-8: Images showing position of thermocouple assembly within furnace hot zone.

The purpose of the thermocouple measurements was to assess the furnace thermal profile for two baffle configurations; a 20 x 10^{-3} m ID baffle as shown in Figure 3-8 and a 110 x 10^{-3} m ID baffle shown in Figure 3-9 which will be used to validate a thermal model for such conditions.

Experimentation such as this is common in industry and before the standard use of CFD analysis would be used to predict the thermal gradients achievable during a casting process; current use of this type of data is to validate thermal models of the casting process in a similar fashion to this work.

In order to ensure the measurement assembly and chill had minimal impact on the thermal profile, the assembly was designed to be sufficiently long to ensure the base and chill always resided in the cold zone of the furnace as shown in Figure 3-9.

Wires from the thermocouple assembly were fed down to the underside of the ram where standard female connectors for such in-situ experimentation are already in place; any exposed sections of wire were protected by thermal packing.

Temperature measurements were recorded using the standard furnace software with the inclusion of the extra thermocouple channel. The thermocouple assembly accuracy was assured by positioning in the same vertical alignment as the control thermocouples and measuring the hot zone temperature; typical deviation was in the order of ±1-2 K and would be expected due to differences in radial position.

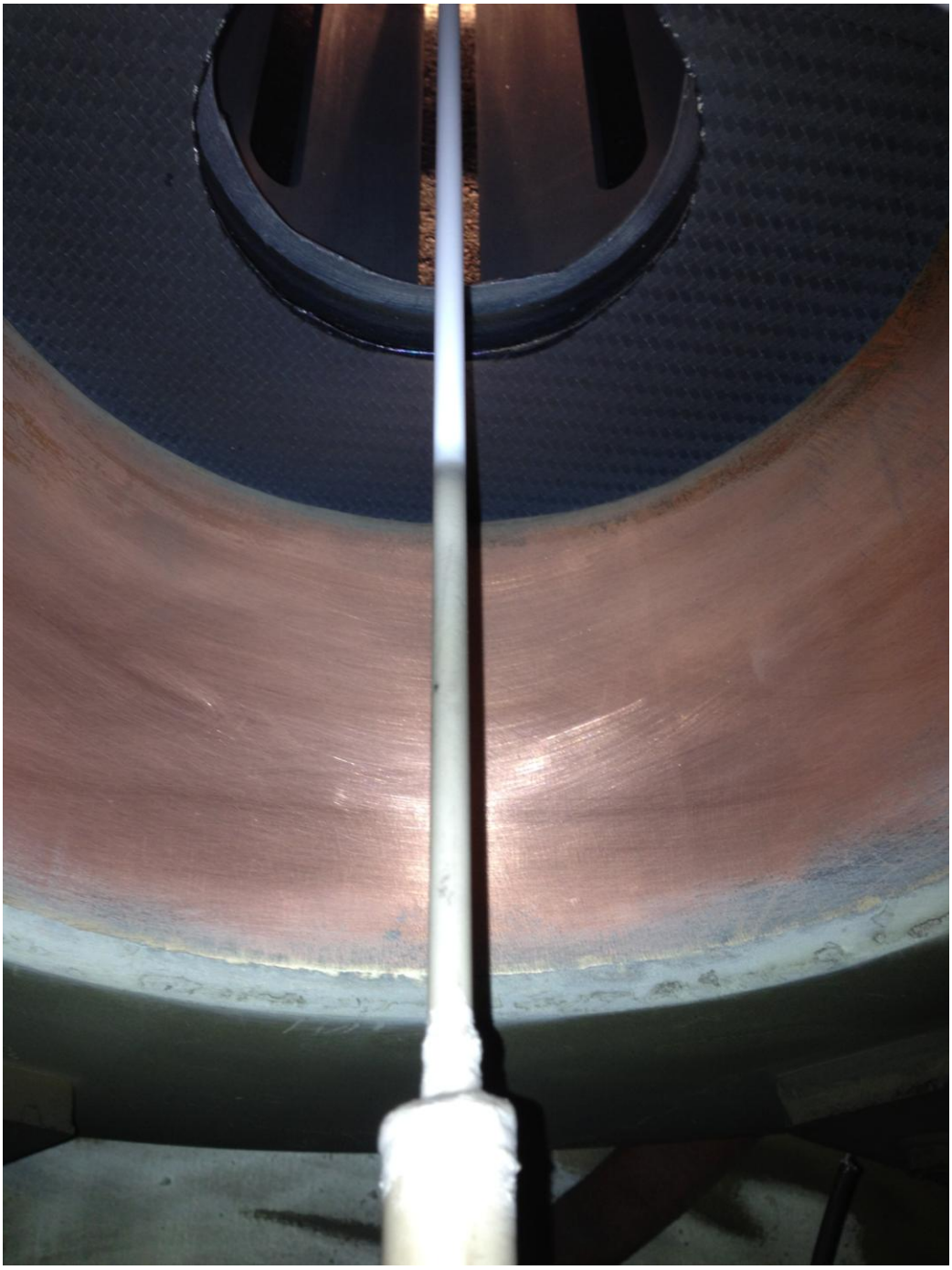


Figure 3-9: Image showing the extent at which the base of the thermocouple assembly and chill resided out of the furnace hot zone.

3.6 Measurement of furnace electrical properties during heating cycles

In order to quantify the effect of furnace configuration on the hot zone power requirements, measurement of electrical current and voltage were required which were then used in the development of a computer model.

The furnace heating element requires a 3 phase AC electrical power input and this is supplied via three cables, predominantly for ease of installation of maintenance, in order to retain some flexibility within the cables. The three power cables connect to a copper terminal block under a safety cover which then passes through a sealed orifice in order to connect to a graphite electrode in the vacuum chamber.

The measuring device used for experimentation was an ISO-TECH IPM6300 Graphical AC Power Quality Analyser; inputs for the device were a single or balanced three phase sensor loop and a common voltage input terminal.

As there was restricted access to attach the sensor loop at a point where the 3 phase supply shares a common terminal, and due to health and safety best practices, measurement was taken from one of the three phase supply cables in a part of the furnace which was readily accessible as shown in Figure 3-10.

In the case of voltage measurement, a voltage input cable was already present as part of the furnace architecture and measured the potential drop between the copper terminal blocks, as close as practically possible to the heating element. The existing cables were simply plugged into the measurement unit.

Data logged on the unit was downloaded using proprietary supplied software.



Figure 3-10: Image showing electrical current sensor loop connected to one of the 3 phase supply cables.

3.7 Computer Modelling

In order to quantitatively describe the thermal field within the Bridgman furnace CFD modelling was used in order to relate the magnitude of electrical power input with the furnace configuration, such as radiation baffles and mould interaction.

Computer modelling offers a number of advantages over successive temperature measurement; firstly for a relatively small number of experimental conditions used for validation purposes, a computer model can be used to predict the outcome of theoretical scenarios.

Secondly, without the aid of a computer model to give predictions of such theoretical conditions, it is unlikely that significant capital expenditure would be invested to bring concepts to fruition.

That said a significant aspect of this process is to ensure the accuracy of the model by validating with experimental results where possible; this is discussed in Chapter 5.

Computer modelling activities were carried out using a High Performance Computer (HPC) cluster at the University of Birmingham. The cluster comprised 50 dual-processor 8-core worker nodes (16 cores per node) resulting in a total of 800 cores being available for calculations, which were shared throughout the institution. The workstation computer permitted interaction with the Graphical User Interface (GUI) with all of the calculations being carried out remotely.

Access to the cluster was via PuTTY while file management was carried out using WinSCP.

This work made use of Ansys CFX and subsequently spanned four releases of the software, V11.0 to V14.5 with no significant issues arising during software updates.

The electromechanical module within CFX was at beta level during V11.0 – V12.0, hence analytical validation work was conducted. Later updates saw release proper with no issues arising.

Models are run independently of the GUI in batch mode and therefore a number of simulations can be carried out simultaneously. Meshing was performed using ANSYS ICEM, exported as a mesh file and then imported into CFX.

A description of the fundamentals of the finite element method can be found in section 2.10 with a more in-depth description of the model setup described in section 5.6.

CHAPTER 4 BRIDGMAN FURNACE

This section will outline predominant characteristics of the single shot Bridgman furnace including the geometry of the furnace architecture, means of hot zone temperature control and magnitude of power input requirements for a number of furnace configurations.

4.1 Background

The single shot Bridgman furnace was a development furnace at the Rolls-Royce turbine aerofoil manufacture facility, CRDF, before being relocated to the University of Birmingham.

The furnace heating chamber consists of a graphite heating element thermally insulated by a cylinder of material (a) that fits together with top (b) and bottom (c) components to form a semi enclosed assembly shown in Figure 4-1 and Figure 4-2.

The top component incorporates a cone shaped cut-out in order for a replaceable pouring cone to be inserted in order to assist with the pouring of liquid alloy into the hot zone from the induction melting apparatus located above.

Above the replaceable pouring cone is a flat cap, manufactured from the same insulation material as the other components, which is movable in order to allow pouring and then add further insulation once the pour is complete. In reality there is a small gap between the pouring cone and the top cap of the furnace in order to allow for such movement, however in the furnace model these two components are modelled without such a gap in order to completely enclose the top portion of the furnace hot zone.

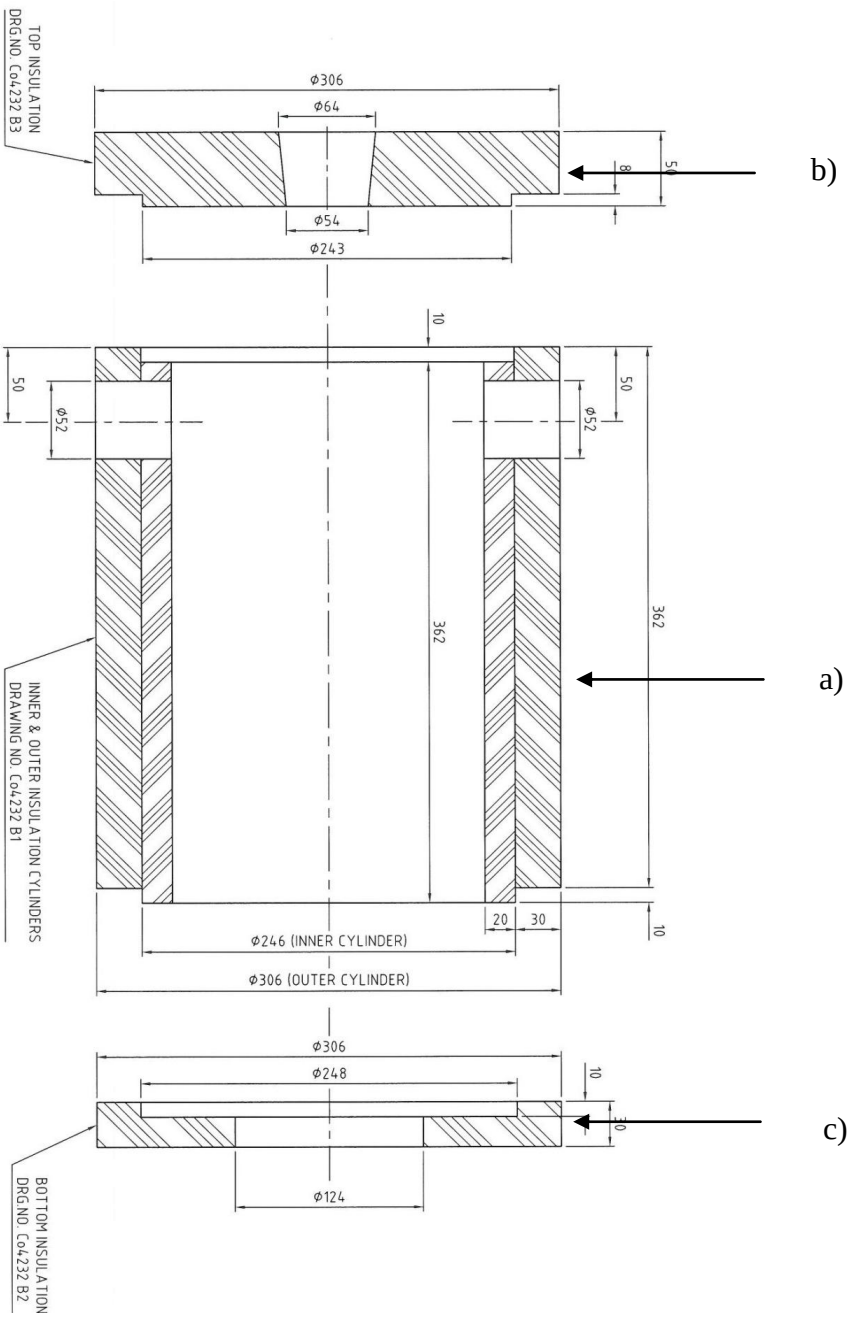


Figure 4-1: Schematic view of heater insulation assembly; dimensions in mm.



Figure 4-2: Photograph showing 'single shot' Bridgman furnace vacuum chamber; including induction melting unit, hot zone insulation surrounding heating element, input electrodes to supply power, control thermocouples and chill spool which forms part of the cold zone.

In this work, primarily in Chapter 6, there are comparisons between results obtained using the single shot Bridgman furnace and the small bore furnace which has been used extensively by Rolls-Royce for the casting of larger multi-component moulds.

The single shot and small bore furnaces both utilise a penny melting system in which a small disk of material, of similar composition to the bulk alloy, is placed in a container blocking an orifice directly above the awaiting mould within the hot zone. When the alloy to be cast is sufficiently melted and possesses enough bulk thermal energy, the penny is gradually melted and releases the alloy into the mould below.

The single vacuum chamber of the single shot furnace is maintained by a mechanical pump in conjunction with a vapour booster and can achieve vacuums in the region of 3×10^{-6} bar (Newell, 2009).

There are a number of key differences between the single shot Bridgman furnace and the small bore furnace; firstly the hot zone of the small bore furnace is large enough to accommodate a graphite susceptor which acts primarily to protect the heating element from alloy splash during pouring. The single shot furnace does not have the capacity to include a susceptor within the hot zone and hence is vulnerable to alloy beads occurring on exposed geometry; an example of this can be seen in Figure 4-3.

Secondly, the chill plate used to mount the casting moulds is smaller in the single shot furnace, around 65×10^{-3} m in diameter compared to 150×10^{-3} m, and can utilise a flat surface clamping system or a bayonet fitting to secure moulds.

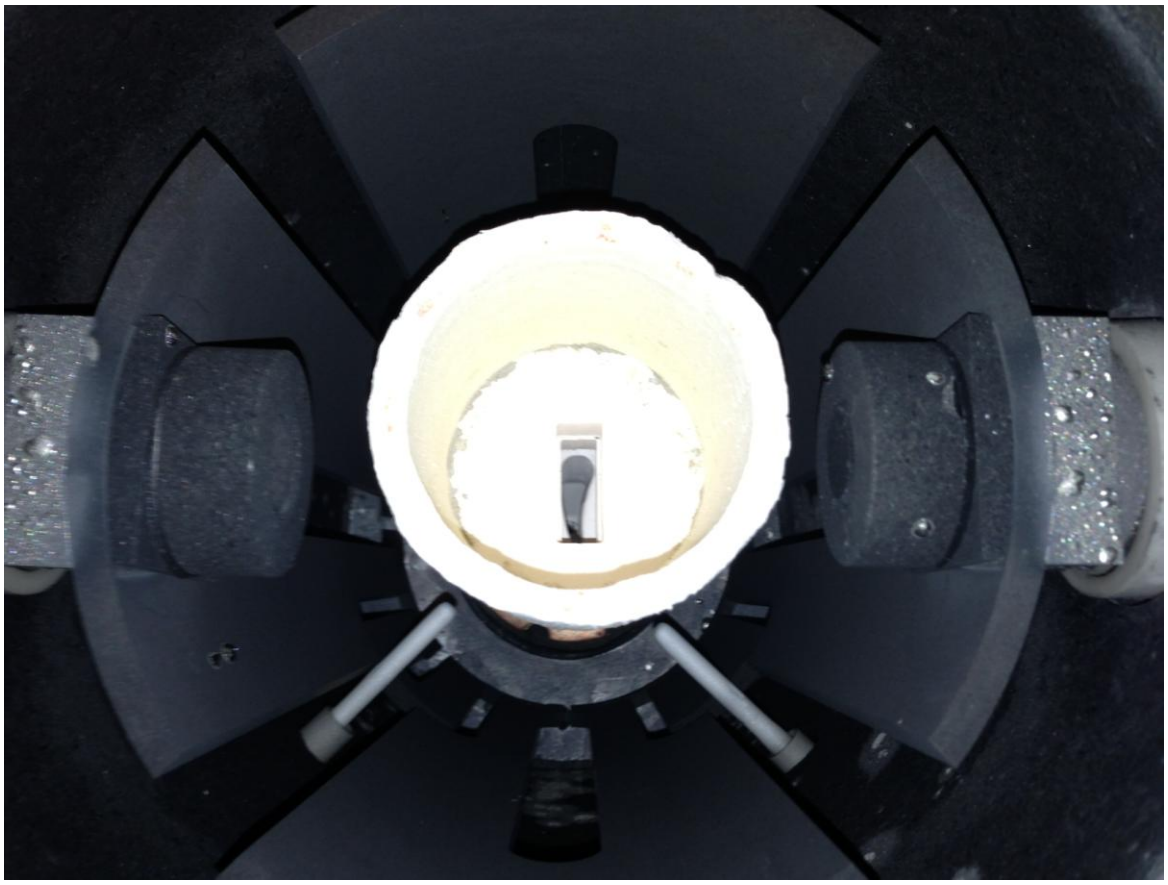


Figure 4-3: View of furnace hot zone, looking down from position occupied by induction melt unit, with VeriCAST mould in place and top insulation removed. This view highlights the space constraints within the single shot furnace hot zone particularly with reference to a susceptor which is not incorporated in this furnace configuration. Control thermocouples can also be seen.

4.1.1 Hot zone temperature control

The furnace hot zone is monitored by two control thermocouples already shown in Figure 4-2 and Figure 4-3 which act to relay temperature information back to the control unit described in section 4.1.2.

The secondary thermocouple is to act as a backup in case of premature failure of the control thermocouple and under such conditions the control software will automatically switch to the remaining thermocouple. A point of note is that the safety case is reliant on a total failure of the primary thermocouple and under circumstances of a partial failure

resulting in intermittent measurements, perhaps due to exposed wires causing a short circuit, the software will not switch. In this case manual override is possible.

An assessment of the difference between the control and secondary thermocouple temperatures for number of experimental conditions are shown in Table 4-1. The errors between the two control thermocouples are typically within 3 K however errors in the region of 7 K have been measured.

The control thermocouples are housed in alumina protection tubes clamped onto two permanent fixtures, shown in Figure 4-2, and during hot zone build up the thermocouples are threaded to the end of the protection tubes and clamped into place.

It has been shown that there is a radial temperature gradient between the centreline and inner circumference of the heating element and the likely cause of erroneous results is the inaccuracy associated with manually placing control thermocouples within the furnace hot zone.

Table 4-1: Comparison of control thermocouple temperature, in bold, and secondary thermocouple temperatures during the steady state soak period for a number of experimental trials.

	Steady State Temperature	
Set Temperature / Parameters	**Thermocouple 1**	Thermocouple 2
1823.15 K / 20 x 10^{-3} m ID baffle	**1823.31**	1824.49
1823.15 K / 20 x 10^{-3} m ID baffle	**1823.33**	1825.74
1823.15 K / 20 x 10^{-3} m ID baffle	**1823.34**	1816.19
1823.15 K / 20 x 10^{-3} m ID baffle	**1823.34**	1816.76
1823.15 K / 110 x 10^{-3} m ID baffle	**1823.31**	1820.35
1823.15 K / 110 x 10^{-3} m ID baffle	**1823.29**	1824.54

Irrespective of errors between the two control thermocouples, the hot zone temperature control shows a good degree of accuracy and is a practical means of carrying out such a function. A typical plot of the prescribed heat up temperature profile and that of the control thermocouples is shown in Figure 4-4.

From observing Figure 4-4 it can be seen that there is some deviation from the pre-set heat up profile by the control thermocouples, which would be expected, as the accuracy of the thermocouples is around 0.25% which result in several degrees deviation. The overall trend however is a close relationship between the specified temperature profile and measured temperature.

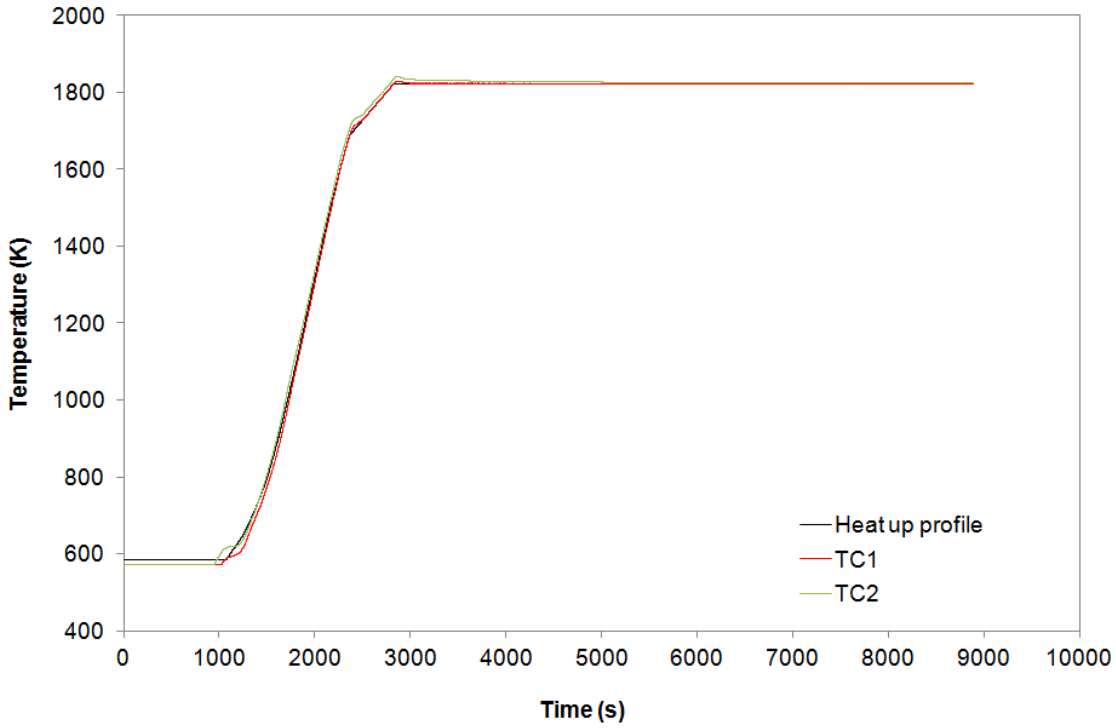


Figure 4-4: Comparison of programmed furnace heat up profile and control thermocouple temperature, comprising heat-up to 1823.15 K and soak period.

4.1.2 Bridgman furnace power input and experimental readings

The furnace hot zone temperature is maintained by a proportional derivative integral (PID) controller which is a standard control loop feedback method and works by monitoring the furnace hot zone temperature from two thermocouples, one acting as a backup as discussed in section 4.1.1. The controller calculates an error as the difference between the control thermocouple measurement and the set hot zone temperature. To reduce the error the controller then varies the electrical energy to the heater.

The PID controller parameters are set by the furnace manufacturer, as is the heat up profile, which tends to gradually build up the temperature over the course of 1800 – 2700 s with the intention of minimising overshoot in the system; a typical data set of voltage and electrical current measurements is shown in Figure 4-5 for a hot zone temperature of 1823.15 K with a 20 x 10^{-3} m ID radiation baffle.

An initial assessment of the magnitude of the effect the radiation baffles have on the system can be made by comparing the electrical inputs for the same hot zone reference temperature but with different radiation baffles, shown in Figure 4-6.

For the same given condition the furnace requires a greater magnitude of electrical power to maintain the same hot zone reference temperature.

Also, as there is more radiant heat being lost from the hot zone when using a standard 110 x 10^{-3} m ID baffle, the time taken to reach the hot zone reference temperature and the electrical parameters to reach steady state is also longer.

The current understanding of the furnace indicates that there is a variation in the hot zone temperature for given baffle configurations; this will be developed further in Chapter 5.

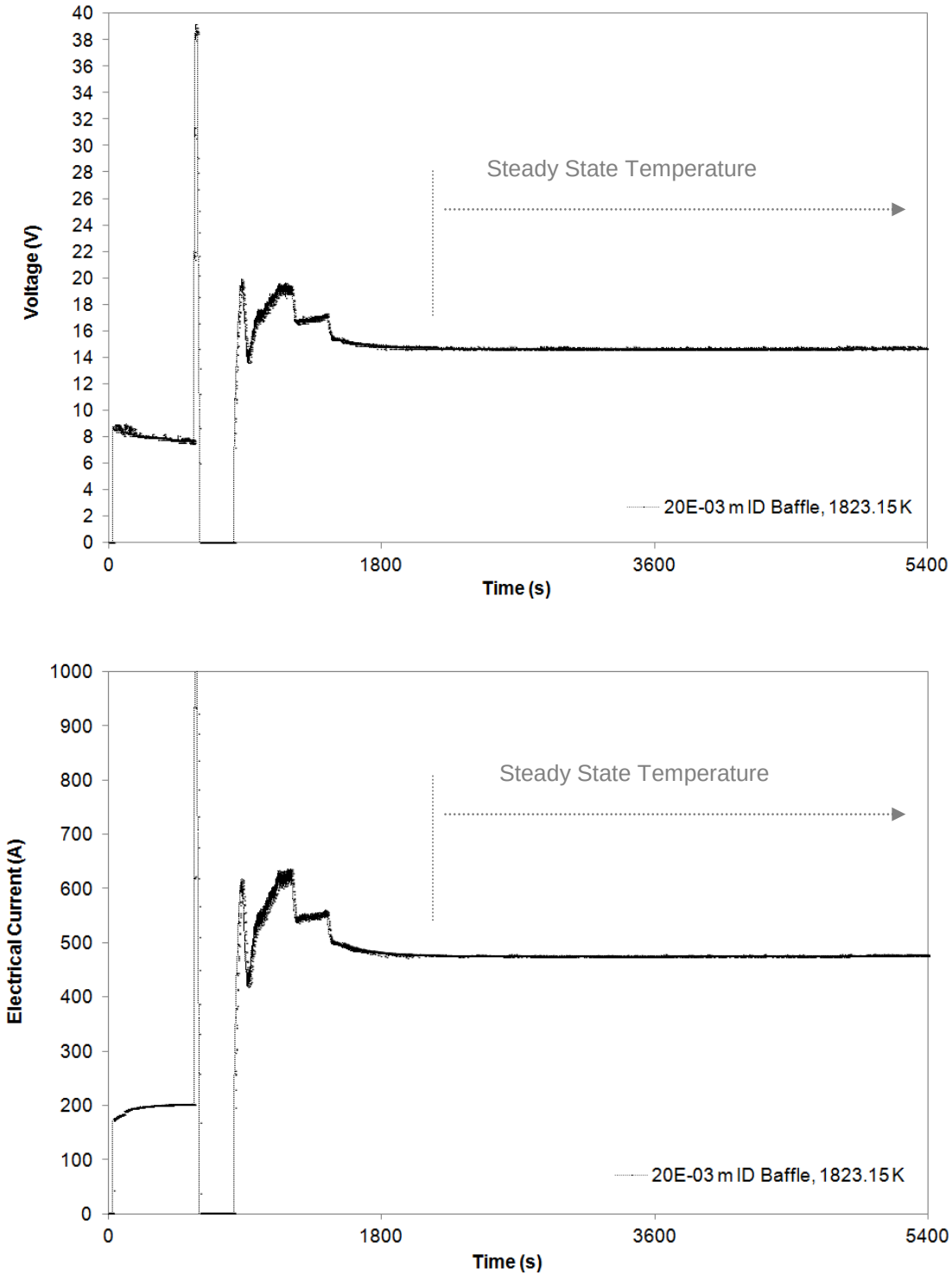


Figure 4-5: Typical electrical current and voltage measurements taken over a 5400s period with the furnace hot zone set to heat up to 1823.15 K and maintain temperature. The furnace configuration used a 20 x 10^{-3}m ID baffle and standard graphite heating element.

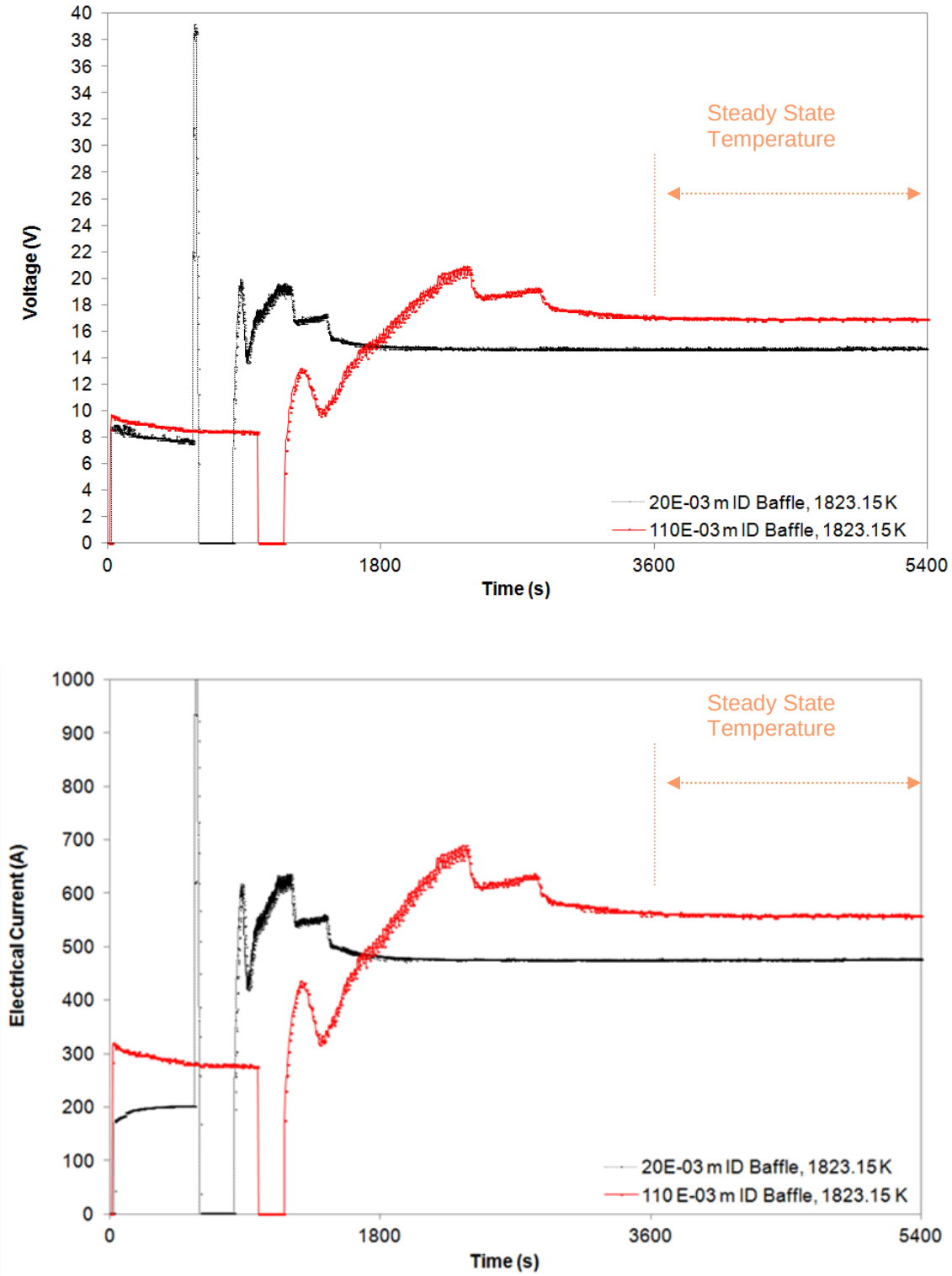


Figure 4-6: Measured electrical current voltage taken over a 5400s period with the furnace hot zone set to heat up to 1823.15K and maintain temperature. The furnace configurations shown use a 20 x 10^{-3} m ID and 110 x 10^{-3} m ID baffle and standard graphite heating element.

As discussed previously the Bridgman furnace is powered by a 3 phase AC supply delivered to a local terminal located on the access platform. The power is further split between three, ideally equally loaded, power supply wires which enter the furnace through an air tight port and attach to electrodes which connect to the heating element via graphite nuts.

The decision to split the input power cables into three was purely design based and intended to increase cable flexibility.

Furnace power measurements were made for a number of hot zone temperatures and baffle configurations over a number of months during the operation of the furnace and resulted in a cumulative total of over 40,000 data points.

The potential voltage difference was measured directly, or as close as practically possible, over the heater input and output electrodes while the electrical current was measured using one of the three power supply cables which was separated from the bundle.

The measurement of electrical parameters to the furnace were intended to serve two purposes; firstly to give some indication of the magnitude of electrical power required which could then be used as input parameters for the CFX model. Secondly, the measured electrical current and voltage, when plotted as a function of one another, can be used to determine the electrical resistance of the heating element. The measured resistance can then be used to calculate the specific electric resistance of the graphite material; this is discussed further in Chapter 5.

Inspection of the measured furnace data highlighted some erroneous non-constant electrical resistance values resulting in the heating element seemingly exhibiting a higher electrical resistance than expected, given the material resistivity values supplied by the

manufacturer.

Observation of the electrical voltage measurements showed a good level of consistency between experimental runs for nominally identical hot zone temperature profiles with the steady state voltage rarely deviating by more than ~1.4%, however it was theorised that any error in the electrical current measurements would potentially skew the results when plotting the electrical current/voltage graph and predict an artificially large or small electrical resistance.

Further evaluation of the furnace parameters were made for a number of hot zone reference temperatures in order to quantify any variation in electrical current between the three input cables. The study was carried out using a hand held clamp ammeter where periodic measurements were taken under steady state temperature conditions over all three input cables in conjunction with the standard electrical data logger fixed to one electrical supply cable; the results of further evaluation are shown in Table 4-2.

The results subsequently showed that the supply cables used, which were assumed to carry 1/3 of an evenly distributed electrical supply in fact did not. The single cable used for all experimental current measurements consistently carried the lowest, or equally lowest, electrical current out of all three cables with exception of Run 1 in which the measurement cable gives a marginally higher reading then cable 2.

Evaluation of the results in Table 4-2 show there was a constant proportional difference between the current values in each of the three cables. The ratio of difference between the measurement cable multiplied by a factor of three and the sum of the electrical current cables was determined to show a mean value in the order of 0.059; in other words the multiplied value from this cable was always in the order of 5.9% lower than the total

current calculated from the sum of all cables.

The consequence of this is explained further in Chapter 5, however in the case of determining the furnace power requirements for different furnace configurations, voltage measurements were taken and electric current estimations were made using the experimentally determined power factor; the results of which are shown in Figure 4-7 to Figure 4-9.

Table 4-2: Comparison of electrical current measured using one of three input cables and measured over all three input cables. The data set includes various hot zone temperatures.

	Cable 1 Measurement Cable / A	Cable 2 / A	Cable 3 / A	3 x Measurement Cable	Sum all cables	Error ratio
Run 1	140	138	166	420	444	0.054054
Run 2	134	137	158	402	429	0.062937
Run 3	135	140	156	405	431	0.060325
Run 4	132	133	156	396	421	0.059382
Run 5	134	134	158	402	426	0.056338
Run 6	133	133	157	399	423	0.056738
Run 7	133	135	158	399	426	0.063380
Run 8	132	133	156	396	421	0.059382
Run 9	84	86	97	252	267	0.056180
Run 10	85	89	97	255	271	0.059041
Run 11	82	87	94	246	263	0.064639
				Mean error ratio ± S.E		0.059309 ± 0.001

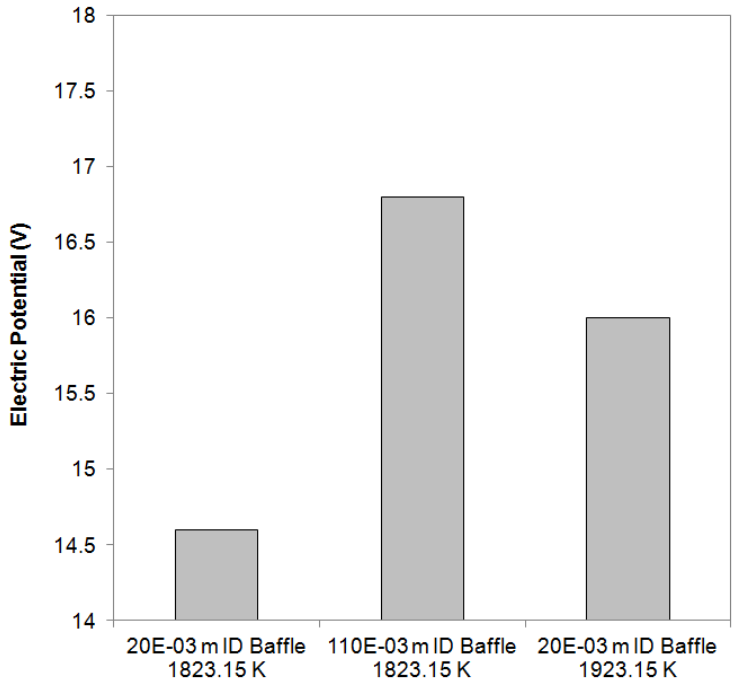


Figure 4-7: Experimentally determined voltage measurements for three furnace configurations, using the standard graphite heating element.

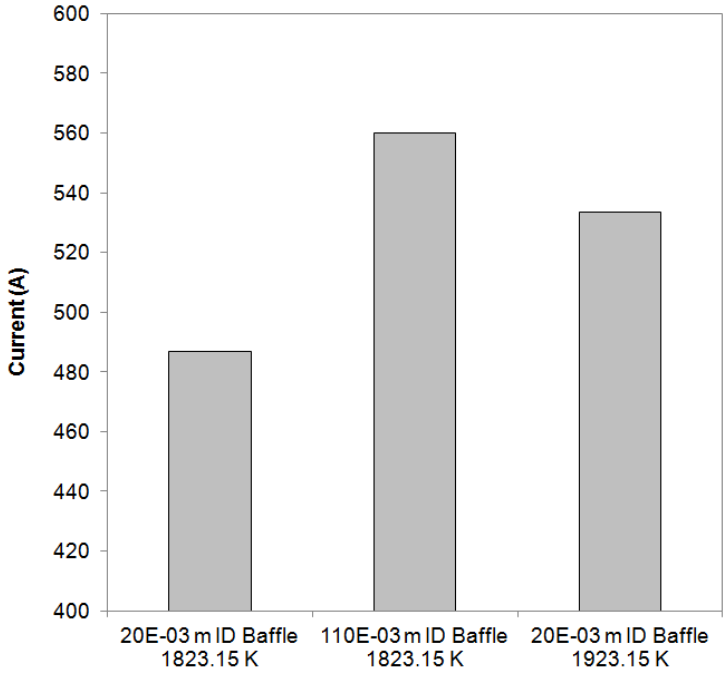


Figure 4-8: Experimentally determined electrical current measurements for three furnace configurations using the standard graphite heating element.

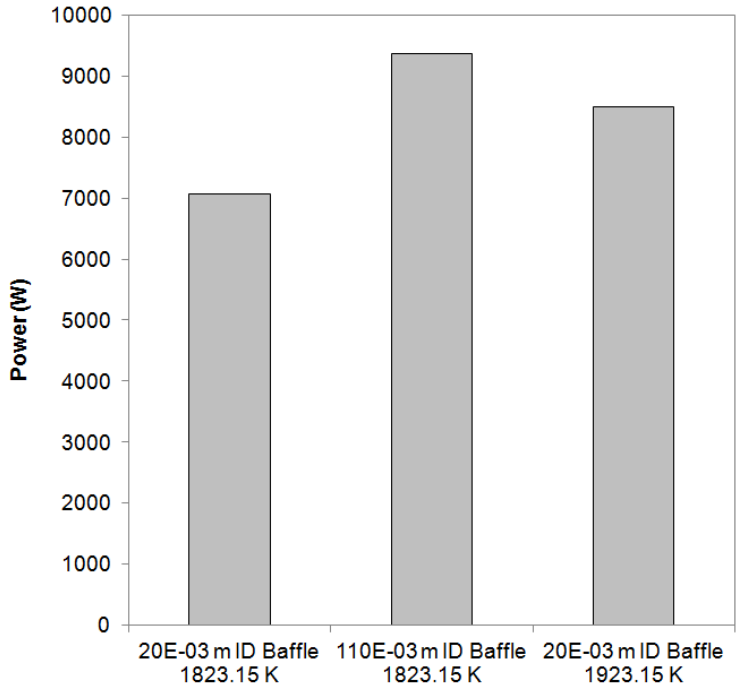


Figure 4-9: Estimate of furnace power for three configurations calculated from experimentally determined current and voltage measurements.

As one may expect, the furnace configurations using a 110 x 10^{-3} m ID baffle requires the most power to maintain the furnace hot zone at the reference temperature of 1823.15 K and uses approximately 32% more power than when set to the same holding temperature but instead using a more restrictive 20 x 10^{-3} m ID baffle.

The effect of the power input and baffle design on the furnace thermal profile will be explored in the next chapter.

CHAPTER 5 CFX FURNACE MODEL

5.1 Introduction

As we have discussed, the current ProCAST model has been validated for a limited number of experimental conditions and is used to simulate the casting process within the Bridgman furnace. To this end the model may be described as a prescriptive model in that the hot zone of the furnace, although discretised to a certain extent, describes the thermal field for a set temperature of 1803.15 K using a 110 x 10^{-3} m ID baffle reasonably well.

The idea behind the development of the CFX model was to produce a fully descriptive model of the furnace hot zone in order to account for the electrical current distribution within the heating element and hence determine variation in the hot zone temperature for a number of furnace configurations that may have an effect.

There were a number of considerations made when choosing a suitable software package to conduct the work; namely the requirement to calculate electrical current distribution in conjunction with radiation and conduction heat transfer.

Continued use of ProCAST was certainly not a viable option as this does not have the capability to calculate electrical current flow and therefore translation to heat energy was not possible. One potential package was Opera Vector fields which has the capability to calculate alternating electrical current and subsequent magnetic fields, however integration of these results into a full thermal model including conduction and radiation heat transfer is difficult and the capability to calculate such models in a multi-core parallel configuration was not possible at the University of Birmingham.

Two potential software packages Ansys CFX and Ansys Fluent are both capable of carrying out heat transfer and fluid flow calculations but are limited to DC electrical current.

Both have the ability to run on cross platform machines in parallel and are arguably of equal stature so in this case, the use of a software code to carry out the study was primarily a matter of personal preference and ultimately CFX was chosen to perform the work.

CFX has a complementary module called Workbench in which geometry can be created and meshed, however this feature was not available at the time of this study and only the core pre, solver and post applications were available, therefore geometry creation was carried out using Unigraphics NX6 and meshing was conducted using Ansys ICEM.

Even though CFX is used as a static model and will not simulate mould withdrawal it is deemed suitable for this application as mould withdrawal rates are deemed slow enough to allow temperature equilibrium to be reached; therefore simulations involving moulds within the furnace will be static.

5.1.1 DC Current approximation

Due to the inability of CFX to calculate alternating current, an assessment of potential errors that may arise must be made.

When an alternating electrical current (AC) is distributed within a conductor there is a tendency for it to become unevenly distributed such that the current density is largest near the surface of the conductor and decreases as the depth into the conductor increases.

This phenomenon is known as the skin effect, as the current predominantly flows at the outer skin of the conductor, and the characteristic depth at which this occurs is called the

skin depth.

Given the electrical resistivity ρ of the material is known ($\Omega.m$), along with the frequency of the AC current f (Hz), the skin depth that would be expected to be encountered with the graphite heating element can be calculated using the following formula:

$$\delta = \sqrt{\frac{2}{\omega\mu\sigma}} \qquad 5.1$$

Where;

$$\sigma = \frac{1}{\rho}$$

$$\omega = 2\pi f$$

However, before the calculation can be carried out the parameter μ must be determined which is defined as the magnetic permeability and can be calculated as follows;

$$\mu = \mu_0\mu_r$$

Where μ_0 is the permeability of free space and is equivalent to $4\pi \times 10^{-7}\ H/m$ and μ_r is the relative permeability which can be calculated from;

$$\mu_r = X_m + 1$$

Where X_m is the magnetic susceptibility, which for graphite is -1.6×10^{-5} (Young, 1992).

Given the known parameters, the skin depth for a graphite material can be determined to be $\sim 246.6 \times 10^{-3} m$.

The maximum thickness of the furnace heating element is $6 \times 10^{-3}\, m$, therefore we can see that simulating an AC power source using DC calculations will not present any significant problems.

Electrical parameters can be entered into the model by means of an electrical current parameter, specified by a current density, or by means of a specified potential difference across the domain in question. As discussed in an earlier section, the experimental measurement of voltage during furnace runs was determined to be the most statistically reliable, predominantly due to the method in which the data was captured. As such, the use of a potential difference was chosen to be the parameter which would be used to determine the magnitude of power in the CFX models.

5.2 Electrical current flow

The geometry of the heating element in the single shot furnace is formed from a serpentine track manufactured from an electrically resistive material and resembles an open ended cylinder, Figure 5-1. In a component such as this, manufactured from a material that is intrinsically required to possess a high electrical resistance, a proportion of the electrical current will preferentially flow around the path of least resistance; hence there will be an accumulation of electrical current around the apex of a turn where the direction of flow is changed by 180° as illustrated in Figure 5-1 a).

During operation of the furnace the heating element degrades by way of slow sublimation and a layer of carbon soot is deposited on surfaces within the furnace chamber; this is discussed in a later section. The sublimation of the graphite changes its surface appearance and areas in which high current flow is limited retain a dark sooty appearance whereas areas in which uniform high current flows appear slightly lighter, Figure 5-1 b).

In order to model the flow of electrical current within CFX it is useful to determine the accuracy of the CFX method by making comparisons with analytical solutions, this will in turn allow some decisions to be made with regard to appropriate mesh size in order to obtain a desired level of accuracy.

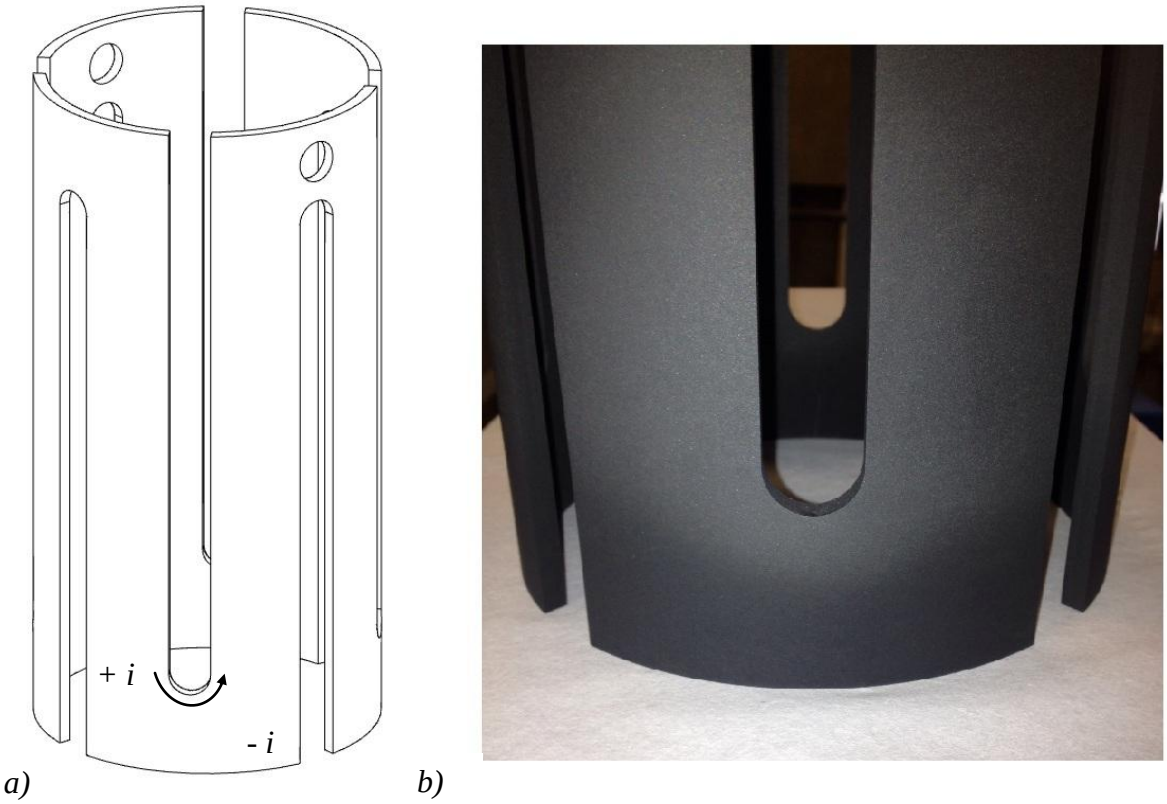


Figure 5-1: a) Geometry of graphite heating element used in the single shot furnace b) Photograph of heating element showing contrasting shades of graphite indicating areas of preferential electrical current flow

5.2.1 CFX benchmark calculation

A numerical solution has been presented (Hagedorn and Hall, 1963), in order to calculate the electrical current distribution and electrical resistance within a thin strip of material, which acts as a conductor, and possesses a 90° bend with chosen inner radius. In this case a thin strip of material has been mapped out, shown in Figure 5-2 with various reference points in the geometry; in particular electrical current i, flowing from the Y leg of the geometry $i_0 y$, to the X leg.

The length of each leg is represented by X^* and Y^*, the horizontal quadrant point, middle point and vertical quadrant point on radius r, denoted by A, B and C respectively and h, g the width of the vertical and horizontal leg.

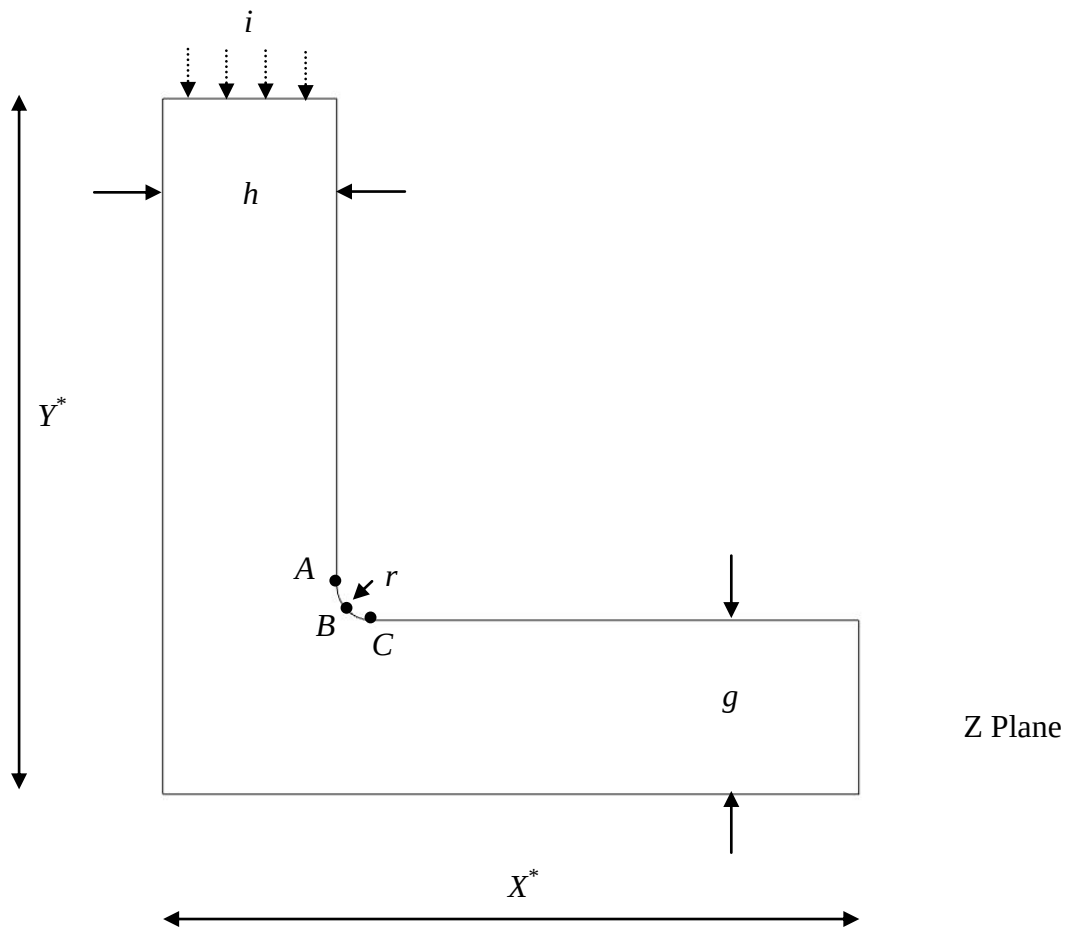


Figure 5-2: Right angle bend in geometry showing coordinate points and subscripts

The geometry shown in Figure 5-2, residing on the z plane is then conformally mapped into a straight strip on the z_1 plane by way of the w plane in order to retain the geometrical association between reference points. Only the derived equations will be discussed here rather than the mathematics of the conformal mapping process, however this has been discussed at great length elsewhere (Smythe, 1950, Hagedorn and Hall, 1963).

In order to derive equations for the electrical current distribution and resistance the following relationships are defined; where in all cases ρ is the electrical resistivity for a given material.

$$S = \frac{g}{h}$$

$$f(S) = \frac{2}{\pi}\ln\left[\frac{4S}{S^2+1}\right] + S - \left[\frac{S^2-1}{\pi S}\right]\cos^{-1}\left[\frac{S^2-1}{S^2+1}\right]$$

$$i_0 y = \frac{i}{h}$$

$$P = \frac{r}{h}$$

Therefore for a given radius and material thickness t, the electrical resistance is defined as:

$$R = \frac{\rho}{t}\left[\frac{X^*}{g} + \frac{Y^*}{h} - f(S) - 0.276(S^2+1)^{\frac{2}{3}}\left(\frac{P}{S}\right)^{\frac{4}{3}}\right] \quad 5.2$$

And the maximum current density around the apex of the right angle bend (points A,B,C) is defined as:

$$i_{ABC} = 1.04\left[\frac{S^2+1}{PS^2}\right]^{\frac{1}{3}} i_0 y \quad 5.3$$

Note that the maximum current density i_{ABC} is defined as a function of the uniform current density $i_0 y$ flowing through the y leg of the geometry. This can be readily calculated by either inputting a known current and dividing by the cross sectional area of the y leg or inputting a known voltage and first dividing by the resistance and then the cross sectional area.

5.2.2 Mesh sensitivity study

In order to assess the sensitivity of the mesh in comparison to the analytical solution a mesh was created using Ansys ICEM, an industry standard meshing package, and then imported into CFX as a CFX5 mesh file, the geometry parameters used are shown in Table 5-1.

Table 5-1: Dimensions of parameters shown in Figure 5-2 used for the mesh sensitivity study

Parameter	Dimension (m)
X^*	200 x 10^{-3}
Y^*	200 x 10^{-3}
g	50 x 10^{-3}
h	50 x 10^{-3}
r	5 x 10^{-3}
t	1 x 10^{-3}

As the geometry in question is effectively two dimensional with a thin finite thickness, the mesh was largely constructed of square hexahedral elements one element thick which ensured that there were only nodes on each outer surface of the geometry. The material used for the calculation is inconsequential providing that the value of electrical resistivity is consistent throughout; in this case copper was used with a resistivity value of 1.68 x 10^{-8} Ω.m (Giancoli, 2009 [1984]), a potential difference of 1V has been used in all calculations.

Two mesh sensitivity studies were carried out with the following assumptions; firstly it is known that a large proportion of the electrical current will flow around the apex of the radius in the geometry and it follows that this region may be sensitive to the mesh size, so in order to assess this, node spacing was kept constant in the x and y legs of the geometry

and only node spacing along the curvature of the radius was varied, illustrated in Figure 5-3 – Study 1.

Secondly, when discretising geometry for computer analysis it is prudent to be economical with the mesh size in order to minimise calculation time, so rather than change the mesh size for the whole geometry a second investigation was carried out in which the node spacing around the curvature of the radius was kept constant and only the node spacing in the uniform x and y legs of the geometry was varied, as shown in Figure 5-3 – Study 2. An additional reason for this approach is that parts of the heating element in which the electrical current changes direction only makes up a small proportion of the volume of the geometry so assessing the mesh criteria separately is a reasonable approach.

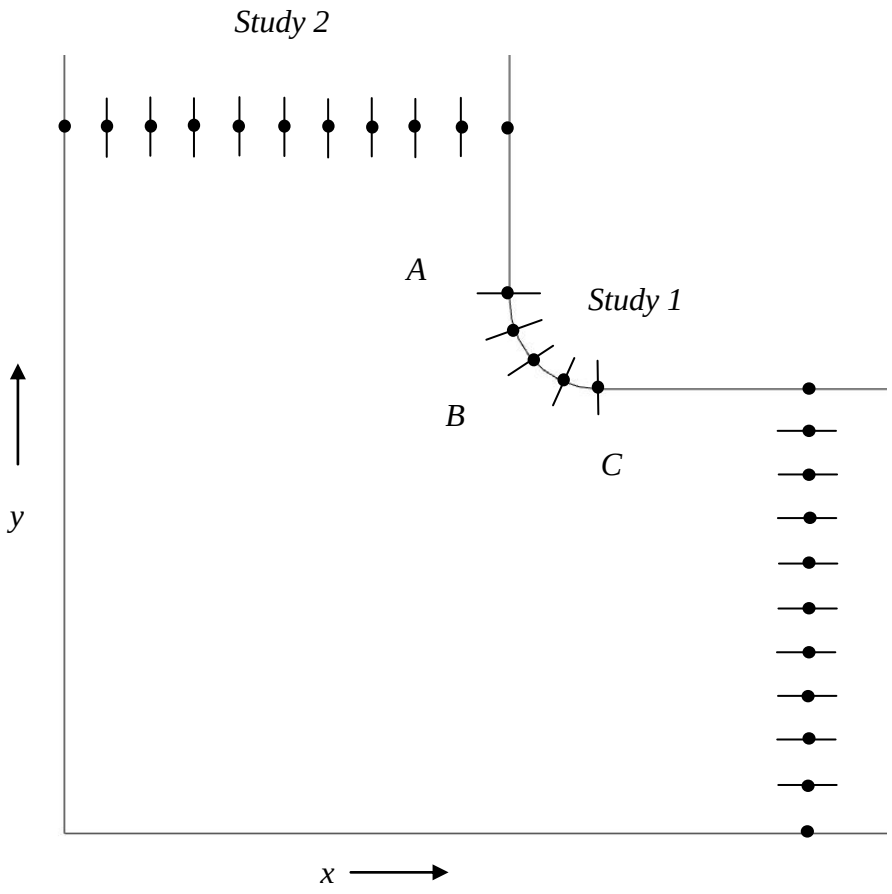


Figure 5-3: Illustration of mesh node spacing as used in the mesh dependency study

When studying the effect of mesh size around the apex of the radius, a constant node spacing of 1.0 x 10^{-3} m was used for the elements in the x and y legs of the geometry and node spacing around the apex varied between 2.5 x 10^{-4} m and 2.0 x 10^{-3} m in a number of increments.

The results of study 1, shown in Figure 5-4, indicate that with a constant leg node spacing of 1.0 x 10^{-3} m and varying apex node spacing the CFX model underpredicts the electrical current density by 6.5% for a 2 x 10^{-3} m node spacing; the most accurate prediction is achieved with a node spacing of only 2.5 x 10^{-4} m with an error of ~5%. This suggests that to a certain degree the accuracy of the solution is insensitive to the node spacing around the apex of the turn

Study 2 was therefore calculated using a fixed node spacing of 2.5 x 10^{-4} m at the apex of turn and a varying node spacing of between 2.5 x 10^{-4} m and 2.0 x 10^{-3} m in the the x and y legs of the geometry. The results, shown in Figure 5-5, indicate that with a node spacing of 5.0 x 10^{-4} m in the x and y legs, rather than 1.0 x 10^{-3} m, the accuracy is increased; reducing the error % from -5.13% to -2.66%. A further reduction to 2.5 x 10^{-4} m makes a negligible improvement. When the x and y leg spacing is increased to 2.0 x 10^{-3} m the accuracy of the solution is reduced, with an error of approximately 9.0%.

The results of the sensitivity study indicate that the accuracy of the CFX results are more sensitive to the mesh node spacing in the x and y legs of the geometry rather than the node spacing at the apex of the turn. This suggests that the area of high gradient is the geometry approaching the apex; perhaps to a set distance away from the apex where sufficient uniformity will be restored. This is considered further on page 140.

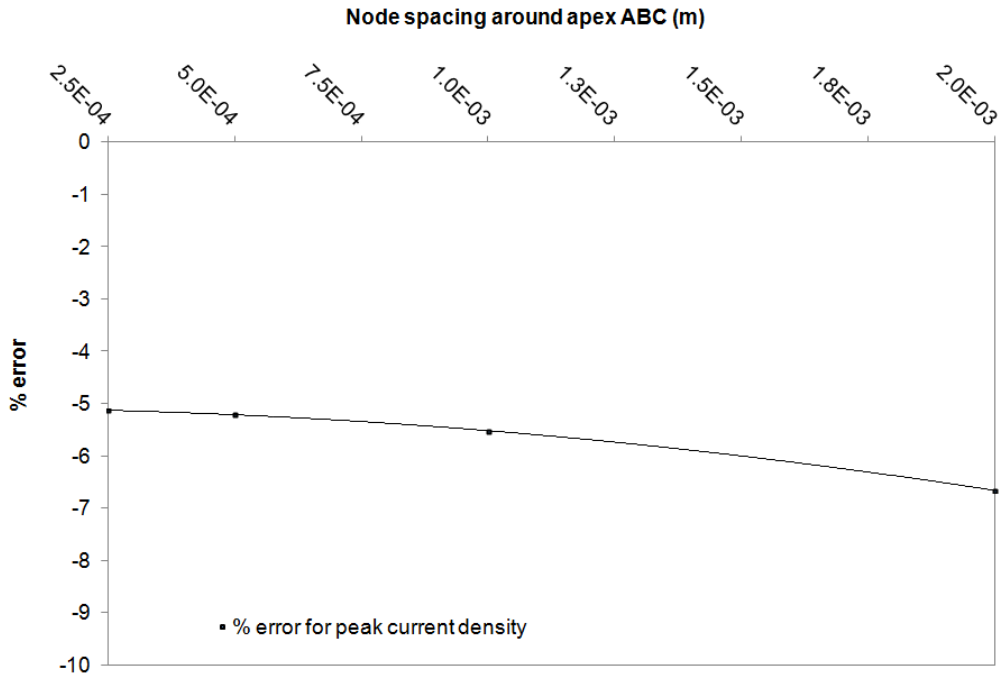


Figure 5-4: % error between analytical solution and CFX results for maximum current density at apex of 90° turn, calculated using fixed node spacing in the x and y legs of the geometry and varying node spacing around the apex

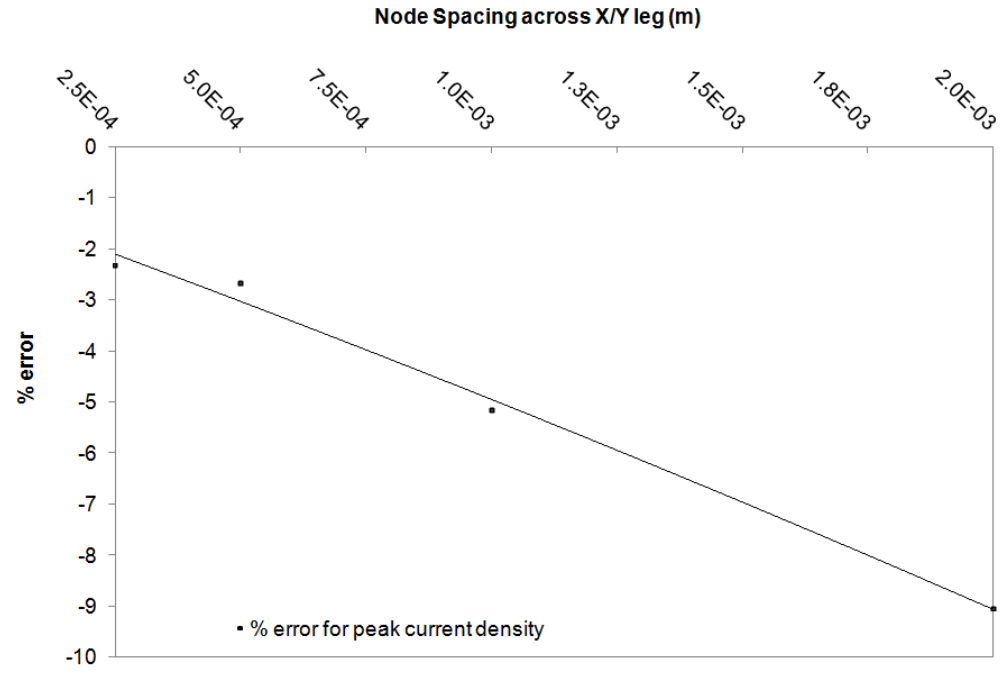


Figure 5-5: % error between analytical solution and CFX results for maximum current density at apex of 90° turn, calculated using fixed node spacing of 2.5 x 10^{-4} m at apex of turn and varying node spacing in x and y legs of geometry

In order to make a full comparison of the CFX calculation with the analytical solution the meshing parameters previously determined to give the most accuracy were used i.e. a node spacing $\leq 5.0 \times 10^{-4}$ m at the apex of the turn and a node spacing $\leq 5.0 \times 10^{-4}$ m in the x and y legs. The radius of the geometry was varied between 1.0×10^{-3} m and 10.0×10^{-3} m.

Figure 5-6 shows a comparison of the CFX results and analytical solution for electrical current density in the geometry shown in Figure 5-2 for a number of radius sizes. The CFX results show good agreement with the analytical solution for both maximum current density and uniform density however some errors are incurred in the calculation of maximum current density when dealing with small radii of less than 5×10^{-3} m.

The % errors between the two calculations are shown in Figure 5-7 and highlight the exponential increase in error as the radius is reduced below 5×10^{-3} m, however for a size of 10×10^{-3} m, which accounts for all the radius on the furnace heating element, the error is in the order of -1.6%.

Results from the CFX calculations showing current density distribution and contour lines are shown in Figure 5-8.

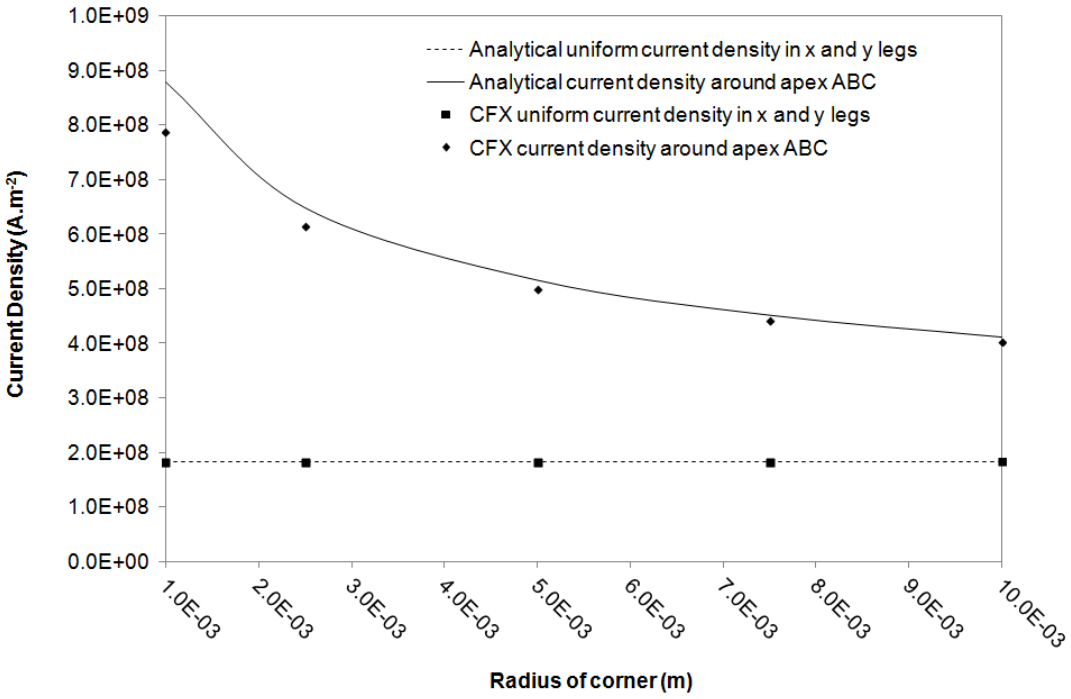


Figure 5-6: Comparison of analytical solution and CFX calculation for uniform electrical current density in the x and y legs of the geometry and maximum current density around the apex of the 90° turn. The radius of the turn varied between 1 x 10^{-3} m and 10 x 10^{-3} m.

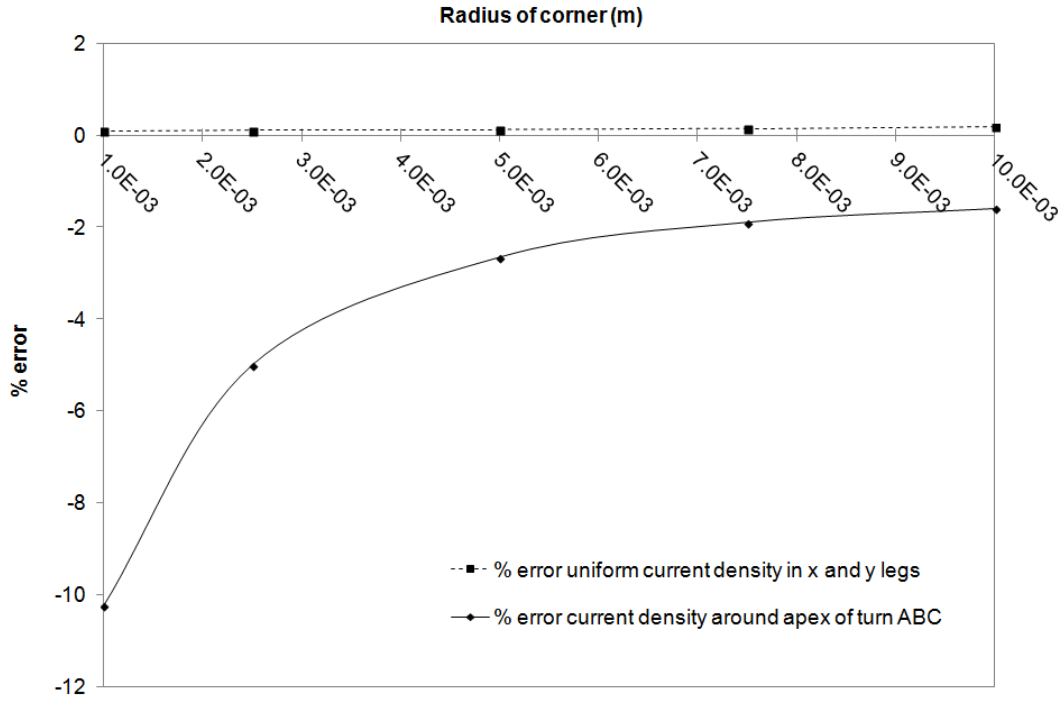


Figure 5-7: Error % between analytical solution and CFX calculations for electrical current density in x and y legs of the geometry and around the apex of the 90° turn.

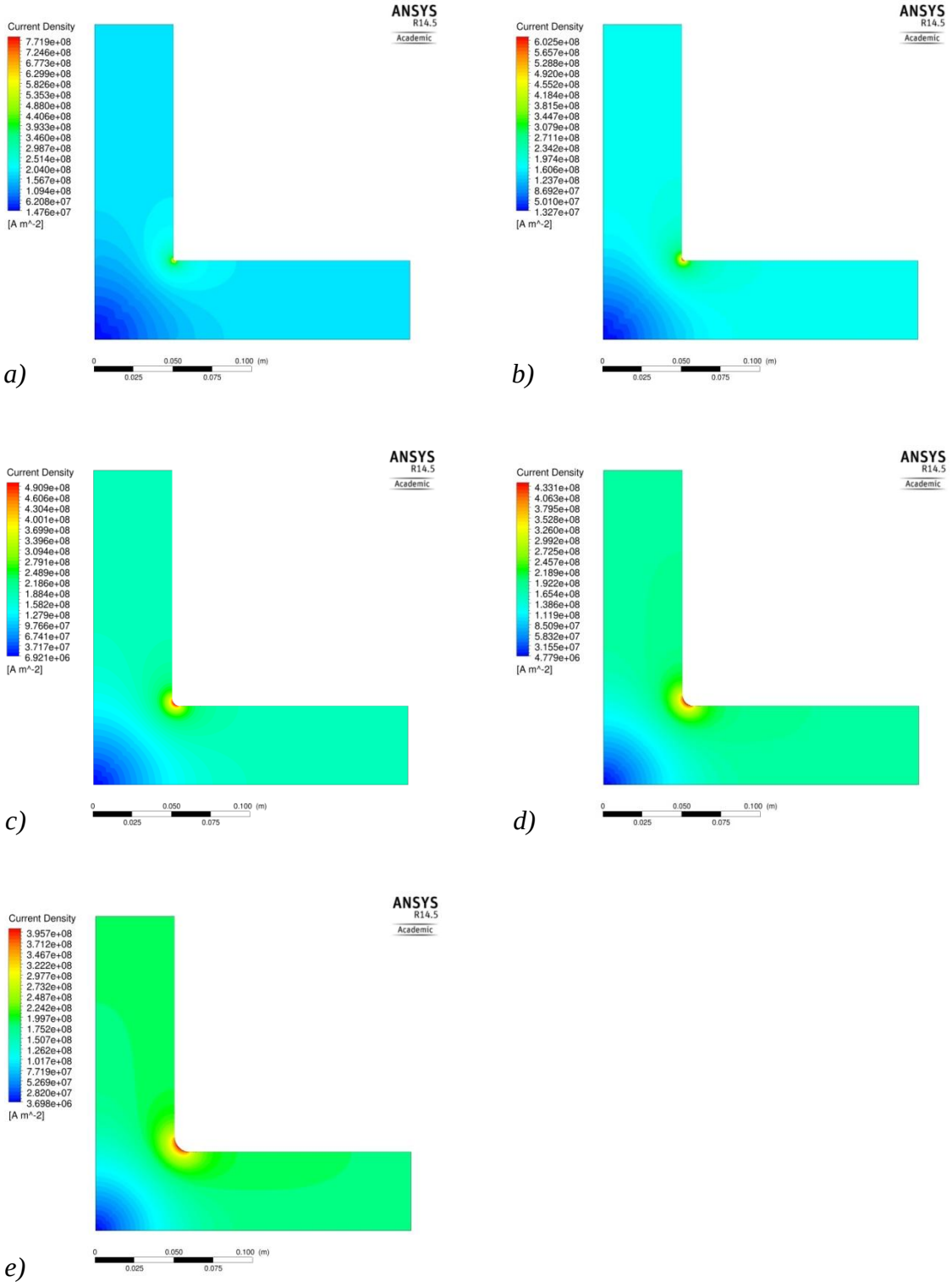


Figure 5-8: CFX calculations of electrical current density showing maximum value around apex of turn for varying radii; a) 1 x 10^{-3} m, b) 2.5 x 10^{-3} m, c) 5 x 10^{-3} m, d) 7.5 x 10^{-3} m, e) 10 x 10^{-3} m.

As expected, the calculations show that there is a local area of current build up around the apex of the turn and conversely an area of current depletion in the area adjacent. Due to the nature of the electrical current flow, when designing a resistive heating element such as one shown in Figure 5-1 it is useful to be able to predict the positions on the geometry at which the current density is uniform and the maximum and minimum values do not deviate from within a set range.

A solution to this has been provided in the following form (Hagedorn and Hall, 1963):

$$N_f = \frac{1}{\pi}\ln\left(\frac{2}{f}\right) + \frac{1}{\pi S}\cos^{-1}\left[\frac{S^2-1}{S^2+1}\right] + \frac{0.553}{[S^2+1]^{\frac{1}{3}}}\left[\frac{P}{S}\right]^{\frac{4}{3}} \qquad 5.4$$

Therefore the number N_f of x leg strip widths from corner D to obtain a desired degree of uniformity f can be calculated; given the strip width ratio S and the normalised radius of the right angle bend P, Figure 5-9. Factors P and S are described on page 136.

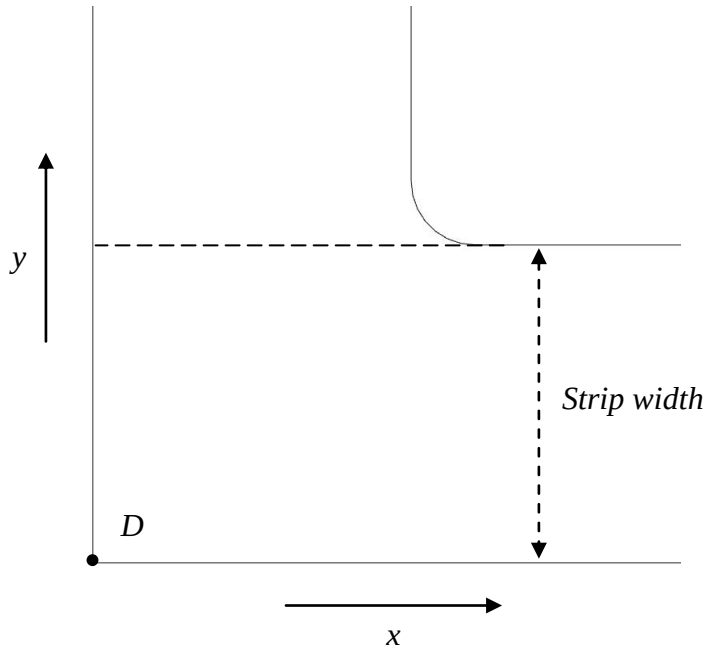


Figure 5-9: Annotation of strip width measurement from reference point D.

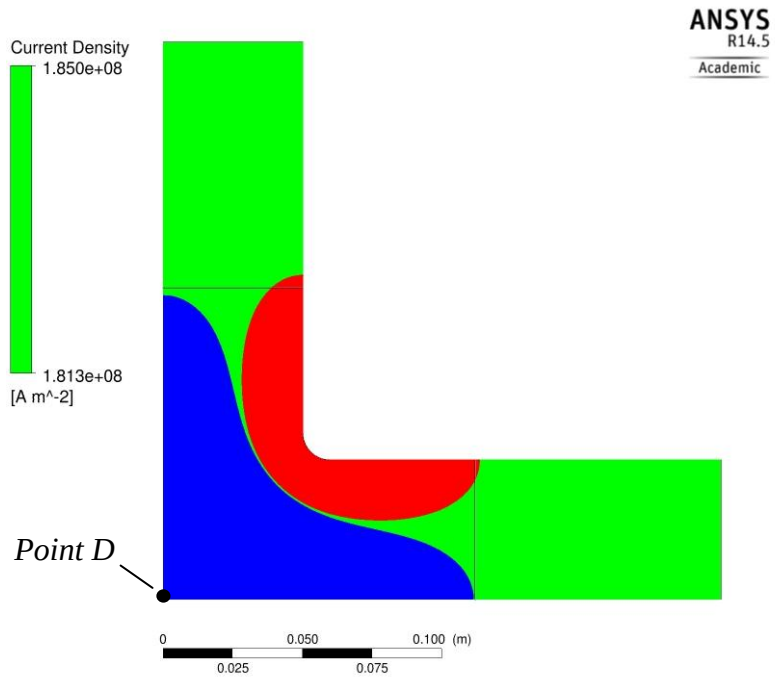
The calculation has been carried out for geometry with a radius of 10 x 10^{-3} m (as this is the same radius as in the furnace heating element) and a x leg strip thickness of 50 x 10^{-3} m for a number of desired uniformities; 1%, 2%, 5% and 10%, detailed in Table 5-2.

Table 5-2: Theoretical calculations for distance from reference point D to achieve a desired degree of uniformity of electrical current density in the x and y legs of the geometry

Desired uniformity	0.01 (1%)	0.02 (2%)	0.05 (5%)	0.1 (10%)
Uniform current density (A.m^{-2})		1.832 x 10^{8}		
Value of current density derived from required uniformity (A.m^{-2})	1.832 x 10^{8} +/- 1.832 x 10^{6}	1.832 x 10^{8} +/- 3.663 x 10^{6}	1.832 x 10^{8} +/- 9.159 x 10^{6}	1.832 x 10^{8} +/- 1.832 x 10^{7}
N_f	2.237843	2.017207	1.725542	1.504907
Distance in x and y direction from reference D (m)	1.119 x 10^{-1}	1.009 x 10^{-1}	8.628 x 10^{-2}	7.525 x 10^{-2}

A comparison of the CFX calculation with that of the numerical solution is shown in Figure 5-10 and Figure 5-11 and show good agreement with a maximum error of less than 5 x 10^{-3} m.

a)



b)

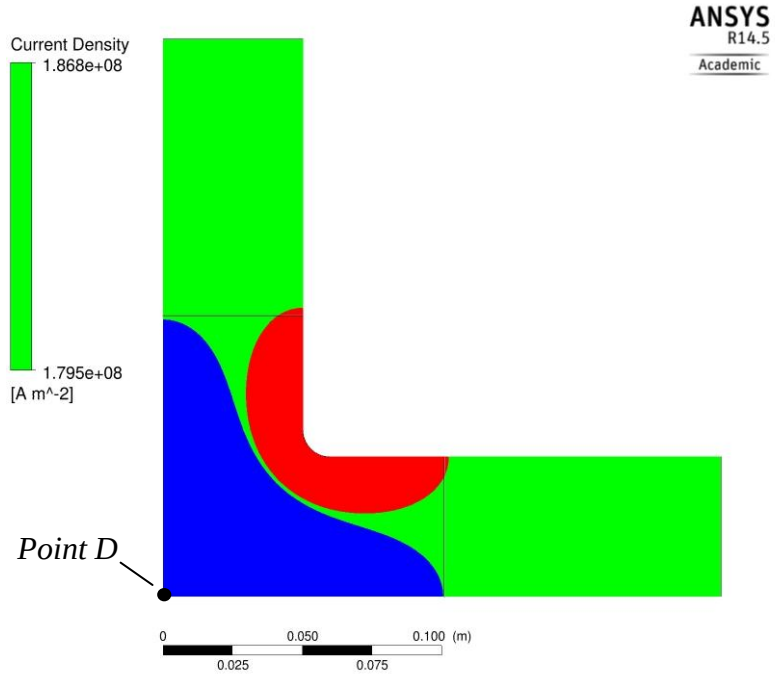
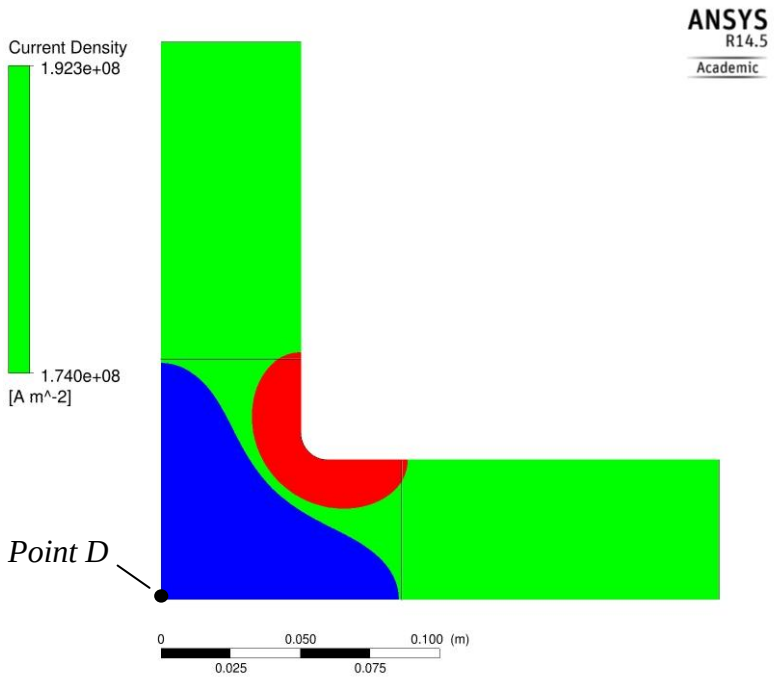


Figure 5-10: Comparison of CFX calculation with analytical solution for distance from reference point D in which electrical current density falls within a specified uniformity range. a) 1% b) 2%. Black line indicates analytical solution distance, green contour is specified uniformity range, red contour is specified uniformity range + f and blue contour is specified uniformity range – f.

c)



d)

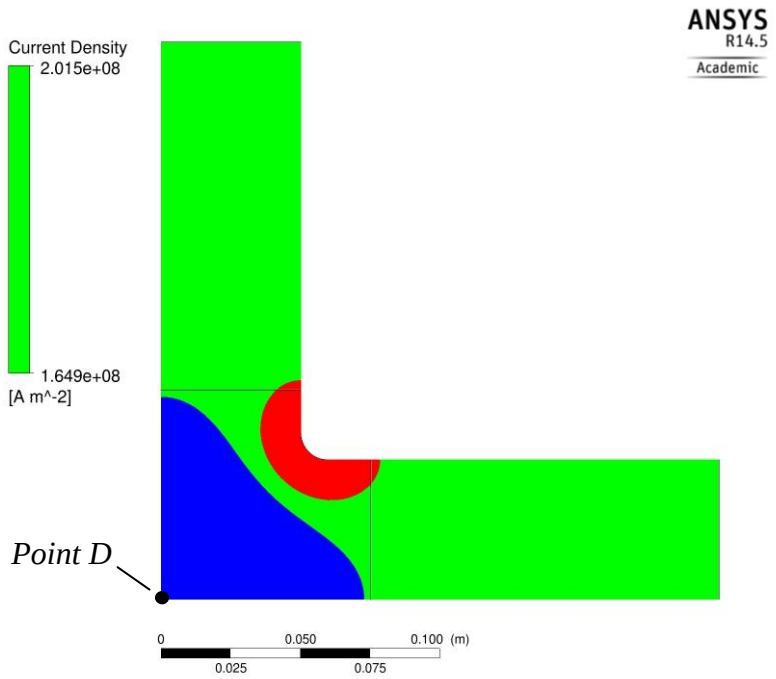


Figure 5-11: Comparison of CFX calculation with analytical solution for distance from reference point D in which electrical current density falls within a specified uniformity range. c) 5% d) 10%. Black line indicates analytical solution distance, green contour is specified uniformity range, red contour is specified uniformity range + f and blue contour is specified uniformity range – f.

As we have seen in the mesh dependency study, to fully quantify the effect of current density variation in the heater geometry an extremely fine mesh is required, however this requirement by definition is only necessary in areas that the current density is expected to vary significantly.

When discretising geometry for a CFD calculation it is prudent to be economical with the mesh element size in order to optimise run time, and the ability to determine the areas in which the electrical current density will be expected to vary the most aids this process.

In this case, the apex of the 10 x 10^{-3} m radius turn in the geometry can be assigned a smaller element size than the majority of the body and when meshing the use of the element size ratio criterion can be used in which adjoining elements are incrementally scaled via a scaling factor e.g. 10% until the element size assigned to the rest of the body is matched. An example is shown in Figure 5-12.

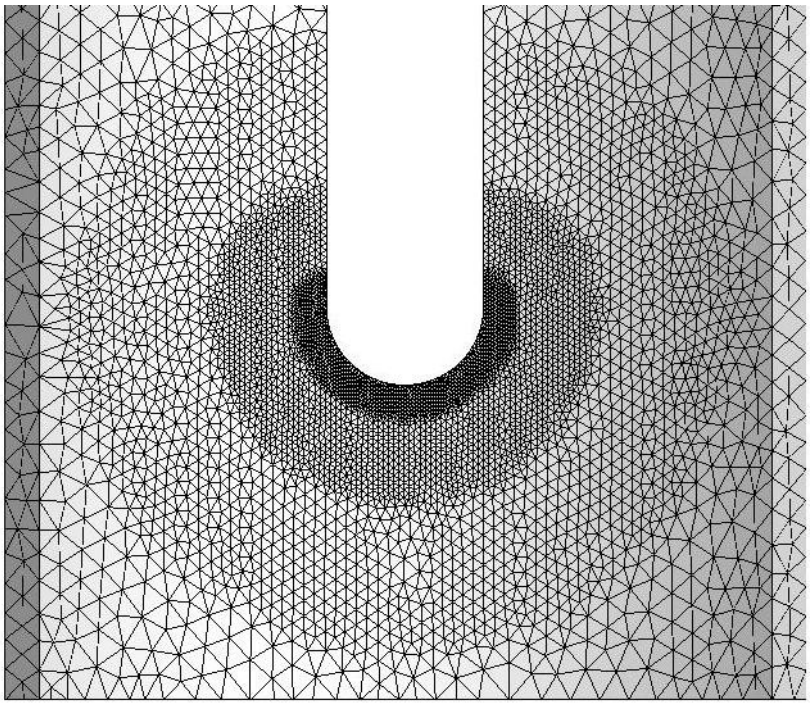


Figure 5-12: An example of optimised meshing of the furnace heating element in which element size is scaled proportionally from the apex of the radius.

5.3 Electrical resistance

An electrical current flowing through a metallic wire for example will inevitably encounter a certain amount of electrical resistance of which the magnitude is dependent on the properties of the material. As a consequence of this, energy will be dissipated in the form of heat.

Assuming the geometry exhibits linear resistance properties in relation to the applied current I and voltage V (known as an ideal resistor) the resistance can be calculated according to Ohm's Law (Ohm, 1827) as:

$$R = \frac{V}{I} \qquad 5.5$$

The two material properties of importance are the electrical resistivity ρ and the electrical conductivity σ. As the act of resistance is broadly speaking the opposite of conductance, this suggests there would be some analytical relationship between the two, and indeed this is the case as electrical conductivity is the inverse of electrical resistivity.

So in the case of a cylindrical wire of finite length l with a constant cross sectional area A, the resistance of the geometry can be calculated as;

$$R = \frac{l}{\sigma A} \qquad 5.6$$

or

$$R = \rho \frac{l}{A} \qquad 5.7$$

Two common configurations of resistors in electrical circuits are those in series or parallel; both have a direct relationship with Kirchhoff's laws (Kirchhoff, 1868) and the nature of the arrangement will have an effect on the equivalent resistance R_{EQ} when carrying out any circuit analysis.

5.3.1 Resistors in series

Electrical resistors are said to be in series if the current from one resistor flows exclusively into the next, therefore from Kirchhoff's law it can be found that all series resistors have the same current (Rizzoni, 2003).

Using Figure 5-13 as an example, the circuit containing four resistors could be replaced by one equivalent resistor in which the value of the equivalent resistor would equal the sum of the individual resistors. This can be described using the general relationship:

$$R_{EQ} = \sum_{n=1}^{N} R_n \qquad 5.8$$

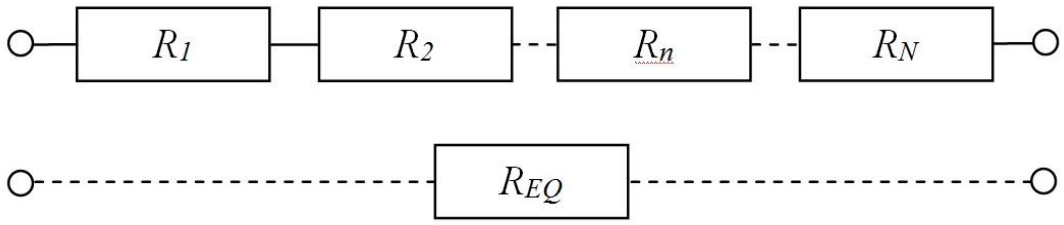


Figure 5-13: Example of N series resistors which are equivalent to a single resistor, adapted from (Rizzoni, 2003).

In this configuration the voltage is divided between the resistors and is directionally proportional to the ratio of individual resistance to the equivalent circuit resistance.

$$V_1 = IR_1 = \frac{R_1}{R_{EQ}}V \qquad 5.9$$

$$V_2 = IR_2 = \frac{R_2}{R_{EQ}}V$$

$$V_N = IR_N = \frac{R_N}{R_{EQ}}V$$

Where;

$$I = \frac{V}{R_1 + R_2 + R_N}$$

5.3.2 Resistors in parallel

Two or more electrical resistors are in parallel when they both share a common terminal, therefore from Kirchhoff's law it can be found that all resistors will have the same voltage (Rizzoni, 2003).

Using Figure 5-14 to show the configuration it can be stated that any number of resistors in parallel can be described as equal to an equivalent resistance by the following expression:

$$\frac{1}{R_{EQ}} = \frac{1}{R_1} + \frac{1}{R_2} \cdots + \frac{1}{R_N} \qquad 5.10$$

This can be written in the following form to describe the equivalent resistance of any number of resistors in a parallel configuration.

$$R_{EQ} = \frac{1}{\frac{1}{R_1} + \frac{1}{R_2} \cdots + \frac{1}{R_N}} \qquad 5.11$$

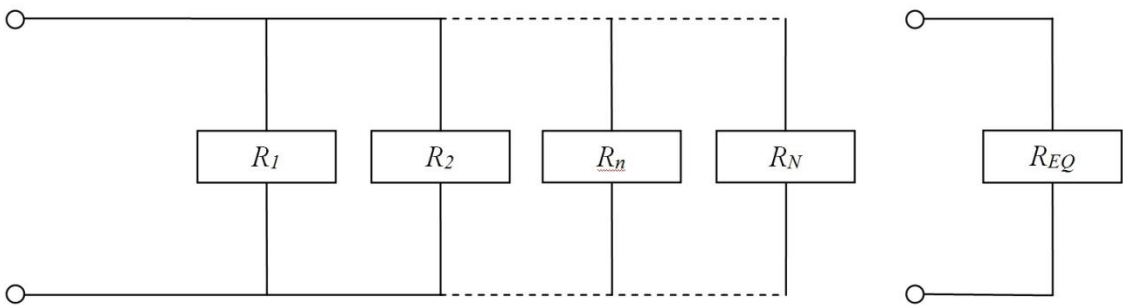


Figure 5-14: Example of N number of resistors in parallel which are equivalent to a single resistor by use of a defined relationship, figure adapted from (Rizzoni, 2003).

So, the electrical current is divided between each parallel resistor and is proportional to the individual resistance.

$$I_1 = \frac{V}{R_1} \qquad 5.12$$

$$I_2 = \frac{V}{R_2}$$

$$I_N = \frac{V}{R_N}$$

Or

$$I_{circuit} = V\frac{1}{R_{EQ}} \qquad 5.13$$

5.3.3 Calculation of furnace heating element electrical resistance

As discussed earlier, the furnace heating element is manufactured from a cylindrical tube which is then machined into a serpentine track of the designer's specifications. The material used for construction is an isotropic grade of graphite with a specific electrical resistance (electrical resistivity) of 12 x 10^{-6} Ωm (Oakley, 2011), SGL Group (2007) and this value shows good agreement with experimental data found in literature (Tyler and Wilson, 1953, Powell and Schofield, 1939).

Even so, as the electrical resistance of the heating element is clearly an intrinsic component in the CFX furnace model, it would be useful to determine the resistance analytically by using the provided material resistivity value and the known geometry of the element.

Firstly, the method of calculating the resistance must be determined. Figure 5-15 a) shows the geometry of the complete heater element with electrical terminals A and B, Figure 5-15 b) shows a representation of the heater geometry analogous to that of a circuit diagram in which electrical current flows from terminals A to B, however at either junction the current can either flow through one half of the heater or the other; in other words both halves of the heater element share a common terminal.

In this case the heating element must be considered two resistors in parallel, R_1 and R_2, and therefore the method detailed in equation 5.11 should be used in order to make an approximation of the total equivalent resistance of the component.

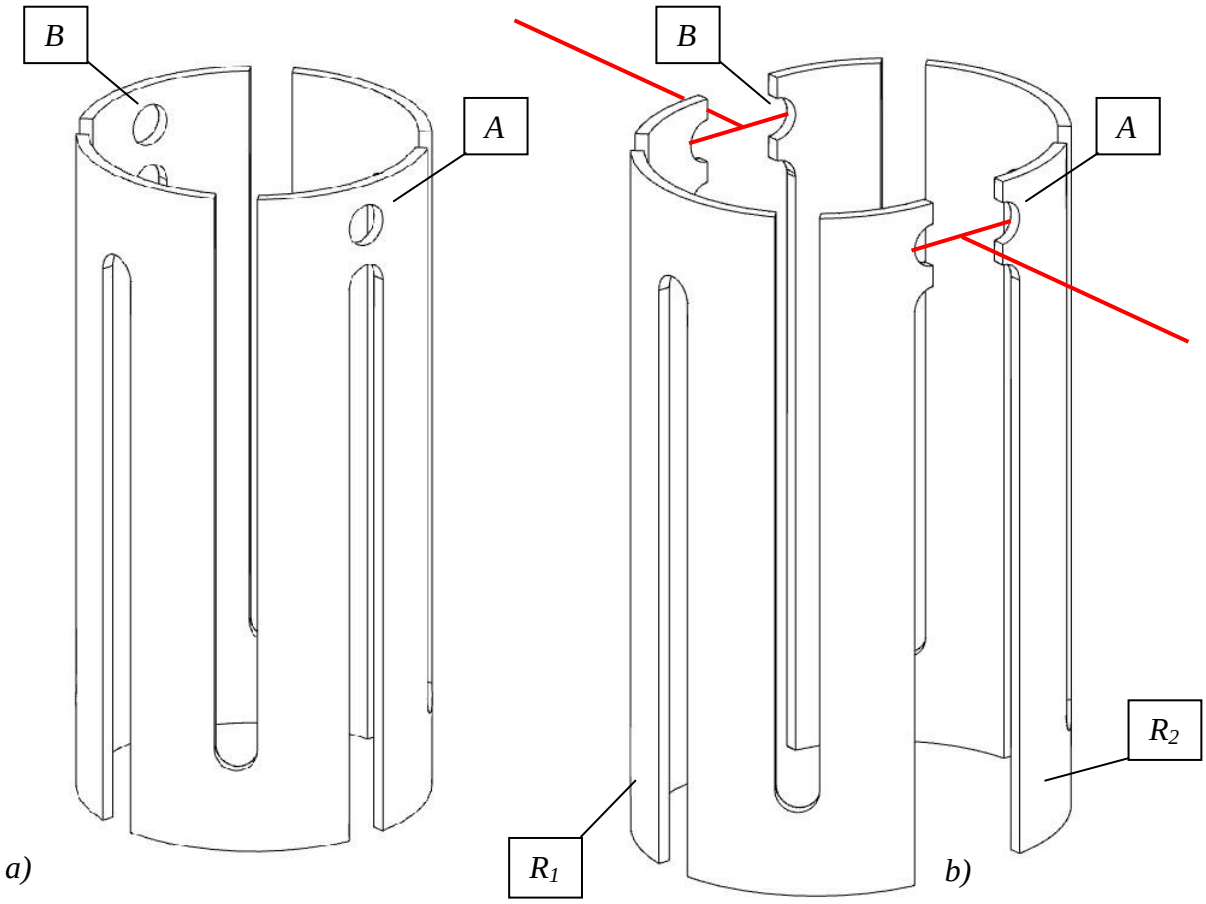


Figure 5-15: Geometry of graphite heating element a) Full heating element as used in practice b) Representation of heating as two parallel resistors, lines emanating from points A & B indicate the terminals are shared between resistors R_1 and R_2.

To calculate the resistance of the heating element it is useful to divide the geometry into segments of which the resistance can be determined, this method is analogous to that of domain discretisaation which is used in the CFX model.

Consider the geometry shown in Figure 5-16; the overall resistance is comprised of 12 series resistors, the resistance of r_2, r_5, r_8 and r_{11} can be calculated in the usual manner given the material resistivity and geometry is known as described in equation 5.7.

Resistors $r_1, r_3, r_4, r_6, r_7, r_9, r_{10}$ and r_{12} can be calculated using equation 5.2 described earlier. So given the two equations and noting that there are four straight sections and eight curved sections in the geometry shown in Figure 5-16, the total resistance of one half of the heating element can be described in the following way:

$$R = 8 \times \left[\frac{\rho}{t}\left[\frac{X^*}{g} + \frac{Y^*}{h} - f(S) - 0.276(S^2+1)^{\frac{2}{3}}\left(\frac{P}{S}\right)^{\frac{4}{3}}\right]\right] + \left[4 \times \left[\rho\frac{l}{A}\right]\right] \qquad 5.14$$

Where;

$$S = \frac{g}{h}$$

$$f(S) = \frac{2}{\pi}\ln\left[\frac{4S}{S^2+1}\right] + S - \left[\frac{S^2-1}{\pi S}\right]\cos^{-1}\left[\frac{S^2-1}{S^2+1}\right]$$

$$P = \frac{r}{h}$$

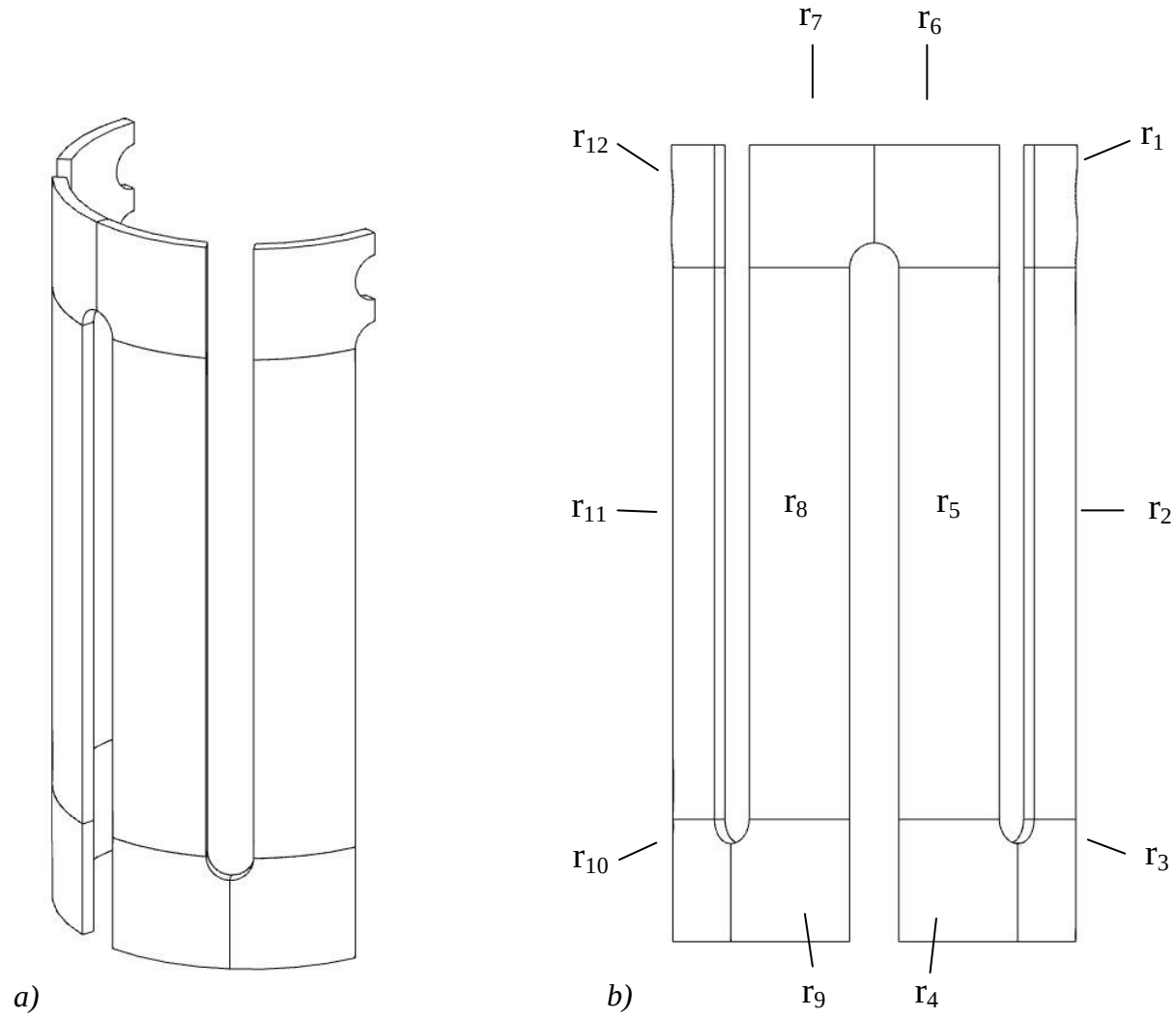


Figure 5-16: a) Isometric view of half heating element split into component series resistors. b) Labelled series resistors representing half heating element, R1 in Figure 5-15.

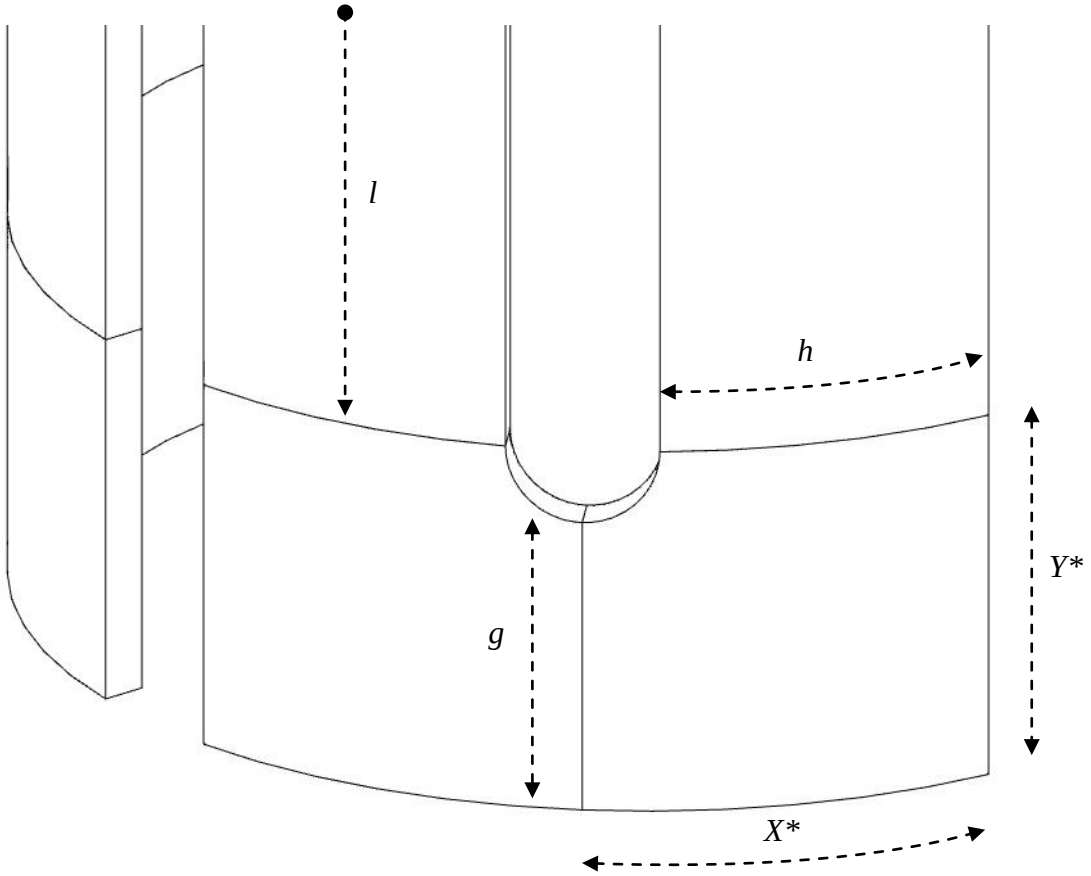


Figure 5-17: View of split heating element showing dimensions X, Y*, g, h and l.*

Referring to Figure 5-2 and annotated on Figure 5-17, the resistance of one half of the heating element can be calculated using equation 5.14 given the values shown in Table 5-3.

Table 5-3: Parameters used to calculate electrical resistance of furnace heating element.

l	$225 \times 10^{-3}\ m$
A	$24.05 \times 10^{-5}\ m^2$
g	$40.08 \times 10^{-3}\ m$
h	$40.08 \times 10^{-3}\ m$
X^*	$50 \times 10^{-3}\ m$
Y^*	$50 \times 10^{-3}\ m$
r	$10 \times 10^{-3}\ m$
ρ	$12 \times 10^{-6}\ \Omega m$

The value of resistance obtained for one half of the heating element is 0.0607 Ω, therefore using this resistance value the total equivalent resistance can be calculated using equation 5.11;

$$R_{EQ} = \frac{1}{\frac{1}{0.0607} + \frac{1}{0.0607}}$$

$$R_{EQ} = 0.0303\ \Omega$$

To determine the resistance calculated from the CFX model, a given potential difference can be applied to the geometry shown in Figure 5-15 given the resistivity value used previously. The electrical current can then be derived from the model results and thus the resistance can be calculated, in this case the CFX calculations result in a resistance value of 0.030 Ω.

This calculation was performed with a mesh similar to that shown in Figure 5-12 in order to optimise computational time however a further calculation was performed in order to characterise the mesh influence on electrical calculations using an extremely fine mesh, node spacing < 0.5 x 10^{-3} m, and variation in results was marginal with an error in the order of 0.1%.

As discussed earlier, providing the heating element exhibits properties of an ideal resistor i.e. linearity between current and voltage, the electrical resistance can be determined experimentally by plotting the current against voltage and calculating the gradient of the slope.

Figure 5-18 shows the experimentally determined voltage and current values for a number of furnace temperature and test conditions, which result in a total of 40387 data points, plotted to include a linear trend line. One immediate observation is that the trend line does not intercept the x,y axis at 0,0 which is an indication that the heating element is not a true perfect resistor, however this is not unexpected, particularly as the operating temperature range of the resistor is in the region of 25 – 1700 °C.

In this case the results are deemed sufficiently linear for Ohm's law to apply and so the equivalent resistance determined by experimental method can be calculated.

From the equation of the linear best fit line shown in Figure 5-18 the gradient of the line is calculated to be $31.96\ A.V^{-1}$, therefore the resistance is the reciprocal of this value and is calculated as;

$$R_{EQ} = \frac{1}{31.96}$$

$$R_{EQ} = 0.0312\ \Omega$$

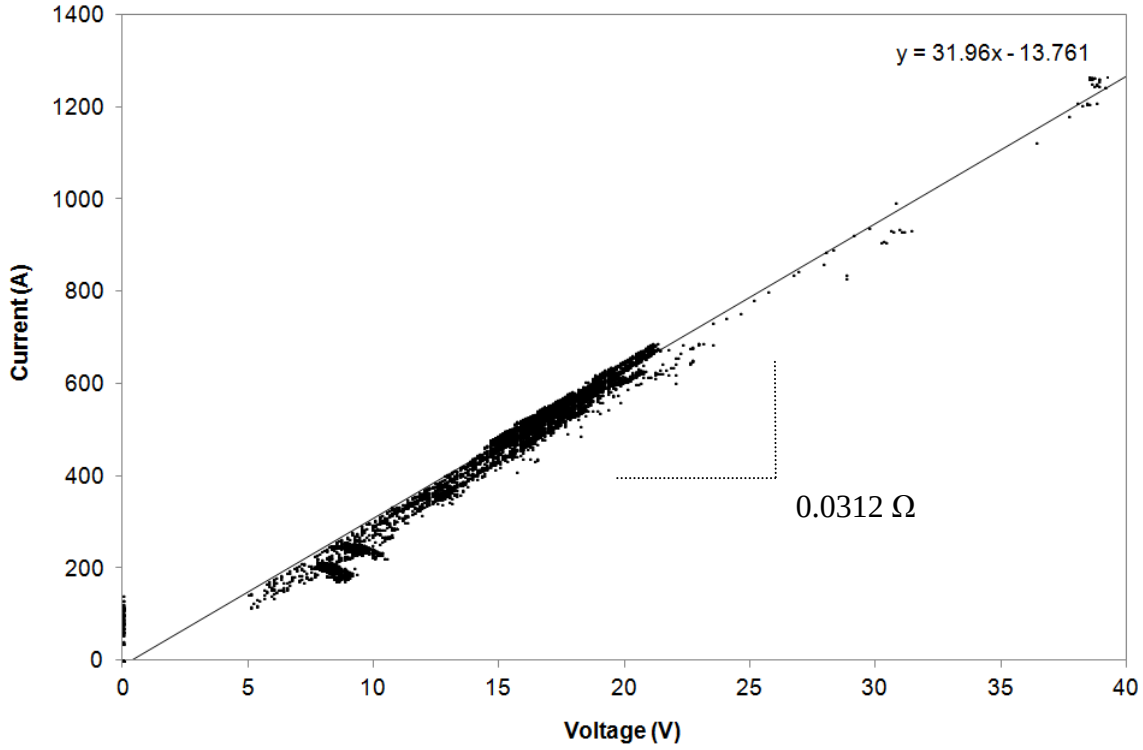


Figure 5-18: Plot of experimentally determined voltage and current values for all experimental trials resulting in a total of 40387 data points.

At this point it is worth noting that there is a certain degree of error between the theoretically calculated resistance value and that obtained experimentally.

As described in the experimental method section, due to the enclosed nature of the furnace electrical components the electrical current is measured from one of the three cables supplying the heating element with the three-phase supply and then multiplied by three in order to obtain a value of the total supplied current; voltage is measured directly across the heating element.

The implication of this method is that any errors arising from differences between the current values in any of the three cables will result in an apparent change in the resistance; an overestimation if the current is lower than average or an underestimation if the current is higher.

Further work was carried out to assess this and quantify, if any, the magnitude of variation between the measurements and the results showed that there was a constant proportional difference between the current values in each of the three cables.

The cable used in all of the experimental trials always gave the lowest or equal lowest current reading; the ratio of difference between this measurement and the sum of the electrical current was determined to be in the order of 0.059; in other words the multiplied value from this cable was always in the order of 5.9% lower than the total current. This would explain the higher than predicted resistance value.

As there was an adequate degree of consistency in these measurements a correction factor can be used in order to calculate a resistance value from all of the experimental trials.

Figure 5-19 shows the corrected voltage –current plots and the slope of the linear best fits line gives a resistance value of 0.0296 Ω. This value is not very far from the predicted value using CFX and the theoretical calculation, a comparison of which is shown in Figure 5-20.

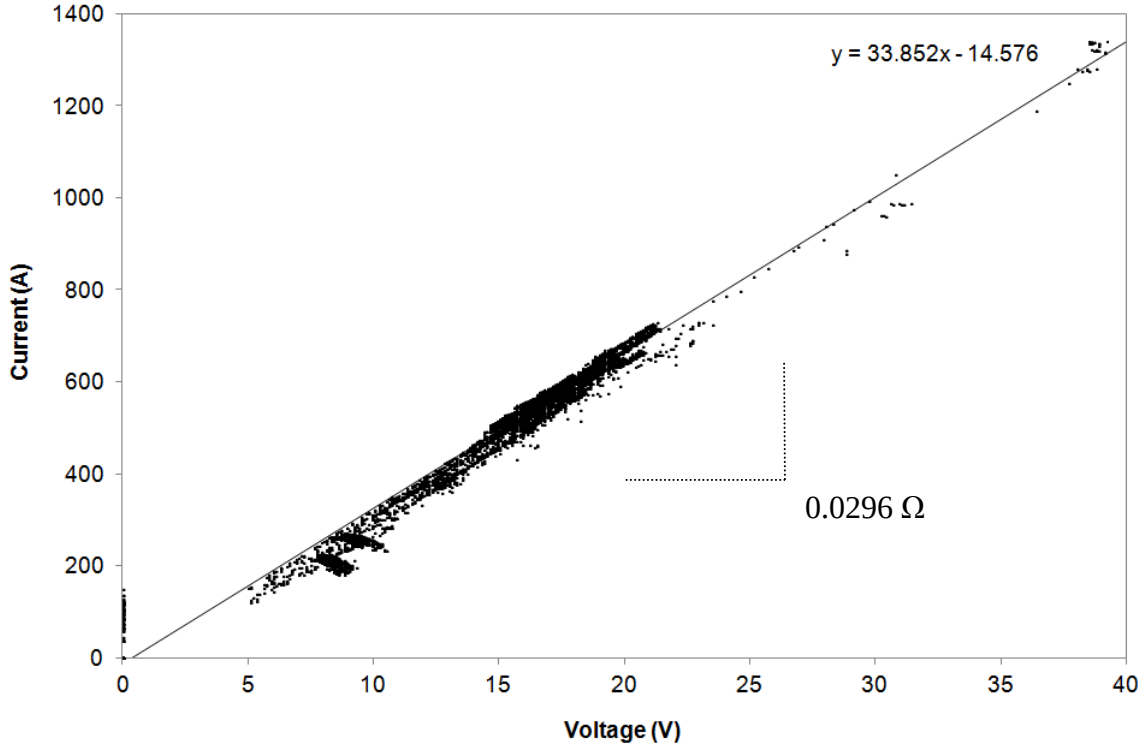


Figure 5-19: Plot of experimentally determined voltage and current values corrected using correction factor.

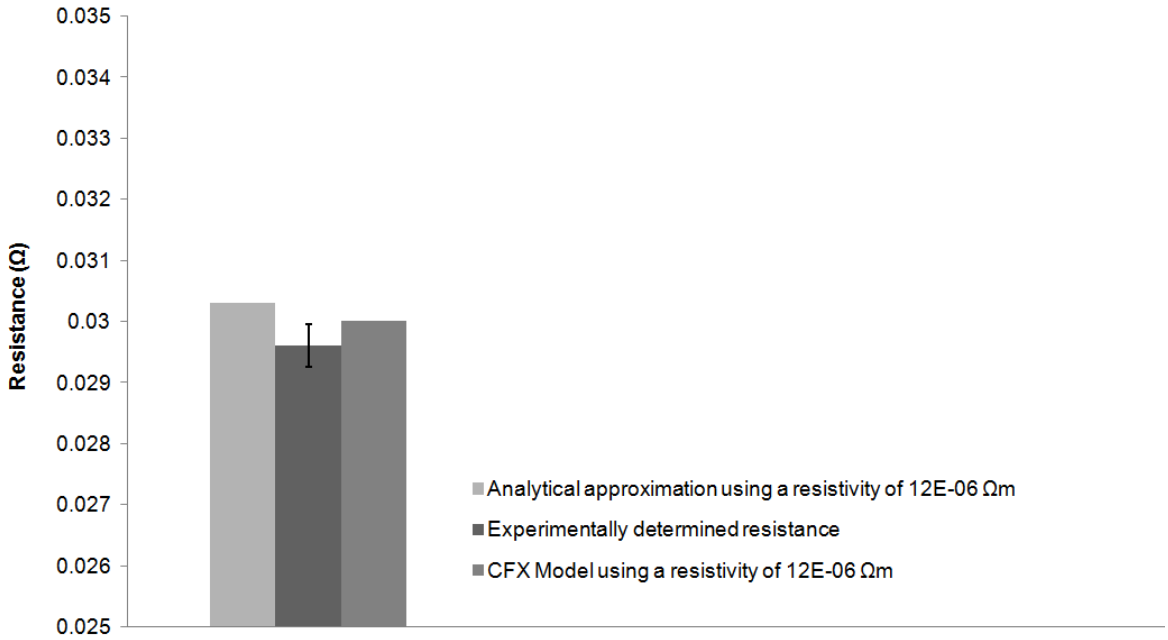


Figure 5-20: Electrical resistance of graphite heater element calculated using an analytical approximation, using CFX and determined experimentally. Error bar on experimental results show the calculated error.

Comparing the experimentally determined resistance values with those calculated using CFX and analytically with a material resistivity value of 12 x 10^{-6} Ωm, there is good agreement between the values, with an error of <1% and may be due to variation in the experimental data.

The purpose of this study was to assess if the graphite resistivity data supplied by the manufacturers was appropriate to be used the CFX model and in all cases there is no sufficient evidence to suggest a significant variation in supplied resistivity data and that derived from experimental results.

5.4 Electrical resistive (Joule) heating

Joule heating occurs when a current flows through a solid or fluid with a finite conductivity; hence electrical energy is converted to heat energy through resistive losses in the material. On a microscale, the effect is created by energy transfer between electrons and the conductor atoms; equilibrium is reached in the conductor by dissipating this energy as heat.

In many applications, such as microelectronics, the Joule heat is unwanted and must be dissipated by some sort of cooling medium, however in many cases such as furnace heaters the Joule effect is utilised in order to provide a controlled heat source.

5.4.1 CFX benchmark calculation of Joule heating in an amorphous wire with uniform heat loss

The aim of the CFX model is to simulate electrical current distribution in conjunction with Joule heating and radiation heat loss. It is therefore useful to further compare such

scenarios against a numerical solution.

One such solution is described when investigating the Joule heating effect in metallic wires (Knobel et al., 1995). The derived equation allow the calculation of surface and core temperatures in an amorphous metallic wire when heat is generated by the Joule effect and thermal equilibrium is reached through radiation heat loss to the surroundings only and does not account for conduction heat transfer to a fluid medium.

Along with the geometry of the wire, the material resistivity ρ and the thermal conductivity k are required for the calculation. Other variables are readily obtained.

Terms particular to this solution are the wire loss parameter P_W which is a function of the emissivity ε and the Stefan-Boltzmann σ constant, and P which is the loss parameter defined in terms of unit volume;

$$P_W = \varepsilon\sigma$$

$$P = \frac{2P_W}{a}$$

where a is defined as the wire radius.

The following equations for T_m, the temperature at the middle of the wire (radial position 0) and ΔT_{MAX} the maximum radial temperature difference between the axis of the wire and its surface can now be solved;

$$T_m = \left[T_0^4 + \frac{j^2\rho}{P}\right]^{\frac{1}{4}} \qquad 5.15$$

$$\Delta T_{MAX} = \frac{1}{4}\frac{j^2\rho}{k}a^2 \qquad 5.16$$

where j is the electrical current density through the wire cross section and k is the material thermal conductivity.

CFX simulations were carried out using a given wire geometry and a varying potential difference applied across the domain. A tetrahedral mesh was constructed in ICEM to represent a wire domain and an enclosing fluid domain at which nodes were shared at the interface.

The discrete transfer radiation model was used for the calculation with surface-to-surface radiation transfer, as opposed to the Monte Carlo method. An advantage of the discrete transfer method is that computational times are generally quicker when compared to the Monte Carlo method. As the fluid region in the test case, and the furnace model, are assumed to be perfect vacuums the Monte Carlo method in not required as there is assumed to be no participating medium or scattering effects. A full description of the methods is available in section 5.5.

Figure 5-21 and Figure 5-22 show the analytically determined values compared with values calculated using CFX and both show good agreement with one another. Some variation is encountered when calculating the wire radial temperature difference; the probable cause attributed to the meshing and errors incurred by the radiation model.

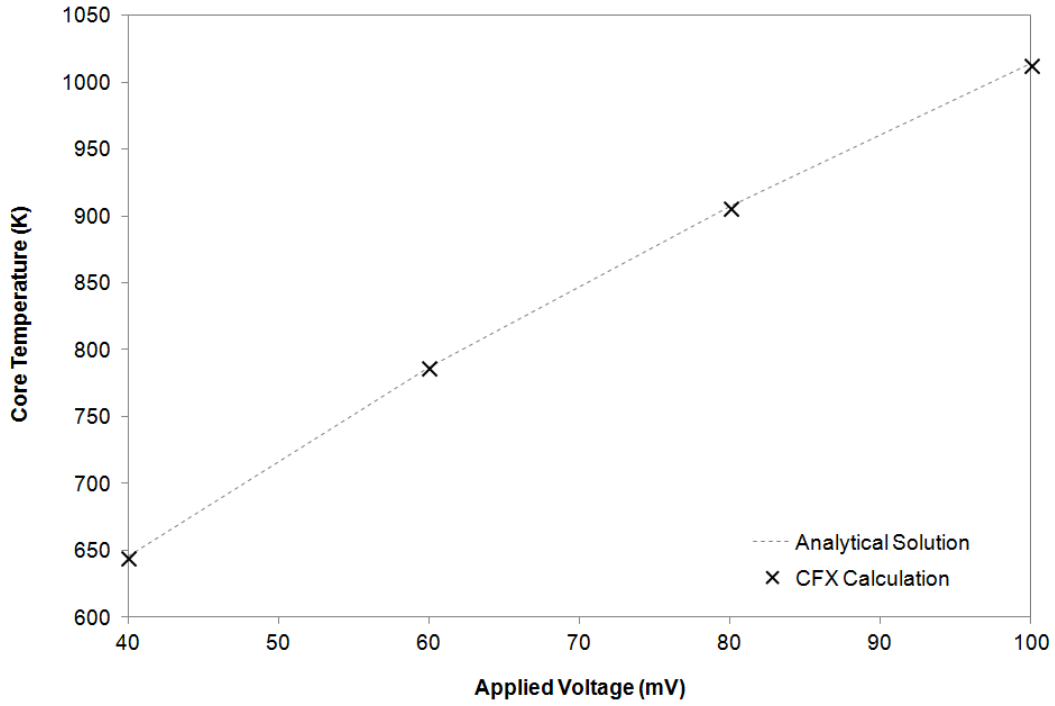


Figure 5-21: Comparison between theoretically calculated values for wire core temperature with those calculated using CFX.

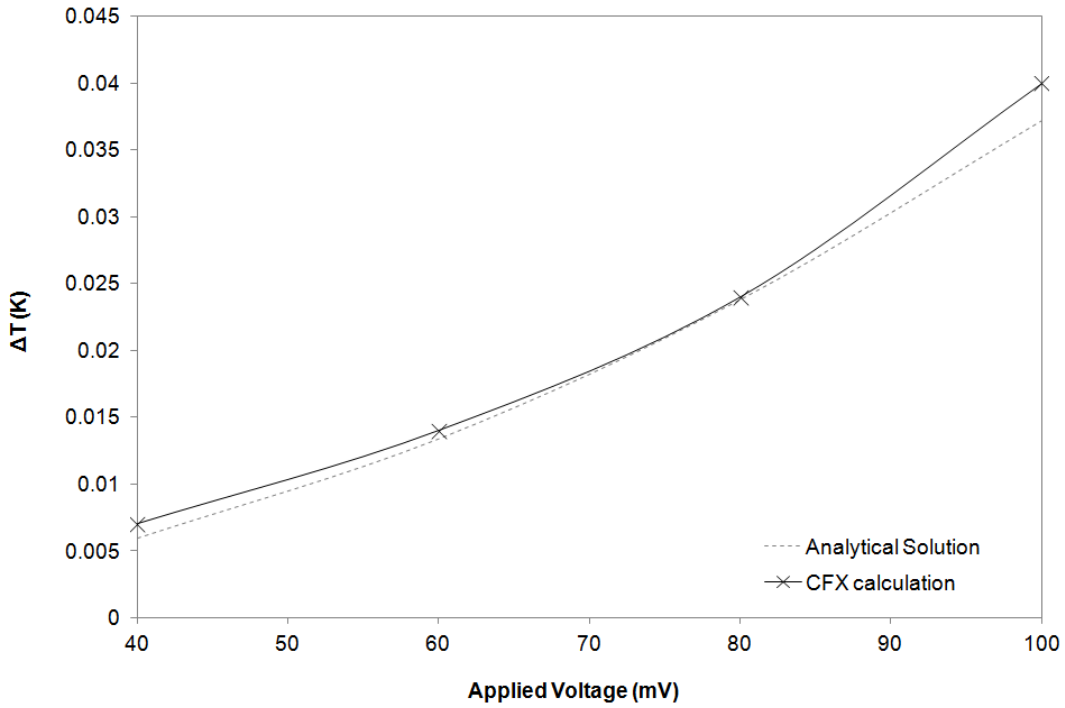


Figure 5-22: Comparison between theoretically calculated values for wire radial temperature difference with those calculated using CFX.

5.5 Radiation heat transfer

Thermal radiation is an electromagnetic phenomenon and in contrast to convective and conductive heat transfer mechanisms is not bound to molecular transport (Knaus et al., 1999).

A number of analytical methods describing the radiation heat transfer have been developed with the aim of calculating a radiation source term for the energy conservation equation and calculating a temperature field.

The first step when choosing an appropriate radiation model is to determine the optical thickness of the domain to be solved; optically thin means the fluid is transparent to the radiation at wavelengths at which the majority of the heat transfer is likely to occur and optically thick means that the fluid will interact with the radiation field and absorb, scatter or re-emit the radiation.

An example of an optically thick radiation problem would be that of combustion, as the resultant gasses would tend to absorb some radiation. By means of contrast, an optically thin problem would be one that is presented in this work, in which radiation heat transfer is occurring in a vacuum domain and heat transfer is only occurring at domain surfaces. In this case the two radiation models recommended are the Monte Carlo model or Discrete Transfer model (Ansys, 2010). Further to this, in gray model cases i.e. the source term does not have a spectral dependency and the radiation field is expected to be reasonably homogenous, the Discrete Transfer model is the most efficient (Ansys, 2010).

The Monte Carlo method and Discrete Transfer Method (Lockwood and Shah, 1981) are both ray tracing methods, however whereas the Monte Carlo method arbitrarily releases

energy bundles from a source term (Ansys, 2010), in the Discrete Transfer method the centre of a boundary is determined and a hemisphere centred at this point is considered and sub-divided into a prescribed number of solid angles (Coelho et al., 1998, Knaus et al., 1999). The source term defined by these solid angles is described as a ray and the magnitude of the solid angle defines the number of rays emanating from a boundary.

One difference between the two methods is that while the Monte Carlo tracks energy bundles from domain interfaces to extinction i.e. until the magnitude of energy has dissipated enough for the bundle to be discounted, the rays in the Discrete Transfer method are not tracked to extinction and terminate on the next boundary (Knaus et al., 1999)at which point the process is repeated. A large proportion of the computational resource in the Monte Carlo method is taken by recording the history of the energy bundles.

The Monte Carlo method is independent of a co-ordinate system and is applicable to complex geometries whereas the Discrete Transfer method was originally proposed for structured Cartesian meshes, however the Discrete Transfer methods application to triangular meshes has been investigated and shown to perform well in this case (Feldheim and Lybaert, 2004).

A determining factor when considering the accuracy of the Discrete Transfer model solution is that of the number of rays specified for the calculation; the Ansys CFX solver allows a maximum of 32 rays with the default set to 8.

A number of assessments have been carried out in order to determine the optimum number of rays required to reach a sufficient approximation of the radiation field. Results range from 16-64 (Lockwood and Shah, 1981), 12-25 in which the majority of cases were only described adequately by 25 (Cumber, 1995) and 8-64/128 in which one case produced

sufficient results with 8 rays and in another case that involved radiation transfer between eccentric cylinders required $\geq$ 64 to resolve sufficiently (Feldheim and Lybaert, 2004).

The conclusion to draw from these results is that the accuracy and resolution required when using the Discrete Transfer model is entirely dependent on the problem to hand and should be determined accordingly. Many papers such as that by (Nielsen et al., 2003) note that the accuracy of the solution when dealing with a large complex problem does not improve significantly when using higher ray numbers.

The Discrete Transfer model was ultimately chosen for this work predominantly due to the models efficiency with respect to computational resources. An evaluation of the ray effect with respect to the analysis at hand is described in 5.6.7.

5.6 Construction of CFX furnace model

The Bridgman furnace and associated ProCAST model have already been discussed in a previous section so the geometry of the model components will not be discussed in great length here other than to say that the component dimensions of the CFX model were based on a combination of manufacturers data (where available) and data taken from the ProCAST model. An assembly of the component parts are shown in Figure 5-23.

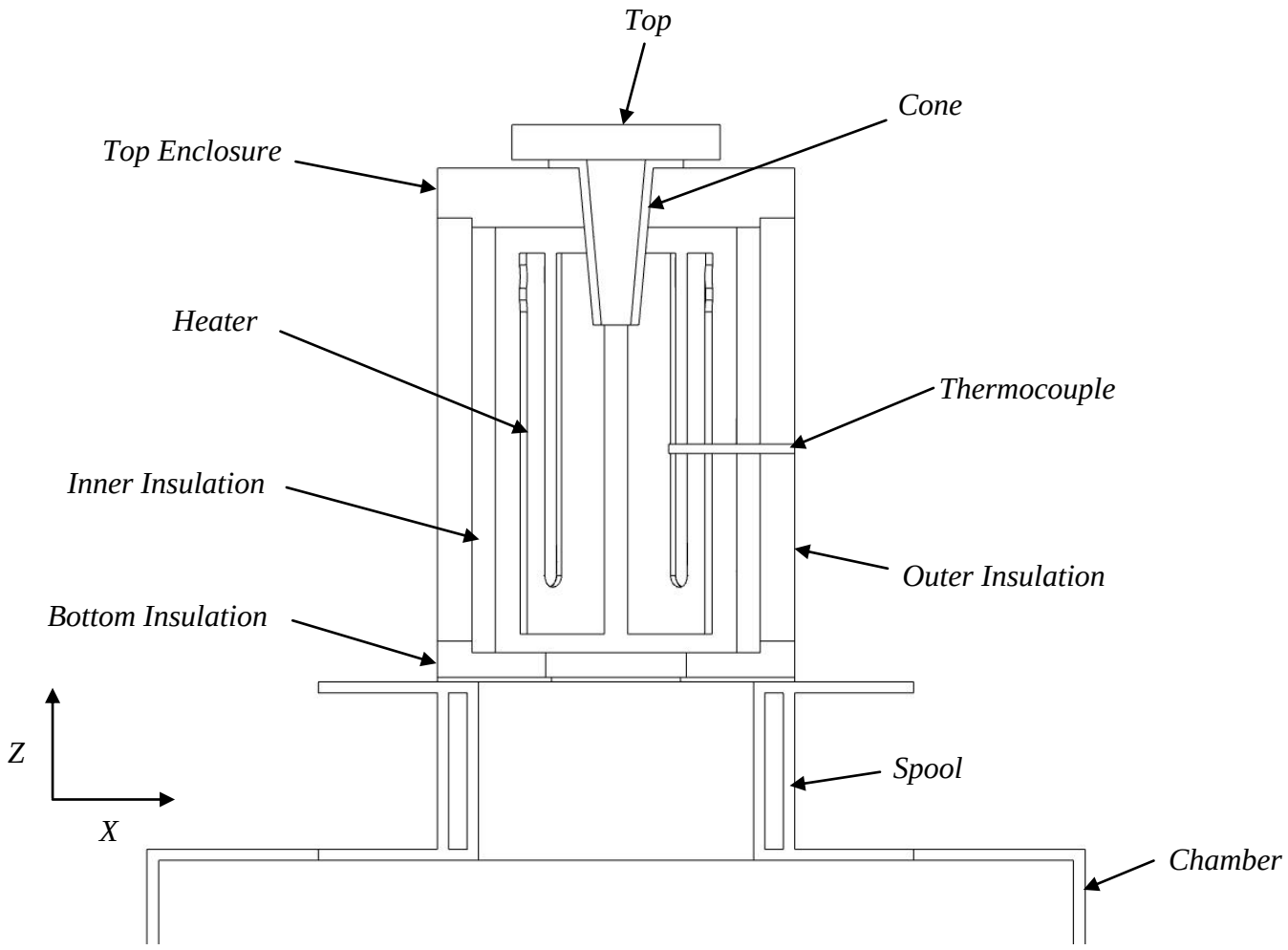


Figure 5-23: Component parts of the CFX furnace model.

For means of simplification the furnace model is assumed to comprise a perfect vacuum in the volume connecting the heating element with the inner surface of the other furnace components. The radiation model used in the CFX requires a domain and subsequent mesh that connects all of these components, therefore this domain is called ‘Vacuum’ and is similar in geometry to that shown in Figure 5-24.

The vacuum is technically a fluid domain, although for means of simplification the fluid solver is not active and therefore convection is not calculated. The overall model consists of twelve solid domains and one fluid domain.

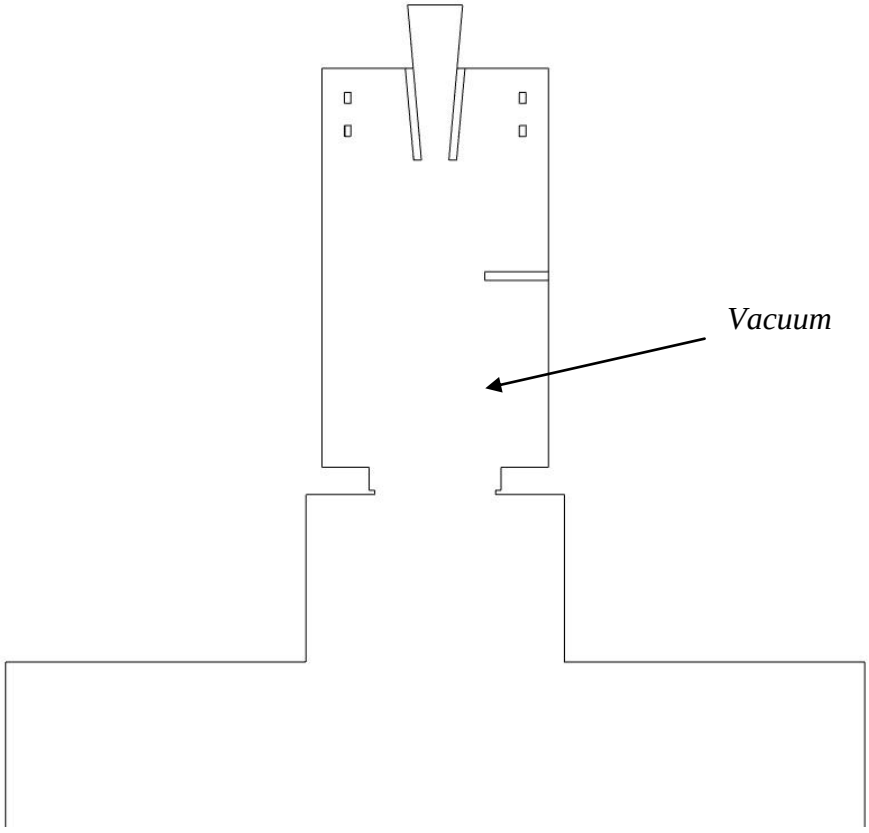


Figure 5-24: Illustration of 'Vacuum' domain in which radiation heat transfer calculations take place.

One notable difference between the ProCAST model and the CFX model is the incorporation of a domain to represent the control thermocouple that is used in the actual furnace to supply temperature data to the PID controller which in turn controls the power input to the heating element, Figure 5-25.

When carrying out simulations using the CFX model the included thermocouple domain will be used to determine the heater set temperature for a given power, in a similar fashion as the actual furnace.

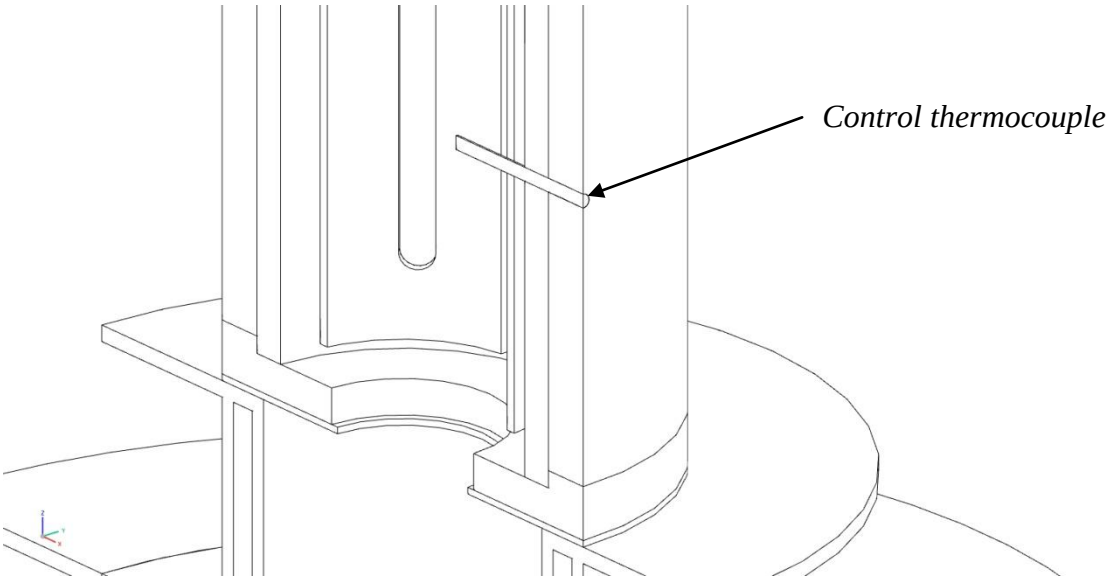
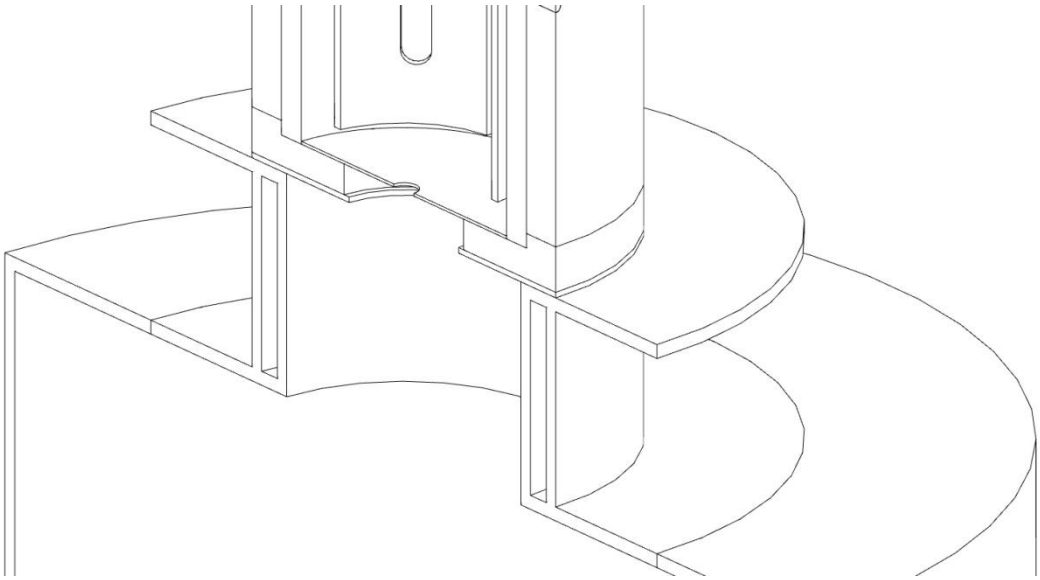


Figure 5-25: Geometry of furnace model showing incorporation of thermocouple protruding into furnace hot zone through the outer and inner insulation.

Four different baffle configurations were used for the CFX models; a 110 x 10^{-3} m Ø baffle which is often referred to as the 'standard' baffle as this is the most commonly used baffle when casting multiple component geometry, a 20 x 10^{-3} m Ø baffle which is used to cast the high thermal gradient single test bars, a double thickness 20 x 10^{-3} m Ø baffle for comparison purposes and a 110 x 10^{-3} m by 30 x 10^{-3} m slotted baffle in order to make comparisons with the ProCAST model.

a)



b)

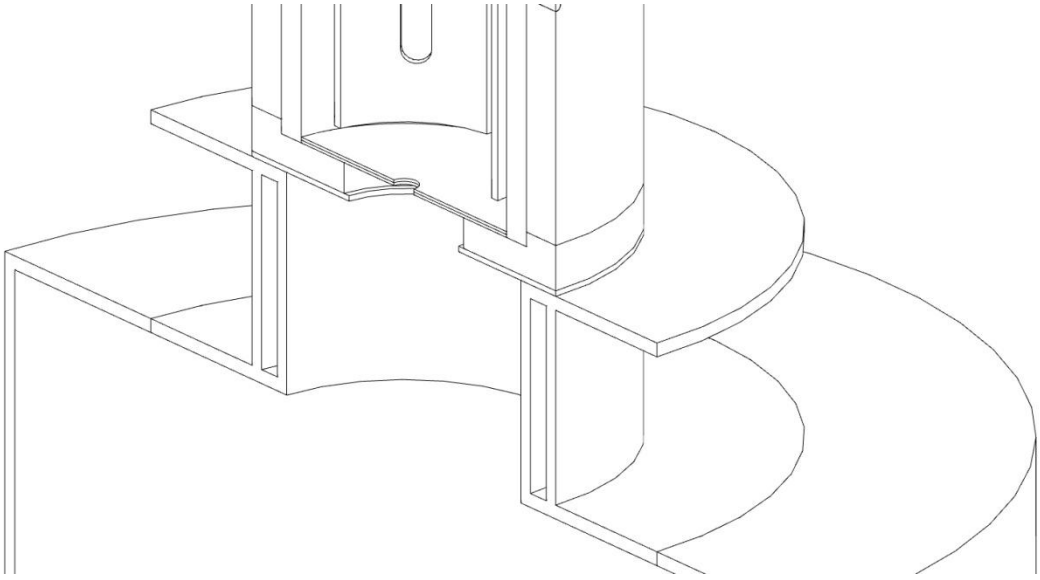
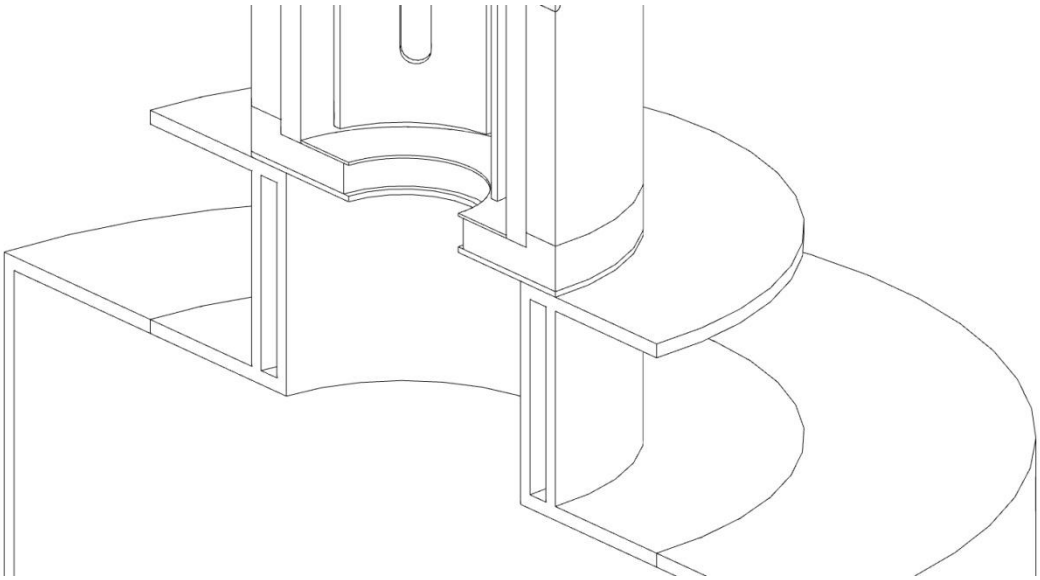


Figure 5-26: Illustration of baffle geometry variation used in the CFX calculations. a) 20 x 10^{-3} m Ø, b) 20 x 10^{-3} m Ø double thickness.

c)



d)

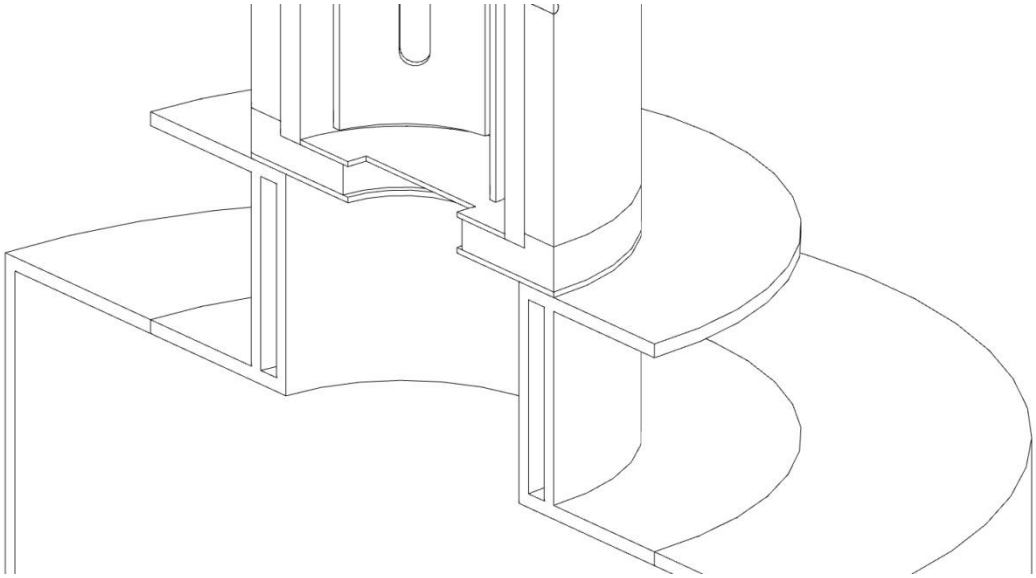


Figure 5-27: Illustration of baffle geometry variation used in the CFX calculations. a) 110 x 10^{-3} m Ø, b) 110 x 10^{-3} m by 30 x 10^{-3} m slotted baffle.

The heater geometry is entirely representative of the actual graphite heating element with the omission of conductive electrodes which pass through the outer and inner insulation and attach to the heater by the cylindrical cut outs at the top of the element; by the same omission, the relevant ports in insulation material were also not modelled.

In the CFX model the electrical energy is added to the system via a wall boundary condition on inner surfaces A and B shown in Figure 5-28.

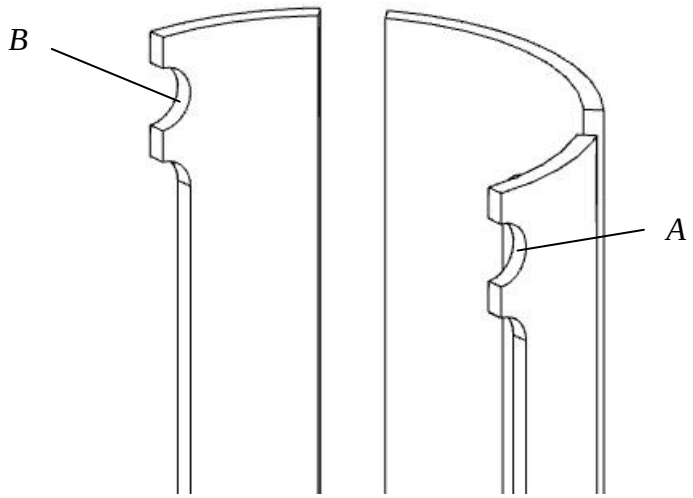


Figure 5-28: Half of the graphite heating element showing positions of electrical input.

5.6.1 Materials

Wherever possible material data has been obtained from supplier's proprietary data, however there were some instances where specific information was not known or there was some form of conjecture. In this case information was obtained from, or confirmed with, academic literature. A full list of component parts, associated materials and references can be found in Table 5-4. A comprehensive overview of all materials can be found in the Appendix.

Table 5-4: Furnace components, materials and material references as used in the CFX model.

Furnace Component	***Material***	***Material References***
Heating Element	*Graphite*	(Butland and Maddison, 1973, Tyler and Wilson, 1953, Powell and Schofield, 1939, 2007, Oakley, 2011)
Insulation Material	*Calcarb*	(Mersen, 2011, Mersen, 2009)
Baffle	*Sigraflex*	(SGL-GROUP, 2008)
Control Thermocouple	*Alsint*	(Multi-Lab, 2011, Electrochemical Society et al., 1967)
Spool, Chamber	*Stainless Steel*	This data is proprietary to the Rolls-Royce ProCAST model and has not been modified in any way

Materials with constant material properties i.e. independent of another variable such as temperature can be inputted into the CFX model in the standard manner one would expect providing the correct units are adhered to.

Temperature dependent material properties can be inputted into the CFX model in one of two ways; using some sort of mathematical approximation to represent the data i.e. a linear

or polynomial approximation or inputting tabulated data for the x, y data set. In all cases the preferred method of material data input was the tabulated data option.

To input tabulated data, firstly a ***function*** needs to be defined within CFX which references argument units (which in the case of a temperature dependent material property working in SI units would be K), results units (which would be the units of the property that is being defined) and interpolation data in x, y data pairs.

As an example, when defining the Graphite specific heat capacity within CFX the following data will be generated as shown from the .OUT file (output file) assuming we name the function Graphite CP;

```
FUNCTION: Graphite CP
      Argument Units = [K]
      Option = Interpolation
      Result Units = [J kg^-1 K^-1]
      INTERPOLATION DATA:
        Data Pairs = \
          293.15,669.8880,400,1004.8320,500,1193.2380,600,1360.7100,700,1486.3\
          140,800,1590.9840,900,1695.6540,1000,1758.4560,1100,1808.6976,1200,1\
          863.1260,1300,1904.9940,1400,1946.8620,1500,1976.1696,1600,1992.9168\
          ,1700,2009.6640,1800,2030.5980,1900,2051.5320,2000,2072.4660,2100,20\
          85.0264,2200,2093.4000
        Extend Max = On
        Extend Min = On
        Option = One Dimensional
      END
```

Following this step, the function is required to be referenced by a created ***expression*** which essentially links the temperature and temperature dependent values specified in the function to the current iterated local temperature value in the domain, of which the default expression in CFX is **T**.

```
Graphite Spec Heat = Graphite CP(T)
```

The name of the final expression can now be inputted into the material definition.

The current version of the CFX GUI only allows the input of isotropic materials data in

other words, by default, material data in the CFX GUI assumes uniformity in all three Cartesian coordinate directions.

Material data obtained from manufacturers' states that there is anisotropy is some materials, particularly the Sigraflex baffle material. In this instance, due to the layered nature of the graphite microstructure the thermal conductivity is approximately three times greater parallel to the layering direction rather than perpendicular.

In order to sufficiently represent this within the CFX model an alteration of the .def file (definition file) at code level is required before submitting the file to the solver.

When entering material data into the GUI, data is written in the following way, using Sigraflex as an example and can be extracted as a .CCL file.

```
LIBRARY:
  &replace MATERIAL: Sigraflex
    Material Group = User
    Option = Pure Substance
    Thermodynamic State = Solid
    PROPERTIES:
      Option = General Material
      EQUATION OF STATE:
        Density = 1020 [kg m^-3]
        Molar Mass = 1.0 [kg kmol^-1]
        Option = Value
      END
      SPECIFIC HEAT CAPACITY:
        Option = Value
        Specific Heat Capacity = Graphite Spec Heat
      END
      REFERENCE STATE:
        Option = Specified Point
        Reference Specific Enthalpy = 0 [J kg^-1]
        Reference Specific Entropy = 0 [J kg^-1 K^-1]
        Reference Temperature = 25 [C]
      END
      TABLE GENERATION:
        Maximum Temperature = 5000.0 [K]
        Minimum Temperature = 100 [K]
      END
      THERMAL CONDUCTIVITY:
        Option = Value
```

```
        Thermal Conductivity = Sig Thermal Cond
      END
    END
  END
END
```

Note that by default the thermal conductivity option is set to ‘value’.

This can be addressed by modifying the .CCL file for the material that is to be altered and will appear as follows;

```
LIBRARY:
  &replace MATERIAL: Sigraflex
    Material Group = User
    Option = Pure Substance
    Thermodynamic State = Solid
    PROPERTIES:
      Option = General Material
      EQUATION OF STATE:
        Density = 1020 [kg m^-3]
        Molar Mass = 1.0 [kg kmol^-1]
        Option = Value
      END
      SPECIFIC HEAT CAPACITY:
        Option = Value
        Specific Heat Capacity = Graphite Spec Heat
      END
      REFERENCE STATE:
        Option = Specified Point
        Reference Specific Enthalpy = 0 [J kg^-1]
        Reference Specific Entropy = 0 [J kg^-1 K^-1]
        Reference Temperature = 25 [C]
      END
      TABLE GENERATION:
        Maximum Temperature = 5000.0 [K]
        Minimum Temperature = 100 [K]
      END
      THERMAL CONDUCTIVITY:
        Option = Orthotropic Cartesian Components
        Thermal Conductivity X Component = Sig Thermal Cond XY
        Thermal Conductivity Y Component = Sig Thermal Cond XY
        Thermal Conductivity Z Component = Sig Thermal Cond Z
      END
    END
  END
END
```

The thermal conductivity option in the modified script can now be expressed in terms of x, y and z Cartesian components. Note that the thermal conductivity option in this script is specified as ‘Orthotropic Cartesian Components’. This modification requires that thermal conductivity expressions for values in the x,y and z directions is specified in the GUI.

The modified .CCL file which can be named ‘Overwrites’ for example, contains the expression ‘&replace’ before the material name, this is intended to permit the CFX solver to overwrite the previous material expression for Sigraflex with this later modified definition.

When submitting definition files to the solver a number of methods can be used, either directly using a single core solver, single node multi –core solver, or in parallel using multi-node multi-core solver.

For all simulations carried out here a parallel configuration was used using a job script as follows;

echo 'module load apps/ansys/v14.5;cfx5-bb-parallel -def MYJOB.def'|qsub -l 'walltime=01:00:00,nodes=4:ppn=4' -d$PWD

The code here states that the CFX version is v14.5, a parallel configuration is used to solve a job with the name ‘MYJOB’ for a run time of 1 hour using 4 nodes and 4 cores per node. In order to incorporate the material overwrites file the script is modified in the following way and anisotropic material properties will be used in the calculation;

echo 'module load apps/ansys/v14.5;cfx5-bb-parallel -def MYJOB.def -ccl Overwrites.ccl'|qsub -l 'walltime=01:00:00,nodes=4:ppn=4' -d$PWD

5.6.2 Meshing

Furnace model geometry was generated using Siemens Unigraphics NX6 solid modelling software and then exported as an Initial Graphics Exchange Specification (IGES) file, which is a neutral data format that allows data exchange between various software programs.

With the exception of the heating element, control thermocouple and the domain representing the vacuum, the other components of the furnace model are largely axisymmetric about the furnace Z-axis, in which case these components would lend themselves to being constructed from a swept mesh of wedge like hexahedral elements rotated about the Z-axis. However due to their complex geometry, the vacuum and heating element domain are best suited to tetrahedral elements.

This would lead to a problem, in the fact that the nodes of the hexahedral mesh elements of the insulation and tetrahedral mesh elements of the vacuum domain should ideally be matched at this interface. Experience has shown that performing an optimisation at this boundary in order to share matched nodes is laborious and often leads to degenerate elements. With this in mind, the use of automatic tetrahedral meshing was used for all domains in the geometry.

As discussed previously, in areas of interest and potentially high change in results, a fine mesh size was specified in conjunction with an appropriate mesh expansion factor. So for example, in the vacuum domain the mesh size is as small as 0.5×10^{-3} m and as large as 40×10^{-3} m without the sacrifice of mesh quality.

5.6.3 Boundary conditions

In order to represent the physics of a problem that is to be solved by FEA or CFD analysis, boundary conditions are often required to simplify the calculation and hence provide bounds in which the partial differential equations can be solved.

5.6.3.1 Symmetry planes

Due to the introduction of the control thermocouple domain and the complex nature of the heater geometry the furnace model does not possess rotational symmetry and the simplest form to which the model can be resolved is a representation containing one plane of symmetry. In this instance the symmetry boundary condition is applied on faces residing on the X,Z plane as shown in Figure 5-23.

5.6.3.2 Emissivity

At the interface between furnace components and the vacuum domain an emissivity value is specified; technically within CFX this value is placed on the vacuum side of the interface. Values obtained are taken directly from the ProCAST model and where deemed necessary justified by comparison with literature; the emissivity values used in the CFX model are in the range 0.4 to 0.95

5.6.3.3 Thermal contact resistances

Thermal contact resistance is numerically the inverse of heat transfer coefficient and this condition is applied to all solid-solid interfaces. The basis of this boundary condition is that there will invariably be voids between the two components in contact, in the case of a vacuum furnace the only heat transfer mechanism applicable at these sited is by radiation. A numerical value of 0.005 $W^{-1}.m^2.K$ has been obtained from the ProCAST model,

however similar values for this have also been calculated elsewhere (Konter et al., 2000).

5.6.3.4 Water cooled components

The spool of the Bridgman furnace contains a water cooled channel approximately 16×10^{3} by 133×10^{-3} m in which water is pumped during operation to assist heat extraction in the cold zone. Rather than a fixed temperature boundary condition, this feature is represented by a heat transfer coefficient of 1000 $W.m^{-2}.K^{-1}$ to a constant temperature, which has been shown through observation to be in the order of 298.15 K (25°C).

5.6.3.5 Boundary conditions on exterior surfaces of the model

In practise, exterior surfaces of the furnace components will lose heat by radiation to an ambient atmosphere. To account for this in the CFX model the following radiation heat transfer equation is applied as an expression on the exterior surfaces;

$$Q = \varepsilon \times \sigma(T_{Ref}^4 - T^4)$$

Where; ε is the emissivity, σ is the Stefan-Boltzmann constant, T_{Ref} is the specified ambient temperature and T is the current iterated temperature of the domain in question. A point of note is that in a purely analytical exercise the area of a surface, A, would need to be included into the equation, however as this is being applied to a domain surface the CFX model takes the area into account and is included in the radiation calculation.

5.6.4 Run Parameters

For a model such as this in which after initial radiation heat transfer is largely conduction dominant, time-steps can be relatively large; up to 2s. The same does not apply to the

calculation of electrical current density with associated Joule heating, and instances in which these time-steps are used can lead to exponentially high temperature values in the heating element and failure of the model. One option available in this case is to use adaptive time-steps in which small initial time-steps are specified and gradually increased to maintain stability of the calculation, however this does sacrifice the CPU time.

A more successful approach is to calculate the electrical current distribution first, with no thermal energy calculation, using the same mesh as the full model and then use the solution of this model as the initial values of the subsequent full model. This approach allows larger time steps to be used from the beginning of the calculation.

Convergence criteria used for all simulations specified a RMS (Root Mean Square) residual target of 1×10^{-5}, in which the solver will terminate when the equation residuals calculated are below the residual target. A conservation target of 0.01 (1%) is also specified to ensure global imbalances are met as the calculation approaches thermodynamic equilibrium.

5.6.5 CFX model 20×10^{-3} m ID baffle

Two CFX models were run using a 20×10^{-3} m baffle; the first with a set hot zone temperature of 1823.15 K, which is a typical temperature when investment casting, the second with a set hot zone temperature of 1923.15 K which will be used experimentally for high gradient casting experiments.

Figure 5-29 shows the furnace with a set temperature of 1823.15 K with contour plots showing the heating element surface temperature and control thermocouple surface temperature. The magnitude of error between the control thermocouple temperature in the

CFX models and that measured experimentally is less than 0.13%, however it should be noted that Type B control thermocouples used in the furnace can fluctuate by up to 6% so this comparison is somewhat qualitative.

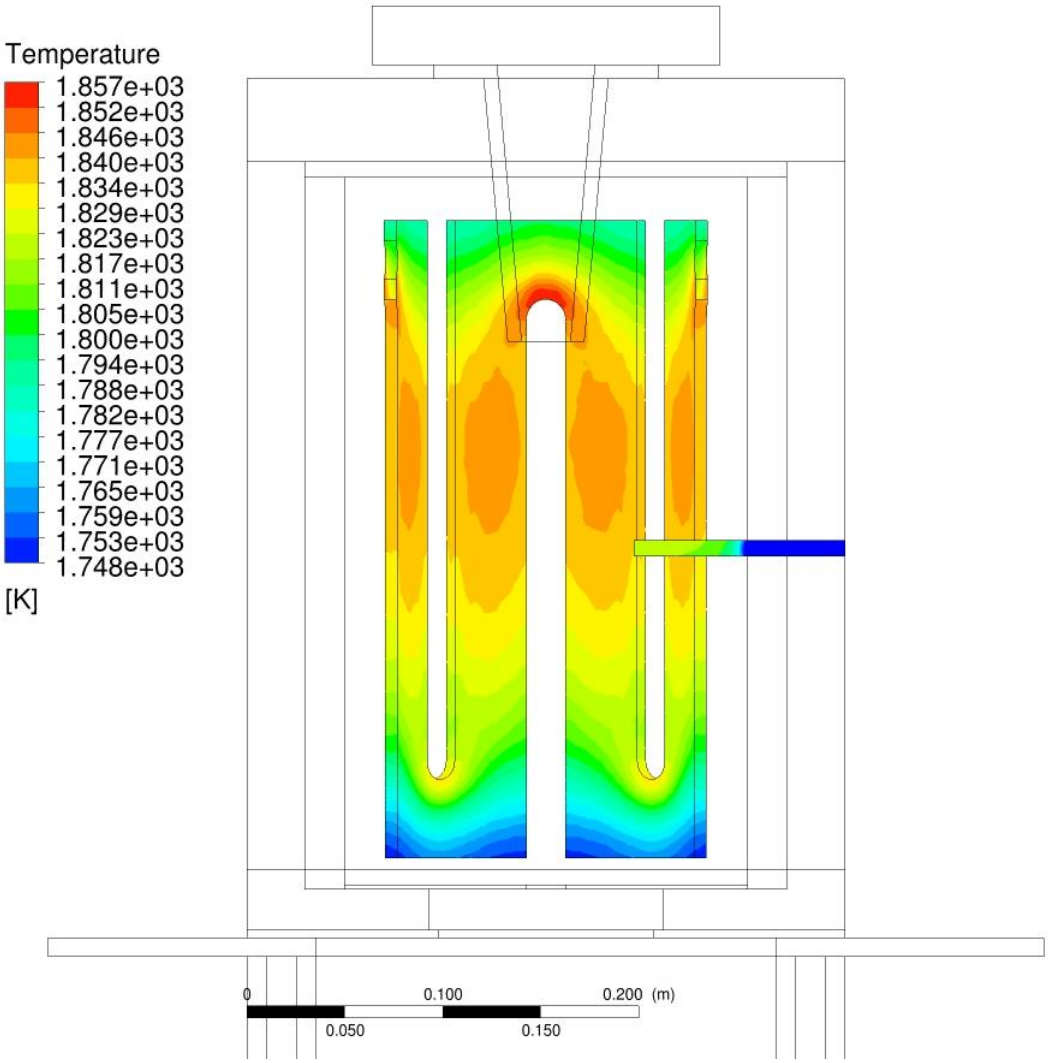


Figure 5-29: CFX model of Bridgman furnace incorporating single layer radiation baffle with 20 x 10^{-3} m diameter cut-out heated to a set hot zone temperature of 1823.15 K. Contour plots show heating element surface temperature and control thermocouple surface temperature.

Shown in Figure 5-30 is a contour plot of the electrical current density in the heating element for applied power corresponding to a set temperature of 1823.15 K, the uniform area of current density along with areas of high and low current can clearly be seen.

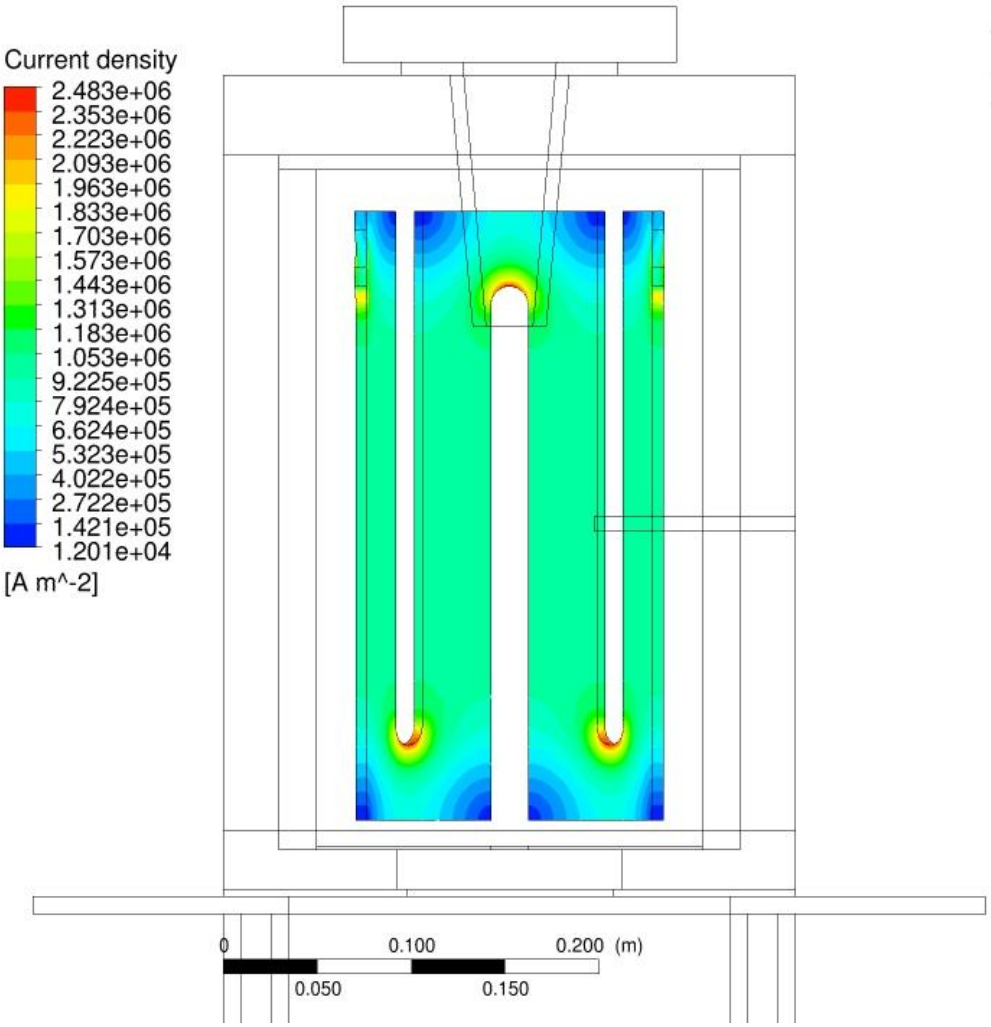


Figure 5-30: CFX model of Bridgman furnace incorporating single layer radiation baffle with 20 x 10^{-3} m diameter cut-out heated to a set hot zone temperature of 1823.15 K. Contour plots show electrical current density with an applied current of 482 A.

Here it may be useful to make another comparison of the electrical current density with the theoretical solution by referring back to equation 5.3. For a radius of 10×10^{-3} m the electrical current density is calculated to be in the order of 2.24 times greater than the uniform. Figure 5-31 shows an enhanced view of the current density contour; it can be seen that the uniform current density lies on the contour with values between 1.001×10^{6} and 1.165×10^{6} Am^{-2} with a value of 1.083×10^{6} Am^{-2}.

Using the analytical solution described previously this would result in a maximum current density of 2.426×10^{6} Am^{-2}, the actual value in the contour plot shown to be 2.483×10^{6} Am^{-2}. The error is not concerning as it is necessary for some compromise to be made with regard to mesh element size as discussed previously.

One point to note when comparing the two figures is that the areas of high current density at the base of the heating element, nearer the cold zone, do not translate to temperature hot spots. This is predominantly due to the fact that the base of the heating element is losing heat to the baffle region separating the hot and cold zones and excess heat generated in this area will be lost by a combination of radiation to the baffle and conduction to cooler parts of the element.

A graphical representation of the heater temperature and current density for a set temperature of 1923.15 K for this furnace configuration are shown in Figure 5-32

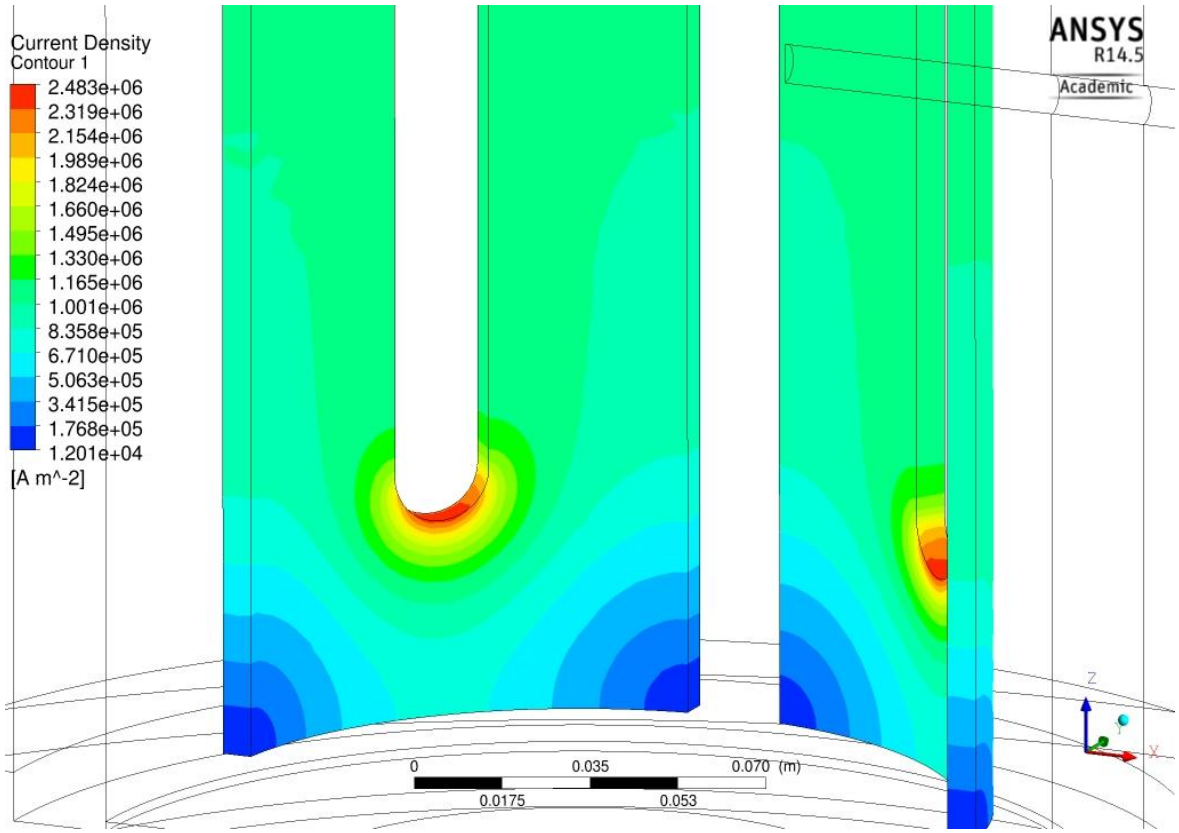
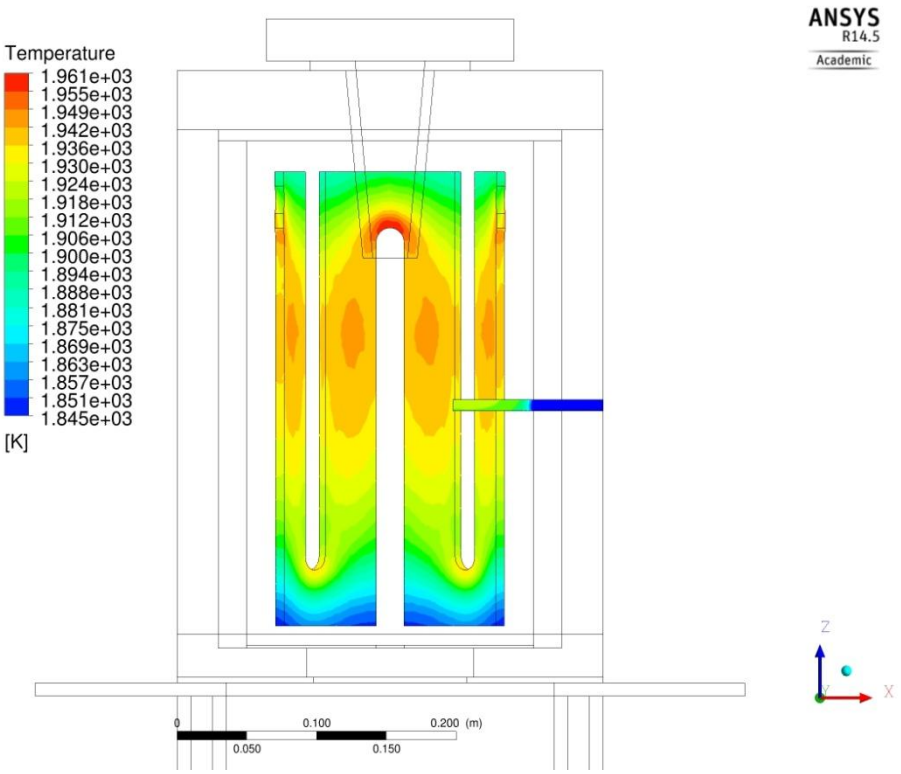
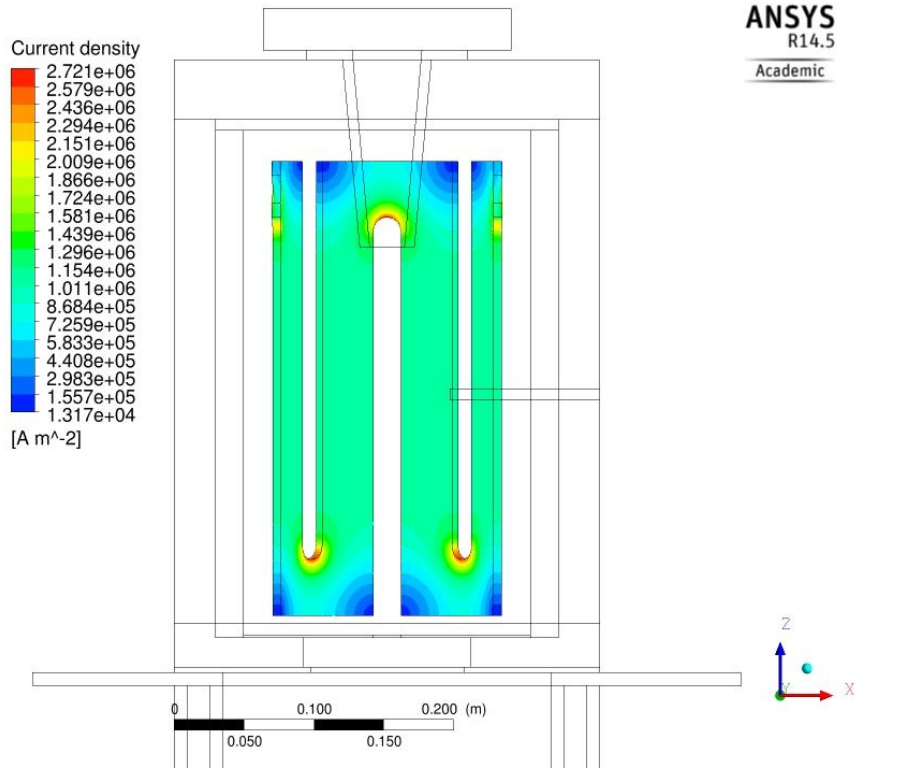


Figure 5-31: Electrical current density contours on heating element with a potential difference of 14.6V.

.



a)



b)

Figure 5-32: CFX model of Bridgman furnace incorporating single layer radiation baffle with 20 x 10^{-3} m diameter cut-out heated to a set hot zone temperature of 1923.15 K. Contour plots show a) Heating element surface temperature and control thermocouple surface temperature b) Electrical current density with an applied current of 528 A.

5.6.6 CFX model 110 x 10^{-3} m ID baffle

A CFX model of the furnace using a 110 x 10^{-3} m ID baffle with a set hot zone temperature of 1823.15 K has been calculated using experimentally determined electrical data and is shown in Figure 5-33.

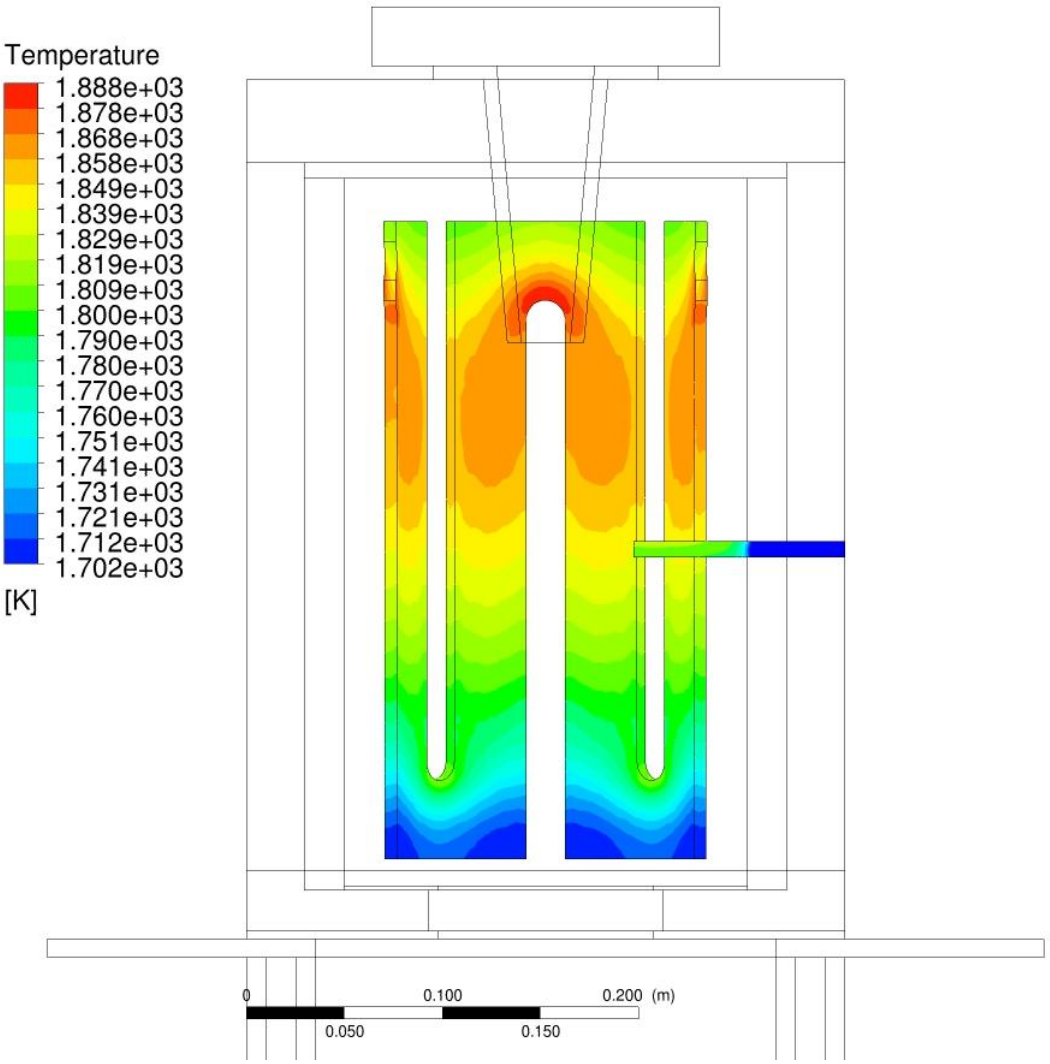


Figure 5-33: CFX model of Bridgman furnace incorporating single layer radiation baffle with 110 x 10^{-3} m diameter cut-out heated to a set hot zone temperature of 1823.15 K. Contour plots show heating element surface temperature and control thermocouple surface temperature.

Here we can make some comparisons of the three calculations carried out thus far; of the two calculations comprising the 20 x 10^{-3} m diameter baffle, the heater temperature varied in both cases by around +1.8% and -4.2% when compared with the control thermocouple temperature and can clearly be seen in Figure 5-29 and Figure 5-32 as a hot zone at the top apex of the heating element and a cooler zone towards the base.

As may be expected, the magnitude of temperature difference is greater in the calculation with a 110 x 10^{-3} m diameter baffle as more radiation is lost to the cold zone. In this case the magnitude of temperature difference is around +3.4% and -7.1%.

5.6.7 Discrete transfer model ray comparison

The radiation model used in all calculations is the Discrete Transfer model and was chosen for a number of reasons; predominantly the efficiency of computer run time.

A significant option available to the user is the number of rays used during the calculation, the CFX default being 8 and the maximum being 32, and increasing the number of rays will increase the complexity of the calculation.

In order to assess the magnitude of difference introduced when changing this variable, two calculations were carried out with a set hot zone temperature of 1823.15 K using the model comprising a 110 x 10^{-3} m diameter baffle i.e. a configuration in which it is expected the most radiation heat transfer will occur into the cold zone; both models had the same energy input into the heating element however one calculated radiation heat transfer using 12 rays and the other 32 rays.

Figure 5-34 shows the heat flux transferred onto the surface of the cold zone chamber for both calculations and a variation between the two models can clearly be seen.

Figure 5-34 a) shows 'hot spots' of higher density heat flux on the bottom surface off the cold zone which is likely due to the fact that there are fewer rays emanating from the hot zone whereas Figure 5-34 b) shows a more homogenous heat flux. However, when calculating the area average heat flux on the inner surface of the cold zone the total heat flux is reasonably similar, with a 12 ray model resulting in a net heat transfer of 233.37 W m^{-2} and a 32 ray model resulting in a net heat transfer of 230.37 W m^{-2}. In both case the control thermocouple temperature deviated by less than 0.5% with the 32 ray model predicting a temperature 8 K hotter.

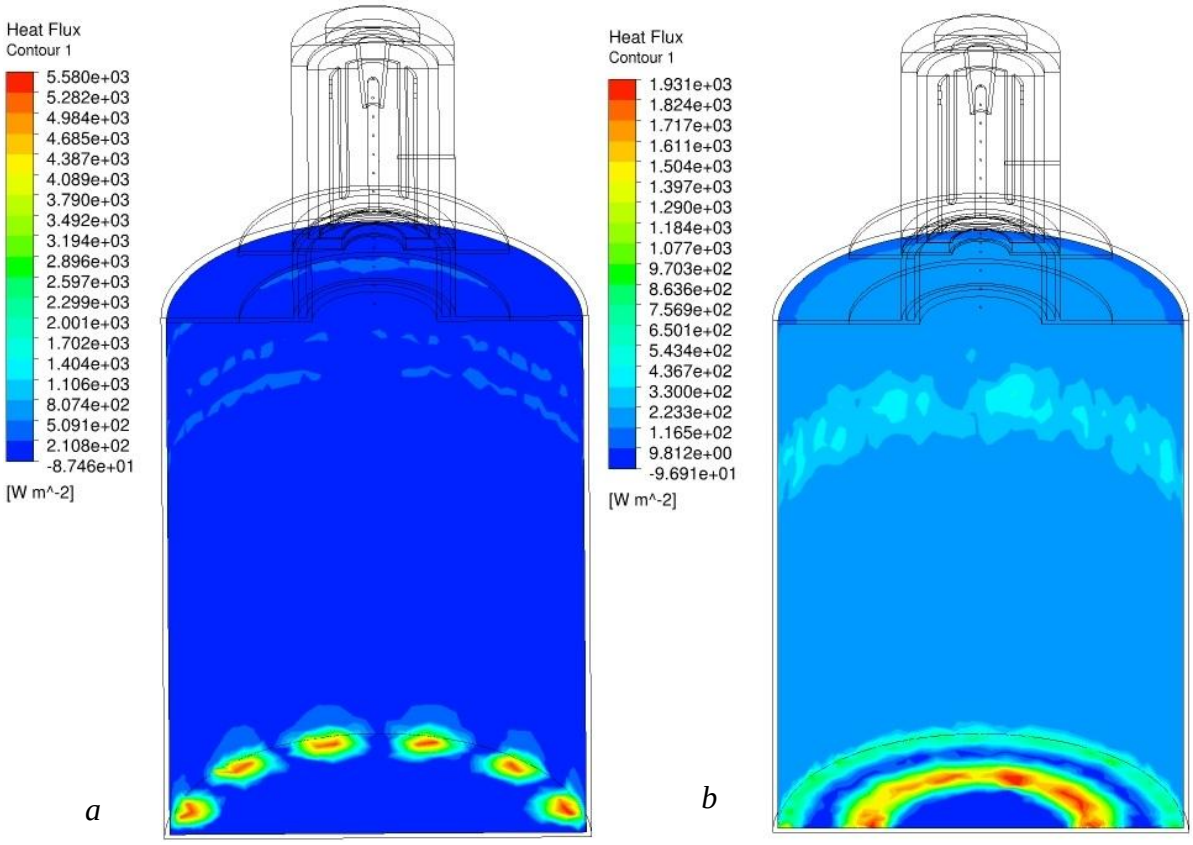


Figure 5-34: Discrete transfer radiation heat transfer results for; a) 12 rays, net heat transfer 233.37 W m^{-2}, b) 32 rays, net heat transfer 230.37 W m^{-2}.

Even though the variation in heat flux on the inner surface of the cold zone is not ideal, this is an area of less interest; the important factor is that the net heat transfer from the hot zone is virtually the same in both cases.

The most important consideration in these cases is the computer calculation time and ideally the most adequate solution should be obtained with the most efficient use of computer resources. In both cases simulations were carried out in parallel on 16 cores (64-bit 2.6 GHz AMD Opteron 2218) processors, with the total calculation time for the 12 ray model being 12 hrs 35 m and for the 32 ray model 49 hrs 44 m.

5.7 Validation of CFX models using furnace centreline temperature

For validation purposes the results of the CFX models can be compared with the furnace centreline temperature recorded with a type B thermocouple as discussed in the experimental methods section. A slow withdrawal rate was used with the aim of allowing the measuring thermocouple to reach thermodynamic equilibrium in each subsequent position along the furnace Z axis; however the mean thermocouple measurements fell below that of the set hot zone temperature in some instances.

Although the maximum error was only in the region of 0.7-0.8% in comparison to the control thermocouple, this is attributed to the slow movement.

The CFX model comprised discrete points represented by spheres of alumina material which were then matched to the corresponding experimental thermocouple position given that the withdrawal rate and starting position and time were known.

Figure 5-35 shows the experimental and CFX model temperature data obtained for a hot zone temperature of 1823.15 K with a radiation baffle comprising a 110 x 10^{-3} m aperture. The comparison of experimental and CFX temperature data for a model comprising the 20 x 10^{-3} m aperture in the baffle is shown in Figure 5-36 for a set hot zone temperature of 1823.15 K and Figure 5-37 for a hot zone temperature of 1923.15 K.

All models show good agreement with experimentation with some error at the beginning of the experiment, between 0s -1000s and later error beyond 6000 s as the thermocouple is in the cold zone.

Error in all models between 0s and 1000s occurred when the measuring thermocouple resides in the pouring cone, therefore this acts as a radiation baffle between the measuring thermocouple and the heating element and accounts for the lower temperatures in this region. Even though the pouring cone is included in the CFX models, the material is highly unstable and degrades during experimental runs. Every care was taken to replace this component periodically, however the degradation would account for some scatter in results.

For the model comprising the 110 x 10^{-3} m baffle there is some variation in temperature, particularly around the baffle region at the transition between the hot and cold zone when compared to experimental data, which could be attributed to inaccuracies in the emissivity values for the baffle material which was obtained from suppliers and not measured directly.

An observed occurrence is the deposit of a soot like layer due to slow sublimation of the heating element, which in conjunction with degradation of the baffle material, may act to alter the surface appearance in the baffle region and dynamically change the emissivity.

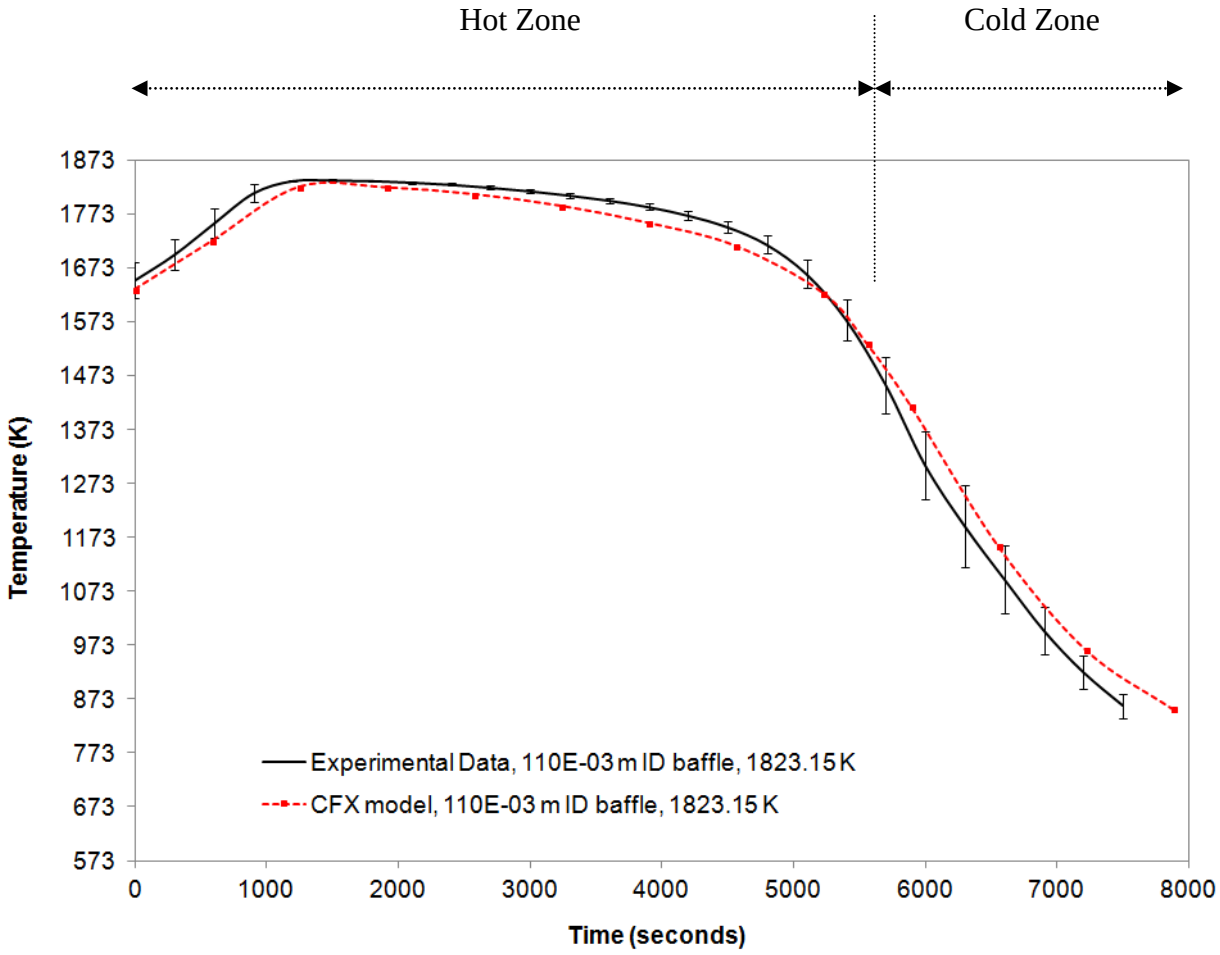


Figure 5-35: Experimental thermocouple temperature data and modelled temperature data of temperature along Z-axis of furnace for a hot zone temperature of 1823.15 K with a 110 x 10^{-3} m diameter baffle. (Graph shows approximate position of furnace hot zone, baffle location and cold zone for clarity).

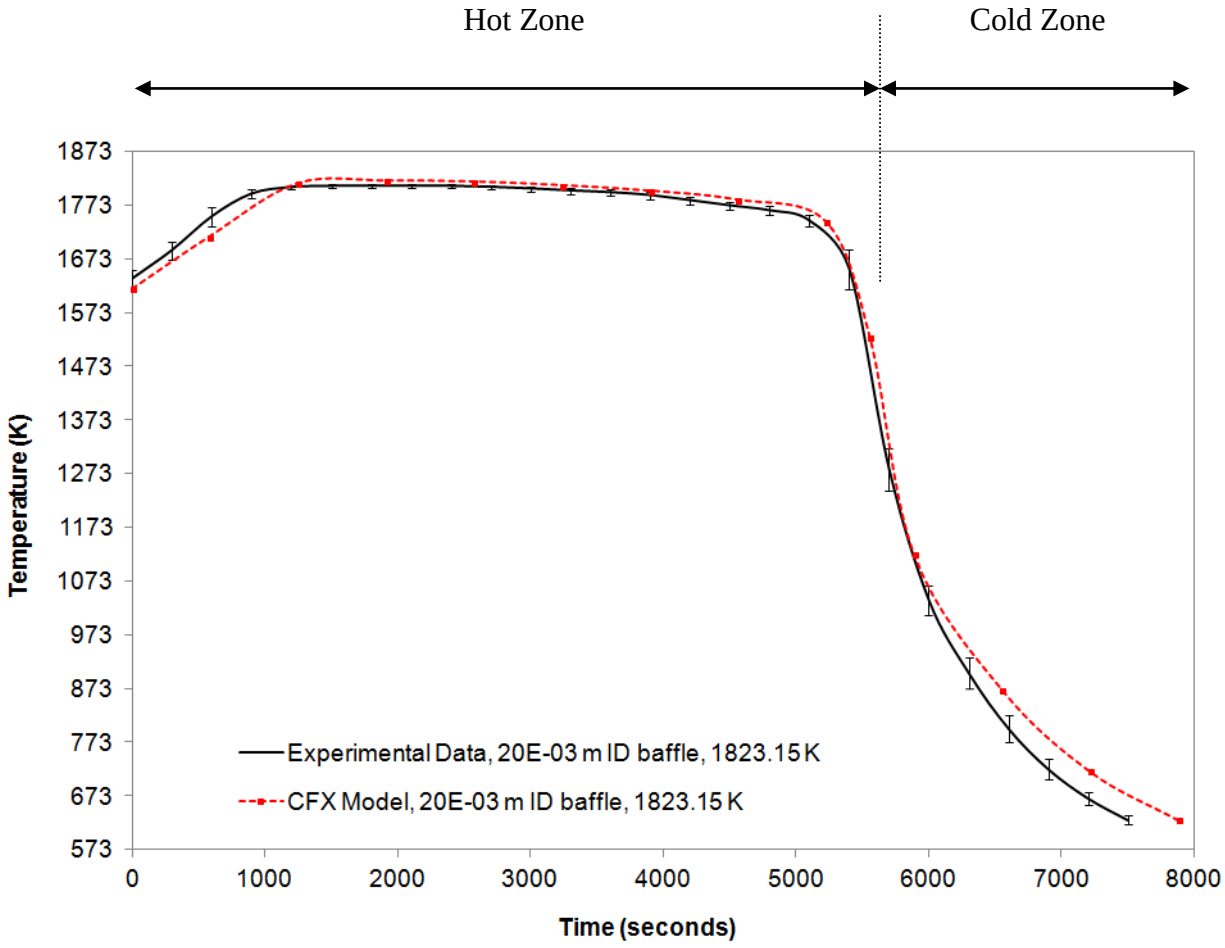


Figure 5-36: Experimental thermocouple temperature data and modelled temperature data of temperature along Z-axis of furnace for a hot zone temperature of 1823.15 K with a 20 x 10^{-3} m diameter baffle. (Graph shows approximate position of furnace hot zone, baffle location and cold zone for clarity).

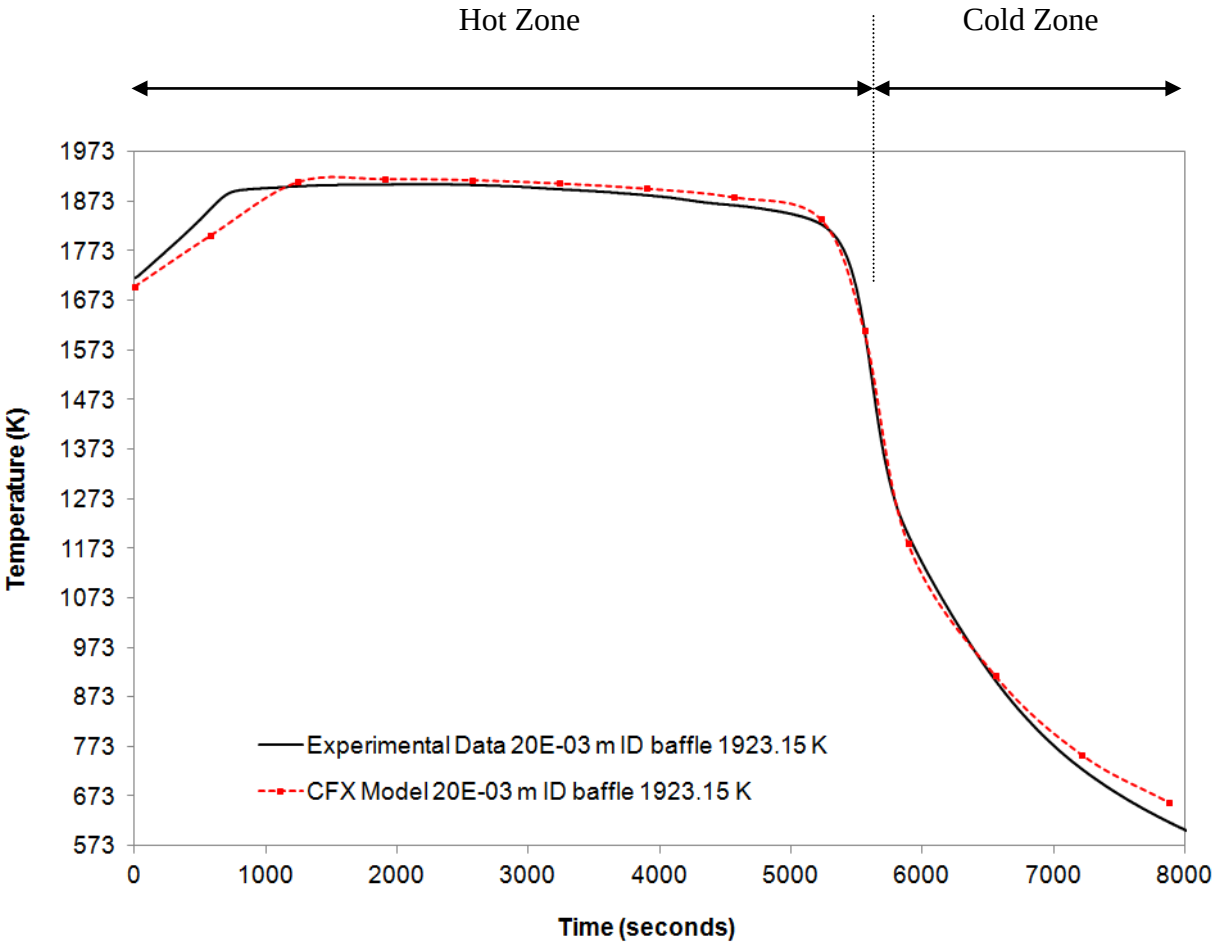


Figure 5-37: Experimental thermocouple temperature data and modelled temperature data of temperature along Z-axis of furnace for a hot zone temperature of 1923.15 K with a 20 x 10^{-3} m diameter baffle. (Graph shows approximate position of furnace hot zone, baffle location and cold zone for clarity).

5.7.1 Comparison with thermal data for 110 x 10^{-3} m by 30 x 10^{-3} m slotted baffle, 1843.15 K

During the validation of the ProCAST furnace model a series of thermocouple experiments were carried out by (Newell, 2009) in order to characterise the furnace thermal profile under different baffle and temperature conditions; one of these experiments incorporated a slotted radiation baffle and a hot zone temperature of 1843.15 K.

Figure 5-38 shows a comparison of results from a CFX calculation with that measured by (Newell, 2009). The original experiment was only concerned with the temperature gradient through the cooling zone therefore approximately only half of the heating element was recorded by thermocouple measurement.

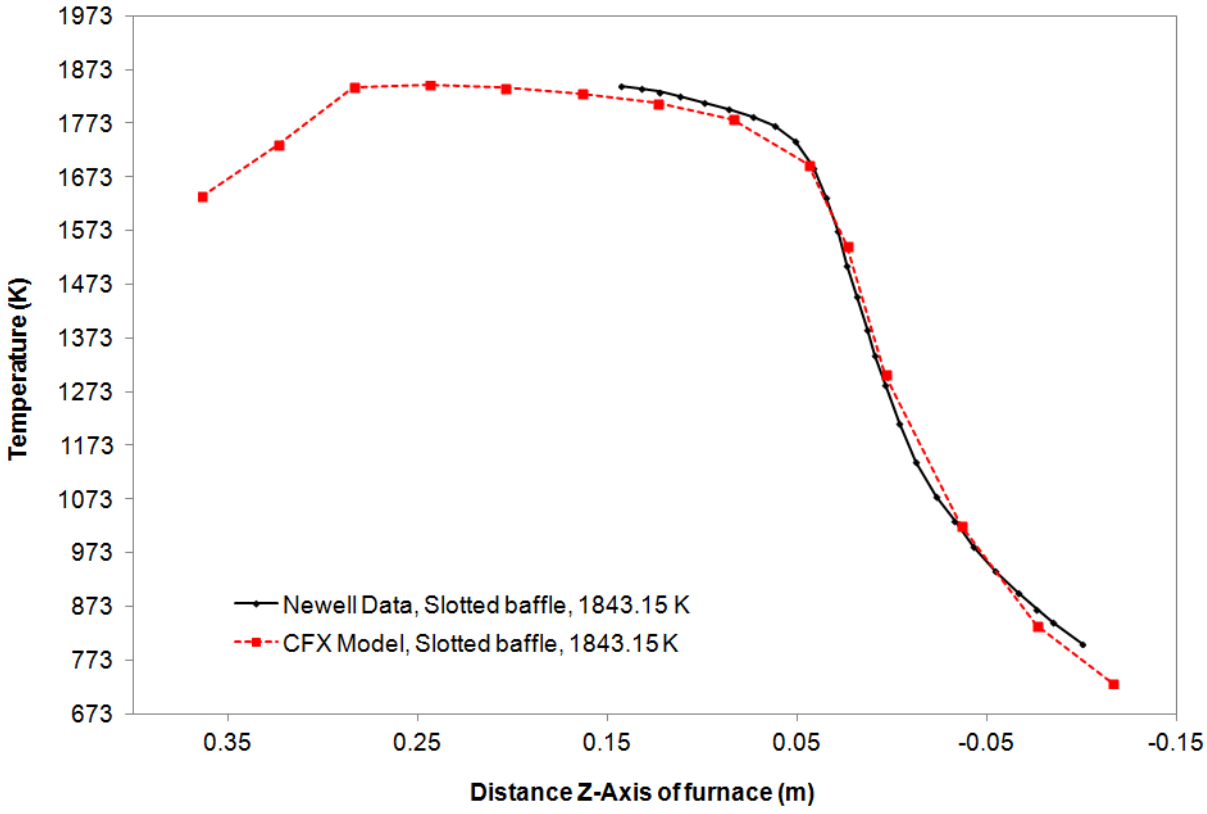


Figure 5-38: Furnace centreline thermocouple data measured by (Newell, 2009) for a hot zone temperature of 1843.15 K with a slotted radiation baffle compared with results from a CFX model.

5.7.2 Comparison with thermal data for 110 x 10^{-3} m diameter baffle 1803.15 K

Another experiment previously carried out to characterise the furnace centreline temperature incorporated a 110 x 10^{-3}m baffle with a hot zone temperature of 1803.15 K; a comparison of the experimental results from (Newell, 2009) with CFX model results are shown in Figure 5-39.

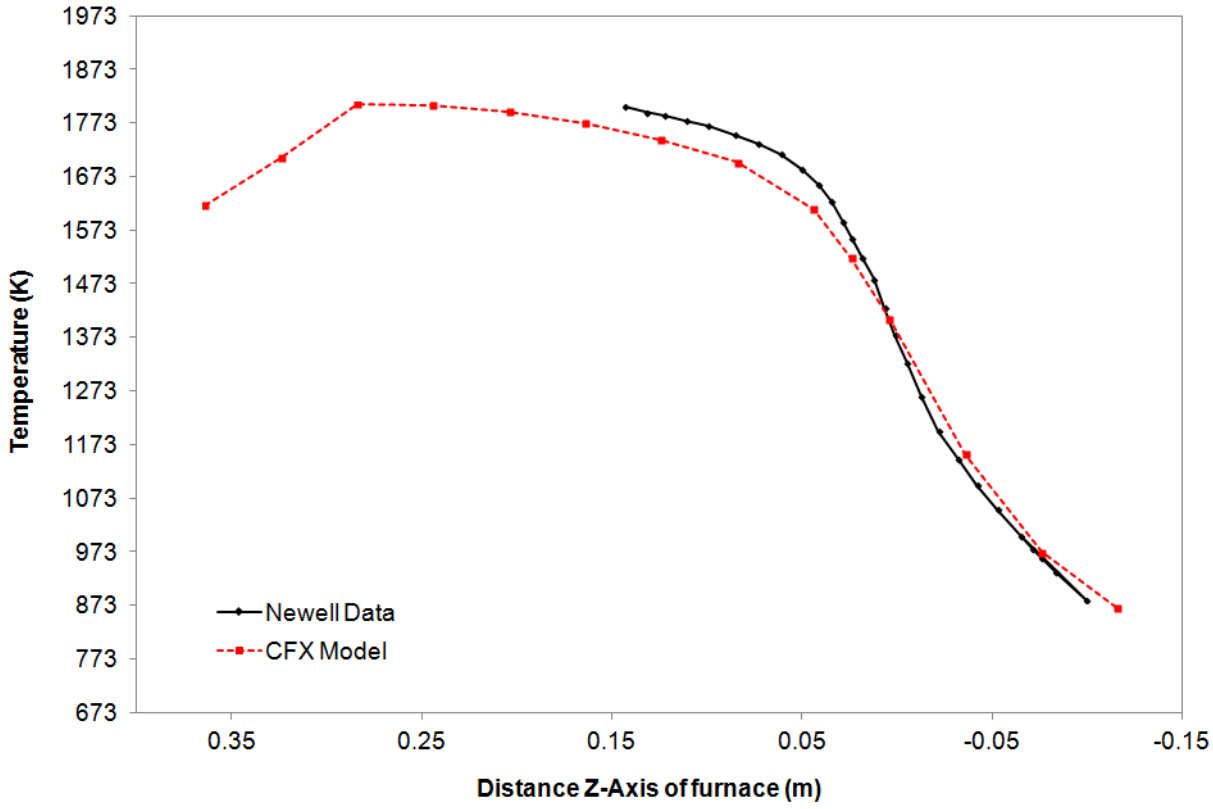


Figure 5-39: Furnace centreline thermocouple data for a hot zone temperature of 1803.15 K with a 110 x 10^{-3} m diameter baffle compared with CFX model results. Experimental data obtained from (Newell, 2009).

5.8 Comparison of CFX thermal profiles with ProCAST model validated using instrumented mould

As discussed in a previous section, the ProCAST model was validated using an instrumented mould and compared against model calculations. The ProCAST model originally used a cylindrical domain to represent the heating element with a uniform constant temperature boundary condition.

The subsequent experimentation led to the optimisation of the model and the modification of the constant temperature boundary condition; as it was discovered that lowering the applied temperature of the bottom 4/10ths of the heating element domain and raising the temperature of the upper 6/10ths provided a closer match to the experimentally obtained data.

The work by (Newell, 2009) essentially led to two conditions at which the furnace model was validated; a hot zone temperature of 1843.15 K, of which the upper part was set to 1873.15 K and the lower part 1783.15 K, comprising a 110 x 10^{-3} by 30 x 10^{-3} m slotted baffle and a model with a hot zone temperature of 1803.15 K of which the upper part was set to 1843.15 K and lower part 1753.15 K with a 110 x 10^{-3} m diameter baffle.

A comparison between centreline thermocouple measurements and CFX models results have already been compared in Figure 5-38 and Figure 5-39. The model comprising a 110 x 10^{-3} m diameter baffle at a set temperature of 1803.15 K showed good agreement with in-situ thermocouple measurements at 7 sites within a VeriCAST2 mould, and calculated temperature gradients differed from experimental measurements by around 0.98 x 10^{3} K.m^{-1}. An example of one thermocouple measurement from work by (Newell,

2009) is shown in Figure 5-40.

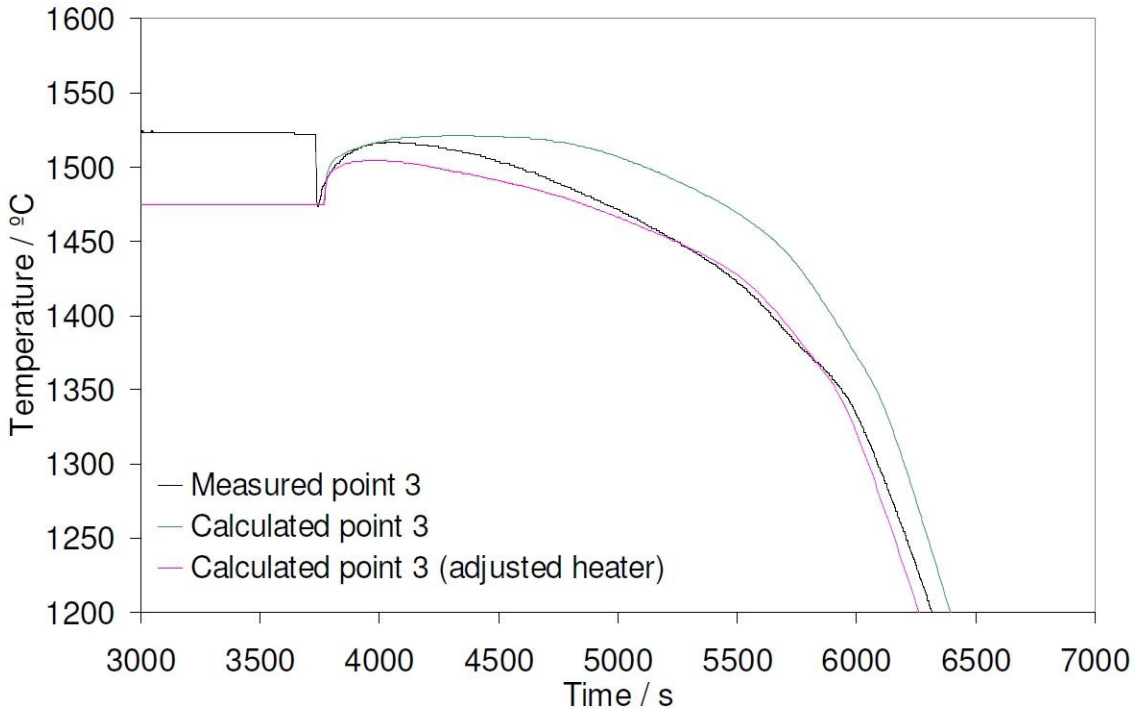


Figure 5-40: Transient thermocouple temperature data for point 3 in VeriCAST2 validation mould. Data obtained from (Newell, 2009).

In order to make a comparison between the ProCAST and CFX models, the temperature distribution of the CFX models for this furnace configuration was calculated in a similar way by taking an area average temperature of an upper and lower portion of the heating element. Figure 5-41 shows a comparison of the ProCAST temperature split and that calculated using the CFX model and both show good agreement with one another; the maximum error between the two approximations being ~0.7%.

Also shown is a temperature contour of the heating element in which blue areas are those in which the temperature falls below that of the control thermocouple temperature, this also highlights the agreement between the CFX model and the ProCAST approximation for this furnace configuration.

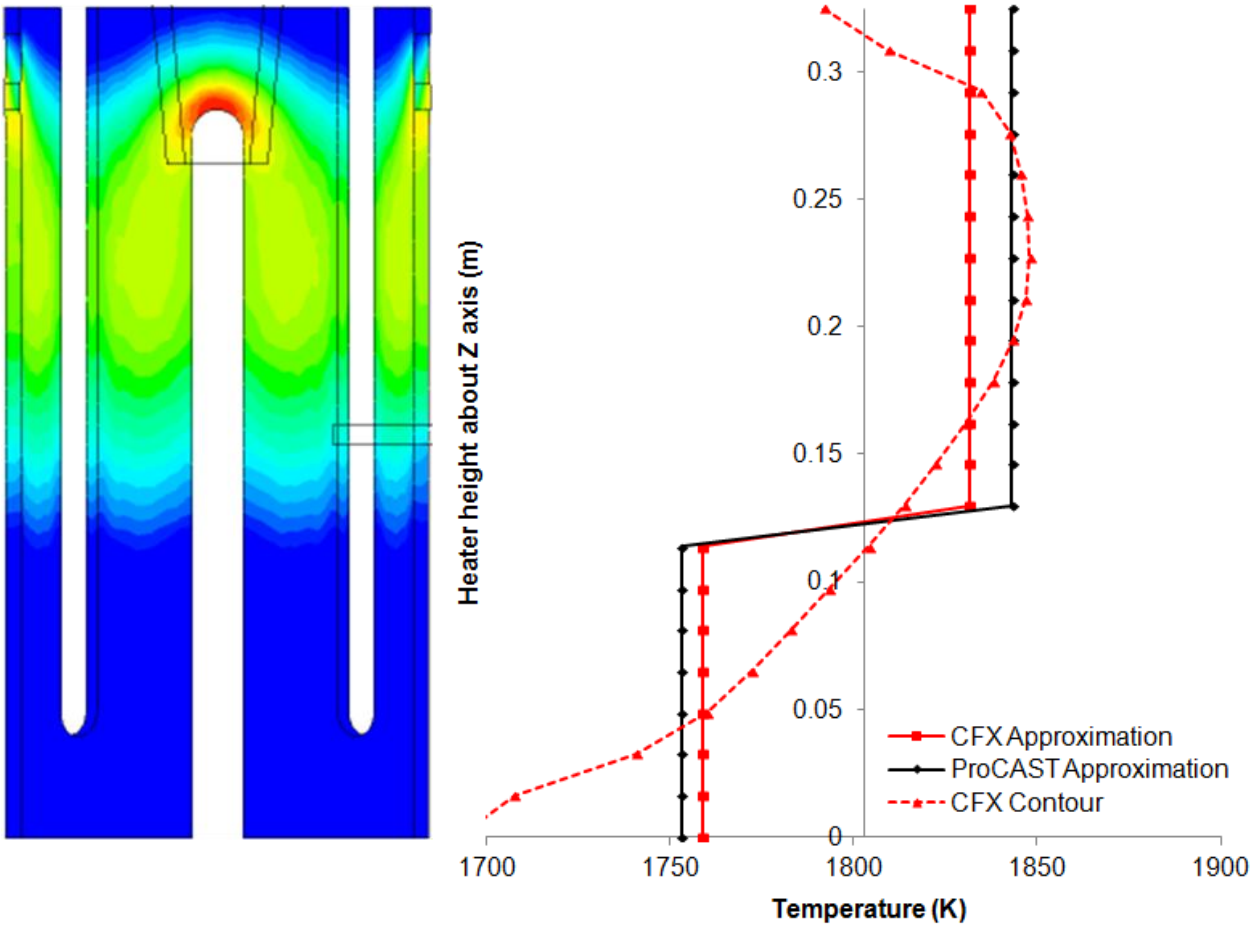


Figure 5-41: Comparison of ProCAST split heater temperature with calculated split heater temperature using CFX. Furnace comprises 110 x 10^{-3} m diameter baffle with set hot zone temperature of 1803.15 K. Full temperature contour of heater surface temperature calculated using CFX is also plotted for reference. Temperature contour of heating element highlights blue areas in which the heater temperature falls below that of the control thermocouple temperature, highlighting the similarity between the ProCAST and CFX models.

The model comprising a 110 x 10^{-3} by 30 x 10^{-3} m slotted baffle with a hot zone temperature of 1843.15 K was also validated, in which the upper part of the heater was set to 1873.15 K and the lower part 1783.15 K for the ProCAST model using the same methodology as for the previous model.

The geometry in which measurement thermocouples were placed consisted of a single tube 12 x 10^{-3} m in diameter with thermocouple placed 40 x 10^{-3} m apart so their starting position during the experiment was in the lower portion of the heating element; around 0.025 m in Figure 5-42.

When comparing these experimental results with the ProCAST simulation a much larger degree of error was encountered, with the largest error in measured and predicted temperature gradient in the order of 1.74 x 10^{3} K.m^{-1}.

An error of this magnitude may not pose significant problems when casting conventional single crystal alloys, however if the aim of a simulation was to predict the achievable growth rate when casting eutectic alloys, an error of this magnitude would prove detrimental to the accuracy of the simulation.

A comparison of the results obtained from the CFX model and the ProCAST approximation is shown in Figure 5-42 with the ProCAST temperature split being 1783.15 K for the lower section and 1873.15 K for the upper, compared to 1819.57 K and 1861.55 K from the CFX calculation. It can be seen that there is a much larger degree of variation between the ProCAST calculation and that of the CFX model, with the ProCAST approximation is in the order of 36 K cooler in the bottom section of the heating element. It is also apparent that position and magnitude of the cooler area is lower than for the 110 x 10^{-3} m baffle; this would be expected as less heat is being lost to the cold zone.

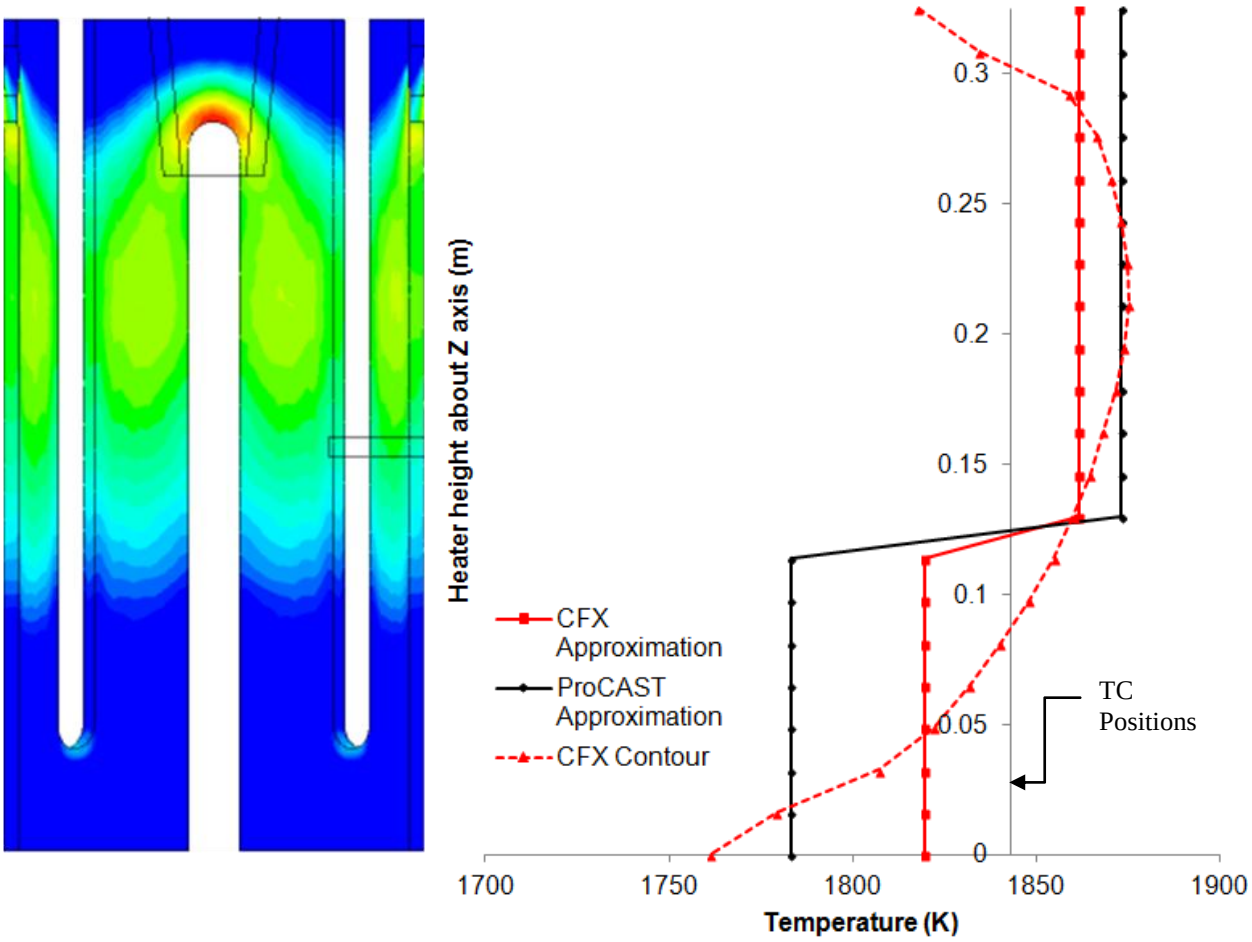


Figure 5-42: Comparison of ProCAST split heater temperature with calculated split heater temperature using CFX. Furnace comprises 110 x 10-3 m by 30 x 10-3 m slotted baffle with set hot zone temperature of 1843.15 K. Full temperature contour of heater surface temperature calculated using CFX shown for comparison.

A modified split heater temperature can therefore be calculated from the CFX model by reducing the area of the lower portion; this yields temperatures of 1810.19 K and 1860.39 K for the lower and upper portions respectively and is shown in Figure 5-43.

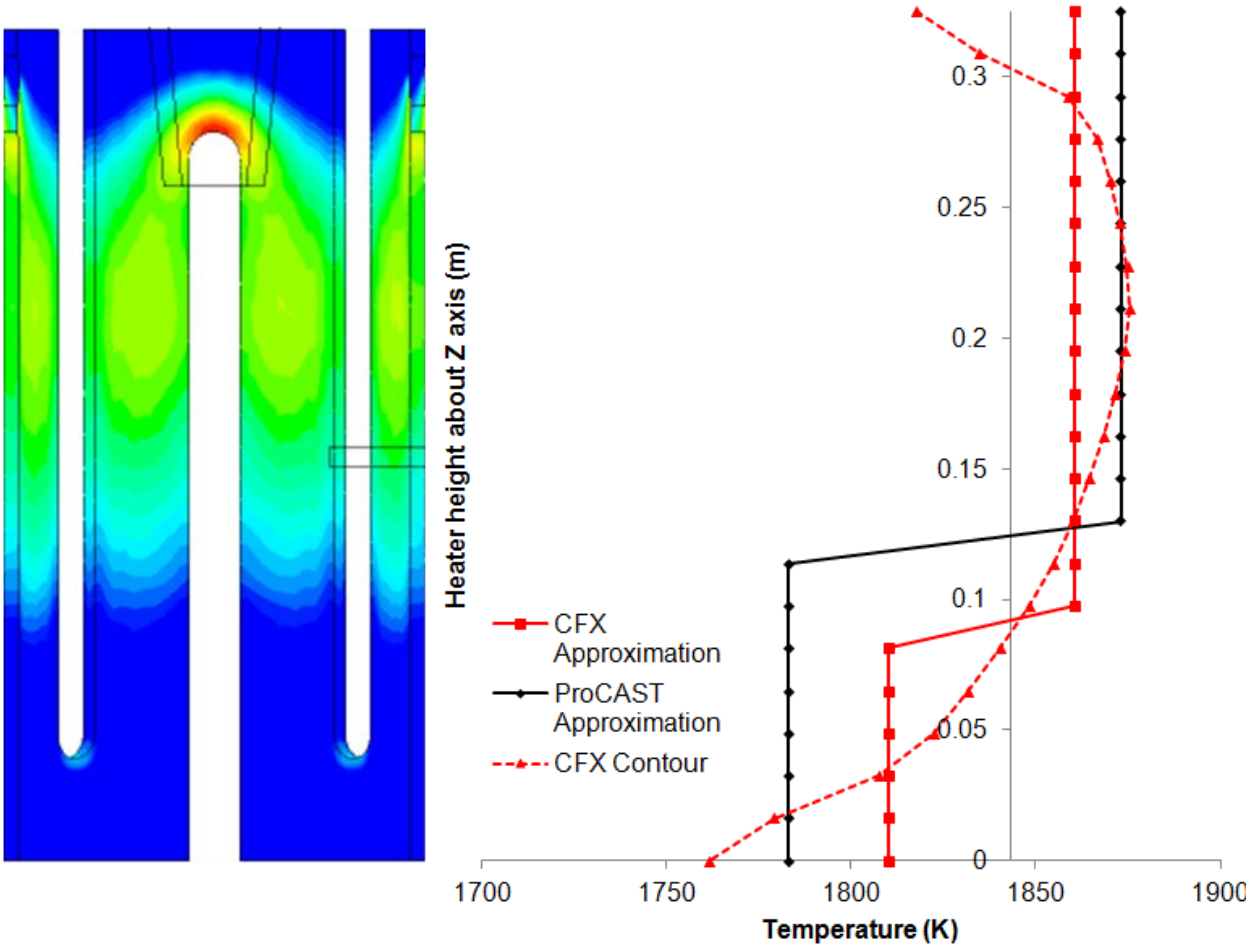


Figure 5-43: Comparison of ProCAST split heater temperature with modified CFX split heater temperature.

This difference is clearly shown in Figure 5-44 and Figure 5-45 where for point 8 the CFX determined temperature matches more closely with the measured data. Point 9 also shows good agreement however this point is closer to the chill and the determined temperatures will inevitably be lower than the heater set temperature due to conduction heat loss.

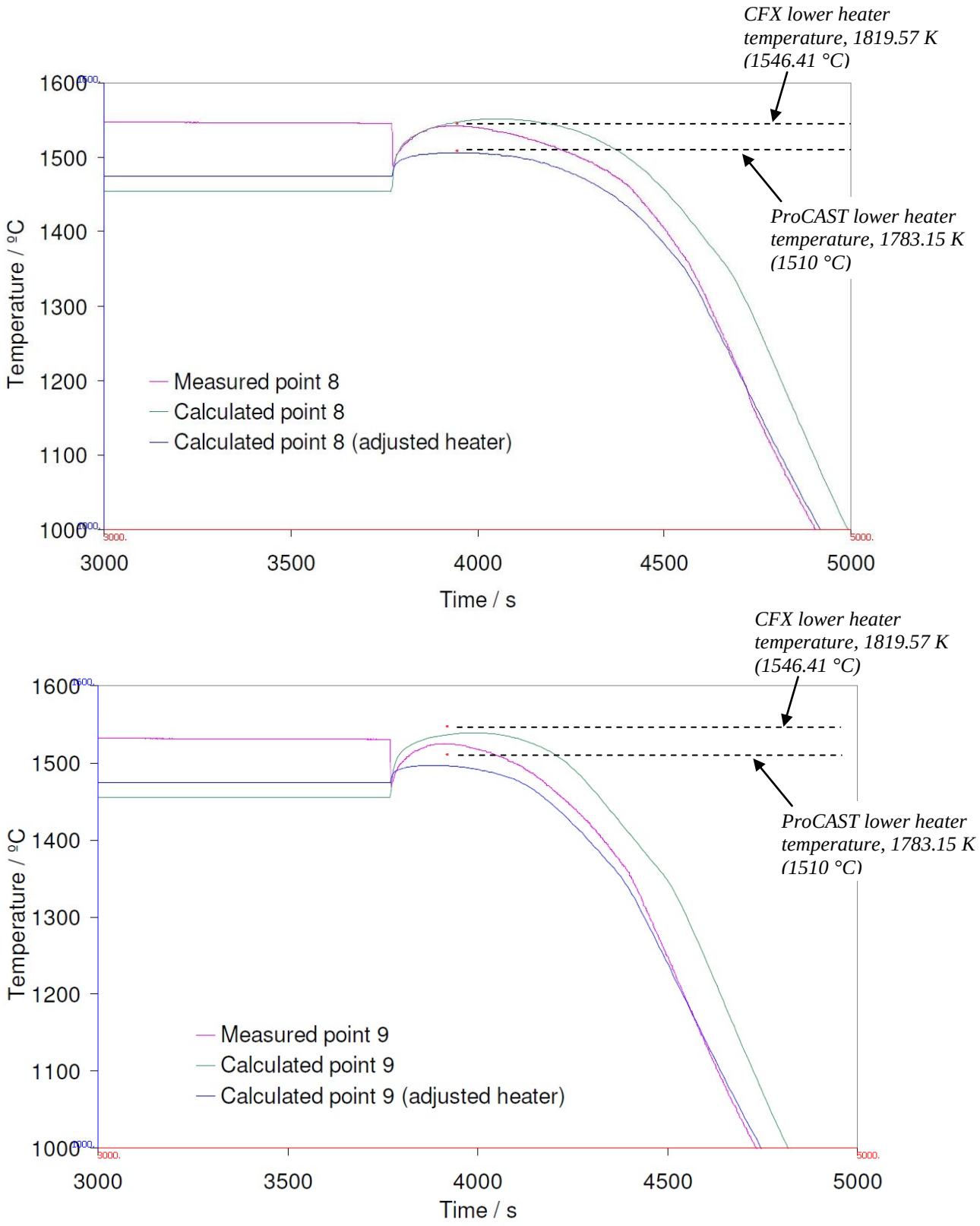


Figure 5-44: Two experimentally determined temperature readings taken using a furnace with a set temperature of 1843.15 K with a 110 x 10^{-3} by 30 x 10^{-3} slotted baffle. Figures show measured temperature data, that calculated using a constant temperature ProCAST model and that with a split heater model. For comparison, calculated lower heater temperature data from ProCAST and CFX models are shown. Experimental data obtained from (Newell, 2009).

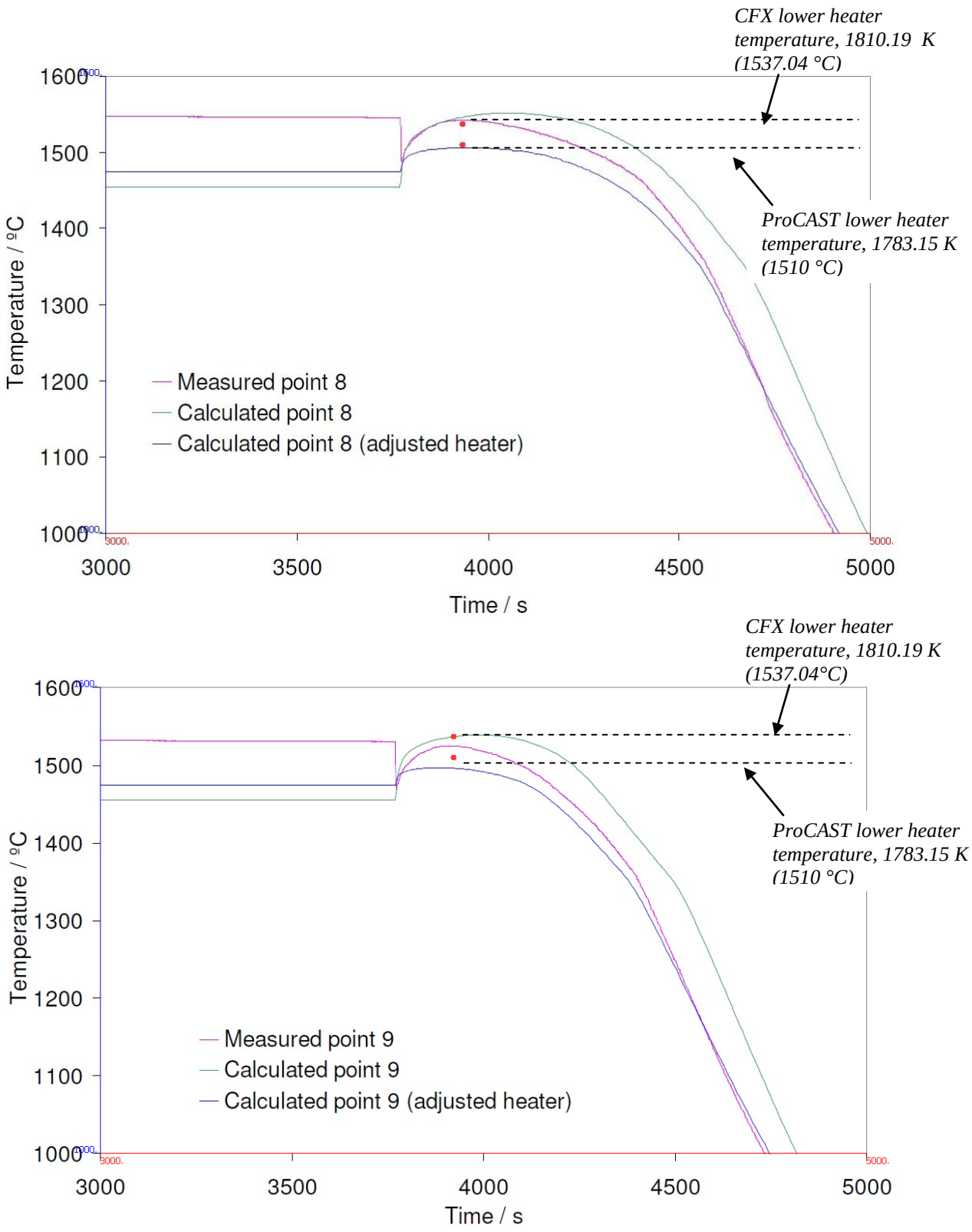


Figure 5-45: Experimentally determined thermocouple data with ProCAST lower heater temperature and revised CFX lower heater temperature shown. Experimental data obtained from (Newell, 2009).

5.9 Preliminary Conclusions

A CFX model of the Bridgman furnace has been developed in order to make predictions of the hot zone temperature distributions for any number of furnace configurations by calculating the heat generated via the corresponding electrical current density at the same time taking into account radiation heat transfer from the heating element to the furnace cold zone.

The furnace model has been validated for three separate configurations, comprising two furnace temperatures and two radiation baffles, by the use of a moving thermocouple recording the furnace centreline temperature. Even though there would expected to be a nominal degree of discrepancy due to the steady state CFX model, the thermal field is deemed to be sufficiently steady state to make the results comparable; a similar method is carried out at Rolls-Royce.

Results of the centreline thermal profiles show good agreement with experimentally measured data for the entire axial height of the furnace from hot zone to cold zone. Centreline temperature data measured by (Newell, 2009) for two other furnace configurations also show good agreement with predictions made by the CFX model.

The current ProCAST furnace model satisfies the varying thermal profile by splitting the heater domain into two sections with the lower part cooler than the upper part. This discretisation took no account of the baffle geometry and the same magnitude of temperature split was used regardless of the baffle geometry.

The heater profile calculated by the CFX model was discretised in a similar manner, and for one case showed good agreement with the current ProCAST temperature split.

However given a different baffle configuration the CFX model differed from the ProCAST temperature split with the CFX model predicting a different magnitude of temperature split with the lower part of the heater predicted to be hotter than previously thought.

This newly calculated heater temperature was compared to previously carried out in-situ thermocouple experiments in which the ProCAST model showed the greatest degree of error and the CFX heater temperature matched more closely with the experimental results.

Should a split heater temperature profile be used, the magnitude of temperature and position of the split has been shown to be dependent on the baffle configuration used.

5.10 Baffle effect on heater thermal profile

It has been determined that the baffle geometry has a clear effect on the thermal profile of the furnace. In this section a comparison will be made for a number of baffle geometries.

5.10.1 Effect of baffle diameter on heater thermal profile

As summarised by the centreline thermocouple experimentation there is clearly an effect that the radiation baffles play on the thermal profile of the furnace. Figure 5-46 shows the surface temperature of the furnace heating element at discrete points along the Z-axis, with 0 being the bottom of the heating element in the vicinity of the baffle region. The hot zone reference temperature was 1823.15 K.

The use of the 20 x 10^{-3} m ID baffle results in a comparatively more uniform heater temperature, as would be expected due to the lower amount of radiant heat leaving the hot zone, whereas the configuration incorporating the 110 x 10^{-3} m ID baffle is considerably cooler in the lower portion of the heating element which also results in a higher than

average temperature towards the top.

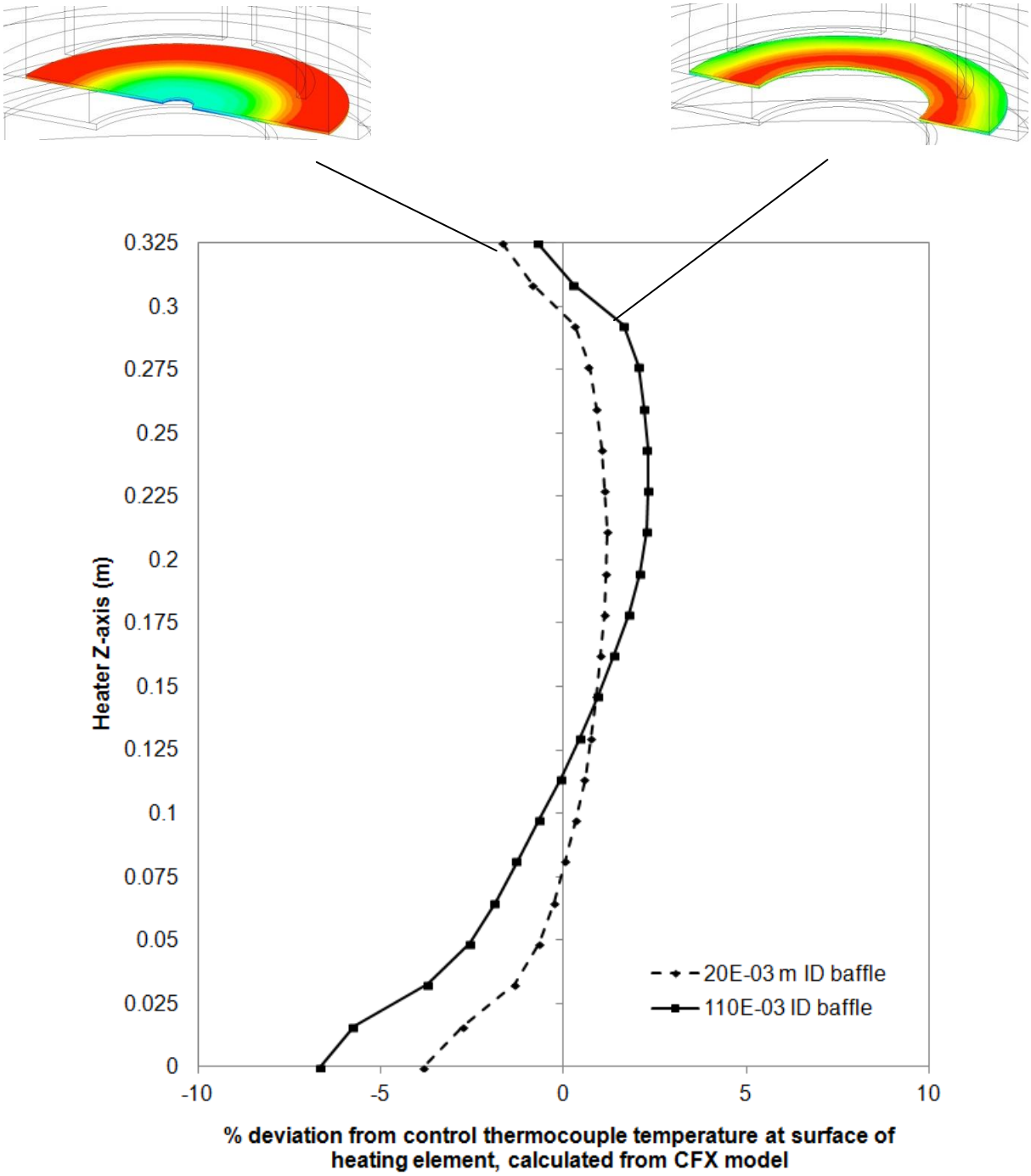


Figure 5-46: Area average heater temperature at discrete positions along the z-axis calculated using CFX model. The graph shows the heater surface temperature for the same prescribed hot zone temperature of 1823.15 K and two baffle configurations.

As discussed in a previous section, if describing the temperature distribution in the heating element by some form of temperature split, the magnitude and position of the temperature split are likely to vary when describing the same hot zone temperature depending on the baffle geometry used. This effect may have repercussions, especially when casting components with varying cross section and will be discussed in section 5.11.

5.10.2 Effect of baffle thickness on heater thermal profile

A similar effect, although to a lesser extent, is also encountered when comparing the surface heater temperature profiles when using a single and double layer 20 x 10^{-3} m ID baffle and can be seen in Figure 5-47.

As may be expected, the heater surface temperature in the lower portion of the hot zone shows less deviation from the set temperature and overall the heater surface temperature is more uniform when a double layer baffle is used.

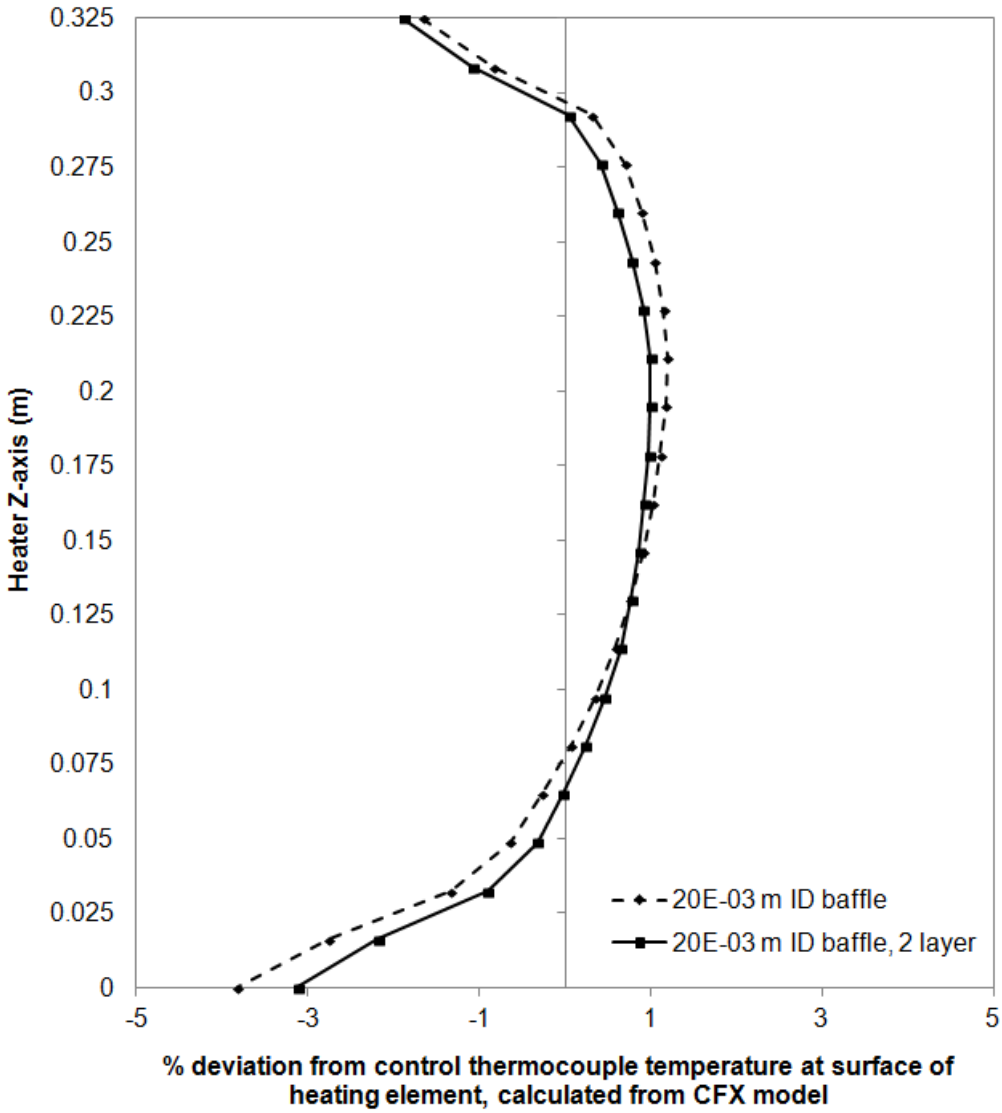


Figure 5-47: Area average heater temperature at discrete positions along the z-axis calculated using CFX model. The graph shows the heater surface temperature for the same prescribed hot zone temperature of 1823.15 K and two baffle configurations.

5.10.3 Discussion

Due to the position of the control thermocouple and the complex view factors associated with this, when requiring a hot zone temperature and when there is a significant amount of radiant heat being lost from the hot zone, the furnace will draw more power into the heating element to reach the required set temperature. This power will manifest itself as a hot zone in the top portion of the heating element to compensate for the lower than prescribed temperature in the lower portion.

If we look at Figure 5-48 it can be seen a trend is emerging; when using the 110 x 10^{-3} m ID baffle the biggest variation in heater surface temperature from the hot zone temperature is seen, followed by the 20 x 10^{-3} m ID baffle and the double thickness baffle.

So in effect, by reducing the amount of radiant heat being lost from the hot zone, the heater surface temperature contour plots are effectively 'flattening out' so if it were possible to completely block all radiant heat from leaving the hot zone, the heater surface plot would be the same temperature as required by the control thermocouple.

It may also be noted that the position at which the CFX temperature contours cross the Y-axis vary depending on the baffle geometry and hence the amount of radiant heat lost.

This effect, although intuitive, is an important discovery and, as shown with the 110 x 10^{-3} by 30 x 10^{-3} slotted baffle in section 5.8 indicates that making some sort of approximation of the heater temperature as per the current ProCAST model is not a simple matter and consideration should be given to the correct method of implementing this.

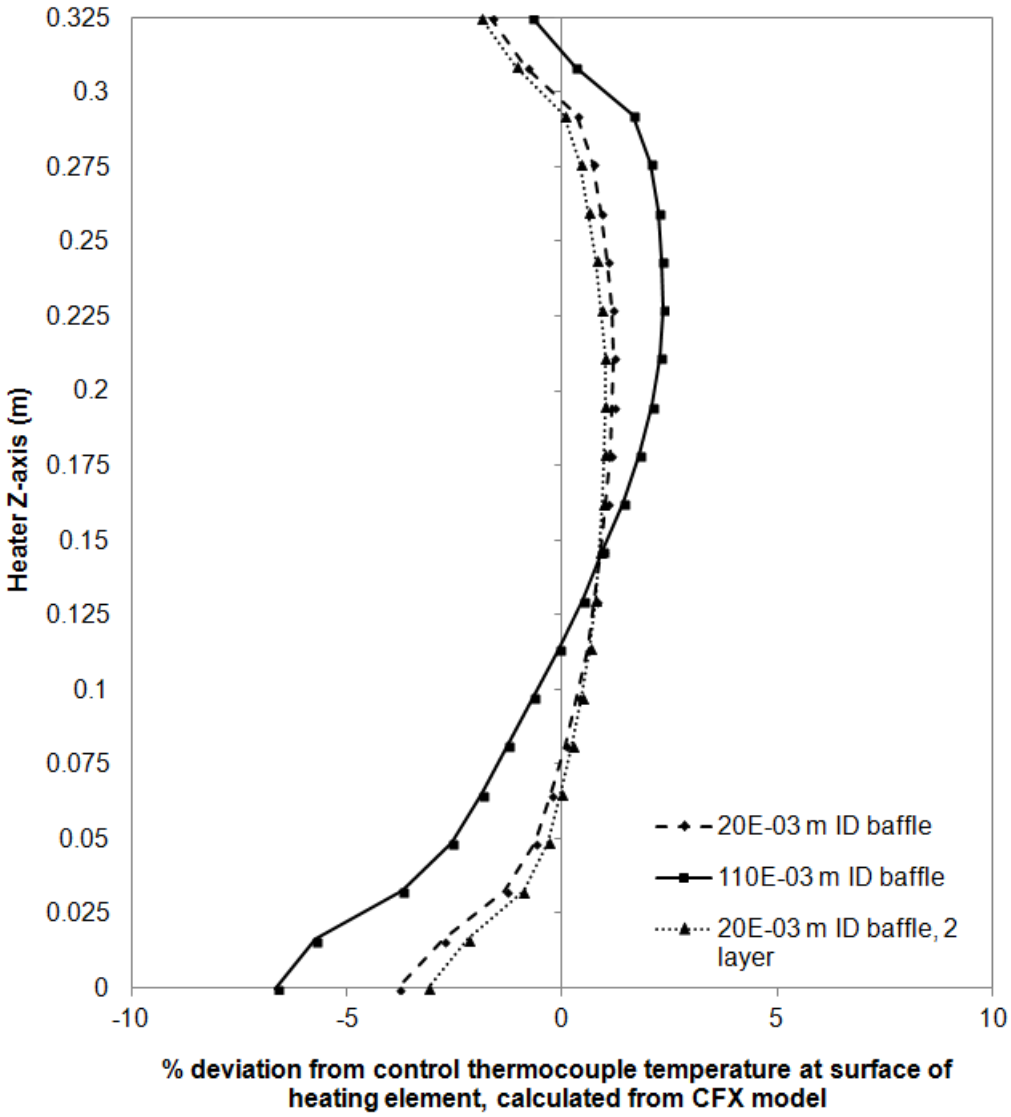


Figure 5-48: Area average heater temperature at discrete positions along the z-axis calculated using CFX model. The graph shows the heater surface temperature for the same prescribed hot zone temperature of 1823.15 K with three baffle configurations with the ability to block successive levels of radiant heat from leaving the hot zone.

5.11 Effect of mould position and transient view factors on heater thermal profile

In order to determine the effect that a moving mould and the associated changing view factors will have on the heater surface temperature the single crystal alloy CMSX-4 was cast using a VeriCAST2 mould with a hot zone temperature of 1803.15 K and a 110 x 10^{-3} m ID baffle while measuring the heating element electrical input, mould position and control thermocouple temperature. The associated transient data is shown in Figure 5-49 while Figure 5-50 shows the position of the VeriCAST2 mould relative to the furnace architecture for the four positions.

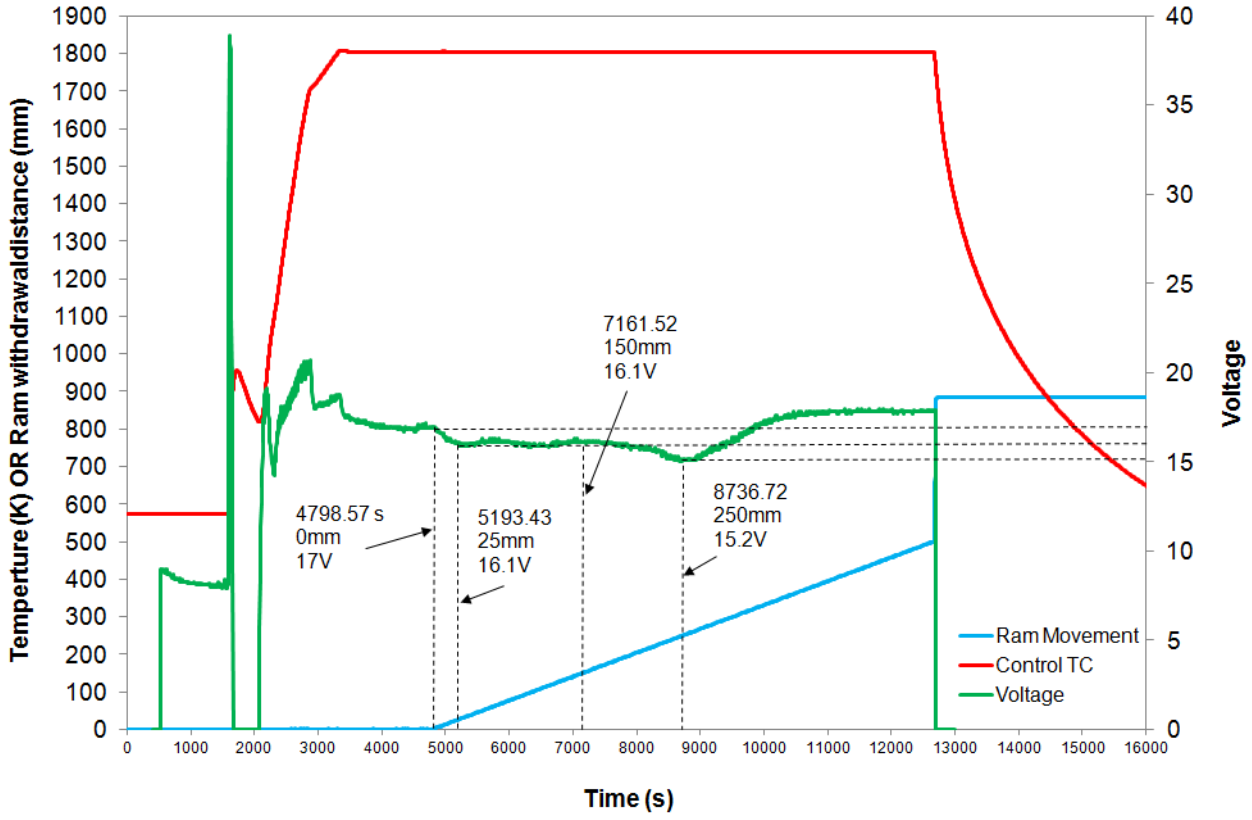


Figure 5-49: Experimentally determined electrical input, and mould position while casting CMSX-4 using a VeriCAST2 mould using a 110 x 10^{-3} m ID radiation baffle and a furnace set temperature of 1803.15 K.

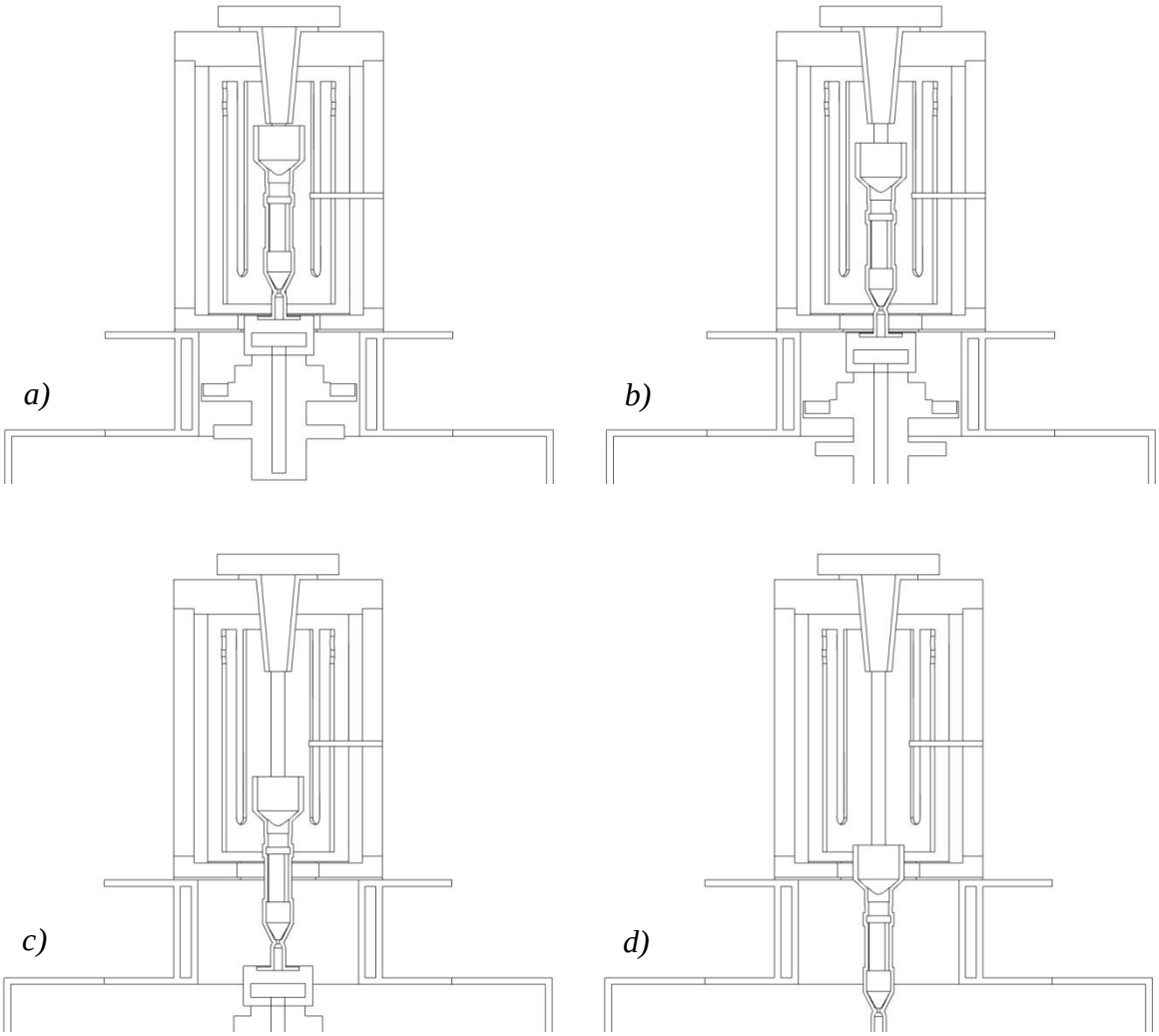


Figure 5-50: Positions of VeriCAST2 mould relating to measured furnace energy input levels. a) 0mm, b) 25mm, c) 150mm and d) 250mm. 0mm is the mould starting position and relates to a position just below the radiation baffle

CFX models were created and run to define the four positions of interest and the associated power inputs to the heating element. During the transient movement of the VeriCAST2 mould the voltage input to the furnace varied from a maximum of 17V to 15.2 V which represents a power range of 566 - 506 W.

Figure 5-51 shows the heater surface temperature variation for the four experimental conditions and it can be seen that between the '0' position and 25 mm position there is little variation in the surface temperature contour.

As may be expected the position of 150 mm, in which the aerofoil section of the mould is midway between the hot and cold zone, is the position which produced the most temperature variation of the heating element. This is not surprising as in this position the biggest area is exposed to the cold zone so the lower portion of the heating element will lose the largest proportion of radiant heat.

The position at a withdrawal distance of 250 mm shows the least amount of deviation from the set hot zone temperature and can be attributed to the cone section of the mould which is residing in the transition between the hot and cold zone acting to reflect radiant heat back into the hot zone due to the mould and alloy being above 1273 K.

As one may expect when examining Figure 5-51 is the greatest proportion of deviation occurs in the lower portion of the heating element at a position similar to that defined in the ProCAST and subsequent CFX model.

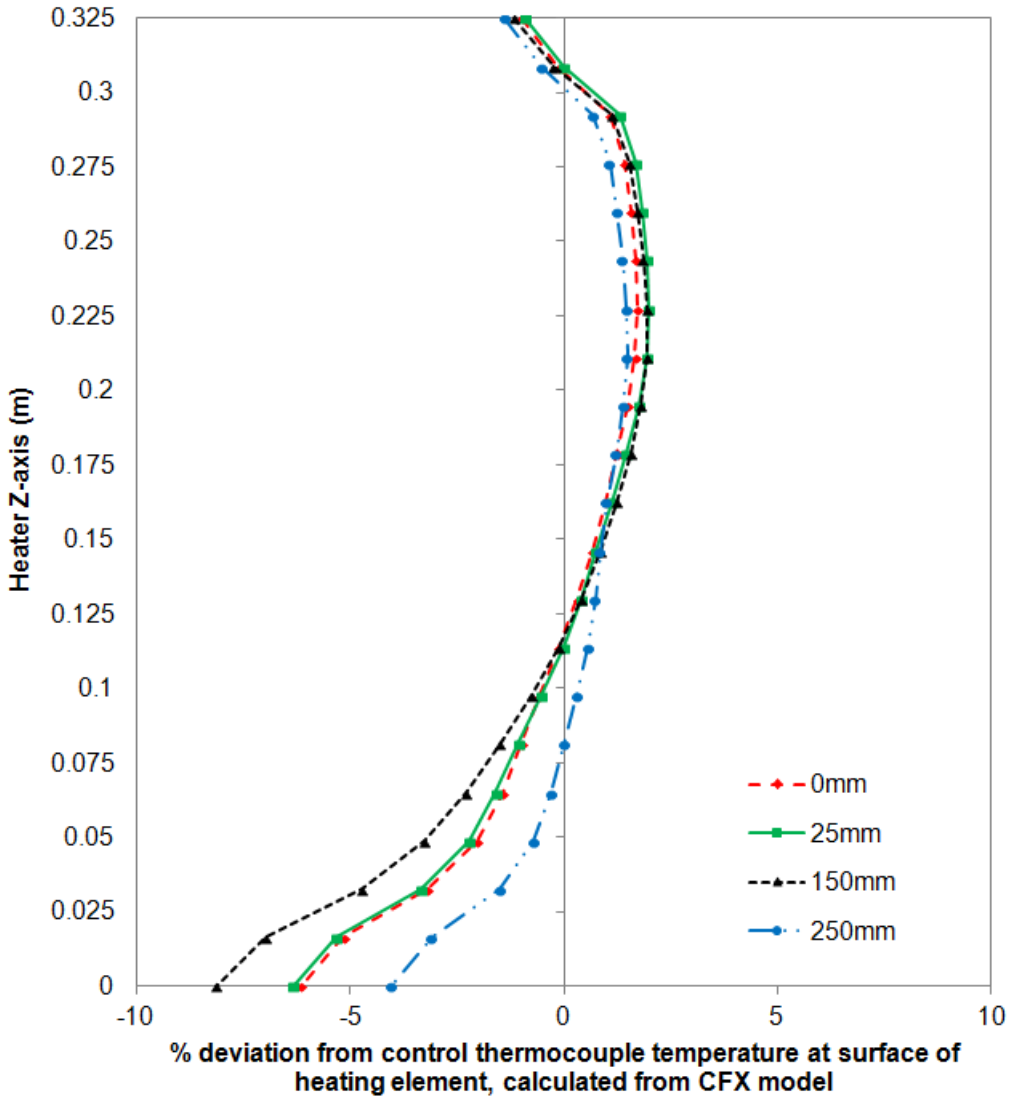


Figure 5-51: Area average heater temperature at discrete positions along the z-axis calculated using CFX model. The graph shows the heater surface temperature for the same prescribed hot zone temperature of 1803.15 K and 110 x 10-3 m ID baffle for four VeriCAST2 mould positions.

5.12 Experimental heater design

The advantage of developing the CFX model of the existing Bridgman furnace is that this allows theoretical experimentation to take place by exploring a number of experimental heater concepts without the significant capital expenditure associated with a traditional approach.

This section will detail the design and construction of an experimental furnace heating element intended to optimise the thermal gradient when casting using a conventional Bridgman furnace.

5.12.1 Design methodology

As has been shown in the previous section the temperature of the standard heating element varies significantly from the prescribed furnace hot zone temperature and is related to the baffle geometry used.

This effect is clearly undesirable when seeking to achieve a high thermal gradient and one speculative method of reversing this effect is to design modifications to the graphite heating element in order to either; a) maintain a uniform heating over the entire length of the heating element or b) impose a localised hot zone in the area above the baffle region.

In order to achieve this, specifications of the design intent are as follows;

- The material used for the experimental heating element must be the same or similar in electrical and thermal properties as the current graphite material.
- By specifying the same electrical properties, namely electrical resistivity, a direct comparison can be made between the current design and experimental designs.

- The nominal overall dimensions of the experimental heating element must be the same i.e. ports for the electrical input electrodes must be in the same position and the nominal size must be sufficiently similar to fit within the insulation assembly.
- The experimental heating element shall remain to be controlled by a control thermocouple located in the same position within the furnace using the same PID controller currently in operation.

If we consider the shape of a single turn in the heating element geometry shown Figure 5-52 it has been shown previously that there is a disparity in the electrical current density around the apex of the turn which translates into a temperature variation. Compare this with Figure 5-53 in which the distance between the apex of the turn and the base of the heating element has been reduced and it can be seen that this modification results in a localised increase in the electrical current density and hence an increase in temperature.

Given this phenomenon it may be useful to design a ring of material at the base of the heating element in which a higher current density will develop and hence a localised variation in temperature, shown in Figure 5-54.

Although this design is arguably an improvement over the standard design in that there is less deviation towards the base of the element, a lower temperature area still exists above the hotter ring of material at the base between a slightly hotter area towards the top.

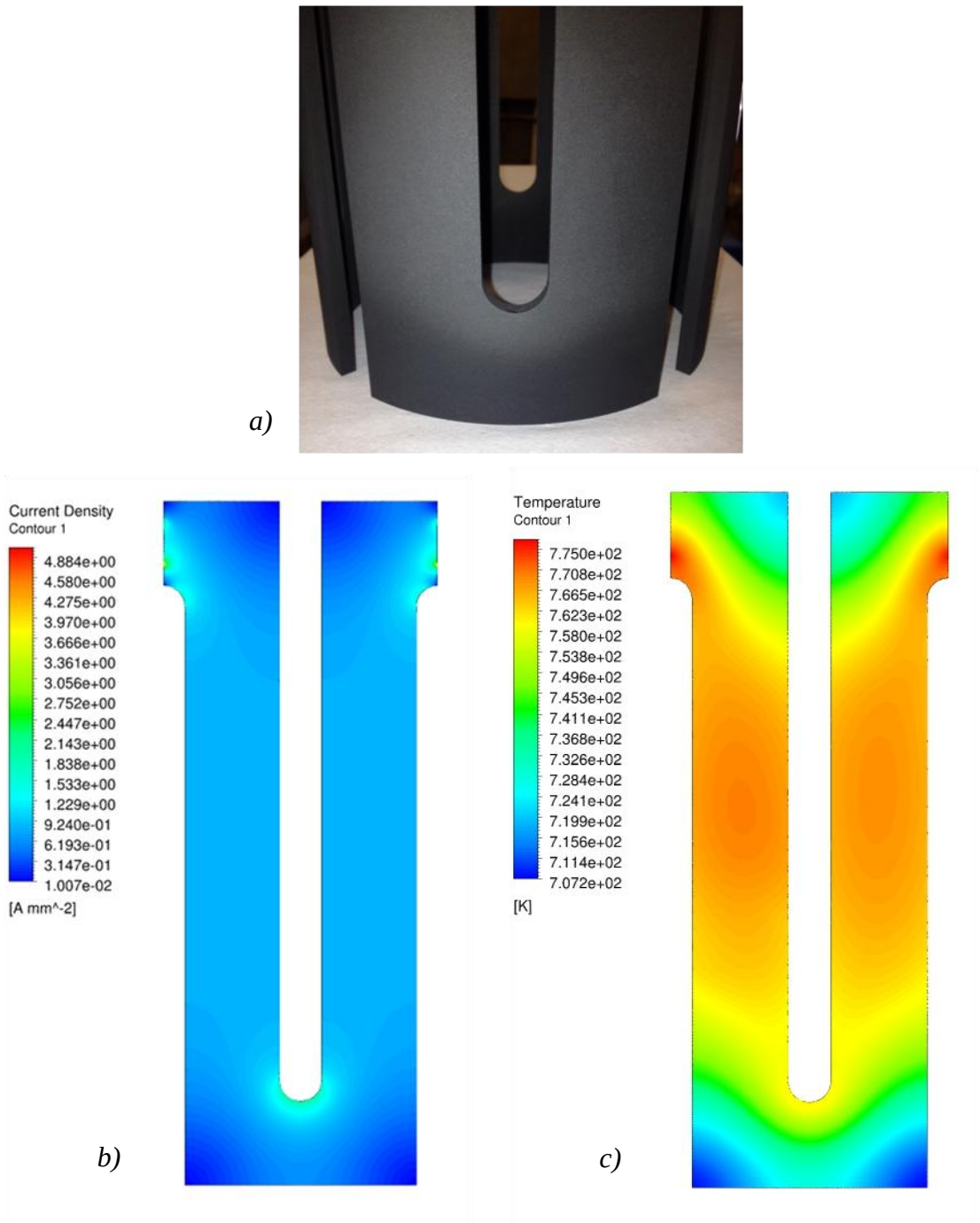


Figure 5-52: a) Geometry of single turn on standard heating element b) CFX calculation of current density in single turn for a given electrical input c) CFX calculated temperature in a single turn, given an electrical input and radiation heat loss to ambient surroundings.

.

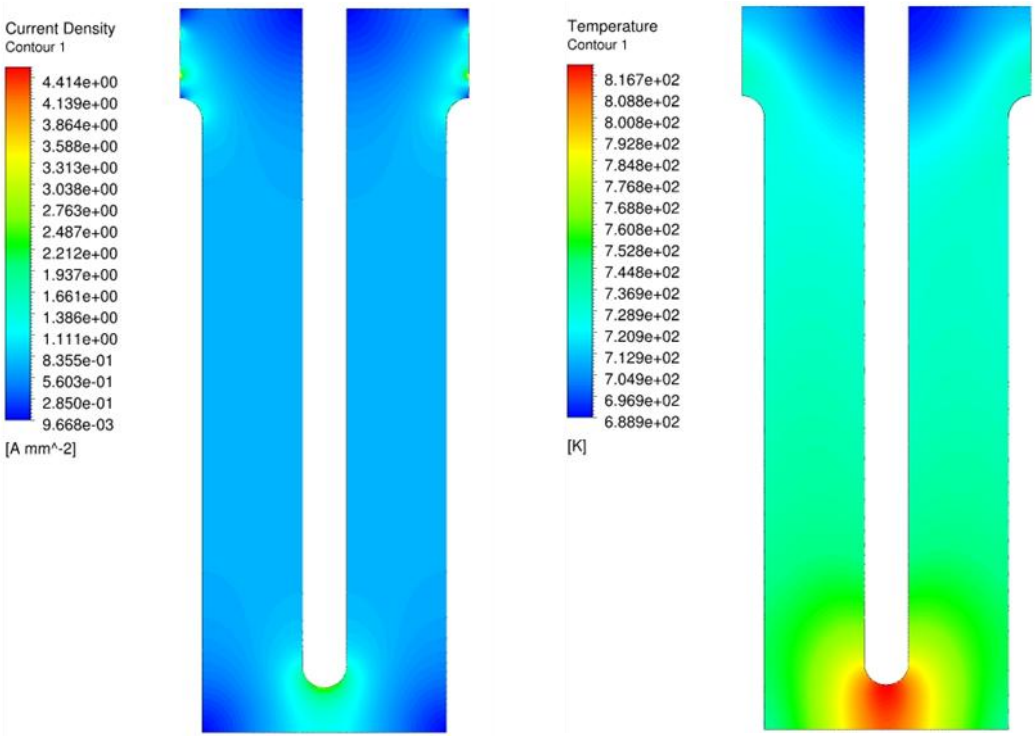


Figure 5-53: Modified geometry to reduce the distance between the apex of turn and bottom of heating element showing electrical current and temperature hot spot.

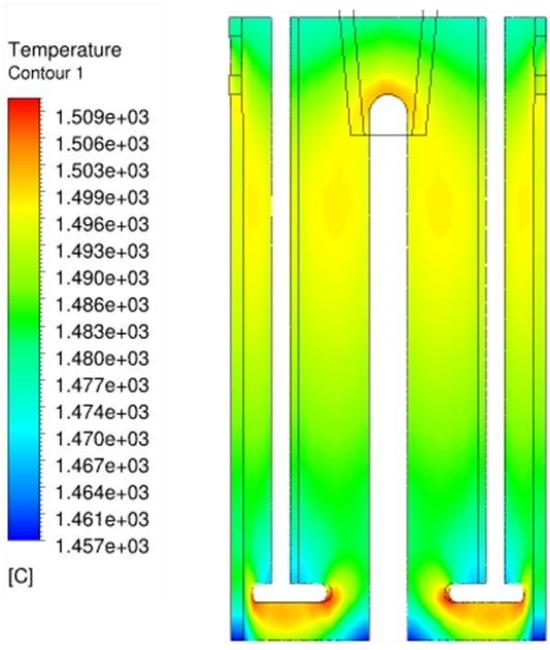


Figure 5-54: Further design iteration comprising narrow channels at the base of the heating element in order to produce a high current density and localised temperature variation.

A standard feature of industrial furnaces such as those used by Rolls-Royce is the inclusion of a twin zone heater which is effectively two separate heating elements with two power controllers; the idea being to increase the temperature of the lower heater in order to optimise the temperature gradient.

The viability of incorporating this design methodology into a single heating element was investigated using the CFX model and consequently a final experimental heater design was produced as shown in Figure 5-55.

The heating element was divided into two regions at a position equivalent to the height derived using the standard heating element at which the surface temperature will deviate from that of the control thermocouple.

In the lower region each leg pair i.e. geometry equivalent to that shown in Figure 5-52 is sub divided into four legs so two changes of current direction reside at the base of the heating element. A strip of material of higher resistance is then formed in a similar fashion to the design shown in Figure 5-54, although in this design formed of 8 segments.

By observing Figure 5-55 it is intuitive to see that towards the base of the heating element the electrical resistance will increase due to the dimensional changes in the design. In turn the design changes will induce higher temperatures in these regions provided a sufficient magnitude of electrical power is supplied.

Comments on the electrical current distribution and temperature are made in section 5.12.4.

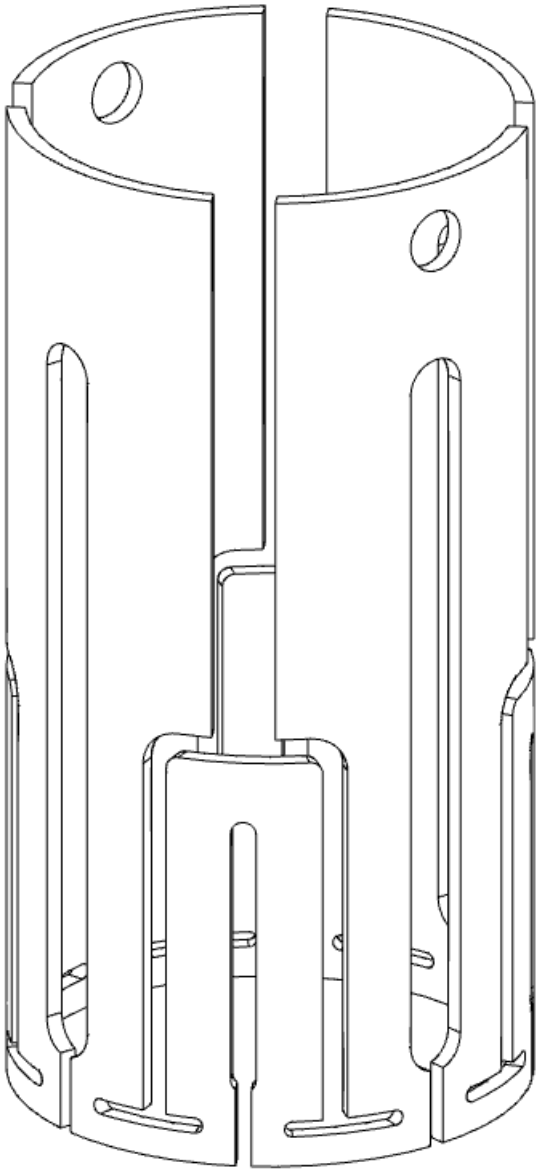


Figure 5-55: Final design of proposed experimental graphite heating element.

5.12.2 Manufacture

As previously discussed, the experimental heating element was intended to be manufactured from the same isotropic graphite material as the existing standard heating element, including identical key dimensions such as overall height, inner diameter, outer diameter and position of electrode input cut-outs. This would ensure compatibility with the existing furnace architecture.

The standard heating element was machined from a single cylindrical block of graphite and the serpentine track formed by milling out material using a CNC (Computer Numeric Control) milling machine. The vertical axis of the graphite cylinder formed a 0’0 datum to which the machining head rotated while the milling tool always was maintained at a tangent to the cylinder surface; a graphical representation is shown in Figure 5-56.

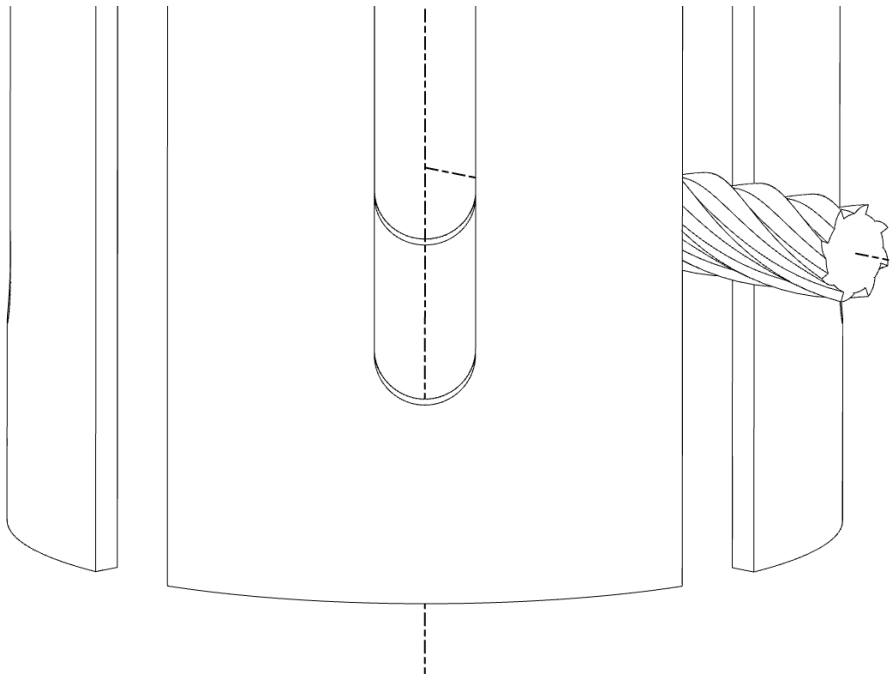


Figure 5-56: Illustration of CNC milling operation used to manufacture the graphite heating elements.

The same methodology was used in order to manufacture the experimental heating element, the key difference being that in this case three sizes of milling tool are required in order to machine the more intricate design adequately.

The smallest cut-out diameter was 5 x 10^{-3} m and was set to ensure there were no sharp internal corners with the intention of minimising the propensity of crack initiation due to thermal cycling and reducing geometric stress concentrations.

The heater solid model and drawing was produced using Unigraphics NX 6.0; the detailed drawing used for manufacture can be seen in the Appendix, the manufactured prototype is shown in Figure 5-57.



Figure 5-57: Photograph showing experimental graphite heating element due to be installed in the Bridgman furnace heating assembly.

5.12.3 Electrical resistance

Electrical resistance data was determined in much the same way as for the standard heating element, by plotting experimentally determined values of current and voltage and calculating the resistance.

The electrical resistance was determined to be in the order of 0.073 Ω which as expected is higher than the standard heating element due to the additional intricacies of the design and the same grade of graphite material used for manufacture.

5.12.4 CFX results for experimental heater incorporated in Bridgman furnace with 20 x 10^{-3} m ID baffle and 110 x 10^{-3} m ID baffle

Figure 5-58 and Figure 5-59 show electrical current density and temperature contours for the experimental heater calculated using the CFX model; Figure 5-58 for a set hot zone temperature of 1923.15K with a 20 x 10^{-3} m ID baffle and Figure 5-59 for a hot zone temperature of 1823.15K with a 110 x 10^{-3} m ID baffle.

The experimental heater is effectively designed to comprise three distinct zones as discussed in section 5.12.1 with the intention of a consecutive increase in temperature towards the base of the element. In contrast to results determined for the standard heater, both figures show a direct correlation between the electrical current density and the temperature profile.

In contrast to the standard heating element, the temperature towards the base of the experimental heater increases by around 3-5% above that of the reference hot zone temperature; a more descriptive comparison of both heater geometries is given in section 5.14.

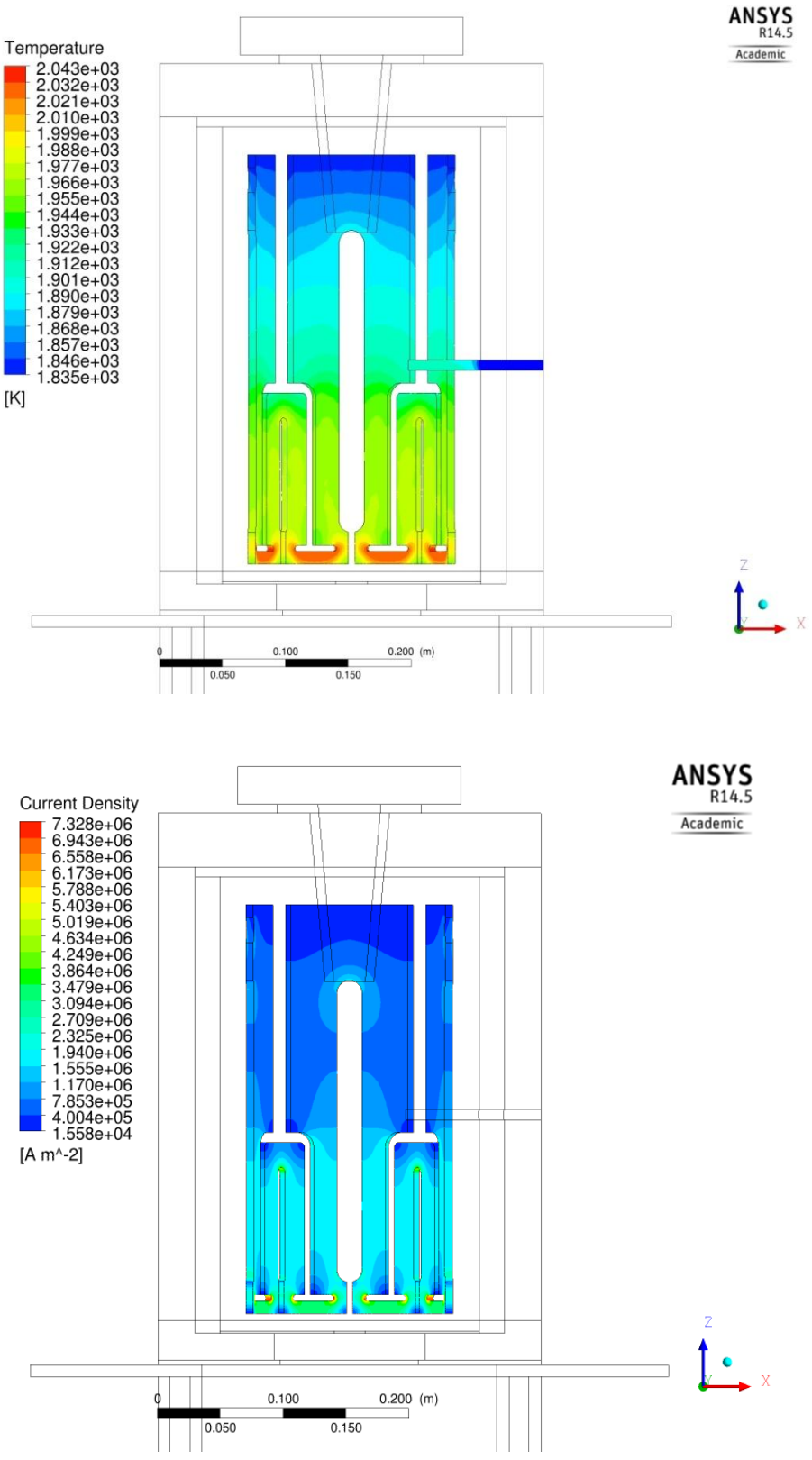


Figure 5-58: CFX model of experimental Bridgman furnace incorporating single layer radiation baffle with 20 x 10^{-3} m diameter cut-out heated to a set hot zone temperature of 1923.15 K. Contour plots show a) Heating element surface temperature and control thermocouple surface temperature b) Electrical current density with an applied current of 331 A.

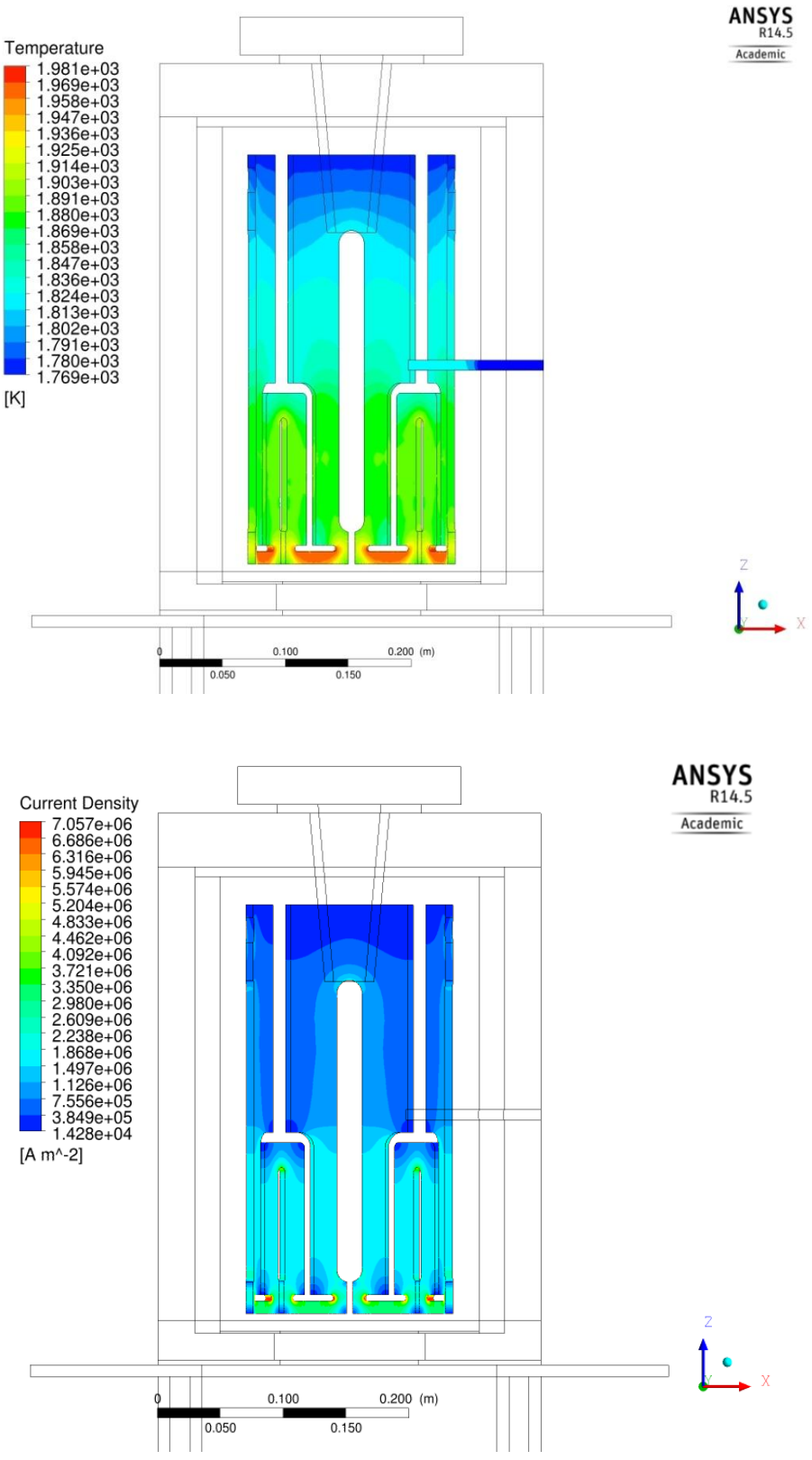


Figure 5-59: CFX model of experimental Bridgman furnace incorporating single layer radiation baffle with 110 x 10^{-3} m diameter cut-out heated to a set hot zone temperature of 1823.15 K. Contour plots show a) Heating element surface temperature and control thermocouple surface temperature b) Electrical current density with an applied current of 402 A.

5.13 Validation of experimental heater model using furnace centreline temperatures

Using the same methodology described in section 5.7 the experimental furnace models calculated using CFX were compared with experimentally determined data.

During the course of this project the type B thermocouple assembly was used extensively to measure furnace temperatures for a number of furnace configurations. Regrettably, the thermocouple assembly failed before the temperature profile of the experimental furnace with a hot zone temperature of 1823.15 K and 20 x 10^{-3} m ID baffle could be determined satisfactorily.

Due to the prohibitive cost of the type B thermocouple assembly, the experimental furnace model could therefore not be validated for this configuration.

Figure 5-60 and Figure 5-61 show experimentally measured temperature profiles compared with temperature profiles calculated using the CFX model for a hot zone temperature of 1923.15 K with a 20 x 10^{-3} m ID baffle and hot zone temperature of 1823.15 K and 110 x 10^{-3} m ID baffle respectively.

When calculating the temperature values of the 20 x 10^{-3} m ID baffle model the CFX models appears to slightly over predict the values when compared to the thermocouple results however none the less are a good match with the experimental data.

The calculated results for the case with the 110 x 10^{-3} m ID baffle also agree adequately with the experimentally determined data; again with some deviation further into the cold zone of the furnace.

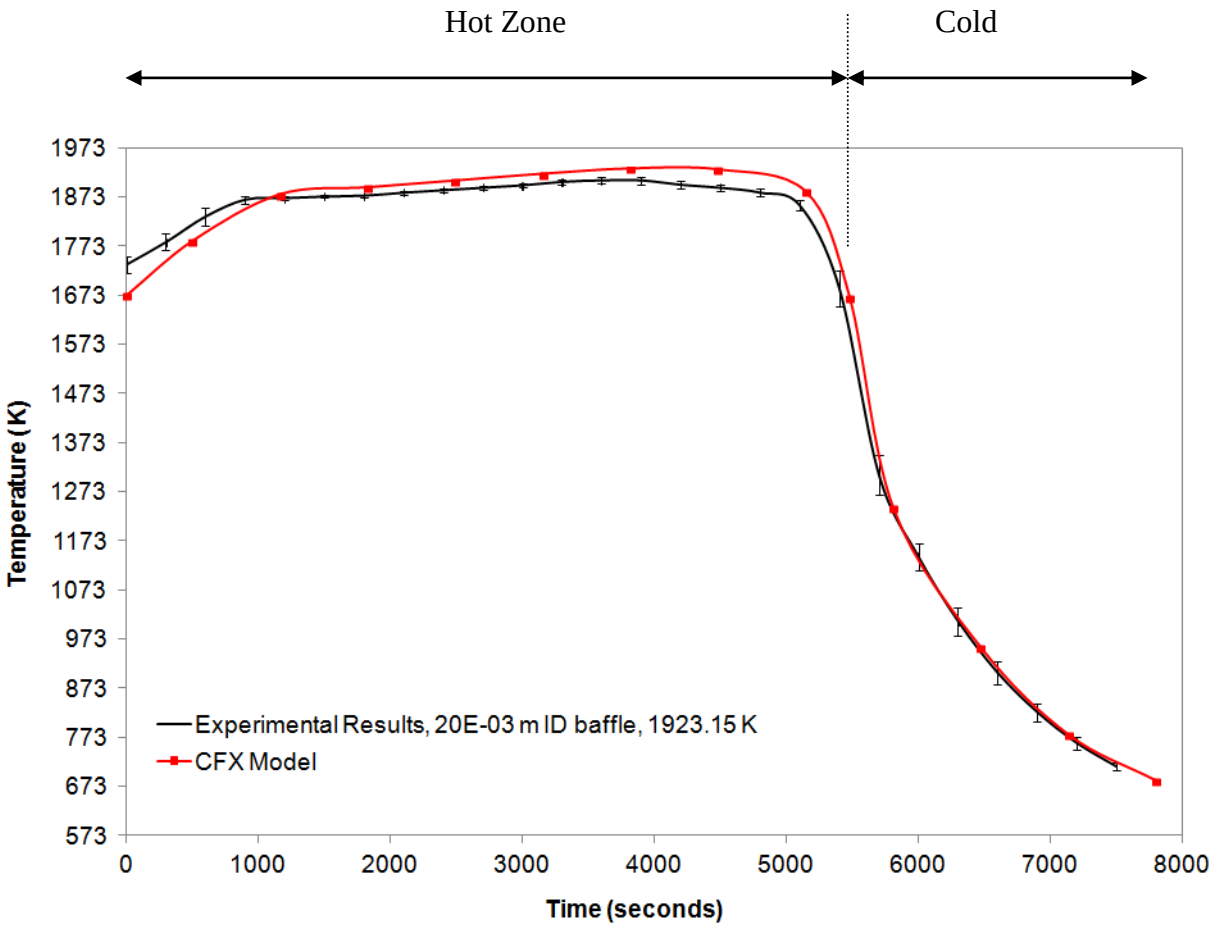


Figure 5-60: Experimental thermocouple temperature data and modelled temperature data of temperature along Z-axis of experimental furnace for a hot zone temperature of 1923.15 K with a 20 x 10^{-3} m diameter baffle. (Graph shows approximate position of furnace hot zone, baffle location and cold zone for clarity)

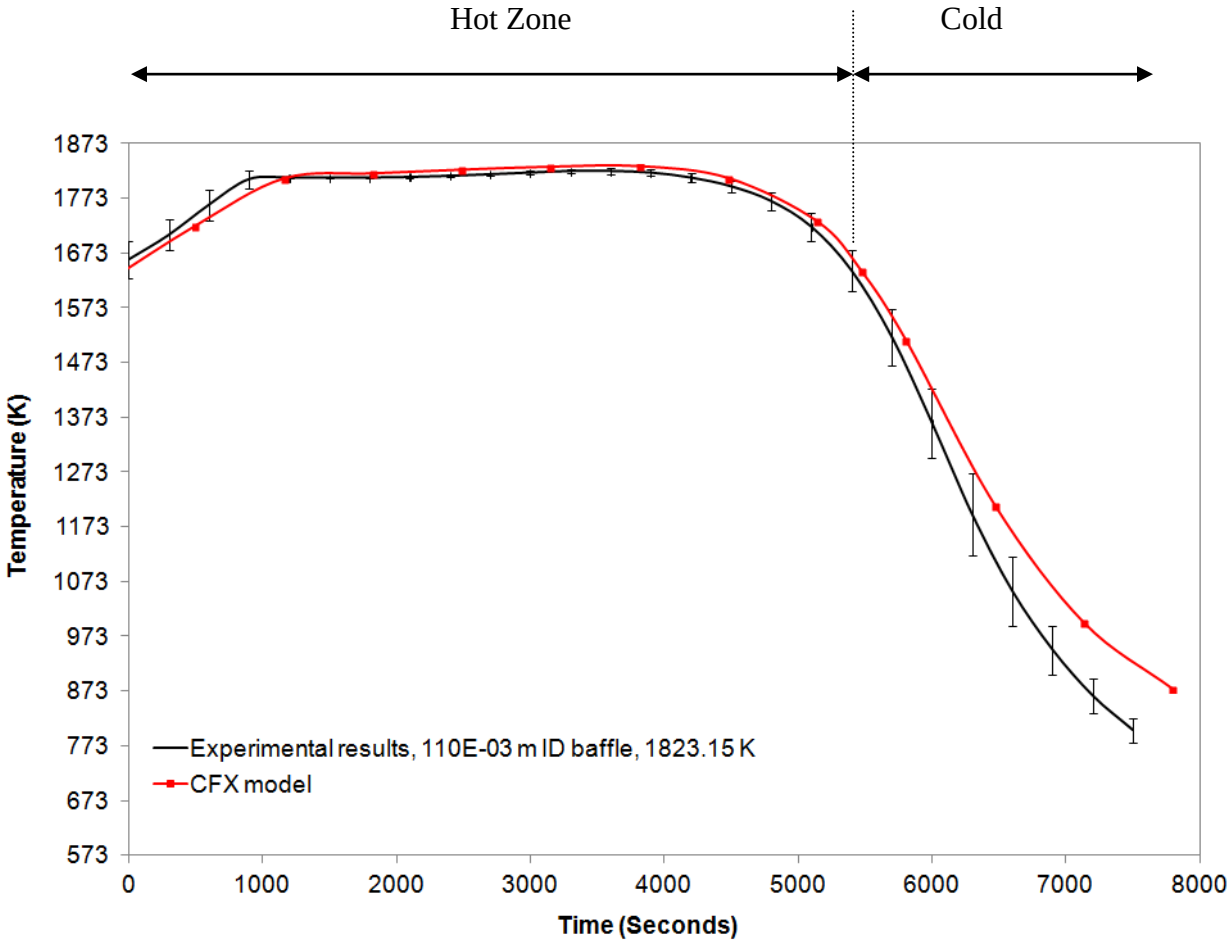


Figure 5-61: Experimental thermocouple temperature data and modelled temperature data of temperature along Z-axis of experimental furnace for a hot zone temperature of 1823.15 K with a 110 x 10^{-3} m diameter baffle. (Graph shows approximate position of furnace hot zone, baffle location and cold zone for clarity)

5.14 Comparison of standard heater and experimental heater thermal profiles

In the following section a comparative assessment of the standard and experimental heaters will be made by analysing the surface heater temperature, calculated using the CFX models, and radiated heat to the furnace centreline (where a mould assembly would reside) measured using the experimental centreline thermocouple.

5.14.1 20×10^{-3} m ID baffle

As discussed previously, the furnace configuration comprising the 20×10^{-3} m ID baffle has been shown to be the most effective at maintaining the uniformity of the hot zone.

A comparison of the furnace centreline temperature profiles for both heaters is shown in Figure 5-62 ; the standard heating element exhibiting a higher temperature towards the top of the element, gradually decreasing towards the baffle region. While the experimental heating element shows an opposite trend in that, as designed, the heating element exhibits an increase in temperature towards the baffle region.

This is further shown in Figure 5-63 which is a representation of the degree of temperature deviation at the surface of the heating elements in relation to the set hot zone temperature and shows the increase in temperature attributed to the modified lower portion. Sub-figures *a* and *b* show the location on the heating elements in which the temperature deviates from the hot zone temperature by +/- 10K (equivalent to 0.5%).

The increase in temperature and the relative position to the baffle region is clearly distinguishable between the two designs with the experimental heater showing a higher

temperature in this region.

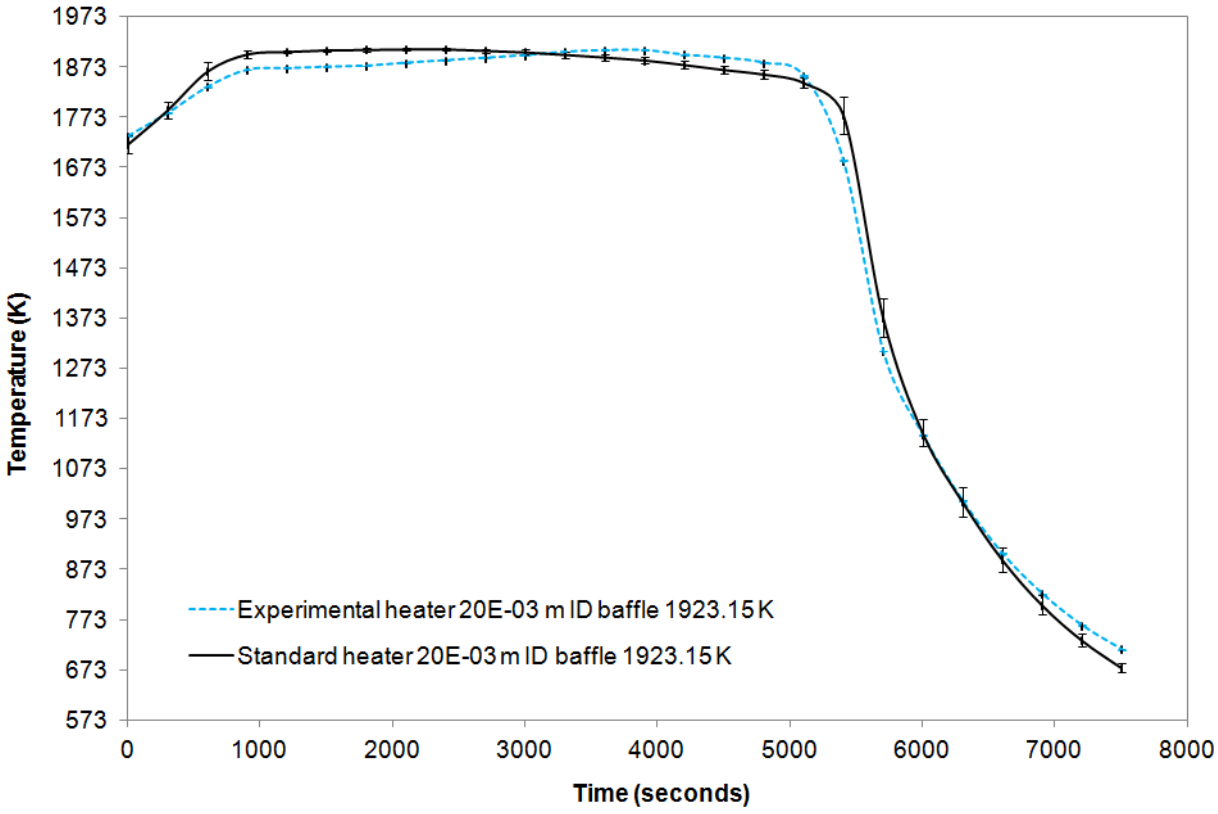
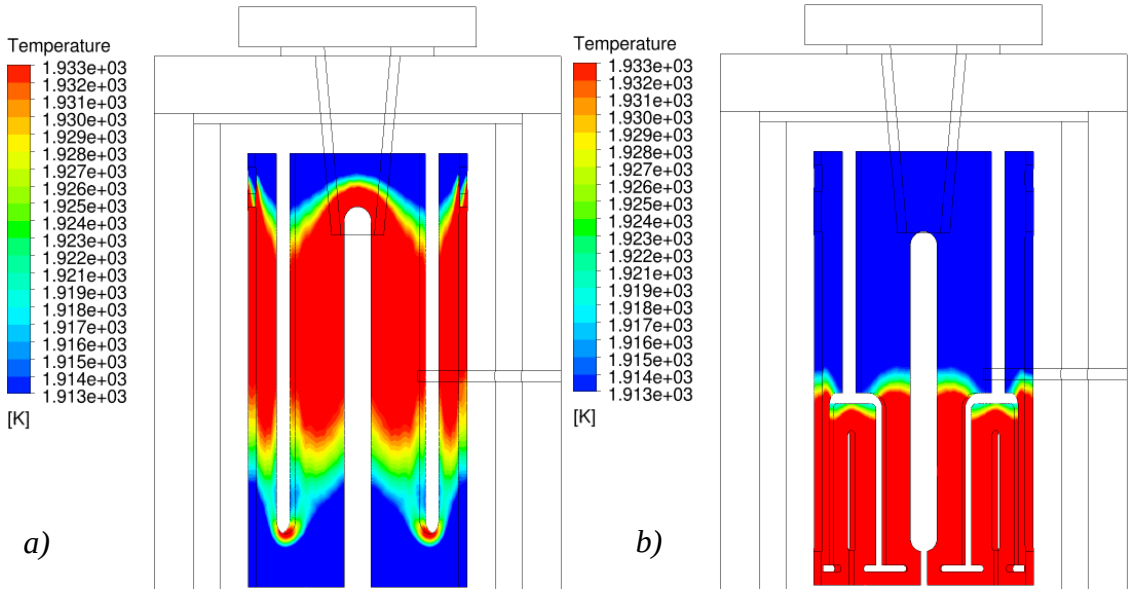


Figure 5-62: Comparison of the experimentally measured temperature data along the Z-axis of the furnace for the standard and experimental heating element with a 20 x 10^{-3} ID baffle and a set hot zone temperature of 1923.15 K.



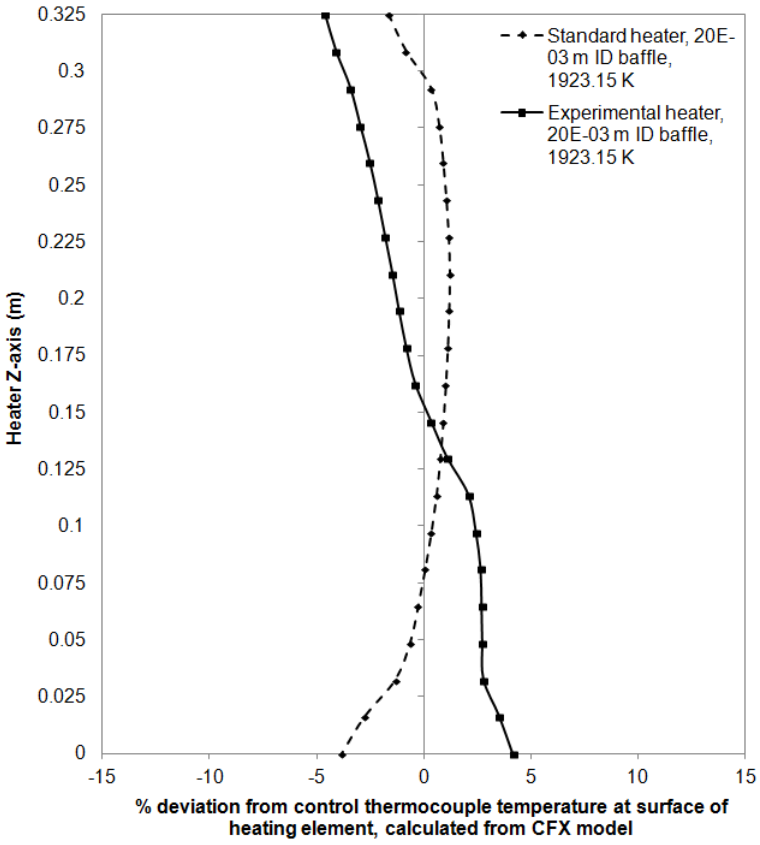


Figure 5-63: Area average heater temperature at discrete positions along the z-axis calculated using CFX model. The graph shows the heater surface temperature for the same prescribed hot zone temperature of 1923.15 K and 20 x 10^{-3} m ID baffle with the standard and experimental heaters. '0' references the bottom of the heating element, '0.325' the top. For illustration, the surface temperature +/- 10K either side of the TC temperature (which equates to +/- 0.5%) is shown to highlight the variation in position of the set temperature between a) standard heater and b) experimental heater.

Figure 5-64 is a further representation of the centreline temperature determined by thermocouple experimentation and shows the % deviation in temperature from the hot zone along the Z-axis of the furnace within the bounds of the heating element (0 being the bottom). Again, this reinforces the improvements made by the experimental heater with uniformity maintained up to a position around 0.0375 m from the bottom.

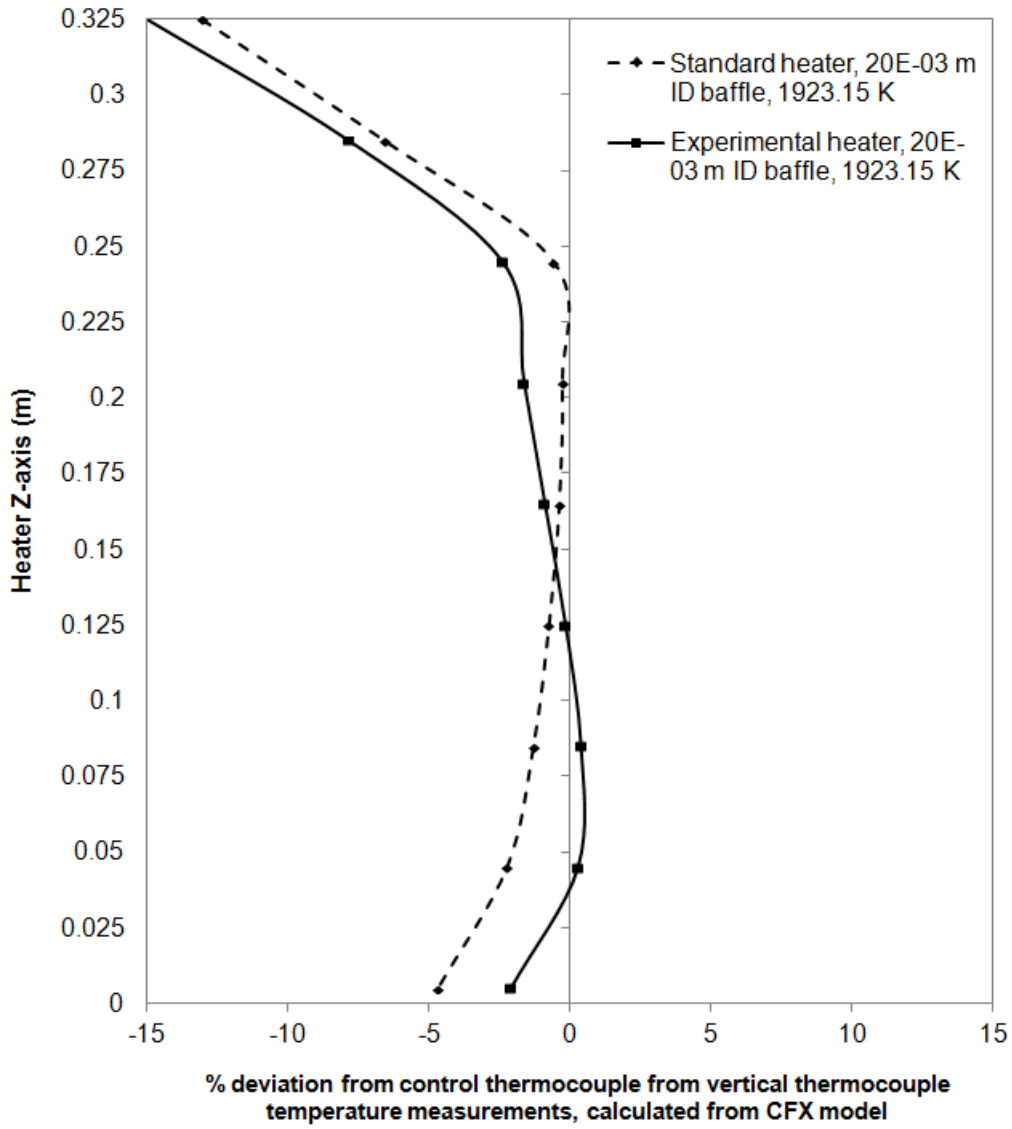


Figure 5-64: An alternative representation of experimentally determined data shown in Figure 5-62 showing the temperature transmitted by radiant heat along the Z-axis of the furnace for a prescribed hot zone temperature of 1923.15 K and 20 x 10^{-3} m ID baffle with the standard and experimental heaters. '0' references the bottom of the heating element, '0.325' the top.

5.14.2 110 x 10^{-3} m ID baffle

When comparing experimental results using the 110 x 10^{-3} m ID baffle the results are much more pronounced.

Figure 5-65 shows a comparison of the centreline temperatures measured using the moving thermocouple, and much the same trend can be observed as with the 20 x 10-3 m ID baffle, however the temperature disparity between the two heating elements towards the baffle region is much greater in this configuration and there is a marginally sharper transition between hot and cold zone.

The temperature disparity is a result of the greater degree of radiation heat loss into the cold zone due to reduced radiation baffling as there is less driving force for heat generating at the base of the standard heating element when compared to the experimental. Essentially in this configuration, by design, the experimental heater maintains a 'flatter' more uniform temperature profile towards the vicinity of the baffle region.

This is shown more explicitly in Figure 5-66 as the % deviation in temperature from the hot zone along the Z-axis of the furnace within the bounds of the heating element (0 being the bottom). Up to a distance of 0.175 m the centreline temperature deviates from the hot zone temperature up to a maximum of 12% when using the standard baffle, whereas for the experimental heating element this is reduced to a distance of 0.075 m and a maximum deviation of <6%.

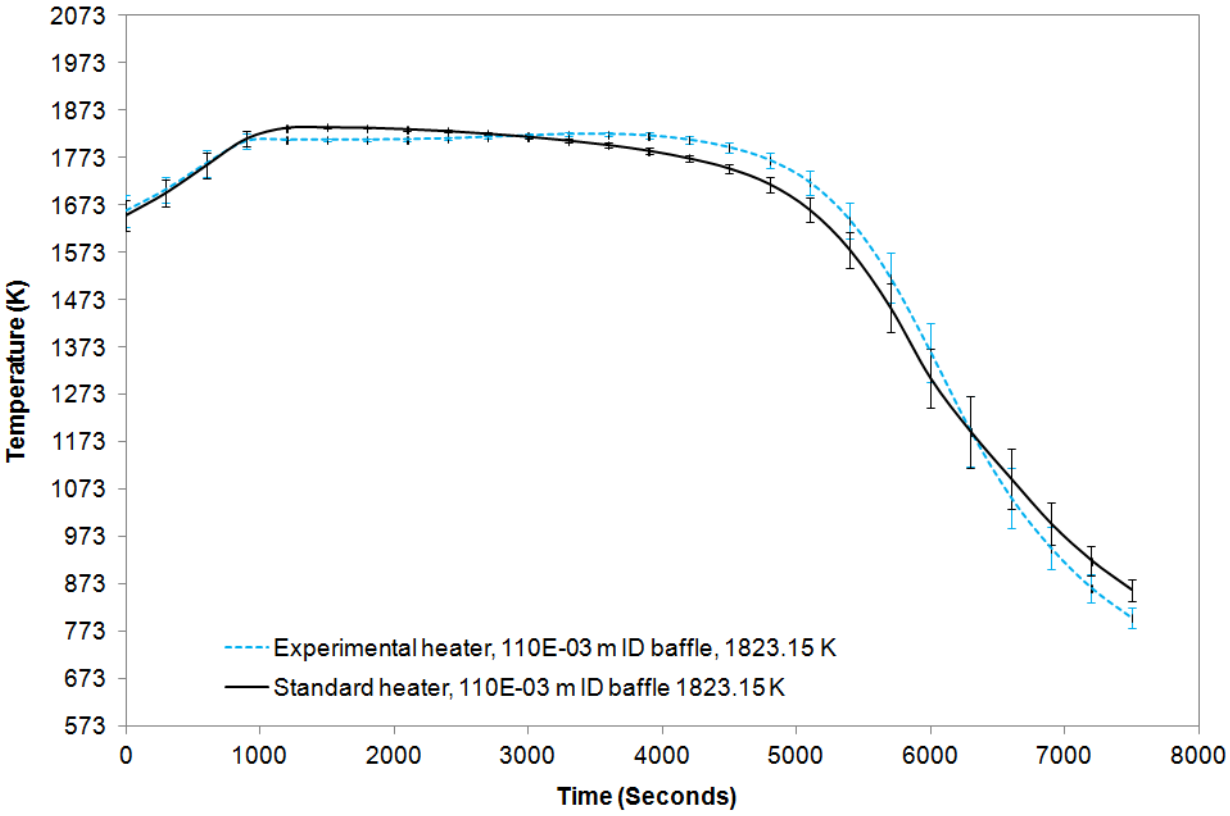


Figure 5-65: Comparison of the experimentally measured temperature data along the Z-axis of the furnace for the standard and experimental heating element with a 110 x 10^{-3} m ID baffle and a set hot zone temperature of 1823.15 K.

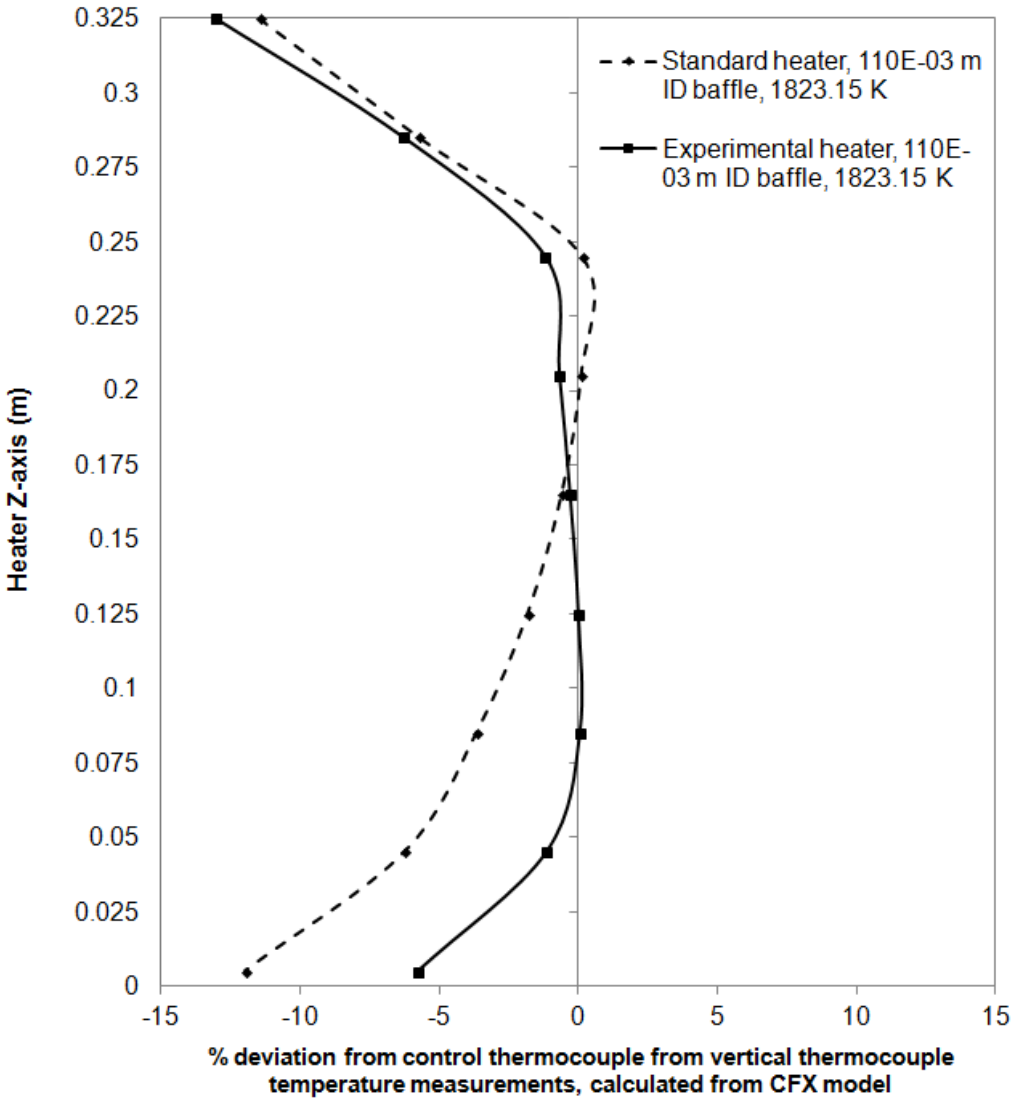


Figure 5-66: An alternative representation of experimentally determined data shown in Figure 1 58 showing the temperature transmitted by radiant heat along the Z-axis of the furnace for a prescribed hot zone temperature of 1823.15 K and 110 x 10^{-3} m ID baffle with the standard and experimental heaters. '0' references the bottom of the heating element, '0.325' the top.

Figure 5-67 is a further representation of the degree of temperature deviation at the surface of the heating elements in relation to the set hot zone temperature and shows the increase in temperature attributed to the modified lower portion. When compared to the 20 x 10^{-3} m ID baffle configuration, again, the magnitude of temperature variation is greater in the case of the 110 x 10^{-3} m ID baffle.

Sub-figures *a* and *b* show the location on the heating elements in which the temperature deviates from the hot zone temperature by +/- 10K (equivalent to 0.5%). When comparing Figure 5-67 a) with Figure 5-63 a) the influence of the baffle geometry is clearly shown resulting in a greater degree of deviation and a much larger deviation zone from the hot zone temperature.

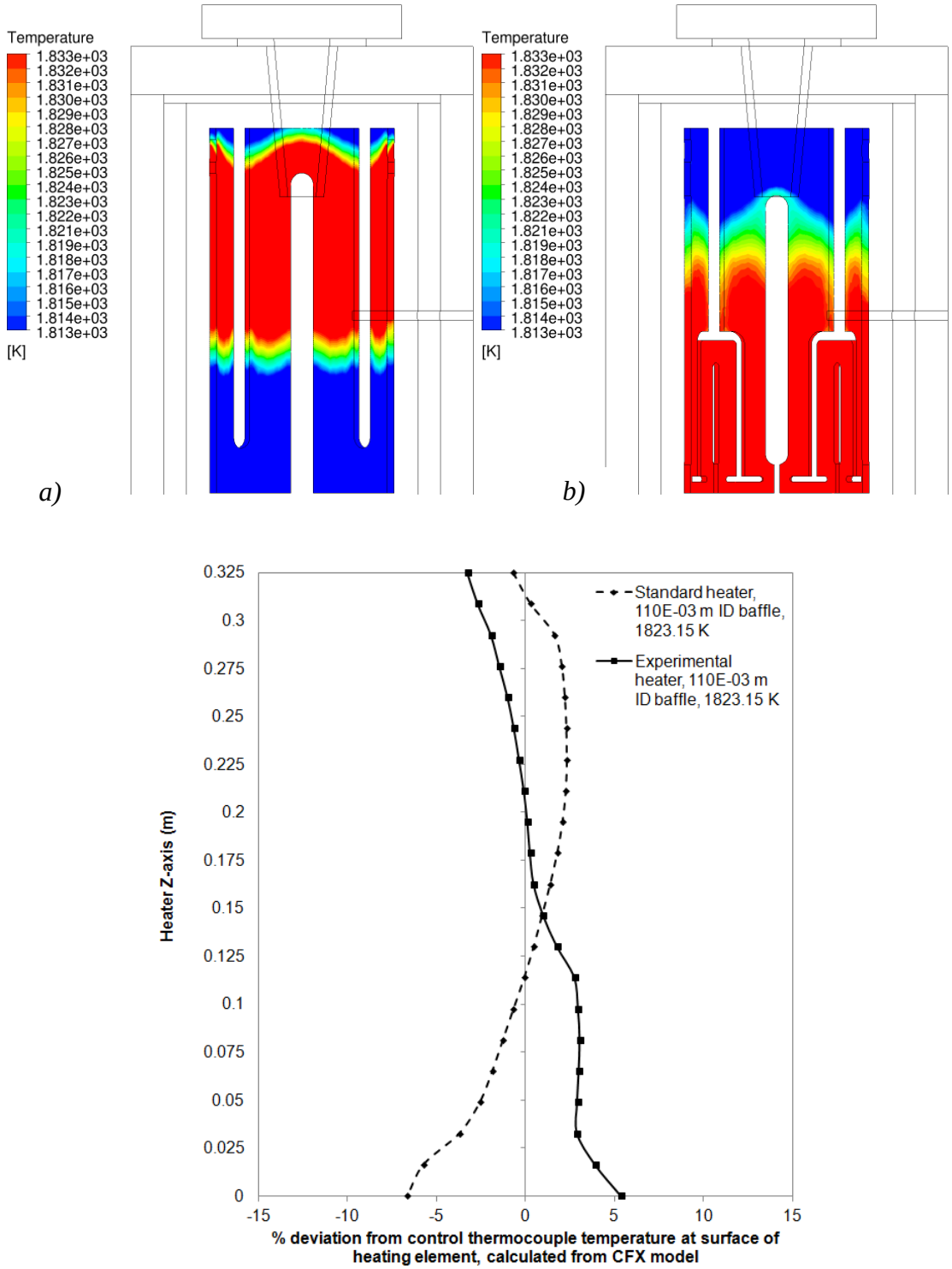


Figure 5-67: Area average heater temperature at discrete positions along the z-axis calculated using CFX model. The graph shows the heater surface temperature for a prescribed hot zone temperature of 1823.15 K and 110 x 10-3 m ID baffle with the standard and experimental heaters. '0' references the bottom of the heating element, '0.325' the top. For illustration, the surface temperature +/- 10K either side of the TC temperature (which equates to +/- 0.5%) is shown to highlight the variation in position of the set temperature between a) standard heater and b) experimental heater.

Experimentation thus far has indicated that scope for improvement using the 20 x 10^{-3} m ID baffle is limited and greater improvements may be achieved by increasing the furnace set temperature when using the experimental heater in conjunction with the 110 x 10^{-3} m ID baffle.

As such a further centreline temperature data set was obtained using the experimental heater and 110 x 10^{-3} m ID baffle with a hot zone reference temperature of 1923.15K, this data is shown alongside measurements for the same configuration at a temperature of 1823.15K in Figure 5-68. Measurements taken using the standard heater, 110 x 10^{-3} m ID baffle and a hot zone temperature of 1823.15K are also shown for comparison.

Determining the temperature gradient by using the melting range of the single crystal alloy CMSX-4 it can be seen that there are consecutive increases in the thermal gradient in comparison to the standard heater as the slope of the temperature data between hot and cold zone increases.

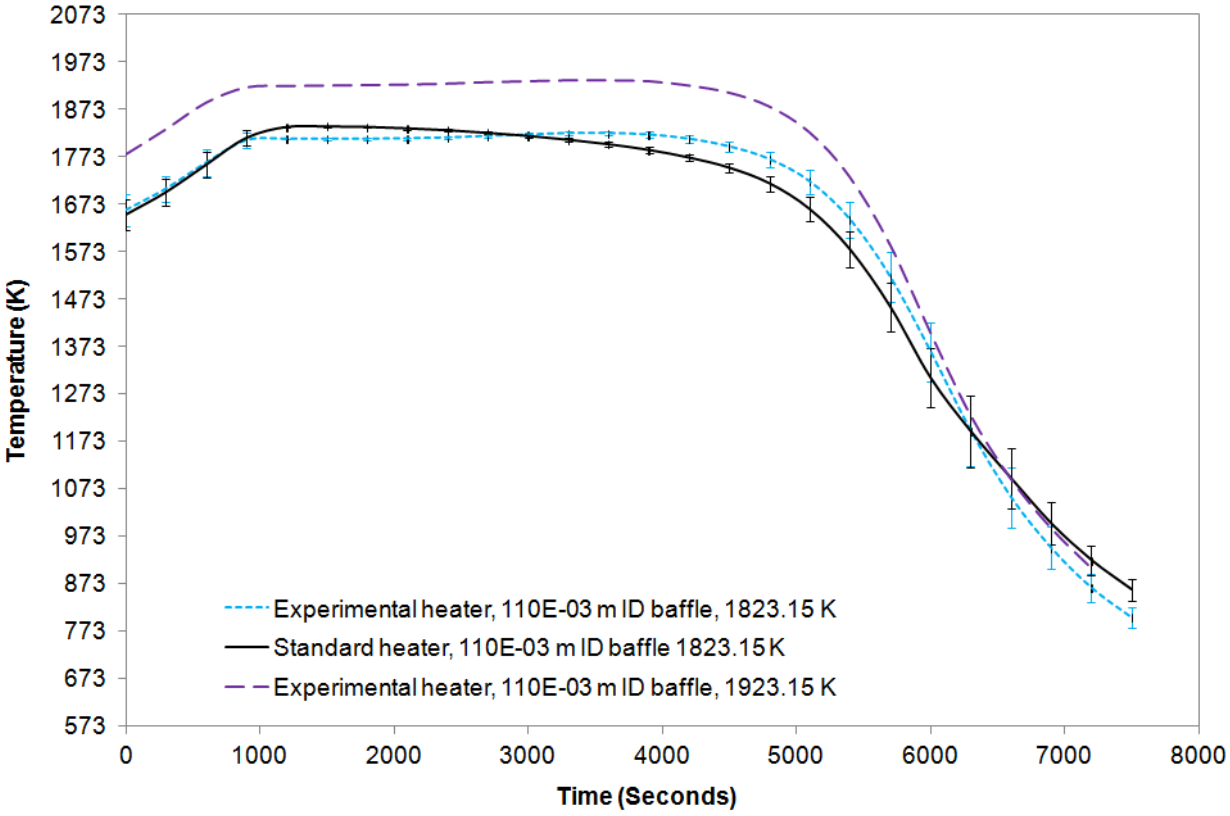


Figure 5-68: Comparison of the experimentally measured temperature data along the Z-axis of the furnace for the standard and experimental heating element with a set hot zone temperature of 1823.15 K and experimental heater with hot zone temperature of 1923.15K. All configurations with a 110 x 10^{-3} m ID baffle.

Thermal gradients determined from all the experimental work conducted are shown in Table 5-5 and several observations can be made; firstly, the difference in thermal gradient between the two heater configurations when using a 20 x 10^{-3} m ID baffle is marginal. This is most likely due to the effect the radiation baffle has on the furnace hot zone and, it seems, that both heater configurations utilise the maximum cooling effect offered by the cold zone.

The real benefits of the experimental heater are shown when using a 110 x 10^{-3} m ID baffle. In this configuration, areas of the standard heating element low in current density lose heat by radiation heat loss to the cold zone, as shown in Figure 5-67, whereas the

experimental heater retains or increases the temperature in this area with respect to the reference temperature, utilising the cooling effect of the cold zone.

These results are only indicative at this stage and a more robust comparison is made in the next chapter.

Table 5-5: Thermal gradient for experimental furnace configurations calculated using centreline thermocouple experimental thermocouple readings.

Condition	**Measured thermal gradient / x 10^3 K.m^{-1}**
20 x 10^{-3} m ID baffle, Standard heater, 1923.15K	27.65
20 x 10^{-3} m ID baffle, Experimental heater, 1923.15K	26.19
110 x 10^{-3} m ID baffle, Standard heater, 1823.15K	5.52
110 x 10^{-3} m ID baffle, Experimental heater, 1823.15K	7.1
110 x 10^{-3} m ID baffle, Experimental heater, 1923.15K	9.63

5.15 Conclusions

5.15.1 Furnace model development

Before this work was undertaken a ProCAST model of the single shot Bridgman furnace existed in its current form and was validated for two experimental conditions. The validation process highlighted that there was some inconsistency in the heating element thermal profile which necessitated splitting the heating element domain into two sections with the lower section ~90 K cooler than the hot zone reference temperature for both conditions. This was attributed to a variation in the electrical current density, particularly around the apex of turns within the serpentine geometry.

It was hypothesised that the thermal gradient of the furnace could be improved by optimisation of the furnace hot zone temperature however methods to attain optimisation of the hot zone temperature profile were limited; laser heating was a viable technique however the capital investment required to bring the idea to fruition made the option untenable.

In order to design a heating element with the purpose of optimising the thermal profile of the hot zone it was clear that a thorough understanding of the furnace would be required. The ProCAST model has been shown to be well equipped to calculate thermal radiation heat transfer problems, however the heating element domain was always represented by a fixed temperature boundary condition and did not interact with other components, such as baffle geometry, which have been shown to have a significant impact on the thermal gradient.

The CFX model is a static model in the fact that, unlike the ProCAST model, it does not

simulate mould movement, however is adept at simulating electrical current flow and radiation heat transfer. As such the model was developed with the aim of understanding the underlying interactions between the heating element temperature and a number of furnace configurations. The first assumption clarified was that the heating element did indeed not possess a uniform temperature profile when under steady state conditions and the temperature was a function of the electrical current density, constrained by heater design.

The CFX model was validated by comparing a centreline temperature profile calculation against experimentally measured thermocouple readings and showed good agreement under all conditions.

The CFX temperature predictions were compared with ProCAST temperature profiles used for the two validated furnace conditions; the validated condition for the ProCAST model comprising a hot zone reference temperature of 1803.15 K with a 110 x 10^{-3} m ID baffle comprised a temperature split of 1753.15 K for the lower part and 1843.15 K for the upper, this is compared to a CFX calculated temperature split of 1758.74 K and 1831.64 K for the lower and upper parts respectively; a 90 K split for the ProCAST model and a 72.9 K split for the CFX calculation.

When validating a hot zone reference temperature of 1843.15 K with a more restrictive 110 – 30 x 10^{-3} m slotted baffle the lower part was 1783.15 K and the upper 1873.15 K for the ProCAST validation, this is compared to 1819.57 K and 1861.55 K for lower and upper parts respectively calculated from CFX. This represents a temperature split of 90 K for the ProCAST model and 41.98 K split from the CFX calculation.

The results indicated that the magnitude of temperature difference between the heating element temperature and that of the hot zone reference temperature was not only a function

of electrical current density but also baffle geometry.

This understanding was extended, and it was proposed that the heating element surface temperature will also vary depending on the geometry being cast.

5.15.2 Experimental heater design

The CFX model has been used as a tool to explore and evaluate new heating element design concepts. A candidate design was chosen and comprised three distinct heating zones; an upper zone, broadly equivalent to or lower than the hot zone reference temperature, a lower zone, equivalent to or higher than the hot zone reference temperature and a final zone of intense overheating at the base of the heating element.

The efficiency of the experimental heating element was assessed for two extreme baffle configurations; an extremely restrictive 20 x 10^{-3} m ID baffle and a standard 110 x 10^{-3} m ID baffle. Thermal gradients measured using a moving thermocouple at the furnace centreline indicated that the improvement offered by the experimental heating element with a restrictive baffle was limited in comparison to the standard, however significant increase in the thermal gradient was observed for the standard baffle configuration.

The objective of designing the experimental heating element with respect to existing furnace architecture was that the experimental heating element should be easily retrofitted into the single shot furnace with no modification to power or control methods necessary.

This goal has been achieved, and no compatibility issues were ever experienced during use.

CHAPTER 6 MICROSTRUCTURE MODIFICATION OF NICKEL BASED ALLOYS

6.1 Introduction

As discussed previously, the relationship between PDAS, the furnace hot zone temperature and withdrawal velocity (which is assumed to be equivalent to the solidification growth front velocity) has been well established (Horrocks, 1990a), Newell, 2009). The aim of this section is to quantify the potential improvements in the Bridgman casting process by analysing the microstructure of the single crystal superalloy CMSX-4 cast using a number of parameters and relating this to temperature profiles calculated using CFX.

In the following section only a single casting for each experimental condition has been analysed, predominantly due to limitations in available CMSX-4 bar stock. However as the furnace thermal profile is well described by the CFX model, and any results deemed erroneous would be re-evaluated, this is deemed acceptable.

6.2 Results and analysis

6.2.1 Multiple-component mould – an analogy of industrial casting conditions

Firstly, let us refer back to the calculations made in Chapter 2 describing the idealised Bridgman process for an infinitely long rod of uniform cross section. The calculation assumes that the furnace hot zone temperature T_f is of uniform temperature, much like the

earlier iteration of the ProCAST model, and the transition between furnace hot zone and cold zone is a perfectly adiabatic interface. We have established this is not the case, and the furnace configuration containing the 110 x 10^{-3} m diameter baffle leads to the biggest deviation between the requirements of a uniform hot zone temperature and an adiabatic interface.

Observation made during analysis of the computer model results showed that the greatest degree of improvement in the uniformity of the hot zone temperature and thermal gradient was achieved when using a large ID baffle arrangement and the experimental heater.

Work conducted by (Newell, 2009) has quantified the improvement in microstructure and hence thermal gradient achievable by the reduction in baffle ID and/or increase in withdrawal velocity; in the case of a multi-component mold, the opportunity for baffle optimisation is limited due to geometry constraints. Therefore, increase in the thermal gradient would be most readily achieved by optimization of the hot zone temperature profile using the experimental heater, and speculatively, an increase in the withdrawal velocity.

Figure 6-1 shows the micrograph taken at 60 x 10^{-3} m away from the seed selector of the single crystal alloy CMSX-4 produced at a withdrawal velocity of 6.36 x 10^{-5} ms^{-1} in a mould assembly consisting of four 12 x 10^{-3} m diameter bars with a spiral seed selector. The furnace hot zone temperature was 1823.15 K using the standard heating element and the baffle contained a 110 xx 10^{-3} m ID orifice, the ‘standard’ baffle. Figure 6-2 shows the corresponding microstructure produced under nominally identical conditions with the exception that the heating element used was the experimental type designed for this work.

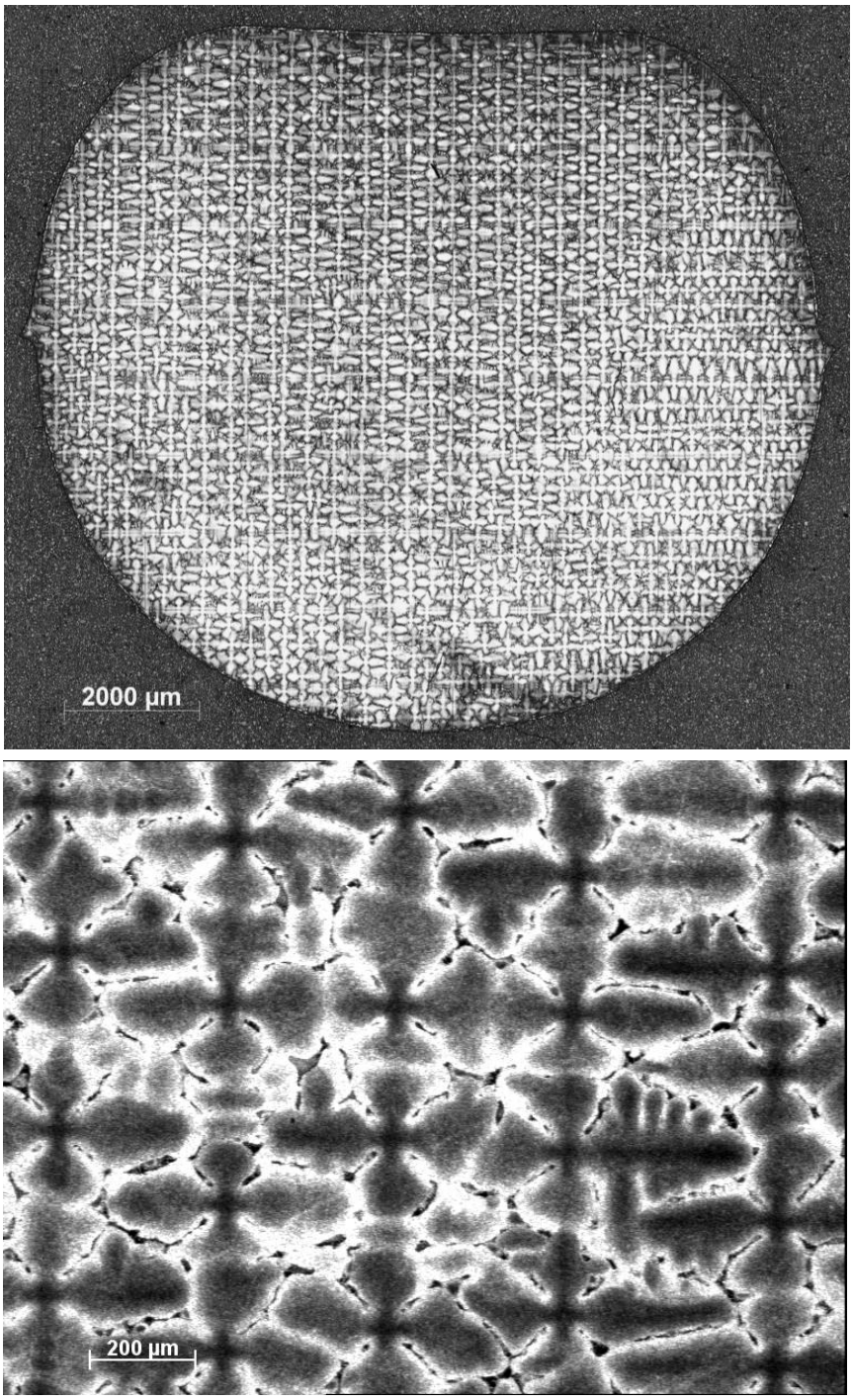


Figure 6-1: Macro image of cross-section (a) and micrograph (taken using a polarized filter in order to highlight dendrite centres) (b) showing primary dendrites in CMSX-4 with a mean spacing of 321.36 x 10^{-6} m. Taken at 60 x 10^{-3} m above spiral seed selector and cast using standard heating element, a hot zone reference temperature of 1823.15 K and a withdrawal velocity of 6.36 x 10^{-5} ms^{-1}. The mould comprised four 12 x 10^{-3} m diameter bars each with a spiral seed selector located on a bayonet fitting equally spaced at the four quadrants on a circle of approximate diameter ~60 x 10^{-3} m (See Chapter 3). The baffle comprised a 110 x 10^{-3} m ID orifice and a nominal thickness of 3.8 x 10^{-3} m.

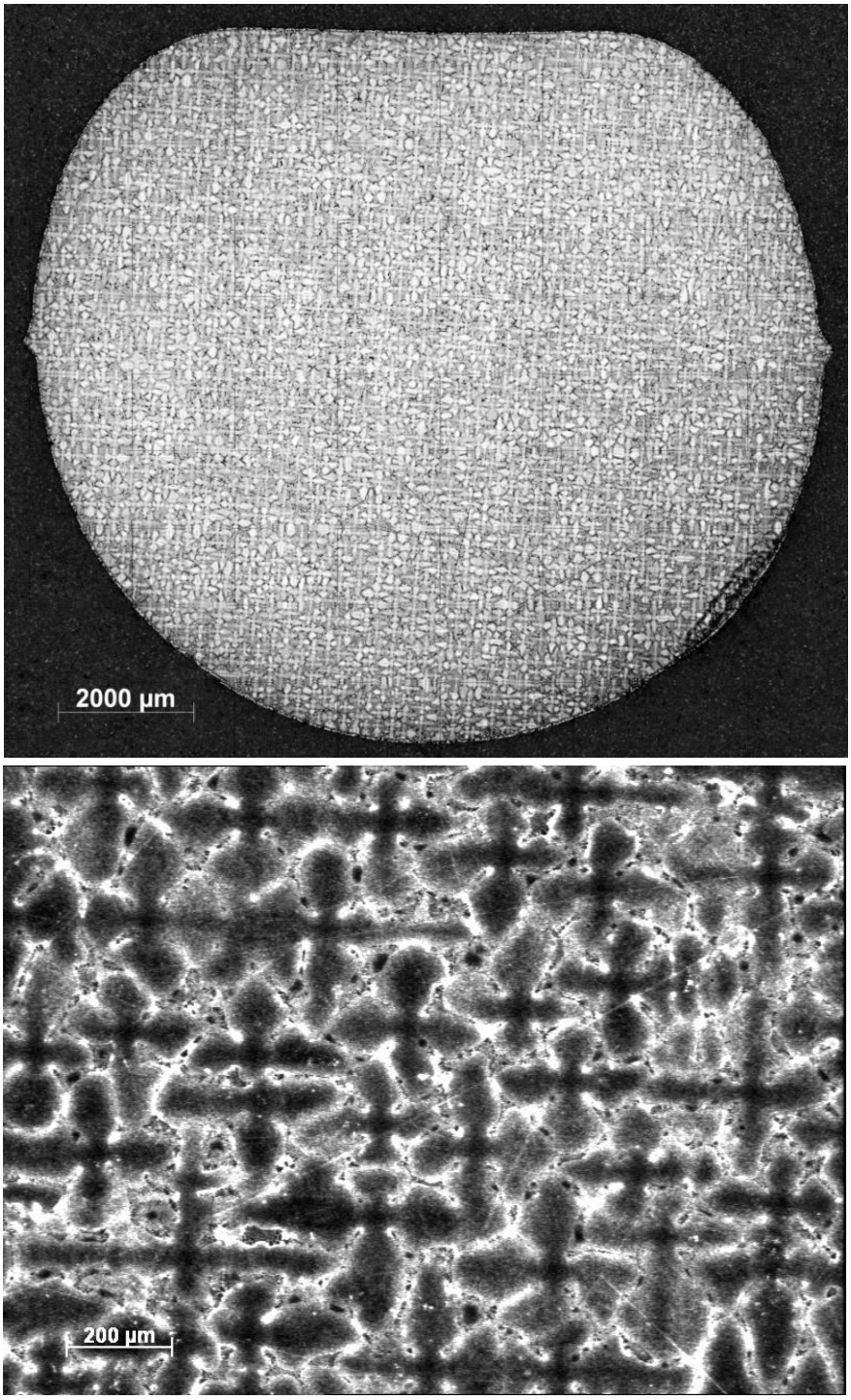


Figure 6-2: Macro image of cross-section (a) and micrograph (taken using a polarized filter in order to highlight dendrite centres) (b) showing primary dendrites in CMSX-4 with a mean spacing of 246.96 x 10^{-6} m. Taken at 60 x 10^{-3} m above spiral seed selector and cast using experimental heating element, a hot zone reference temperature of 1823.15 K and a withdrawal velocity of 6.36 x 10^{-5} ms^{-1}. The mould comprised four 12 x 10^{-3} m diameter bars each with a spiral seed selector located on a bayonet fitting equally spaced at the four quadrants on a circle of approximate diameter ~60 x 10^{-3} m (See Chapter 3). The baffle comprised a 110 x 10^{-3} m ID orifice and a nominal thickness of 3.8 x 10^{-3} m.

Experiments using the 110 x 10^{-3} m ID baffle and a set hot zone temperature of 1823.15 K were subsequently repeated using the standard and experimental heaters for a withdrawal rate of 10.67 x 10^{-3} ms^{-1}. The corresponding mean PDAS values for all experimental conditions are summarised in Table 6-1.

The mean has been calculated from sites examined over a distance of 100 x 10^{-3} m, from a position of 20 x 10^{-3} m - 120 x 10^{-3} m above the seed selector; the standard error of the mean values is relatively low indicating a tight distribution in the data set, which would be expected given the number of measurements made.

The 95% confidence interval is a probabilistic estimate and is a description of the range in values in which you would expect the majority of casts to fall, i.e. 5 out of 100 may be outside of this range.

From observing Table 6-1 it can be seen that there is a significant difference between the measured PDAS values when comparing the standard and experimental heaters for withdrawal rates of 6.36 x 10^{-3} ms^{-1} and 10.67 x 10^{-3} ms^{-1}, with a maximum reduction in PDAS of around 23% for the 6.36 x 10^{-3} ms^{-1} withdrawal velocity.

When comparing the PDAS values obtained using the standard heating element for both withdrawal velocities there is a reduction in mean PDAS for a given higher withdrawal velocity with the mean and range in confidence interval lower for the velocity of 10.67 x 10^{-3} ms^{-1}.

This is in contrast to the PDAS values obtained when casting at varying velocities using the experimental heating element; in this case the difference in mean PDAS values are marginal and the confidence interval values overlap, indicating that a higher withdrawal velocity has little statistical impact when using the experimental heater.

Table 6-1: Mean dendrite arm spacing for a range of test bars produced using the standard and experimental heaters at a set hot zone temperature of 1823.15 K while the withdrawal velocity was varied from 6.36 – 10.67 x 10^{-5} ms^{-1}. The baffle geometry used was 110 x 10^{-3} m ID Sigraflex. The standard error is an estimation of the amount the sample mean deviates from the actual mean of a population and is estimated as s/√n, where s is the sample standard deviation and n is the number of observations. The 95% confidence interval is calculated as $\bar{x} \pm 1.96 \times standard\ error$. The value of 1.96 is the normal distribution value for 95% confidence taken from normal distribution tables.

Furnace heating element	**Withdrawal rate / x 10^{-5} ms^{-1}**	**Mean PDAS ± standard error / x 10^{-6} m**	**Dendrite count**	**95% confidence limits for mean / x 10^{-6} m**
Standard	6.36	321.36 ± 1.16	1793	319.08 – 323.64
Experimental	6.36	246.96 ± 1.12	1794	244.77 – 249.15
Standard	10.67	310.27 ± 1.31	1803	307.70 – 312.83
Experimental	10.67	243.89 ± 1.11	1743	241.71 – 246.08

The distribution of dendrite arm spacing is shown as a box plot diagram in Figure 6-3. The centre horizontal line in the box represents the median value and the outer horizontal lines on each box represent the upper and lower quartile. The solid vertical lines go to the most extreme value that is not an outlier; the outliers, shown as a cross, are calculated in the following way;

$$PDAS < \left[Q_1 - [1.5 \times IQR]\right]$$

$$PDAS > \left[Q_3 + [1.5 \times IQR]\right]$$

Where;

Q_1 is the 25th percentile, Q_3 is the 75th percentile and IQR is the inter quartile range.

When examining Figure 6-3 it can be seen that there appears to be a large proliferation of upper value outliers, although due to the large number of experimental measurements taken the outliers represent < 3% of the total number.

The fact that the outliers all lie in the upper bounds of the measured PDAS values can also be rationalised and is a result of the measuring technique, described in detail in Chapter 3.

In this method a micrograph of the dendrite structure is analysed and the dendrite centre's identified and then marked. Any operator error that arises when this process is carried out will logically result in dendrite centres not being identified and therefore not counted, rather than other features in the microstructure being misconstrued as dendrites.

As such, missed dendrites will result in artificially large measurements in relation to adjacent dendrite centres, which have been discounted as outliers.

This plot shown gives a clear representation of the positive effect the experimental heater has on the PDAS when casting CMSX-4, which is of greater magnitude than increasing the withdrawal velocity using the standard heating element.

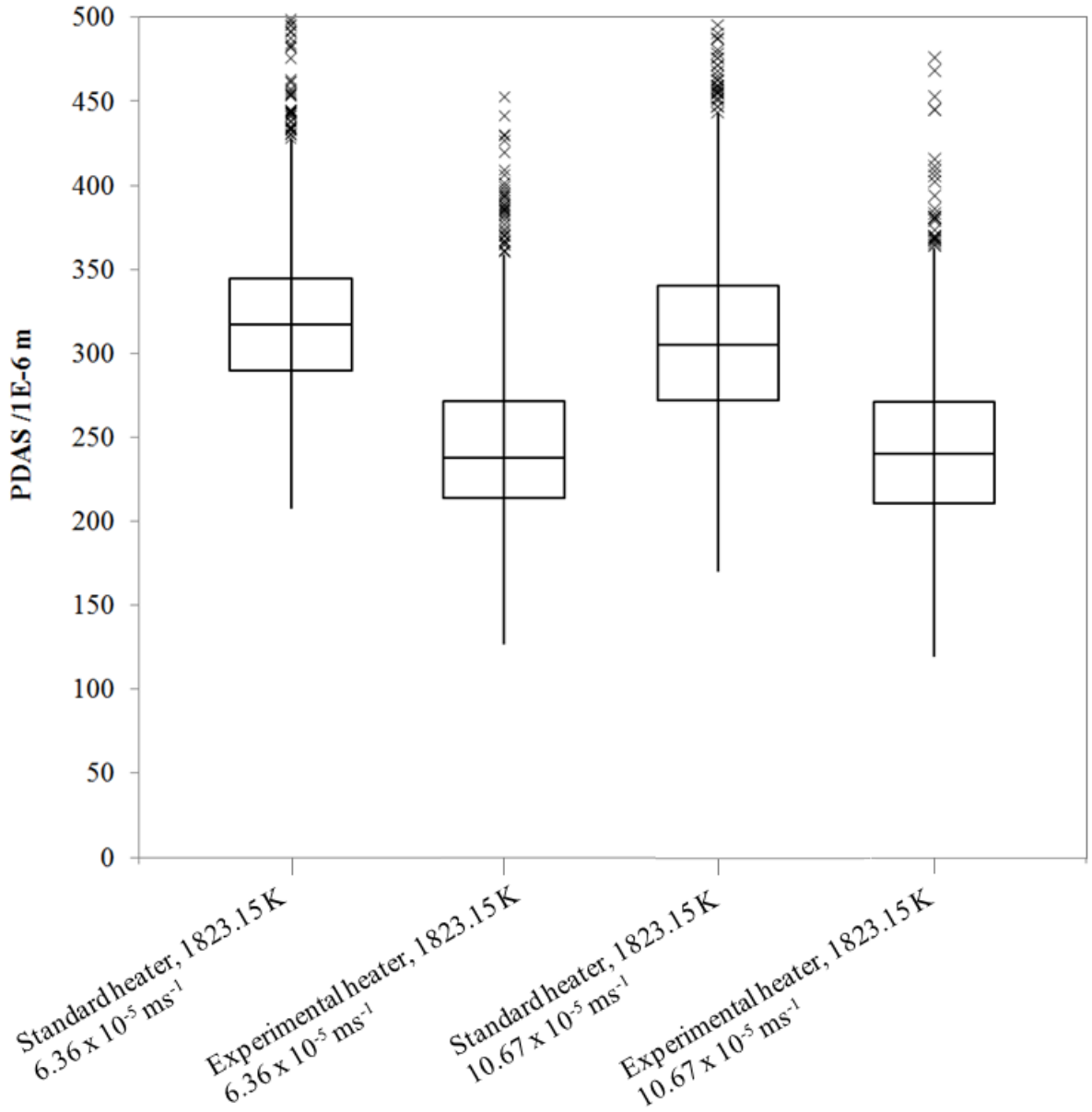


Figure 6-3: Box plot representation of primary dendrite arm spacing averaged over a distance between 20 x 10^{-3} and 120 x 10^{-3} m above the restriction showing the effect of heater design and withdrawal speed on the microstructure.

The variation in dendrite arm spacing within each test bar for withdrawal velocities of 6.36×10^{-5} $m.s^{-1}$ and 10.67×10^{-5} $m.s^{-1}$ is shown in Figure 6-4 and Figure 6-5 respectively, where the linear trend lines for PDAS distribution with each sample is also plotted.

With the exception of the sample cast using the experimental heater at a withdrawal velocity of 6.36×10^{-5} $m.s^{-1}$ all the other samples show the same trend of the PDAS reducing (indicating a slight increase in the thermal gradient given a constant solidification front velocity) as the distance away from the seed selector, and hence chill, is increased. The PDAS for all specimens varies from the mean by between 3 - 6.2%.

This seems counter intuitive as one might expect the thermal gradient to be at its maximum, and hence PDAS at its minimum, in areas close to the chill and seed selector where heat loss by radiation is also contributed to by conduction heat loss through the chill.

It is not clear whether there is any correlation between the PDAS values along the length of the test bars and the furnace condition or if the variation is an occurrence of statistical variations.

One plausible explanation is that in the initial stages of a casting, the solidification front, which is assumed to be the same as the ram withdrawal velocity, is maintained in a higher than normal position with respect to the radiation baffle by the enhanced conduction cooling through the chill.

Upon commencing the withdrawal, the effect of the conduction cooling will gradually decrease and therefore the position of the solidification front will move towards an equilibrium position which will effectively increase the solidification velocity and hence the apparent withdrawal velocity, thus marginally reducing the PDAS.

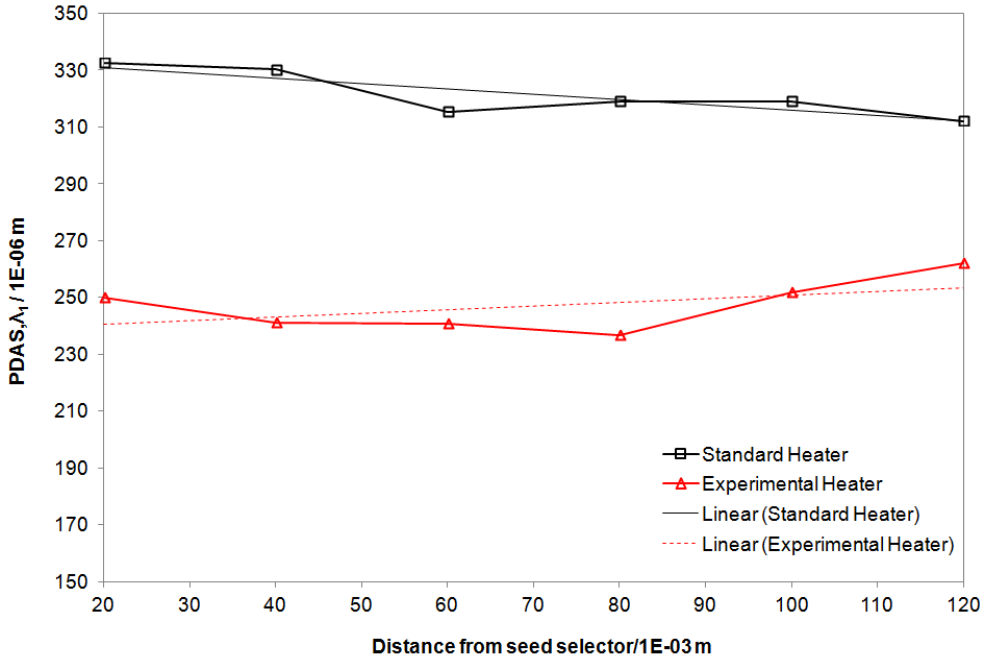


Figure 6-4: Variation in PDAS as a function of height within the test bar i.e. axial distance from the seed selector, where the seed selector = 0. The furnace parameters were a hot zone reference temperature of 1823.15 K, a 110 x 10^{-3} m ID baffle and a withdrawal velocity of 6.36 x 10^{-5} m.s^{-1}.

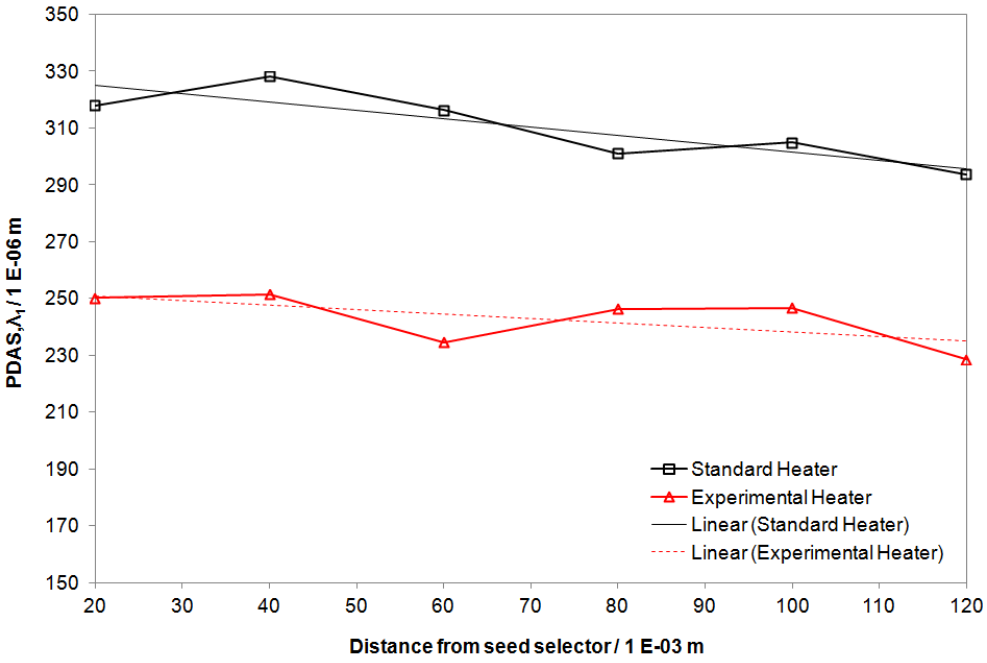


Figure 6-5: Variation in PDAS as a function of height within the test bar i.e. axial distance from the seed selector, where the seed selector = 0. The furnace parameters were a hot zone reference temperature of 1823.15 K, a 110 x 10^{-3} m ID baffle and a withdrawal velocity of 10.67 x 10^{-5} m.s^{-1}.

The thermal gradient achieved during casting can also be derived from the relationship between solidification velocity, and dendrite arm spacing described by equation 2.21 and is shown in Figure 6-6 and Table 6-2.

It can be seen from Figure 6-6 that the maximum thermal gradient achieved occurred when casting at the slower withdrawal velocity; this is a function of the mushy zone geometry and position.

The experimental heater showed the greatest degradation of thermal gradient; a decrease of around 26% in comparison to the standard heating element of around 17% during the transition between the withdrawal velocities of 6.36×10^{-3} $m.s^{-1}$ 10.67×10^{-3} $m.s^{-1}$, however at either withdrawal velocity the experimental heater produced the greatest thermal gradient.

Table 6-2 give a summary of the mean measured PDAS and derived thermal gradient for all experimental conditions. It can be seen that for this furnace set-up, and nominally identical casting conditions, the experimental heater shows a clear improvement in both reducing PDAS and increasing thermal gradient.

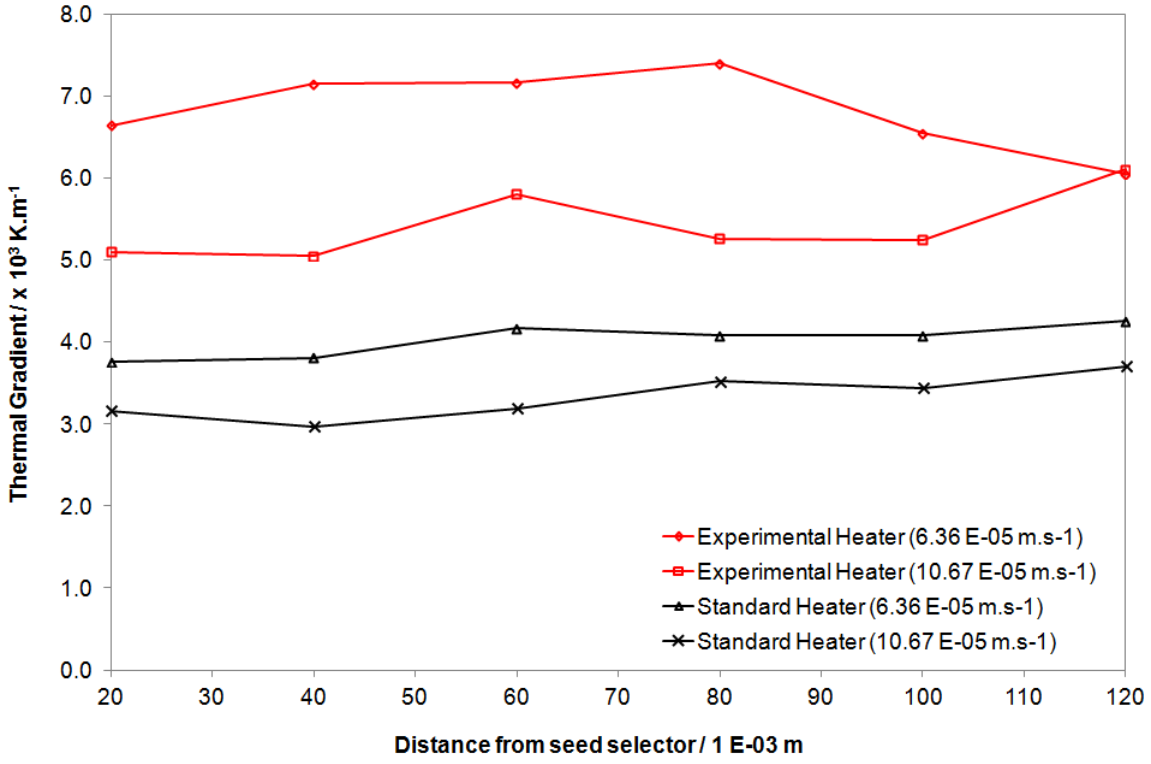


Figure 6-6: Derived thermal gradient as a function of height within the test bars for all experimental conditions. The constant furnace parameters were a hot zone reference temperature of 1823.15 K and 110 x 10^{-3} m ID baffle.

Table 6-2:Thermal gradients derived from mean PDAS measurements taken for all experimental casts produced with test bar cluster.

Furnace heating element	**Withdrawal rate / x 10^{-5} ms^{-1}**	**Mean PDAS ± standard error / x 10^{-6} m**	**Dendrite count**	**Derived mean thermal gradient ± standard error / x 10^{3} $K.m^{-1}$**
Standard	6.36	321.36 ± 1.16	1793	4.02 ± 0.03
Experimental	6.36	246.96 ± 1.12	1794	6.80 ± 0.06
Standard	10.67	310.27 ± 1.31	1803	3.32 ± 0.03
Experimental	10.67	243.89 ± 1.11	1743	5.37 ± 0.05

6.2.2 Single component mould with use of extensive radiation baffling

When performing the computer models, one emerging trend was that the scope for improvement in the furnace temperature gradient and hence microstructural refinement was limited when casting with extensive baffling.

When carrying out thermocouple furnace validation experiments it appeared that, for a temperature of 1923.15 K at least, the measured thermal gradient was marginally higher when using the standard heating element in comparison to the experimental. One possible explanation is that at a temperature of 1923.15 K the temperature at the base of the experimental heating element is simply too high and produces a heat flux beyond the cooling capabilities of the furnace.

Having said that, the magnitude of difference between the thermal gradients for both heating element designs were marginal when using extensive baffling and were obviously not as clear as the increase in thermal gradient when experimenting with a standard 110 x 10^{-3} m ID baffle, again indicating that a balance between effective heat input in the hot zone and extraction in the cold zone is being reached.

The following experiments will quantify the finest microstructure that would be expected to be achievable by casting at a withdrawal velocity of 10.67 x 10^{-5} m.s^{-1} and explore the effect of varying hot zone temperature.

Figure 6-7 shows a range of micrographs taken of the single crystal alloy CMSX-4 cast at a withdrawal velocity of 10.67 x 10^{-5} m.s^{-1} with a baffle comprising a 20 x 10^{-3} m ID orifice, under a range of experimental conditions shown in Table 6-3.

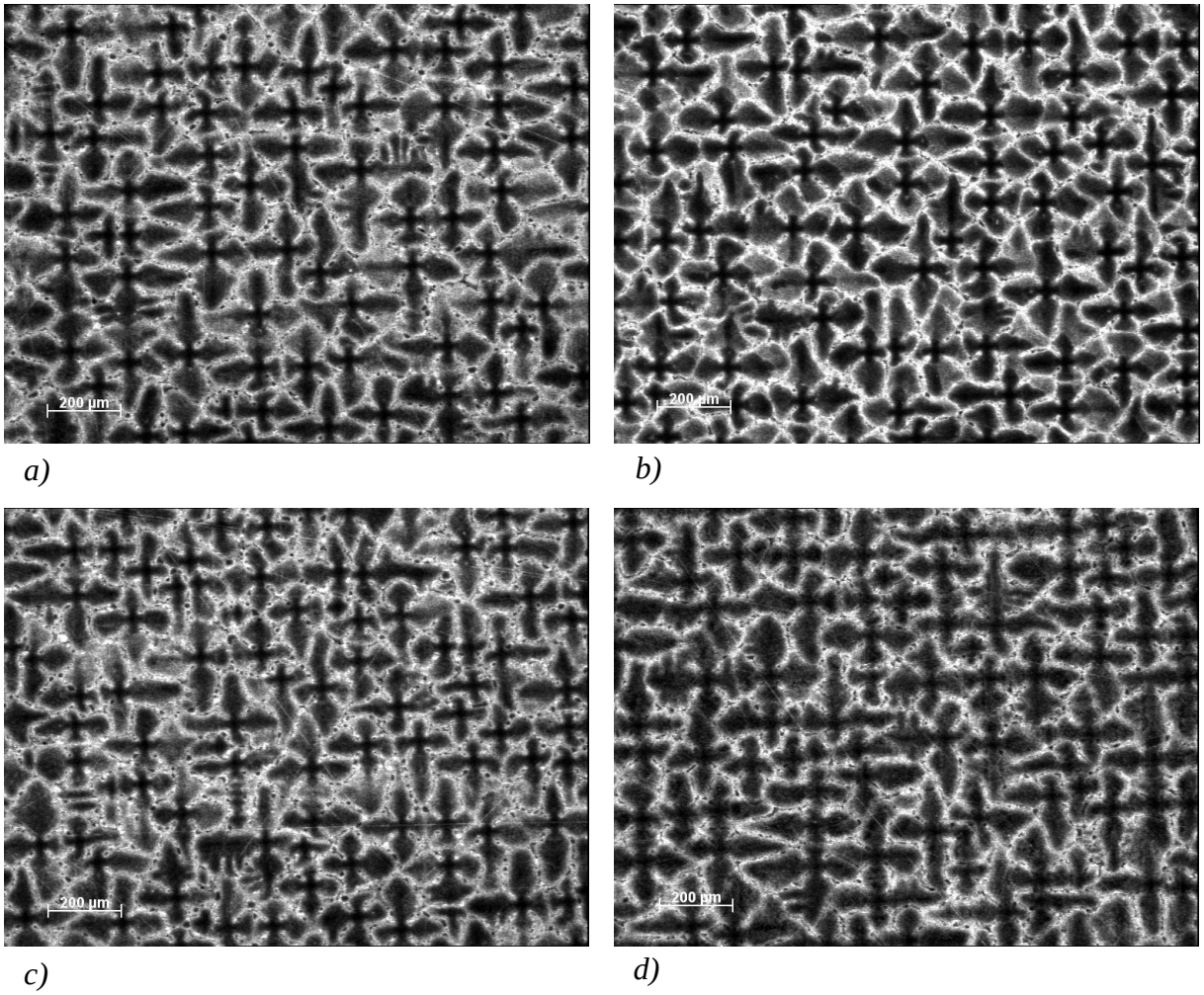


Figure 6-7: Micrographs, taken using a polarising filter in order to highlight dendrite centres, of a cross section of the single crystal alloy CMSX-4 taken at a distance of 60 x 10^{-3} m above the chill, cast at a withdrawal velocity of 10.67 x 10^{-5} m.s^{-1} with a radiation baffle comprising a 20 x 10^{-3} m ID orifice and a nominal thickness of 3.8 x 10^{-3} m. The mould comprised an alumina tube with nominal wall thickness of 2 x 10^{-3} m supported on the chill by a copper stand. The micrographs represent a combination of heater geometry and temperature; a) Standard heating element 1823.15 K, mean PDAS 169.12 x 10^{-3} m. b) Experimental heating element 1823.15 K, mean PDAS 165.63 x 10^{-3} m. c) Standard heating element, 1923.15 K, mean PDAS 153.17 x 10^{-3} m. and d) Experimental heating element, 1923.15 K, mean PDAS 154.47 x 10^{-3} m.

Experimental results for castings using a single tubular mould and a 20 x 10^{-3} m ID baffle are shown in Table 6-3 for a range of heater configurations and hot zone reference temperatures. The mean has been calculated from sites examined over a distance of 80 x 10^{-3} m, from a position of 60 x 10^{-3} m - 140 x 10^{-3} m above the seed selector; the standard error of the mean values is relatively low indicating a tight distribution in the data set, which would be expected given the number of measurements made.

Table 6-3: Mean dendrite arm spacing for a range of test bars produced using the standard and experimental heaters at a set withdrawal velocity of 10.67 x 10^{-5} $ms^{-1}$with a varying hot zone temperature of 1823.15 K or 1923.15 K. The baffle geometry used was 20 x 10^{-3} m ID Sigraflex. The standard error is an estimation of the amount the sample mean deviates from the actual mean of a population and is estimated as $s/\sqrt{n}$, where s is the sample standard deviation and n is the number of observations. The 95% confidence interval is calculated as $\bar{x} \pm 1.96 \times standard\ error$. The value of 1.96 is the normal distribution value for 95% confidence taken from normal distribution tables.

Shown in Figure 6-7	Furnace heating element	Hot zone reference temp / K	Mean PDAS ± standard error / x 10-6 m	Dendrite count	95% confidence limits for mean / x 10-6 m
a)	Standard	1823.15	169.12 ± 0.89	1527	167.37 – 170.87
b)	Experimental	1823.15	165.63 ± 0.84	1282	163.98 – 167.29
c)	Standard	1923.15	153.17 ± 0.79	1550	151.62 – 154.71
d)	Experimental	1923.15	154.47 ± 0.78	1479	152.94 – 155.99

The results indicate that when using either heating element there is a decrease in PDAS for the higher temperature configuration which is in agreement with previous work which recommends that the furnace hot zone temperature should be set as hot a possible where practicable (Horrocks, 1990a), Newell, 2009). Using either furnace heating element there is a distinct difference between calculated confidence intervals for hot zone temperatures of 1823.15 K and 9123.15 K.

The lowest PDAS was achieved using the standard heating element with a hot zone reference temperature of 1923.15 K, which is in agreement with the earlier validation work which indicated that in this configuration the standard heater may offer a slightly higher thermal gradient. However as also suggested earlier, the results in this configuration are marginal as shown by the calculated confidence intervals for the expected range of PDAS values.

At a hot zone temperature of 1823.15 K the experimental heating element produces the lowest PDAS values with no overlap between the confidence interval PDAs values.

The distribution of dendrite arm spacing is shown as a box plot diagram in Figure 6-8. The centre horizontal line in the box represents the median value and the outer horizontal lines on each box represent the upper and lower quartile. The extended vertical lines reach maximum and minimum values that are not outliers.

As discussed in the previous section, the proliferation of outliers in the upper PDAS value range are likely due to the interpretation technique and only represent a small percentage of the entire dataset.

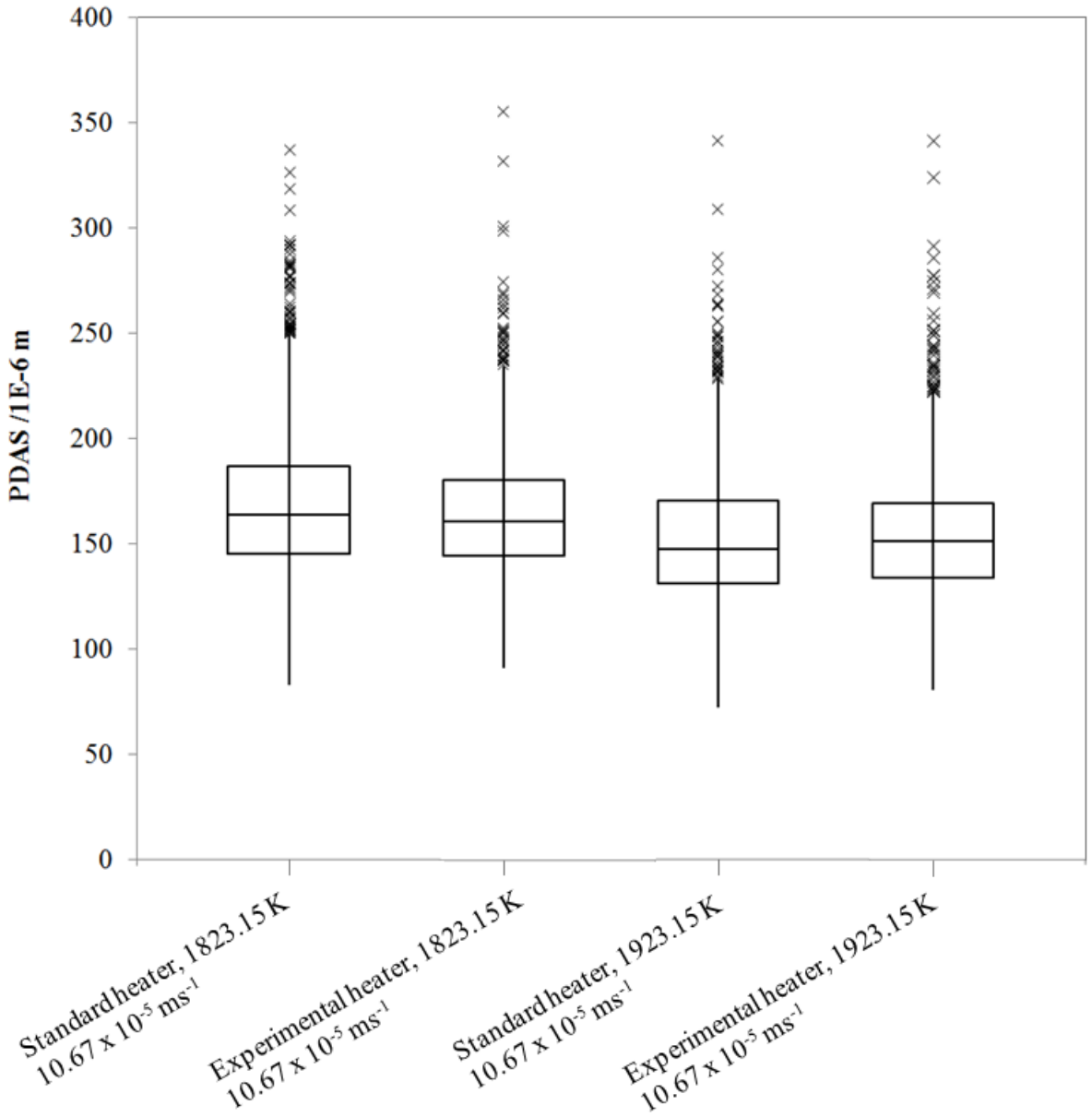


Figure 6-8: Box plot representation of primary dendrite arm spacing averaged over a distance between 60 x 10-3 and 140 x 10-3 m above the restriction showing the effect of heater design and hot zone reference temperature on the microstructure.

The variation in PDAS values along an 80 x 10^{-3} m section of the test bars are shown in Figure 6-9. There is a high degree of uniformity within each sample and a clear distinction between the 1823.15 K and 1923.15 K temperature ranges as also discussed previously and shown in Table 6-3.

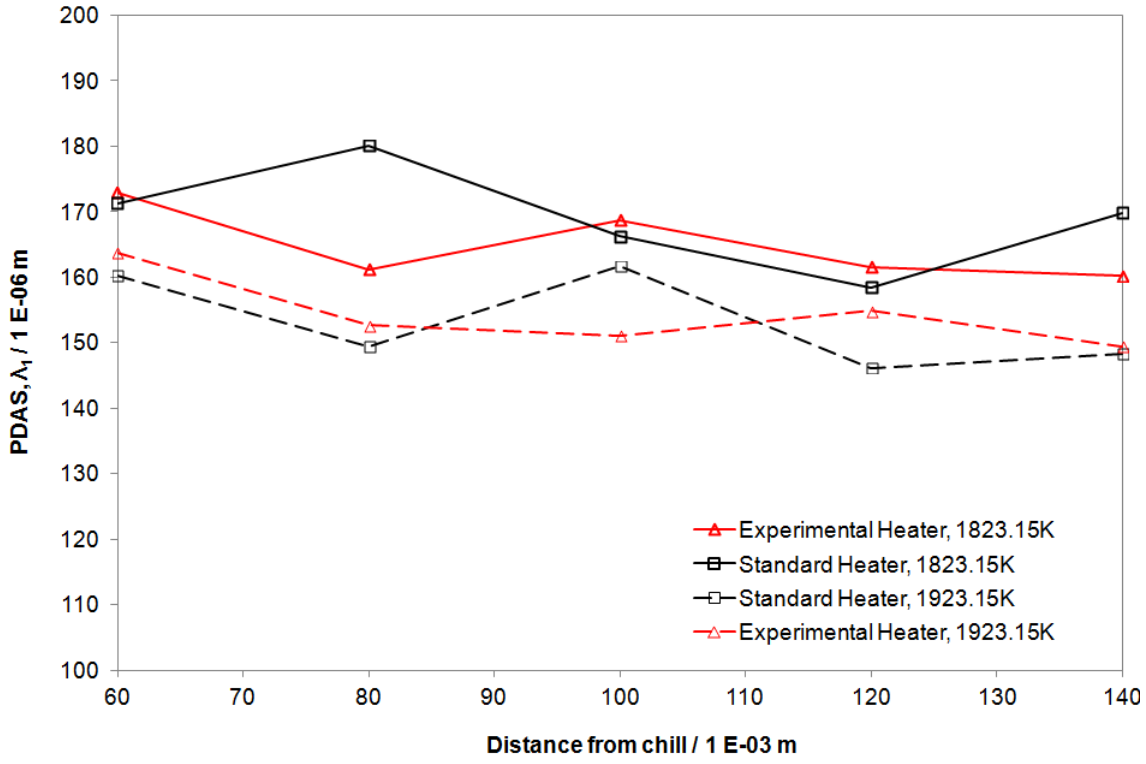


Figure 6-9: Variation in PDAS as a function of height within the test bar i.e. axial distance from the seed selector, where the seed selector = 0. The furnace parameters were a withdrawal velocity of 10.67 x 10^{-5} m.s^{-1}, 20 x 10^{-3} m ID baffle and hot zone reference temperature of 1823.15 K or 1923.15 K.

The thermal gradient achieved during the casting has also been determined from the standard relationship discussed previously and is shown in Figure 6-10 at given positions along the test bar corresponding to locations where PDAS has been measured; linear trend lines have also been plotted.

Again, a distinction between the thermal gradients achieved and the corresponding hot zone reference temperature is observed.

Plotted linear trend lines indicate, as expected from the PDAS results, that for a higher furnace hot zone temperature the standard heating element shows a marginally higher thermal gradient whereas the opposite trend is observed at a lower temperature.

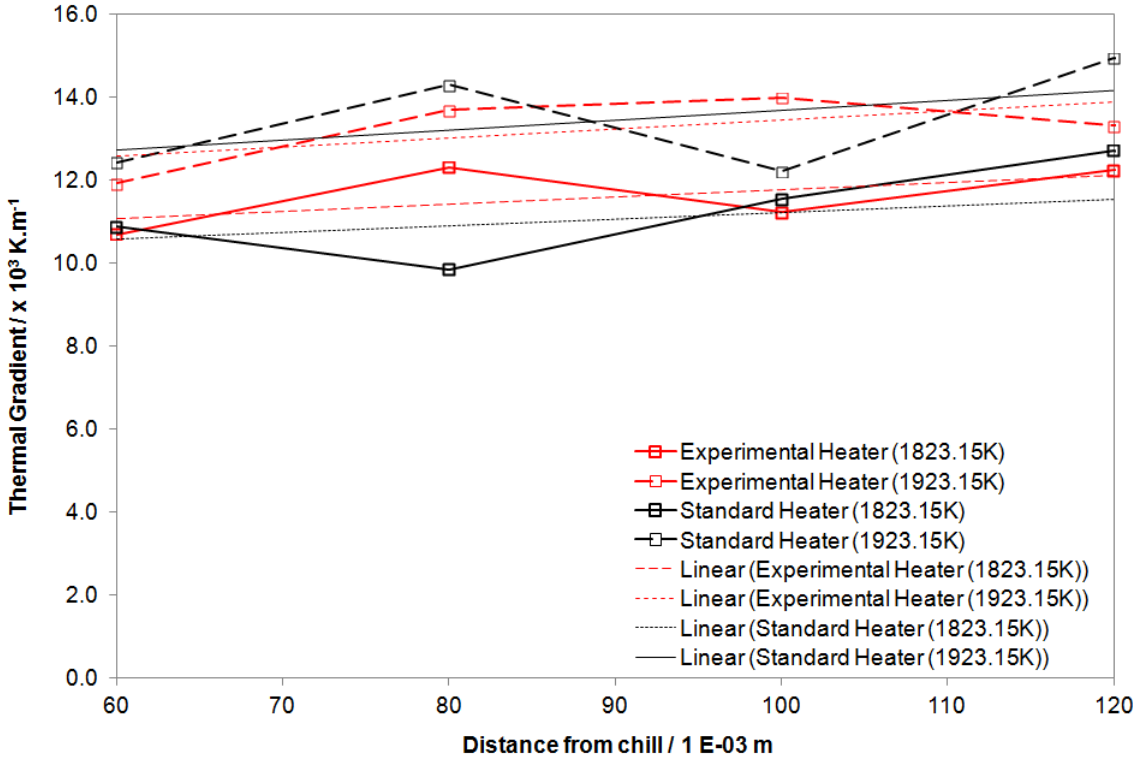


Figure 6-10: Derived thermal gradient as a function of height within the test bars for all experimental conditions. The constant furnace parameters were a withdrawal rate of 10.67 x 10^{-5} m.s^{-1} and 20 x 10^{-3} m ID baffle.

Table 6-4 shows the derived mean thermal gradient calculations along with measured PDAS for all experimental conditions and it can be seen from these results that the effect of using a modified heating element is limited when using extensive radiation baffling.

The greatest reduction in PDAS when comparing both heating elements occurs when using the experimental heating element with a hot zone reference temperature of 1823. 15 K, and represents a ~2% reduction in comparison to the values obtained using the standard heating element.

Overall, the greatest reduction occurs when changing the hot zone reference temperature from 1823.15 K to 1923.15 K for both heating elements, with a 9.4% reduction in PDAS for the standard heating element and a 6.4% reduction for the experimental.

Table 6-4: Thermal gradient measurements derived from mean PDAS measurements for all experimental conditions. The constant furnace parameters were a withdrawal rate of 10.67 x 10^{-5} m.s^{-1} and 20 x 10^{-3} m ID baffle.

Furnace heating element	**Hot zone reference temp / K**	**Mean PDAS ± standard error / x 10^{-6} m**	**Dendrite count**	**Derived mean thermal gradient ± standard error / x 10^{3} K.m^{-1}**
Standard	1823.15	169.12 ± 0.89	1527	11.16 ± 0.12
Experimental	1823.15	165.63 ± 0.84	1282	11.63 ± 0.12
Standard	1923.15	153.17 ± 0.79	1550	13.60 ± 0.14
Experimental	1923.15	154.47 ± 0.78	1479	13.38 ± 0.13

6.2.3 Eutectic alloy casting

The single crystal alloy cast thus far using the 20 x 10-3 m ID baffle have resulted in microstructures that, once extrapolated, result in a thermal gradient higher than has currently been achieved using the Bridgman furnace in question (Newell, 2009).

This is a direct result of driving up the hot zone temperature to the limits of the controllable level, optimised heat input position, by use of the experimental heater, and the use of restrictive baffle geometry.

Consequently, these furnace parameters will be useful in order to determine the feasibility of casting eutectic alloys and also make estimations of the limits of the furnace capability in this respect.

The CFX model is a steady state model and does not easily calculate transient problems in which domains are required to move i.e. 'moving meshes'; an important characteristic when simulating the Bridgman casting process. This is an attribute that the ProCAST model performs particularly well.

However, owing to the particularly slow withdrawal/solidification velocities unique to eutectic alloy casting (which are an order of magnitude slower than when casting single crystals), an estimation of the thermal profile achievable when casting eutectic alloys has been made using CFX by modelling an in-situ stationary mould. This has been made on the assumption that the withdrawal velocity is slow enough to negate any transient heat fluxes that may affect the position of the solidification front.

The eutectic alloys selected for this study were COTAC 744 and $\gamma - \gamma' - \delta$ (the Cr containing version) which showed the greatest creep potential when examined in

These alloys were primarily chosen by Rolls-Royce due to the promising creep potential and the relatively simple alloying elements which omit Re and Ru.

Due to an absence of adequate material data from the literature, material data required to define the alloy was calculated using JMatPro, an industry wide thermo mechanical database, based on the exact composition obtained for the γ-γ'-δ and COTAC 744 alloys, described in the Appendix.

The liquidus and solidus temperatures calculated showed reasonable agreement with published data; the melting range of the γ-γ'-δ alloy was found to be within 0.68 K of published data (Lemkey, 1973) and the onset of melting temperature of the COTAC 744 alloy was calculated to be within 9 K of published data (Rabinovitch et al., 1983, Stohr and Khan, 1980).

Table 6-5 shows the results of the CFX calculations which were carried out using the standard and experimental heating elements with hot zone reference temperatures of 1823.15 K and 1923.15 K in which the CFX control thermocouple domain was not allowed to deviate by more than ±5 K; the average temperature drift often encountered by the control thermocouples during operation.

The liquidus and solidus positions are shown for reference only and relate to the positional change to a '0, 0' reference datum within the model, however comparing the position of the interface with the calculated thermal gradient is useful.

A visual representation of selected model results calculated using the COTAC alloy are presented in Figures 6-11 to 6-14 in where the incremental increase in thermal gradient

when casting the COTAC alloy is shown for a number of heater and hot zone temperature configurations.

Table 6-5: Estimated thermal gradient achieved using standard and experimental heating elements for two eutectic alloys. The furnace parameters used were a double layer 20 x 10^{-3}m ID sigraflex baffle and hot zone reference temperatures of 1823.15 K and 1923.15 K. Calculations were made using CFX model with additional domain geometry to represent alloy, mould, chill and ram. Eutectic material data was calculated using JMatPro.

Hot Zone Temp / K	**Control TC Temp / K**	**Alloy**	**Liquidus Position / x 10^{-3} m)**	**Solidus Position / x 10^{-3} m**	**Thermal Gradient / K.m^{-3})**
Standard Heating Element					
1823.15	1818.21	COTAC	55.282	50.095	7.13
	1818.22	$\gamma - \gamma' - \delta$	38.044	36.638	12.80
1923.15	1923.2	COTAC	39.744	36.963	13.30
	1923.22	$\gamma - \gamma' - \delta$	30.495	29.272	14.72
Experimental Heating Element					
1823.15	1825.99	COTAC	47.231	43.662	10.37
	1825.98	$\gamma - \gamma' - \delta$	34.864	33.560	13.80
1923.15	1922.17	COTAC	38.446	35.834	14.17
	1922.16	$\gamma - \gamma' - \delta$	29.850	28.603	14.42

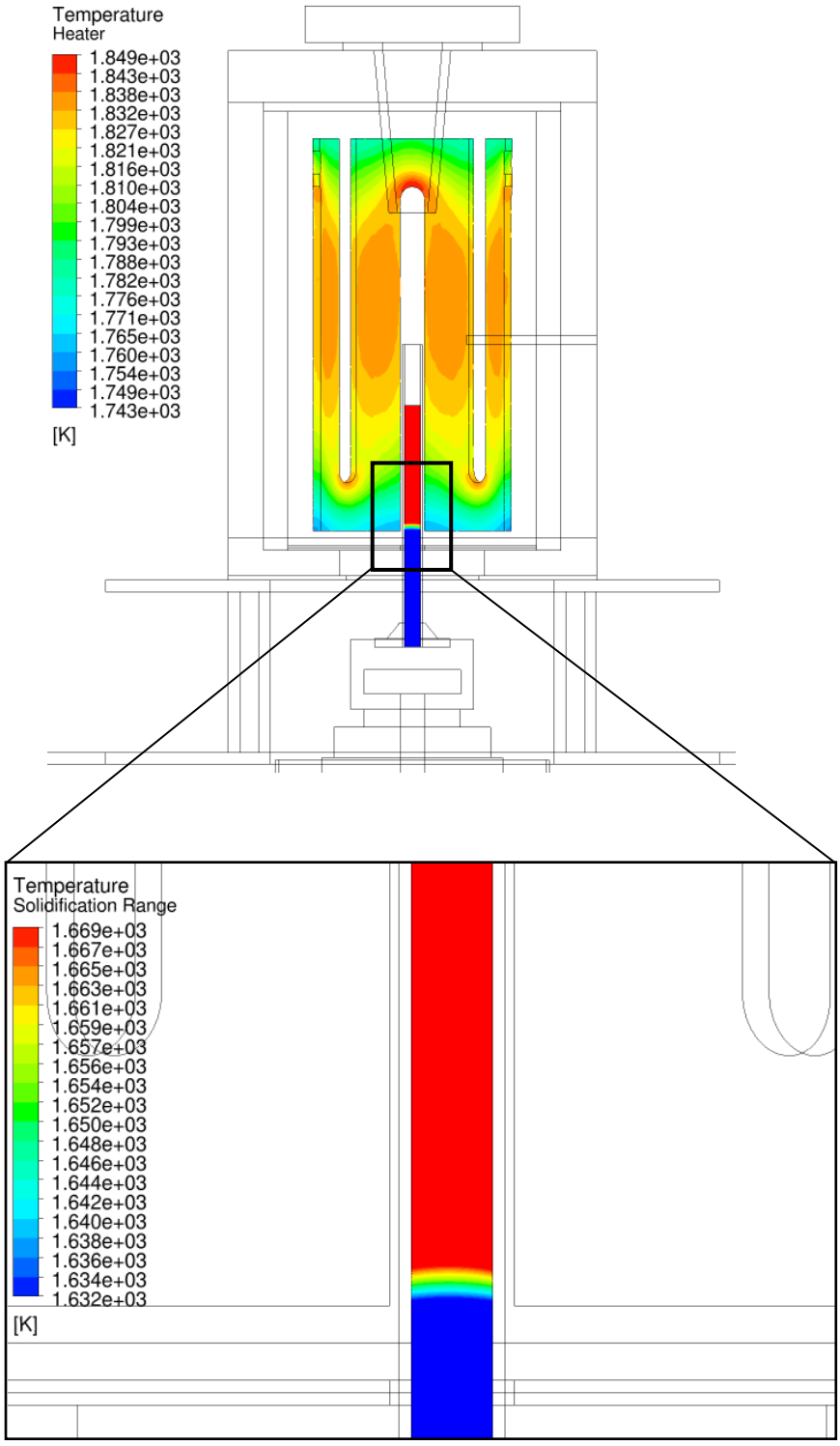


Figure 6-11: CFX model results for COTAC 744 cast in a 13 x 10^{-3} m ID alsint tube. The furnace parameters were a hot zone reference temperature of 1823.15 K using the standard heating element and a double layer 20 x 10^{-3} m ID baffle. Shown in main view is the heating element temperature contour; enlarged is the liquidus and solidus temperature range of the alloy (red liquid, blue solid).

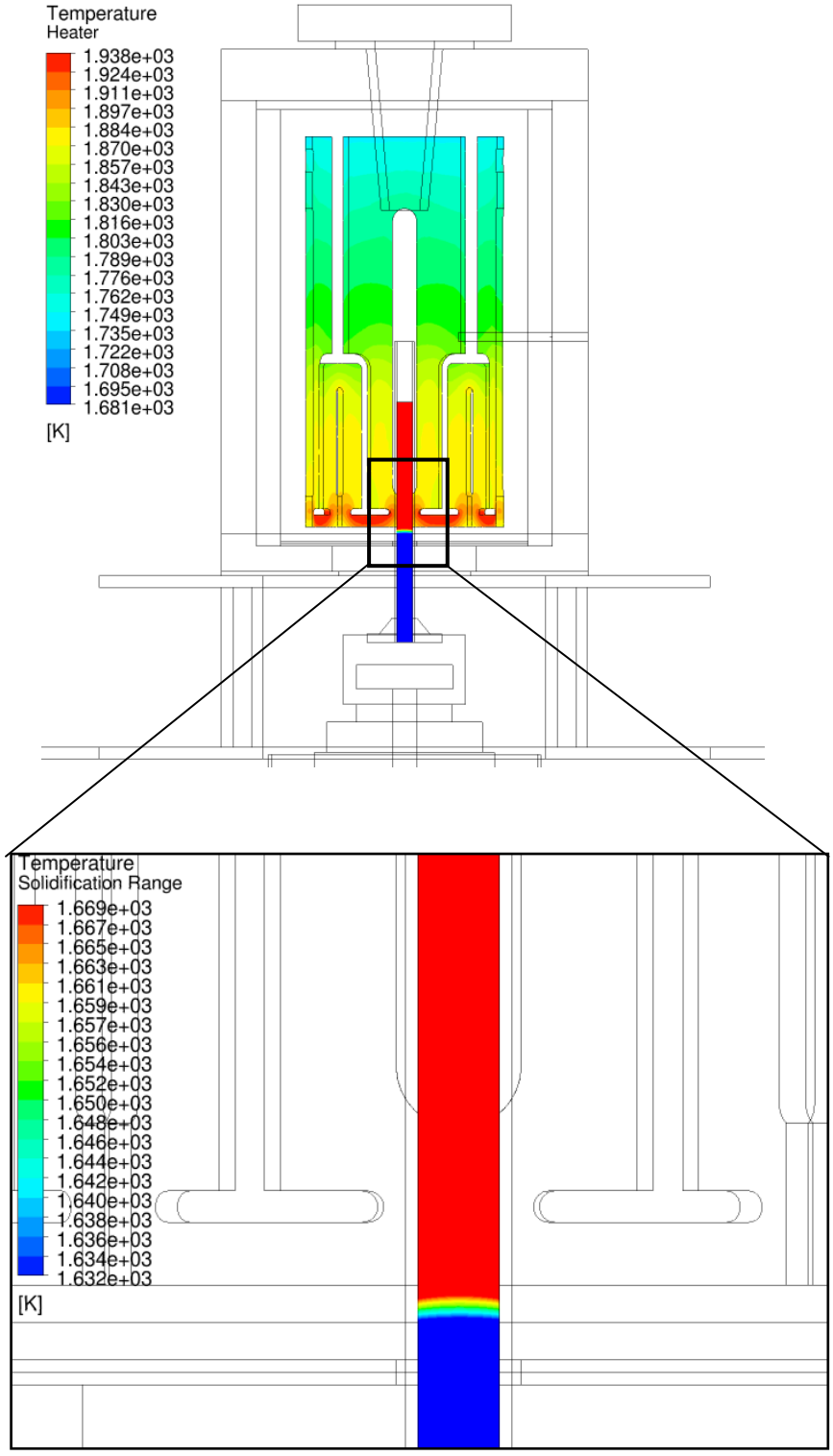


Figure 6-12: CFX model results for COTAC 744 cast in a 13 x 10^{-3} m ID alsint tube. The furnace parameters were a hot zone reference temperature of 1823.15 K using the experimental heating element and a double layer 20 x 10^{-3} m ID baffle. Shown in main view is the heating element temperature contour; enlarged is the liquidus and solidus temperature range of the alloy (red liquid, blue solid).

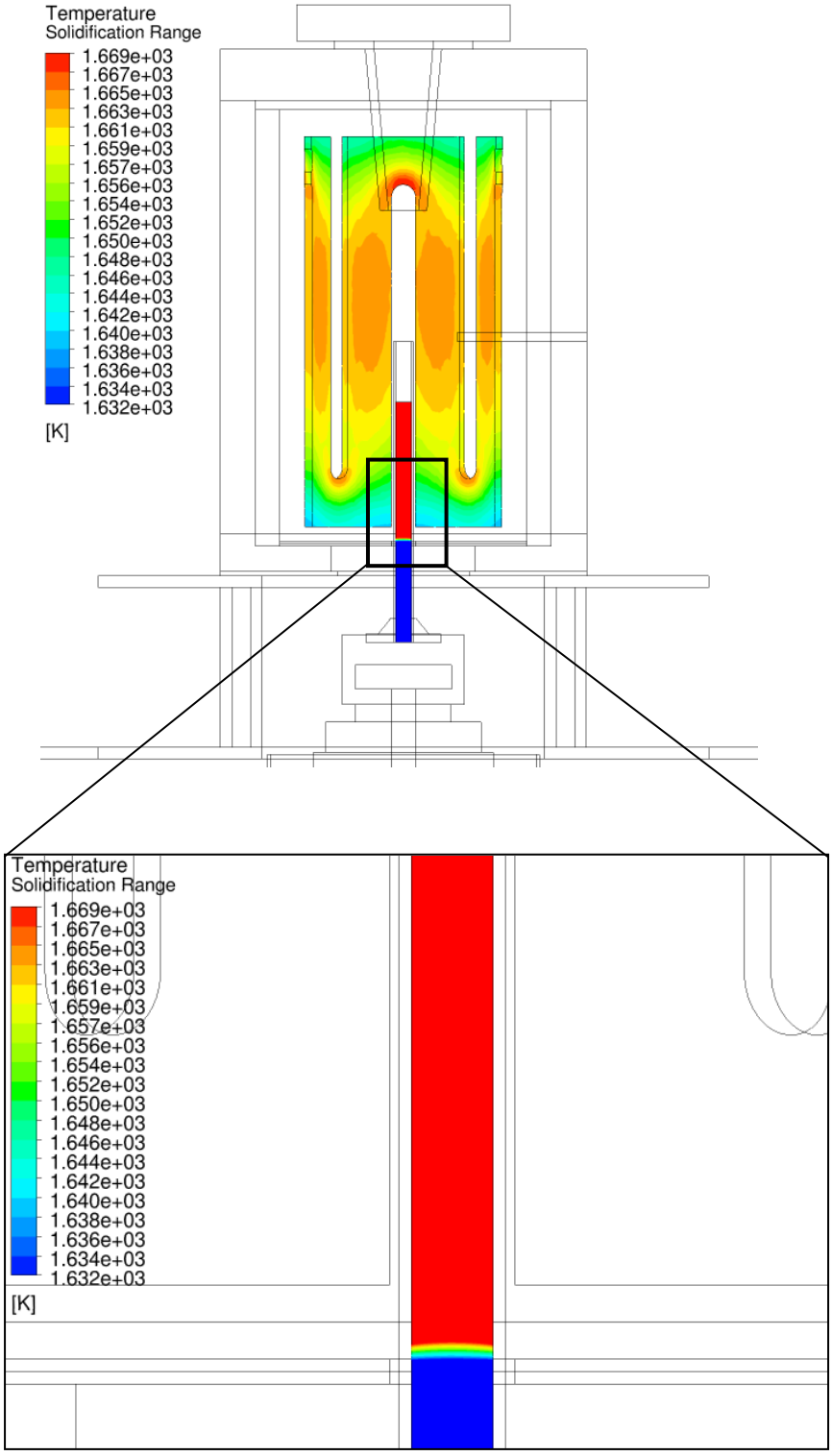


Figure 6-13: CFX model results for COTAC 744 cast in a 13 x 10^{-3} m ID alsint tube. The furnace parameters were a hot zone reference temperature of 1923.15 K using the standard heating element and a double layer 20 x 10^{-3} m ID baffle. Shown in main view is the heating element temperature contour; enlarged is the liquidus and solidus temperature range of the alloy (red liquid, blue solid).

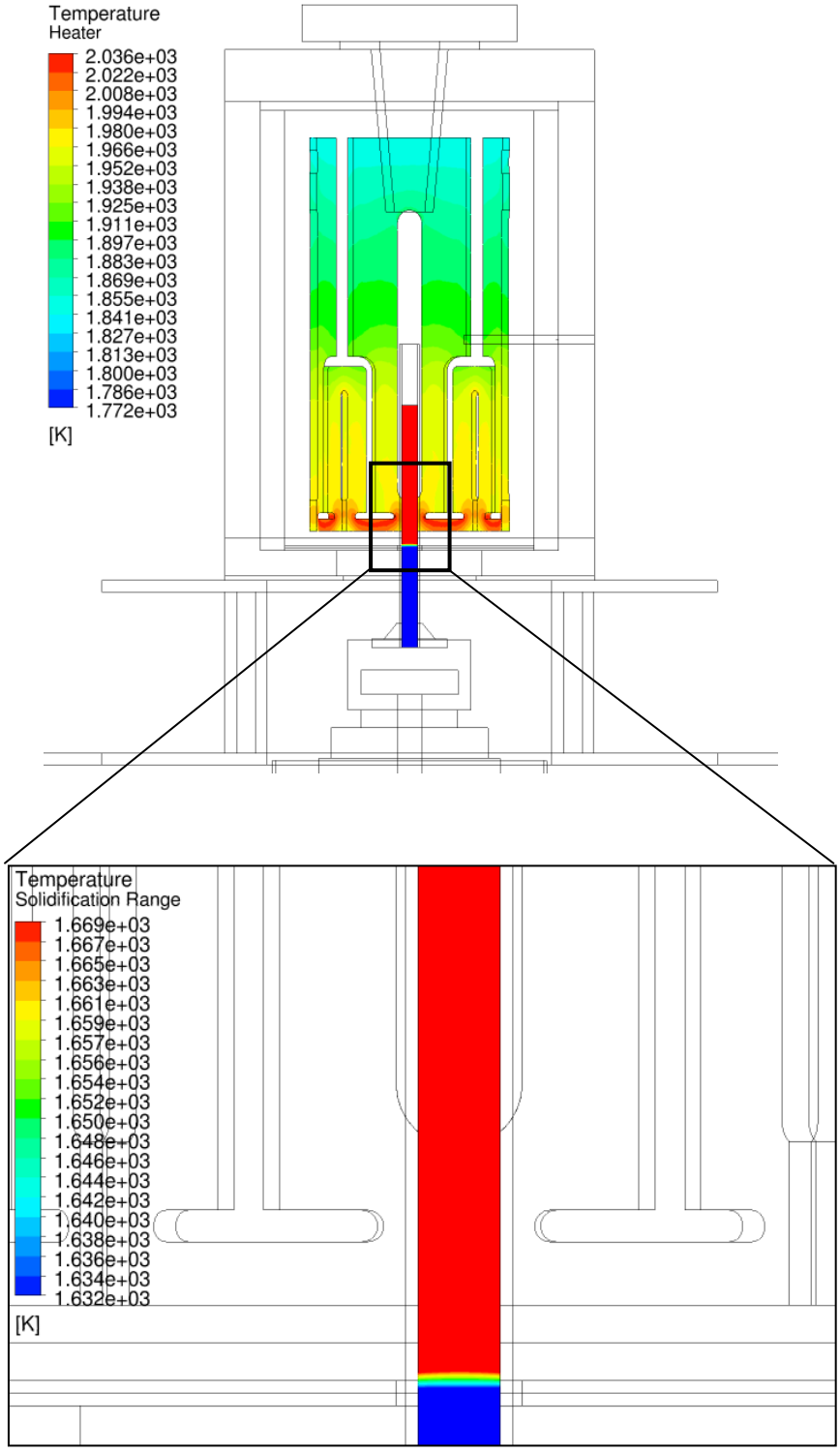


Figure 6-14: CFX model results for COTAC 744 cast in a 13 x 10^{-3} m ID alsint tube. The furnace parameters were a hot zone reference temperature of 1923.15 K using the experimental heating element and a double layer 20 x 10^{-3} m ID baffle. Shown in main view is the heating element temperature contour; enlarged is the liquidus and solidus temperature range of the alloy (red liquid, blue solid).

In a similar manner to the single crystal casting results, the highest thermal gradient is achieved with the corresponding higher hot zone reference temperature with the exception of the $\gamma - \gamma' - \delta$ alloy at a hot zone temperature of 1923.15 K in which the standard heater shows a marginally higher thermal gradient than that of the experimental heater; one possible explanation for this is the lower solidification range of the $\gamma - \gamma' - \delta$ alloy.

Due to the lower melting range, when observing the results for the experimental heater at a temperature of 1923.15 K, the solidification front can be seen to be driven down to a lower position in the cold zone with respect to the standard heater in this configuration; shown in Figure 6-15.

Even though this effect is marginal it will act to increase the mushy zone height and expose more of the mould above the liquidus temperature of the alloy to the cold zone and therefore decrease the thermal gradient. In this case the heating potential of the experimental heater essentially exceeds the cooling potential of the cold zone of the furnace.

This phenomenon does not appear to occur for the COTAC alloy as the higher melting range will require more thermal energy to alter the position of the solidification front which can be provided by the optimal heater design.

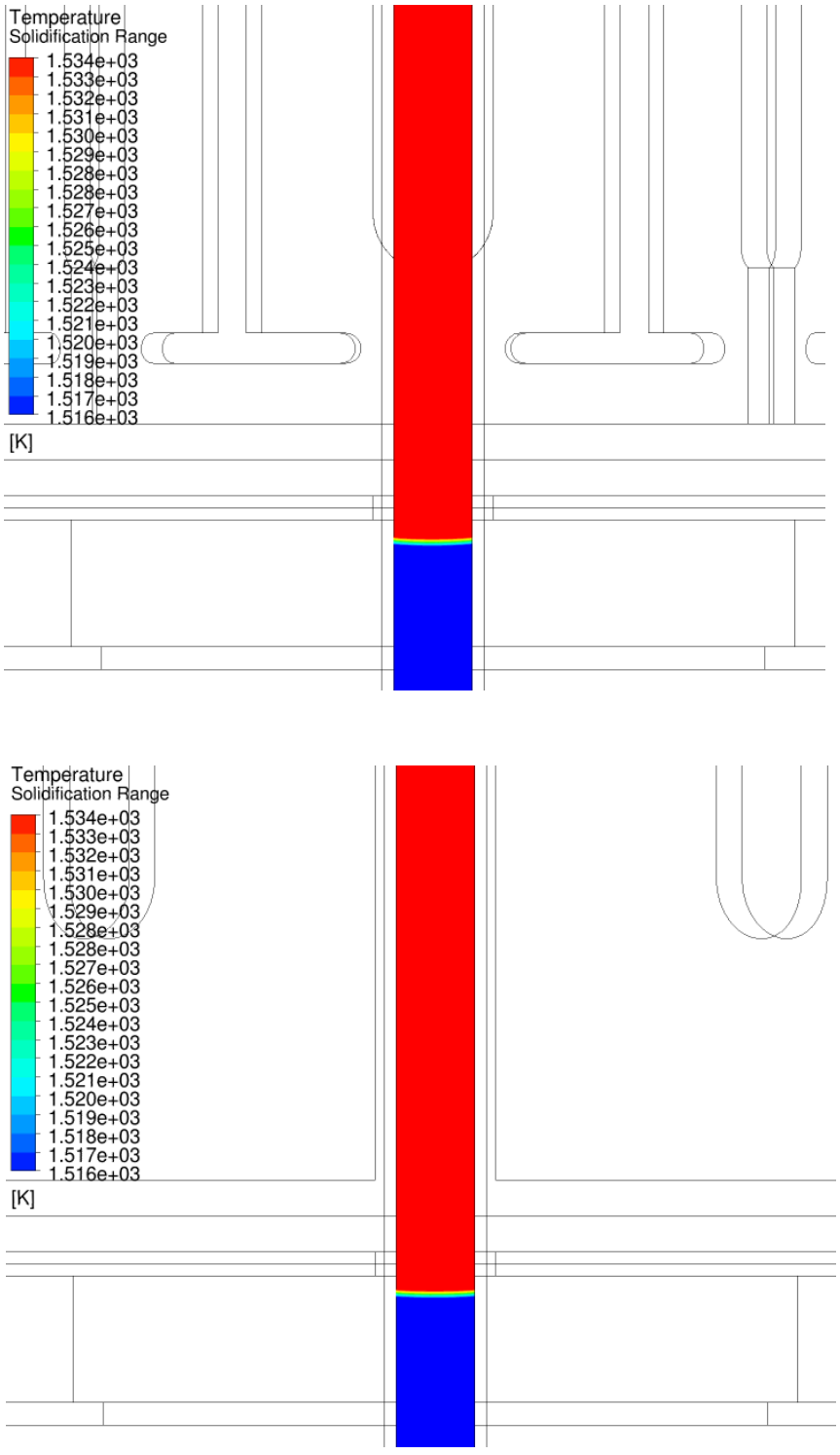


Figure 6-15: $\gamma - \gamma' - \delta$ eutectic alloy calculated using the experimental heating element (top) and standard heating element (bottom). The furnace parameters were a set hot zone temperature of 1923.15 K and comprised a 20 x 10^{-3} m ID double layer baffle.

One conclusion that may be proposed thus far is that it appears that the enhanced heating offered by the experimental heater at 1923.15 K in combination with the withdrawal rate of 10.67 x 10^{-5} m.s^{-1} for CMSX-4 has an equally negative impact of the thermal gradient as the lower melting range of the $\gamma - \gamma' - \delta$ alloy; both attributed to the deficiency of the cooling offered by the radiation dominant cold zone.

A number of experimental casts were carried out using the COTAC alloy, as this is more castable in comparison to the $\gamma - \gamma' - \delta$ alloy, noted by the lowest reported G/V ratio (Lemkey, 1973, Stohr and Khan, 1980).

The alloy was cast for a number of withdrawal velocities, varying from 9 x 10^{-3} m.hr^{-1} to 15 x 10^{-3} m.hr^{-1}. As the thermal gradient can be determined from the CFX calculations, a table of solidification velocity, V and G/V can be compiled giving reference to the as-cast microstructure, and is shown in Table 6-6.

From these results the associated G/V ratio of the alloy composition can be determined and is within the range of 0.94-1.09 K hr mm^{-2} which is consistent with values reported in literature; approximately 0.96 – 1.25 K hr mm^{-2} (Stohr and Khan, 1980).

Table 6-6: Summary of withdrawal velocity and G/V ratio on the microstructure of COTAC 744 alloy

Withdrawal Velocity / x 10^{-3} m.hr^{-1}	Calculated G/V ratio / K hr mm^{-2}	Microstructure Comments
9.48	1.40	Aligned, coarsely spaced fibres
10.43	1.28	Aligned. Large increase in number of fibres i.e. spacing reduced
11.38	1.17	Aligned
12.26	1.09	Aligned, further reduction in fibre spacing
14.22	0.94	Initial formation of cellular boundaries
15.14	0.88	Cellular

Metallographic analyses were carried out on successful casts with an aligned microstructure by polishing and etching. Figure 6-16 shows a longitudinal micrograph of an aligned COTAC 744 test bar cast at a withdrawal velocity of 12.26 x 10^{-3} m hr^{-1}, the enlarged view showing the transition from aligned to dendritic structure achieved by accelerated withdrawal and quench in the cold zone, while Figure 6-17 shows a further magnified view of the strengthening fibres along with an SEM image showing the precipitate strengthening within the Ni matrix.

Transverse sections and are shown in Figure 6-18 and Figure 6-19 for a number of withdrawal velocities ranging from 9.48 – 12.26 x 10^{-3} m hr^{-1}.

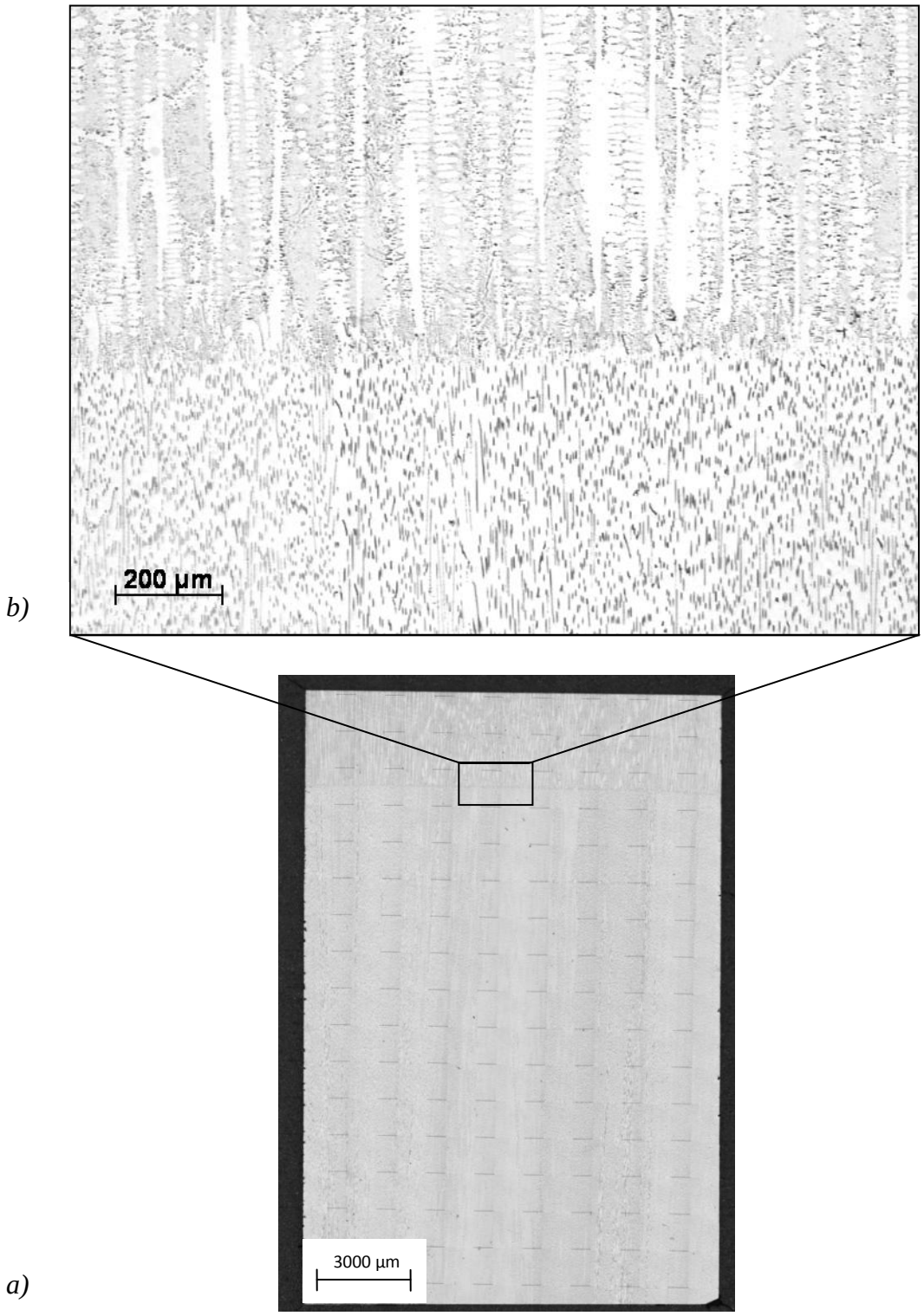
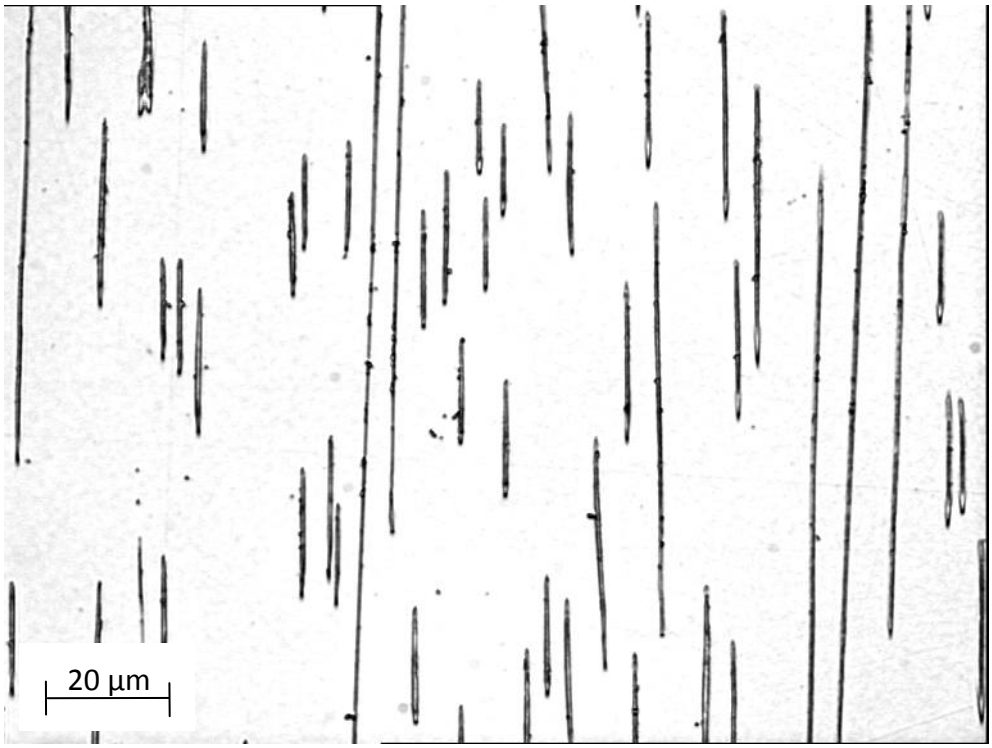


Figure 6-16: Micrograph of longitudinal section of COTAC 744; a) View of entire cross section of 12 x 10^{-3} m diameter test bar. b) Enlarged view of section showing aligned to dendritic transition

a)



b)

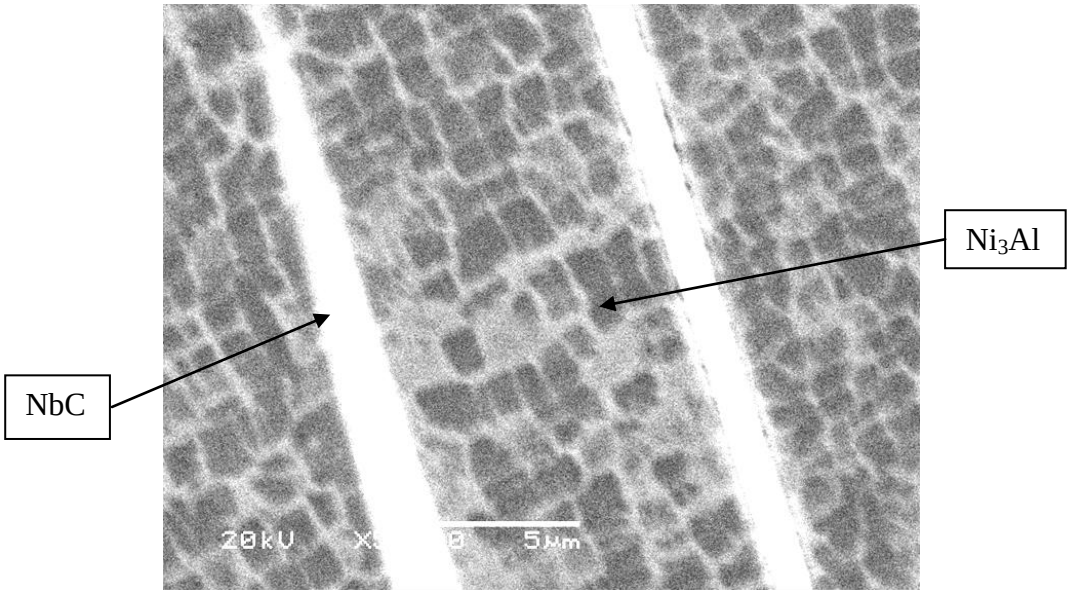


Figure 6-17: a) magnified longitudinal view showing strengthening fibres within Ni matrix. b) SEM image showing precipitate strengthening phase within the matrix and strengthening fibres

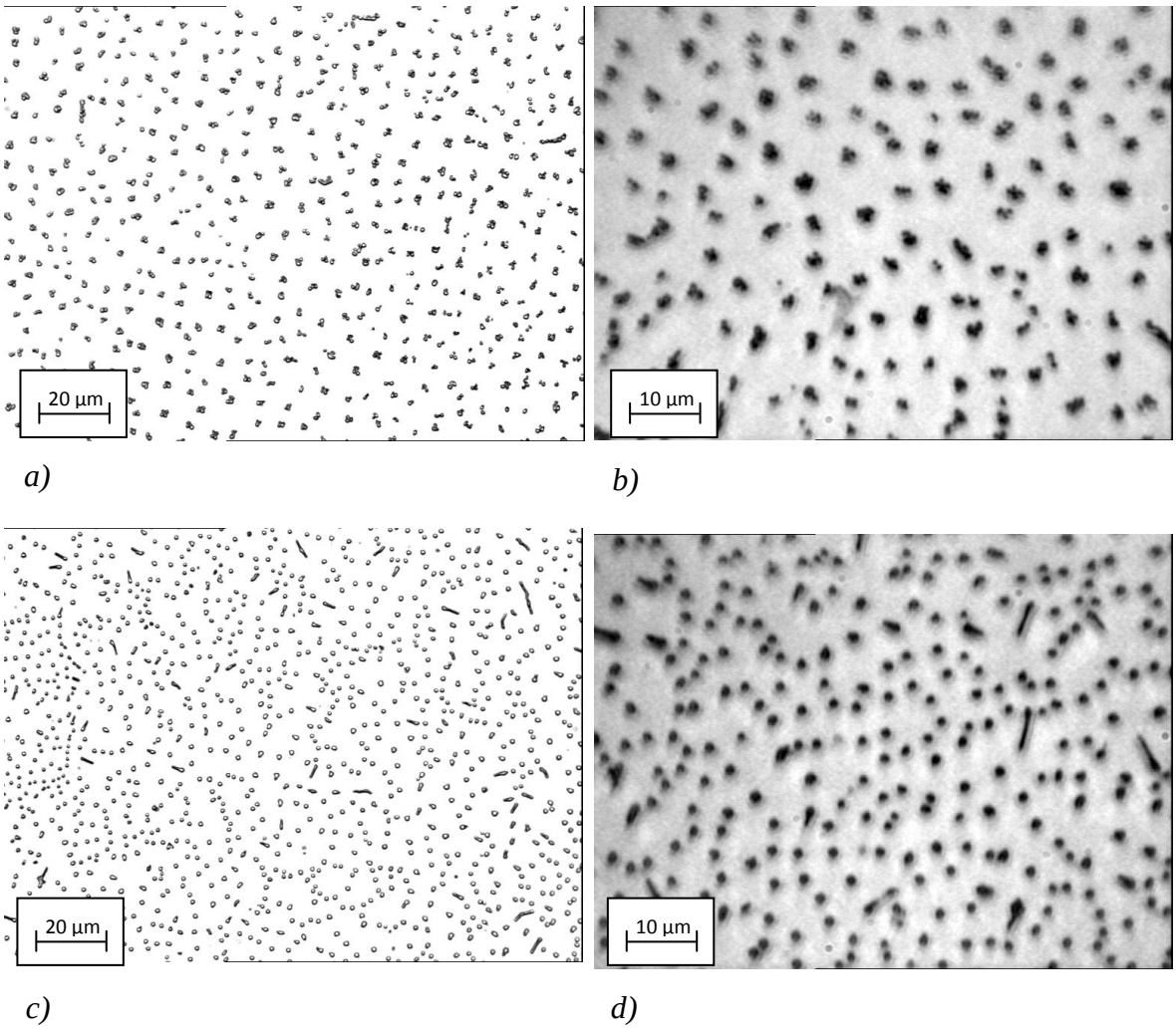


Figure 6-18: Micrographs showing transverse sections of eutectic alloy COTAC 744 cast at varying withdrawal velocities, assumed to be equivalent to solidification velocity; a) 9.48 x 10^{-3} m/hr 50x magnification, b) 9.48 x 10^{-3} m/hr 100x magnification c) 10.43 x 10^{-3} m/hr 50x magnification d) 10.43 x 10^{-3} m/hr 100x magnification.

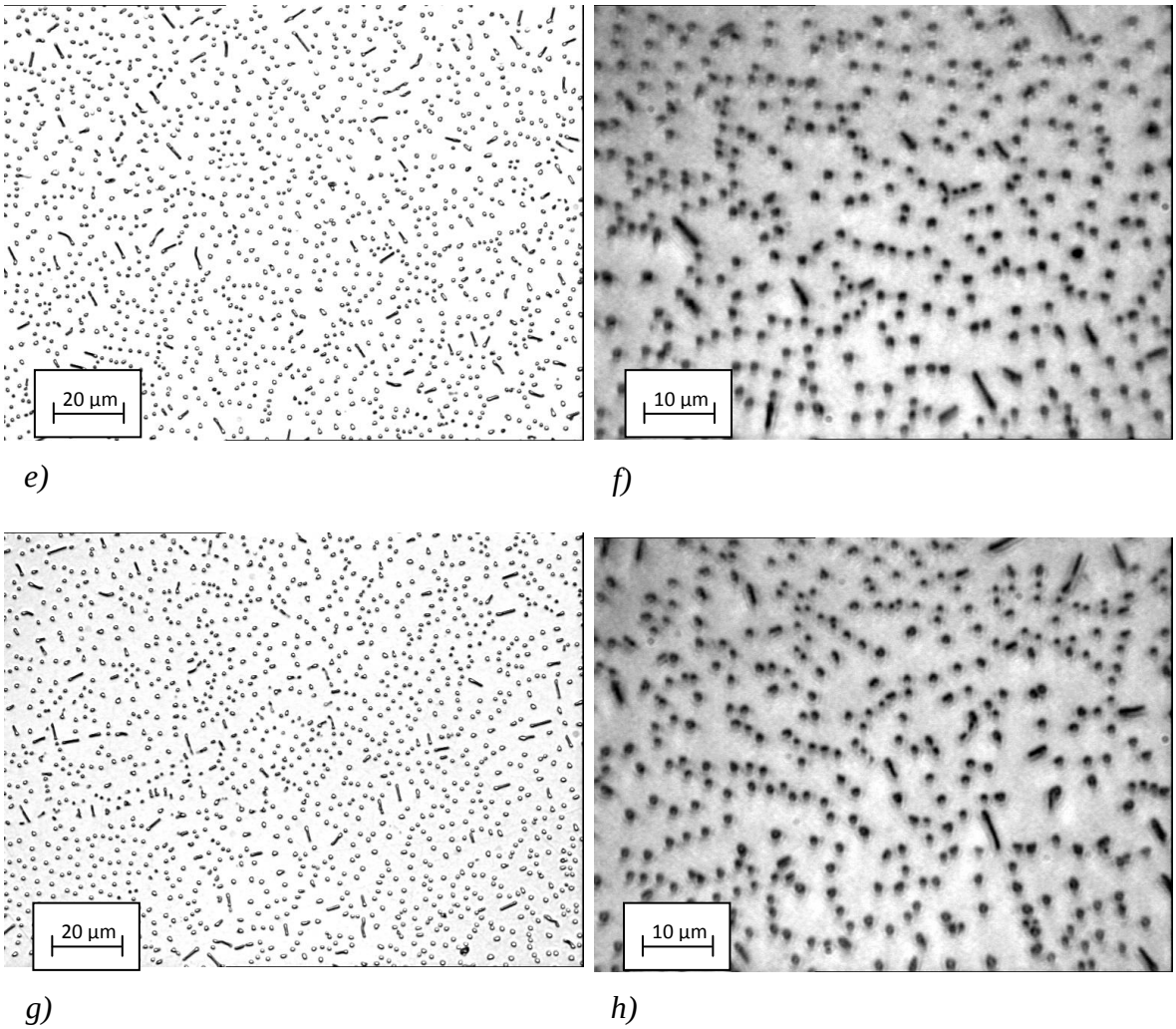


Figure 6-19: Micrographs showing transverse sections of eutectic alloy COTAC 744 cast at varying withdrawal velocities, assumed to be equivalent to solidification velocity; e) 11.38 x 10^{-3} m/hr 50x magnification, f) 11.38 x 10^{-3} m/hr 100x magnification g) 12.26 x 10^{-3} m/hr 50x magnification h) 12.26 x 10^{-3} m/hr 100x magnification.

The variation of phase spacing for a given solidification rate, which has been discussed in Chapter 2, can clearly be seen when observing Figure 6-18 and Figure 6-19; measurements of phase spacing for a number of cross sections have been taken and are shown in Figure 6-20.

The data trend appears to deviate slightly from the 'standard' derived $\lambda^2 V = K$ relationship; however the refinement of the microstructure with increased withdrawal velocity is clearly evident.

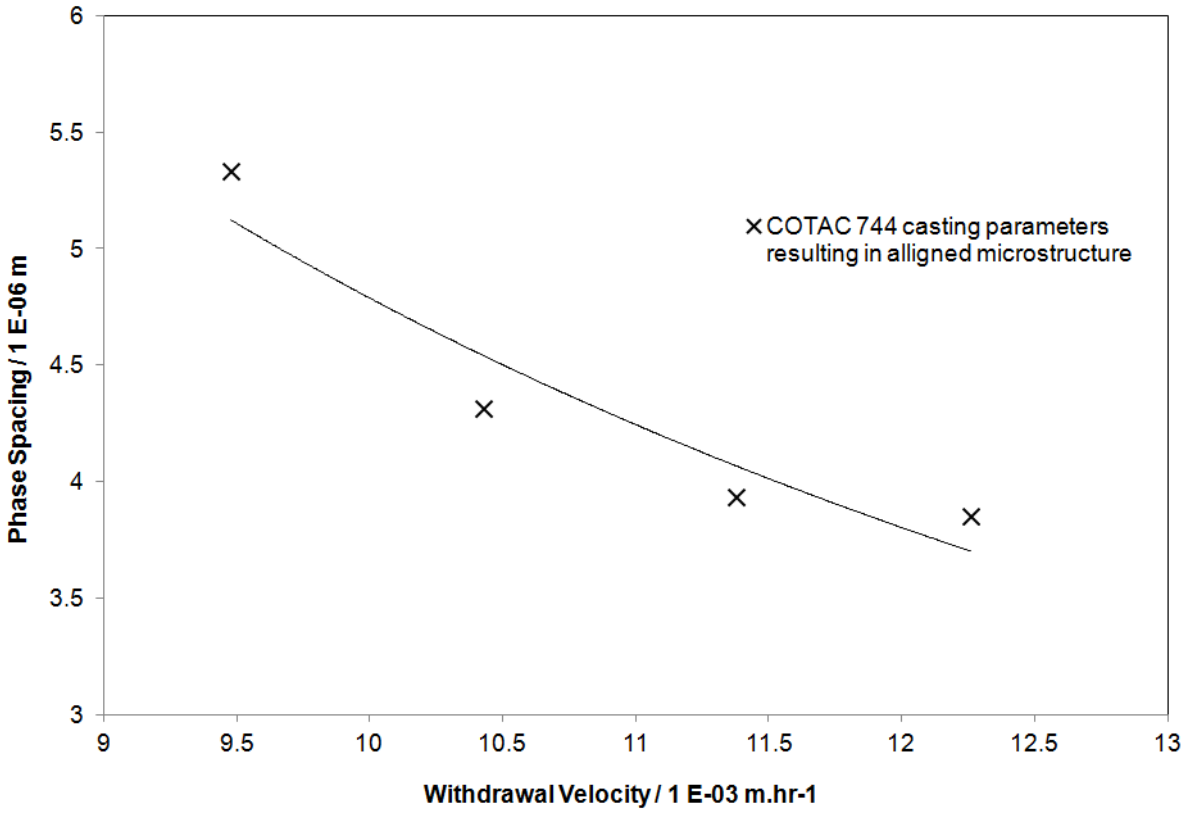
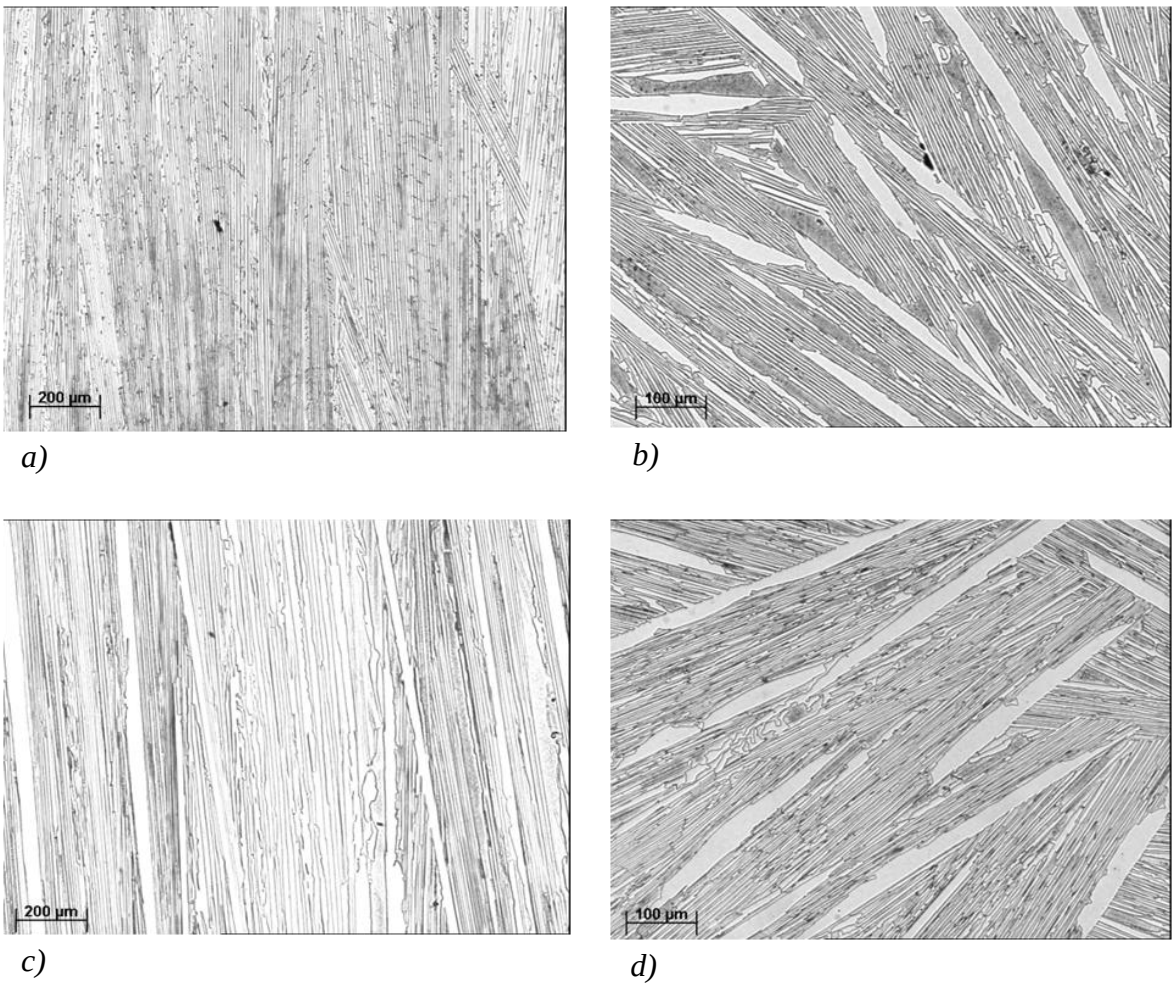


Figure 6-20: Variation in phase spacing for rate of solidification (assumed to be equivalent to withdrawal velocity) when casting COTAC 744.

The $\gamma - \gamma' - \delta$ alloy was also cast experimentally, although as this alloy exhibits a larger G/V ratio of around 1.5 K hr mm^{-2} (Lemkey, 1973), the alloy was only cast at one withdrawal velocity of 8 x 10^{-3} m hr^{-1}, as the restriction in casting velocity limited the number of casts that could be carried out and therefore the velocity increments would not be sufficiently different to make any kind of statistical statement about the microstructure.

Nonetheless, observations of the microstructure have been made and are shown in Figure 6-21.



a) *b)*

c) *d)*

Figure 6-21: Longitudinal, a) & c), and transverse, b) & d,) sections of the $\gamma - \gamma' - \delta$ alloy, cast at a withdrawal velocity of 8 x 10^{-3} m hr^{-1}.

When comparing micrographs a), b) and c),d) a certain degree of coarsening of the microstructure can be observed where sections a) and b) are located closer to the chill, ~60 x 10^{-3} m away, while sections c) and d) are located further up the test bar. A magnified view of a longitudinal section can be seen in Figure 6-22.

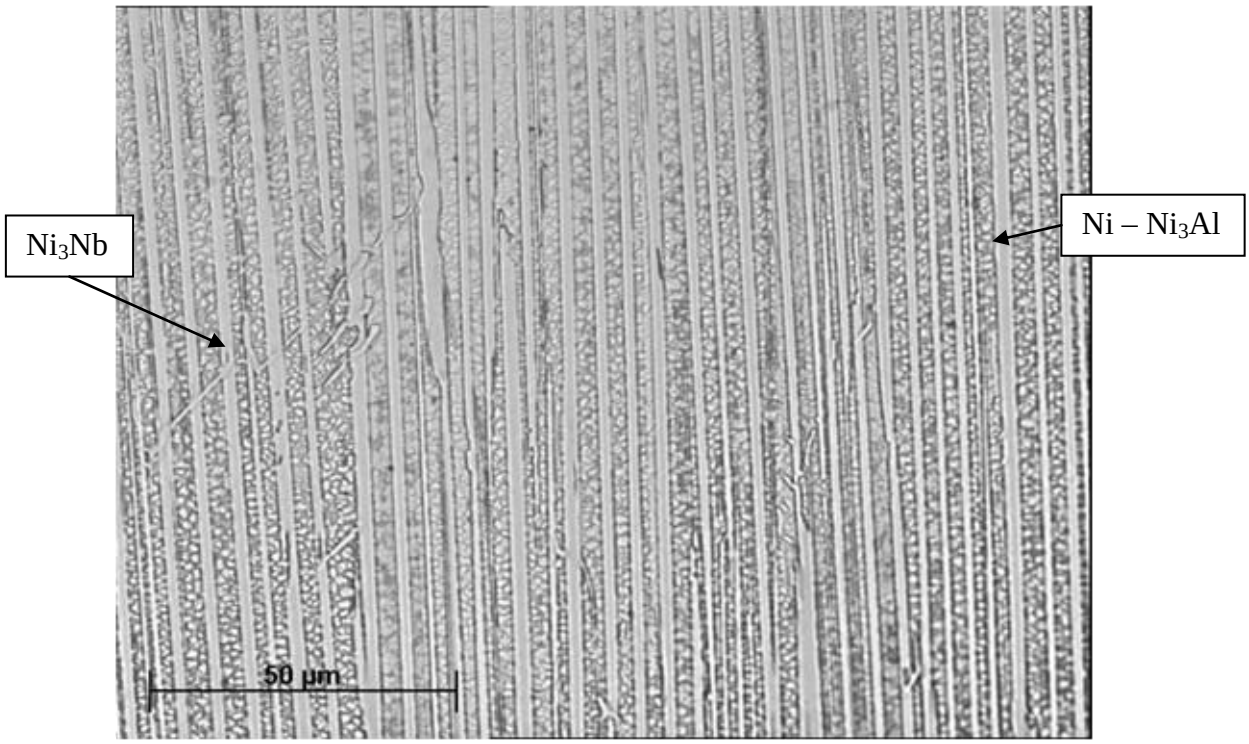


Figure 6-22: Longitudinal section view of the eutectic alloy $\gamma - \gamma' - \delta$ annotated to show the matrix and precipitate phase and the Ni_3Nb strengthening phase.

An interesting comparison and 'sanity check' with regard to the CFX models is to compare the interface shapes of the $\gamma - \gamma' - \delta$ and COTAC alloy experimental casts with results from the CFX models when both are cast at the same hot zone reference temperature; shown in Figure 6-23 for the $\gamma - \gamma' - \delta$ alloy and Figure 6-24 for COTAC 744.

Owing to the lower melting range of the $\gamma - \gamma' - \delta$ alloy, the interface shape observed is concave, predominantly due to the lower amount of heat energy required for the phase change from solid to liquid. In this case the heat energy supplied by the hot zone appears to

be greater than the heat lost in the cooling zone; in effect an energy imbalance.

This has been discussed earlier, and is a probable reason why the experimental heater was less effective at casting the $\gamma - \gamma' - \delta$ alloy when set to a higher hot zone reference temperature, as the enhanced heat energy supplied in the hot zone was not needed in such magnitudes to melt the alloy and could simply not be dissipated into the cold zone.

This is in contrast with the COTAC alloy which has a higher melting range and as such requires more thermal energy to melt. The interface shape for this alloy has been observed to be convex/flat given identical casting conditions as the $\gamma - \gamma' - \delta$ alloy.

Given that an 'ideal' flat solid liquid interface is required, the experimental heating element would be expected to offer the greatest thermal gradient in such a case.

Lessons learnt from this experimentation are that, as reported, the thermal gradient is not an independent variable and is intrinsically linked to interface position and alloy properties.

Any deficiencies in furnace capability, not only cooling but also heating, will have ramifications when casting such alloys.

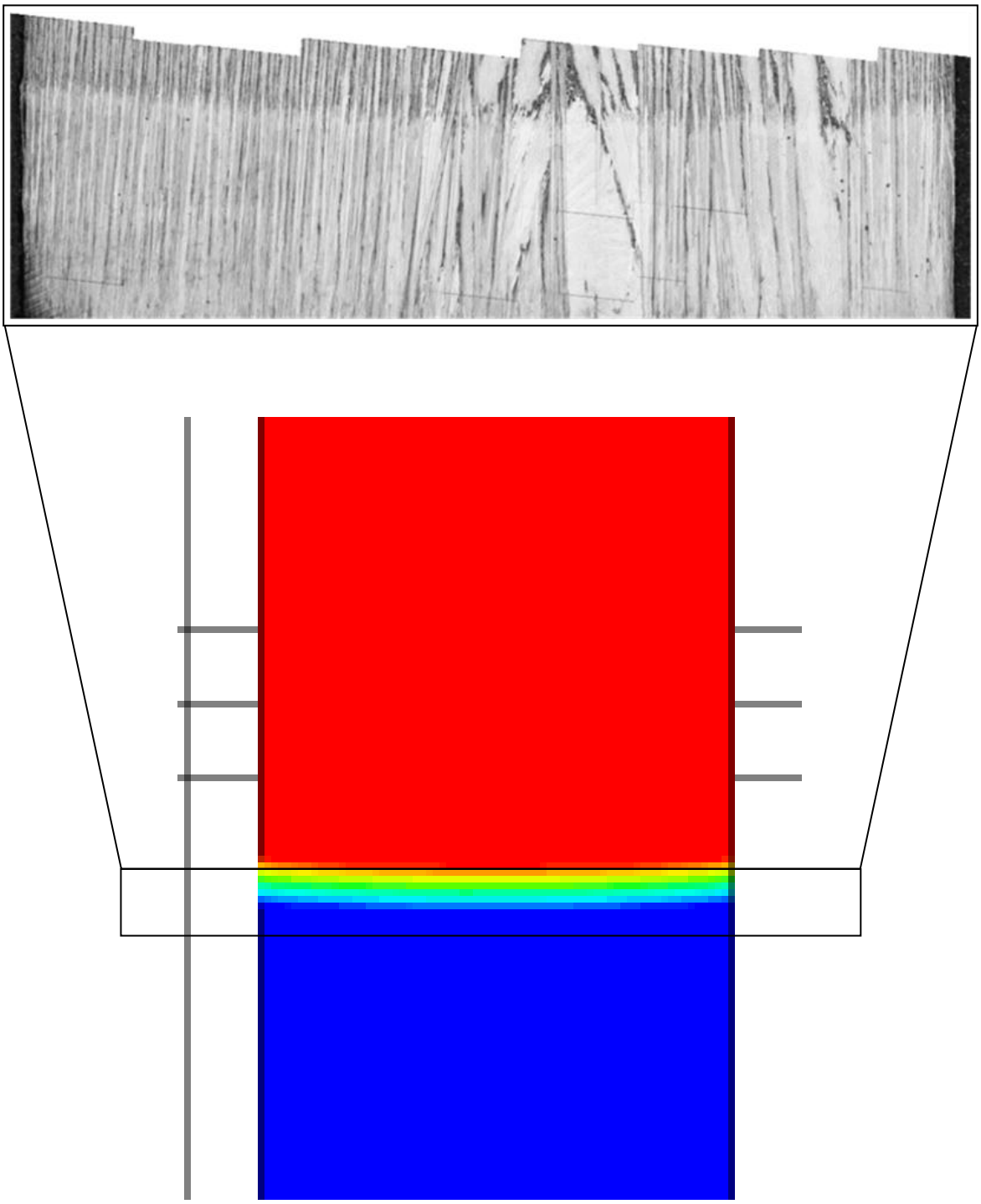


Figure 6-23: Micrograph showing interface shape of $\gamma - \gamma' - \delta$ alloy when cast using the standard heater, hot zone reference temperature of 1923.15 K and then 'quenched' in the cold zone to induce an aligned to dendritic transition. This can be compared with the solid liquid interface shape calculated using the CFX furnace model for identical conditions. The furnace baffle comprised of a two layer Sigraflex material with a 20 x 10^{-3} m ID.

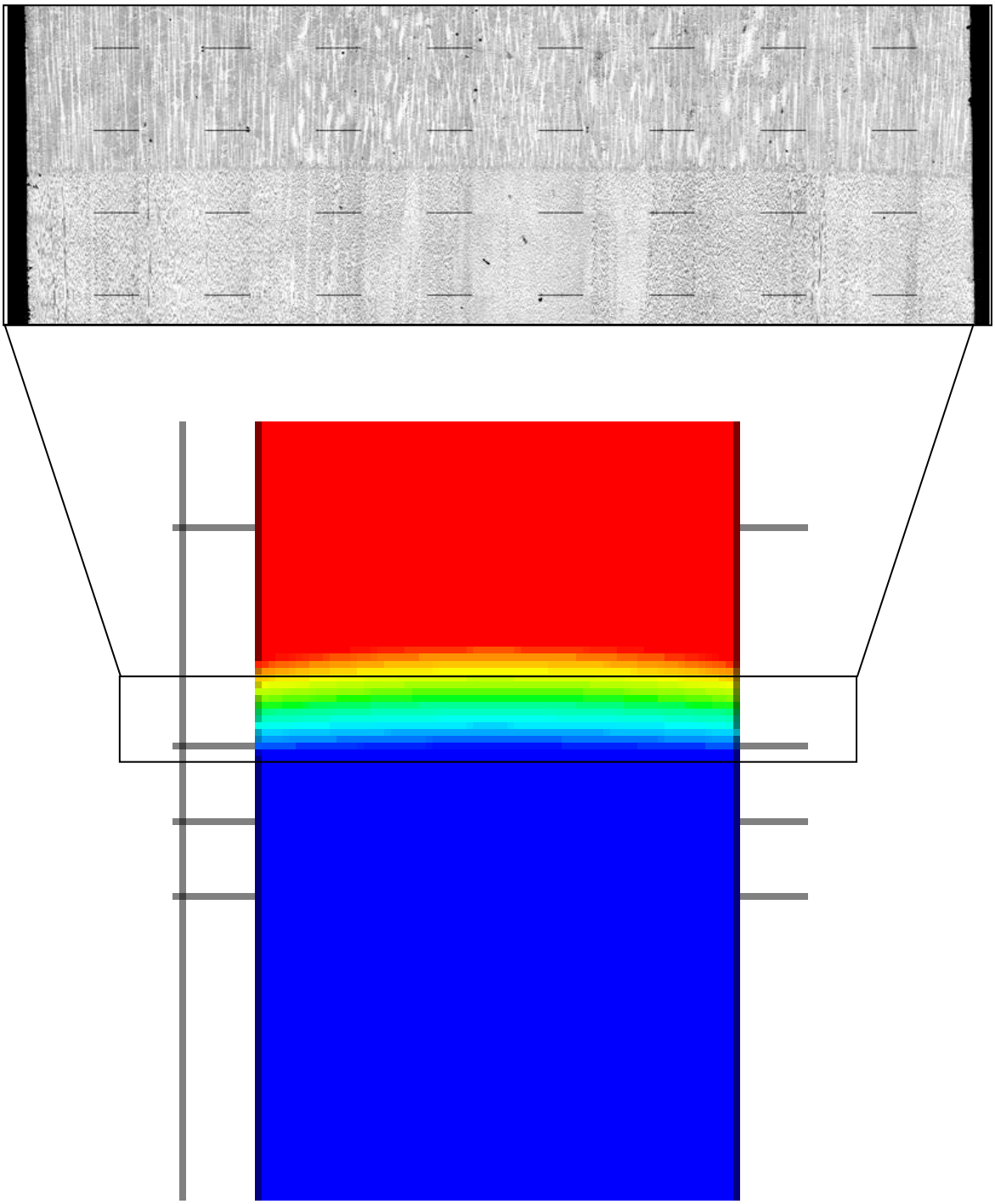


Figure 6-24: Micrograph showing interface shape of COTAC 744 alloy when cast using the standard heater, hot zone reference temperature of 1923.15 K and then 'quenched' in the cold zone to induce an aligned to dendritic transition. This can be compared with the solid liquid interface shape calculated using the CFX furnace model for identical conditions. The furnace baffle comprised of a two layer Sigraflex material with a 20 x 10^{-3} m ID.

6.2.4 VeriCAST2 validation geometry

6.2.4.1 Introduction

The VeriCAST geometry has been used on numerous occasions in order to quantify the casting capabilities of Bridgman type furnaces by analysing the microstructure of cast components; key work in this area is that by (Jennings, 1996) and (Newell, 2009).

This section will make a comparative assessment of the microstructure obtained when casting VeriCAST geometry using the experimental heater with observations made in other work in order to quantify the improvements made.

Jennings categorised the capability of the Rolls-Royce small-bore furnace using VeriCAST moulds and provided metallographic information about the as-cast microstructure within the VeriCAST test piece along with in-situ thermocouple data.

In this work the VeriCAST test piece was sectioned in seven positions as shown in Figure 6-25 and metallographic analysis was conducted in order to determine PDAS.

The work conducted by Jennings was concerned with casting a blade assembly, consisting of four VeriCAST moulds, and while the work in the present study and work by Newell have only cast a single VeriCAST mould, other furnace parameters are near identical so comparisons may be useful.

Newell carried out work in a similar vein to that carried out previously; by casting an instrumented VeriCAST test piece, this time in the ‘single shot’ Bridgman furnace that was relocated to Birmingham. The locations of in-situ thermocouples used by Newell are shown in Figure 6-26; metallographic analysis was carried out at 110mm, 135mm and ‘top aerofoil’ which is not shown.

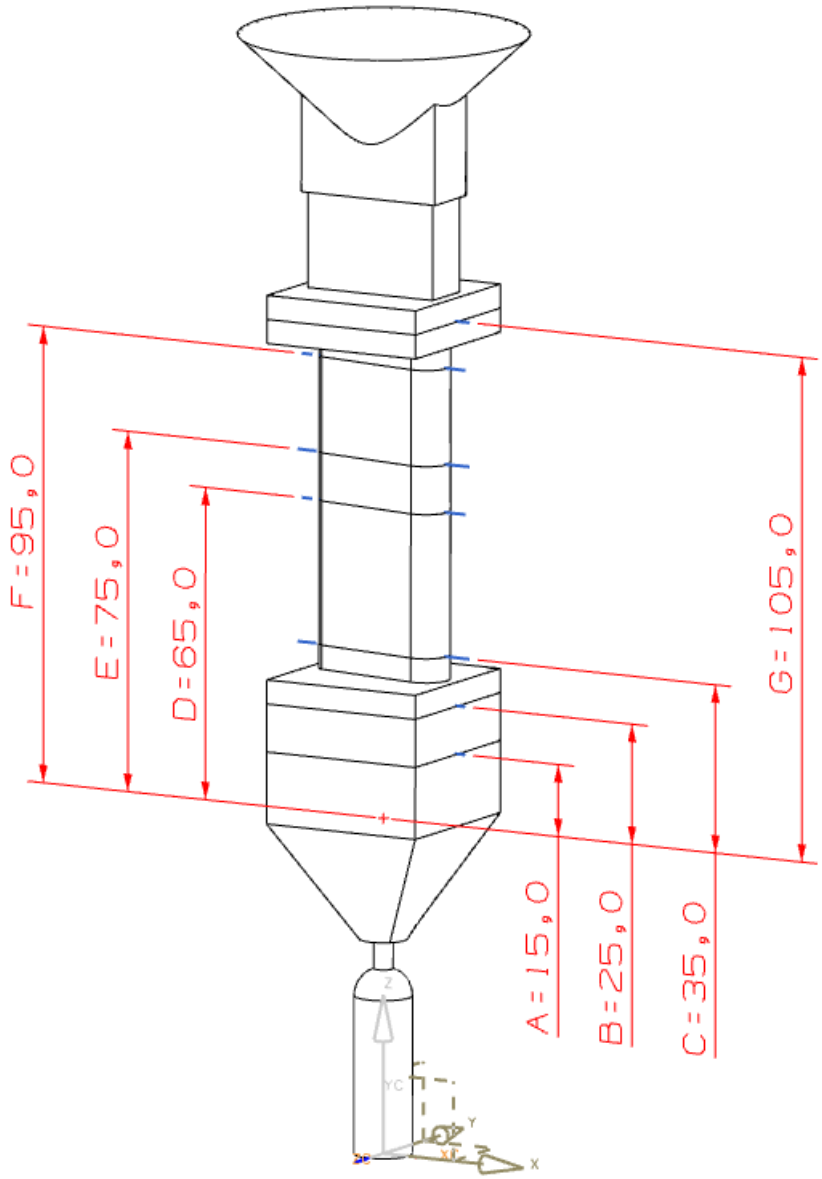


Figure 6-25: VeriCAST geometry showing positions of sections taken for metallographic analysis in work conducted by (Jennings, 1996).Dimensions shown in mm (1 x 10^{-3} m).

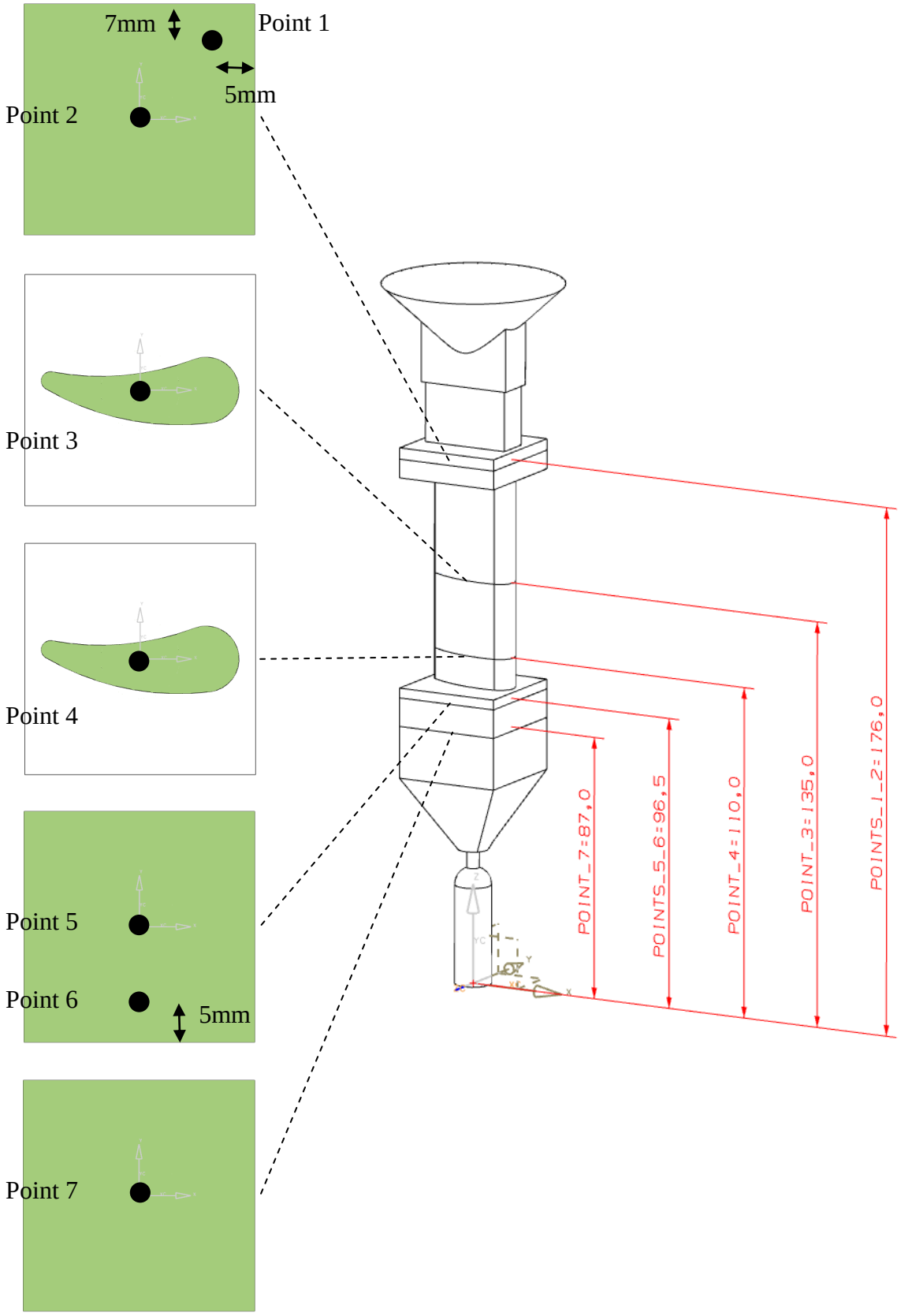


Figure 6-26: Positions of in-situ TC measurements taken by (Newell, 2009). Metallographic analysis conducted at 110mm, 135mm and 'top' (not shown). Dimensions in mm (1 x 10^{-3} m).

It is desirable that work conducted in this study using the experimental furnace and VeriCAST mould should be comparable to previous work. To do this, the VeriCAST test piece produced will be sectioned so that comparisons can be made to both.

Figure 6-27 shows the sections taken from the VeriCAST test piece cast using the experimental heating element; sections A_A, B_B, Bottom, Middle and C_C coincide with sections taken from (Newell, 2009) to allow comparisons to be drawn with respect to in-situ thermocouple locations ; the ‘Top’ section is taken from position detailed in (Jennings, 1996). The positions combined from work by Jennings and Newell results in a maximum deviation in section position of only 5.24 mm which occurs at ‘Bottom’ section.

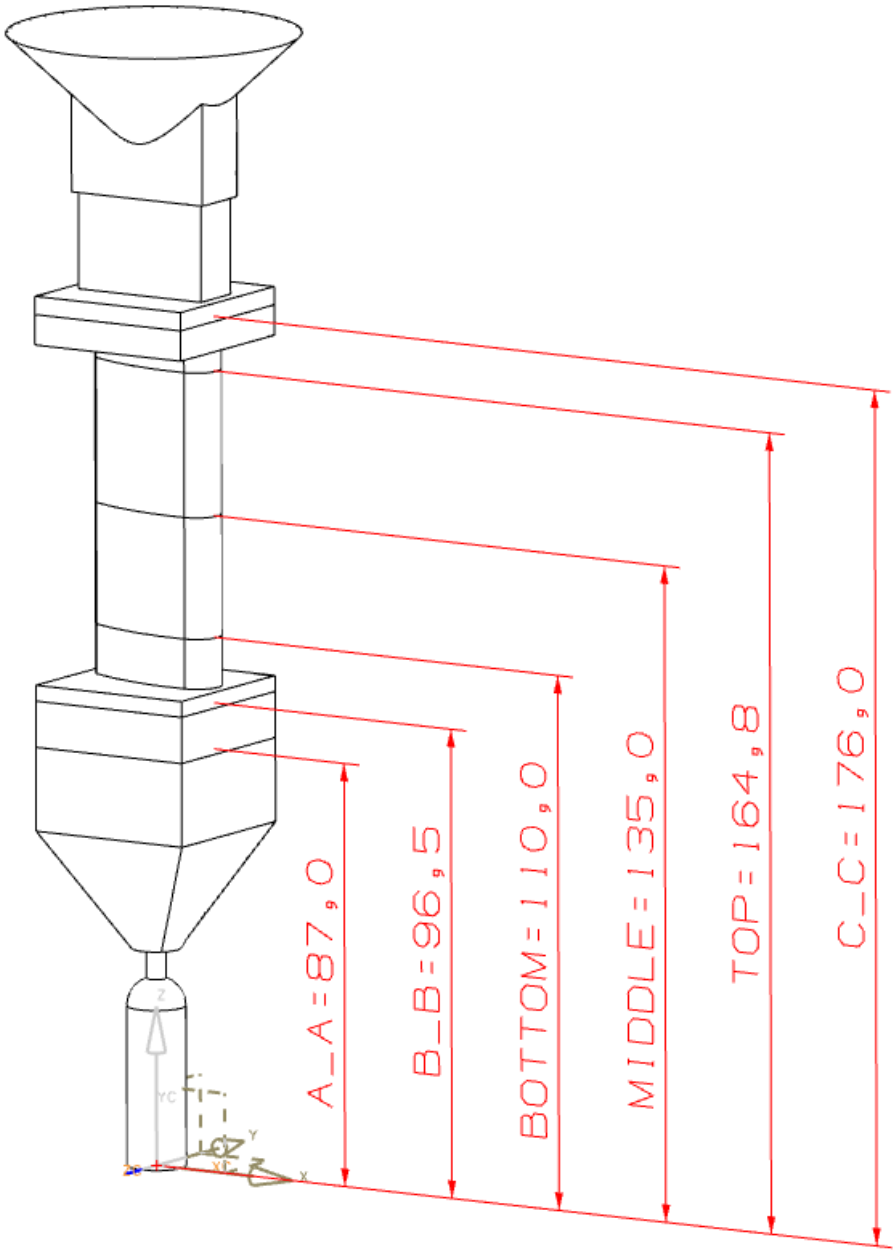


Figure 6-27: Section positions to be taken from VeriCAST test piece for this work. Section A_A corresponds to Newell TC point 7 and Jennings position A, Section B_B corresponds to Newell TC points 5 & 6 and Jennings position B, 'Bottom' section corresponds to Newell TC point 4 and Jennings position C, 'Middle' section corresponds to Newell TC point 3 and Jennings position D, 'Top' section taken from Jennings position F, and section C_C corresponds to Newell TC points 2 & 1 and Jennings position G.

6.2.4.2 Results

A significant part of the Bridgman furnace pre-move and post move validation involved the casting of VeriCAST blade geometry using the single crystal alloy CMSX-4 (Newell, 2009). The process eventually produced 6 cast components; 5 produced using the furnace in its new location at Birmingham and 1 produced prior to relocation.

All casts were produced using VeriCAST moulds made at the CRDF (prior to relocation) using the standard procedure; the casting parameters were a set hot zone temperature of 1803.15 K, a 110 x 10^{-3} m ID baffle and a withdrawal velocity of 6.36 x 10^{-5} ms^{-1}.

Metallographic examination was carried out on sections of the aerofoil at three locations; bottom, middle and top, which represent a distance of 110 x 10^{-3} m, 135 x 10^{-3} m and 164.8 x 10^{-3} m respectively from the chill, as shown in Figure 6-28.

In this work the aerofoil was evaluated at two discrete locations; position 1 and position 2, shown in Figure 6-29.

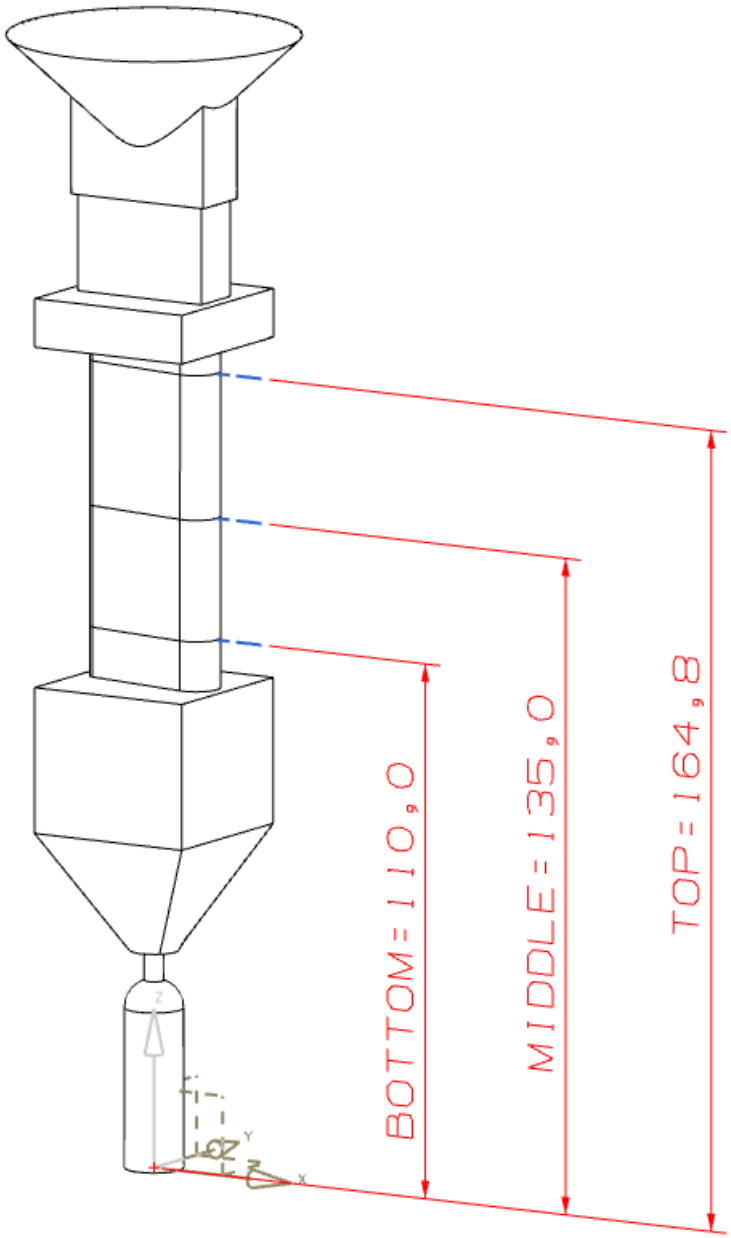


Figure 6-28: VeriCAST geometry showing positions of metallographic analysis along aerofoil.

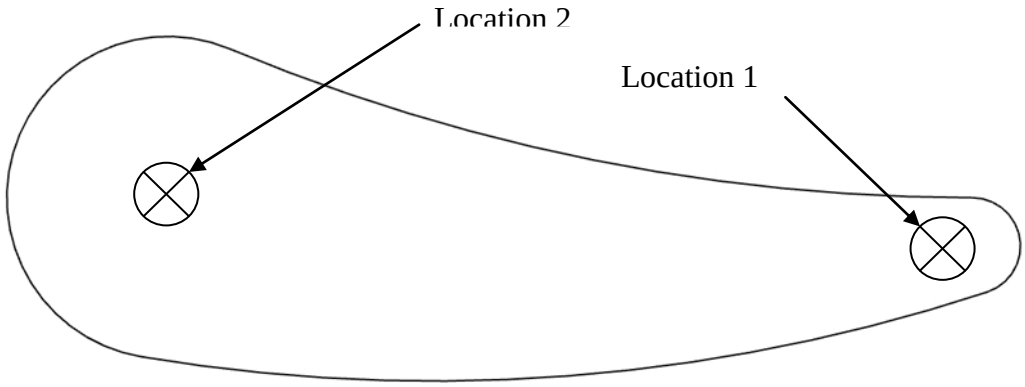


Figure 6-29: Cross-sectional illustration of aerofoil showing two locations of analysis

In order to compare the potential improvements of the experimental heater; CMSX-4 specimens were cast using the VeriCAST mould with identical furnace parameters used by Newell with the exception of the experimental heater geometry.

To enable continuity when comparing experimental data with that obtained from literature, VeriCAST moulds made at the CRDF left over from previous work were used for this study. This did however, lead to several issues; the moulds were exposed to atmospheric conditions for a period before this work began and as such several mould failures were encountered, most likely due to moisture ingress and associated thermal cracking.

However a successful VeriCAST single crystal cast was achieved with the experimental furnace setup and summarised results from literature and those from this work are shown in Table 6-7 along with macro and micrograph images of the microstructure obtained shown in Figure 6-30.

A plot showing the results obtained for the top, middle and bottom position of the aerofoil is shown in Figure 6-31, which correspond with positions C,D and F from (Jennings, 1996) and thermocouple positions 4 and 3 from (Newell, 2009).

Table 6-7: Results of PDAS evaluation for two locations at the bottom, middle and top of the VeriCAST aerofoil section. CRDF and SS002-10 data obtained from (Newell, 2009), results using the experimental heater from this work. All casts we carried out using the same nominal furnace conditions; hot zone reference temperature of 1803.15 K, 110 x 10^{-3} m ID radiation baffle and a withdrawal velocity of 6.36 x 10^{-5} ms^{-1}.

	Location 1			**Location 2**		
	Bottom	**Middle**	**Top**	**Bottom**	**Middle**	**Top**
CRDF	***347.08***	***340.59***	***386.19***	***353.95***	***390.87***	***369.02***
SS002	317.86	395.73	357.54	343.79	369.02	369.02
SS003	278.09	347.08	337.48	312.85	357.54	350.46
SS006	323.11	337.48	315.87	325.84	347.08	401
SS009	292.39	365.07	361.25	312.85	334.45	325.84
SS010	276.39	334.45	328.63	305.77	301.3	308.07
B'ham Mean	***297.68***	***355.96***	***340.15***	***320.22***	***341.89***	***350.89***
Experimental Heater	***271.61***	***283.33***	***296.96***	***293.21***	***303.9***	***307.58***

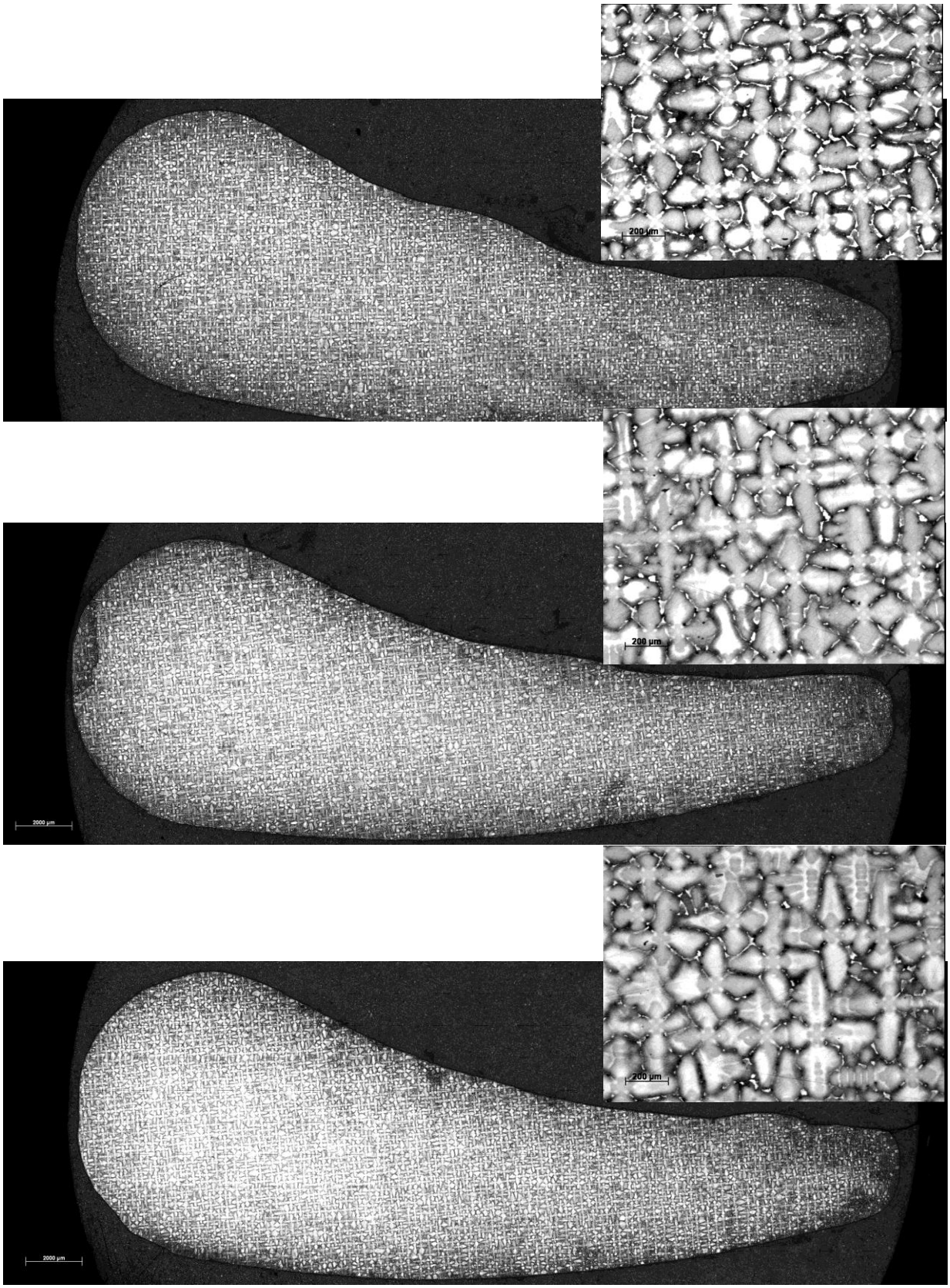


Figure 6-30: Macro images and micro images (inset) of VeriCAST aerofoil section cast using the experimental heating element. a) Bottom, b) Middle, c) Top.

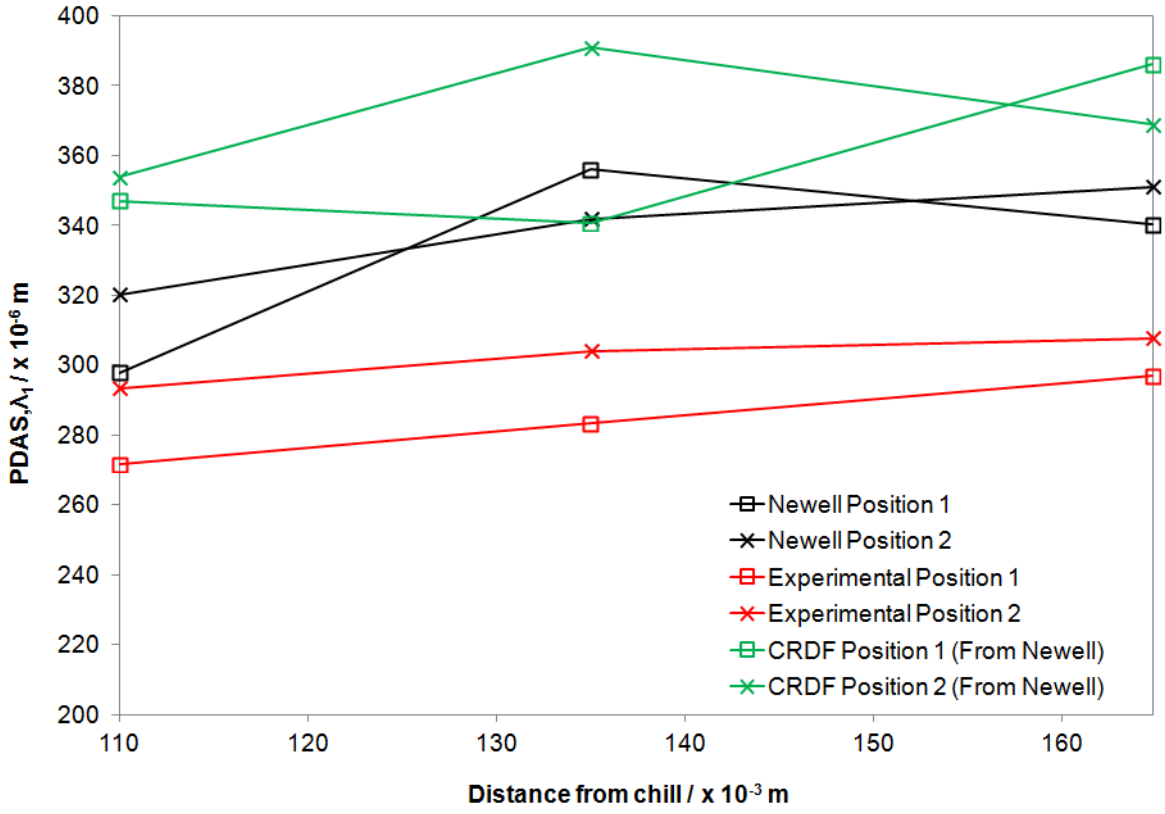


Figure 6-31: Plot showing PDAS values obtained from sections at top, middle and bottom of aerofoil from casting produced at the CRDF and at Birmingham using the standard heating element and from this work using the experimental heating element; CRDF and Newell values obtained from (Newell, 2009). The furnace parameters were a hot zone reference temperature of 1803.15 K, a withdrawal velocity of 6.36 x 10^{-5} ms^{-1} and a 110 x 10^{-3} m ID radiation baffle.

Work conducted by (Jennings, 1996) has determined the PDAS of the VeriCAST test geometry at a total of seven sections (A-G); this study has determined the PDAS at six sections (A_A, B_B, Bottom, Middle, Top, C_C) which coincided with thermocouple locations 7,6,5,4,3,2 and 1 from Newell's work and A-G (omitting E) from (Jennings, 1996).

Work by (Newell, 2009) determined the PDAS at three locations (Bottom, Middle and Top) which coincided with two thermocouple locations, point 4 and point 3.

Section A_A, B_B and C_C from this work are shown in Figures 1-33 to 1-35; along with Figure 6-30 these show the microstructure at all sites examined.

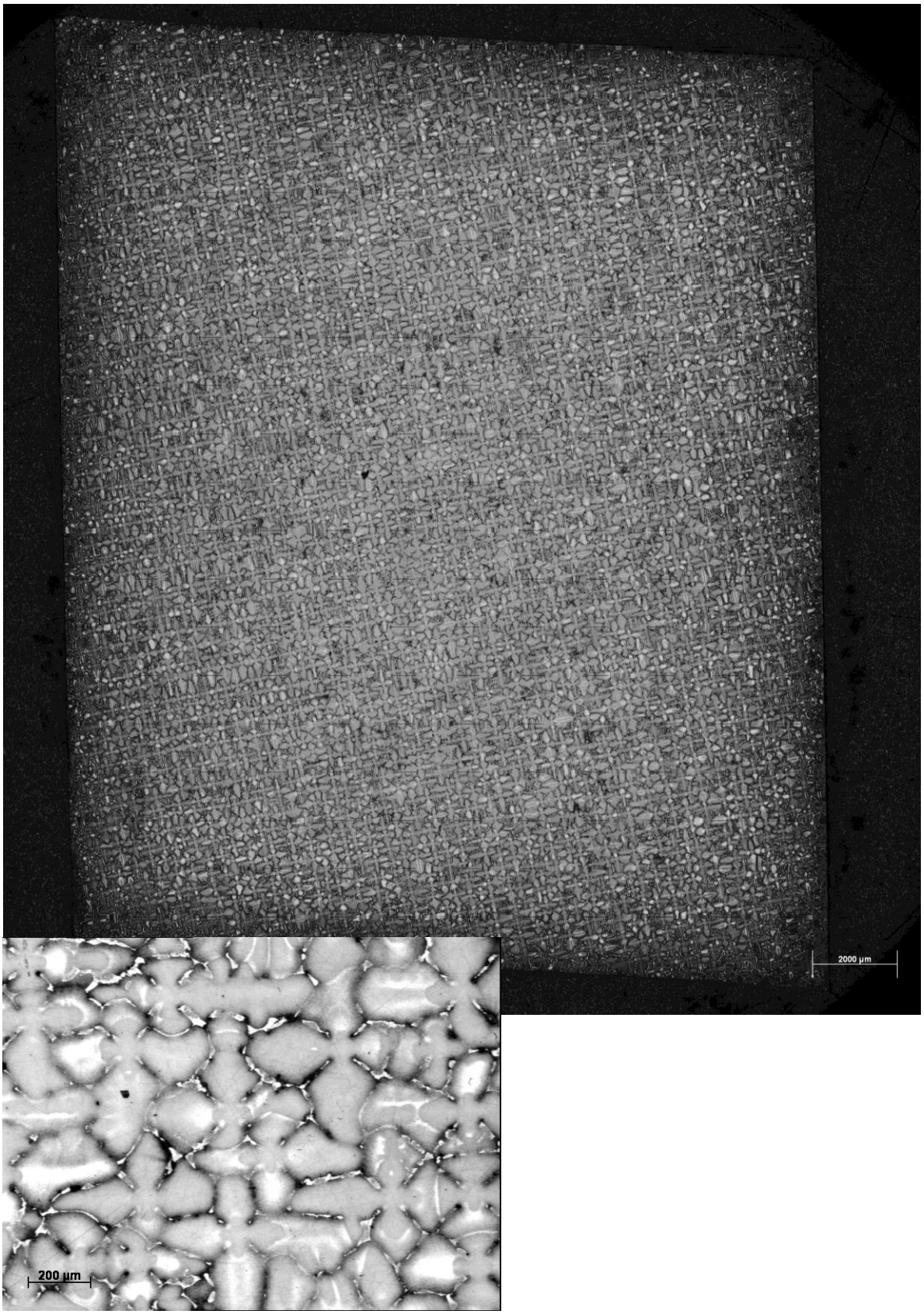


Figure 6-32: Section A_A which coincides with section A from (Jennings, 1996) and TC position 7 from (Newell, 2009).

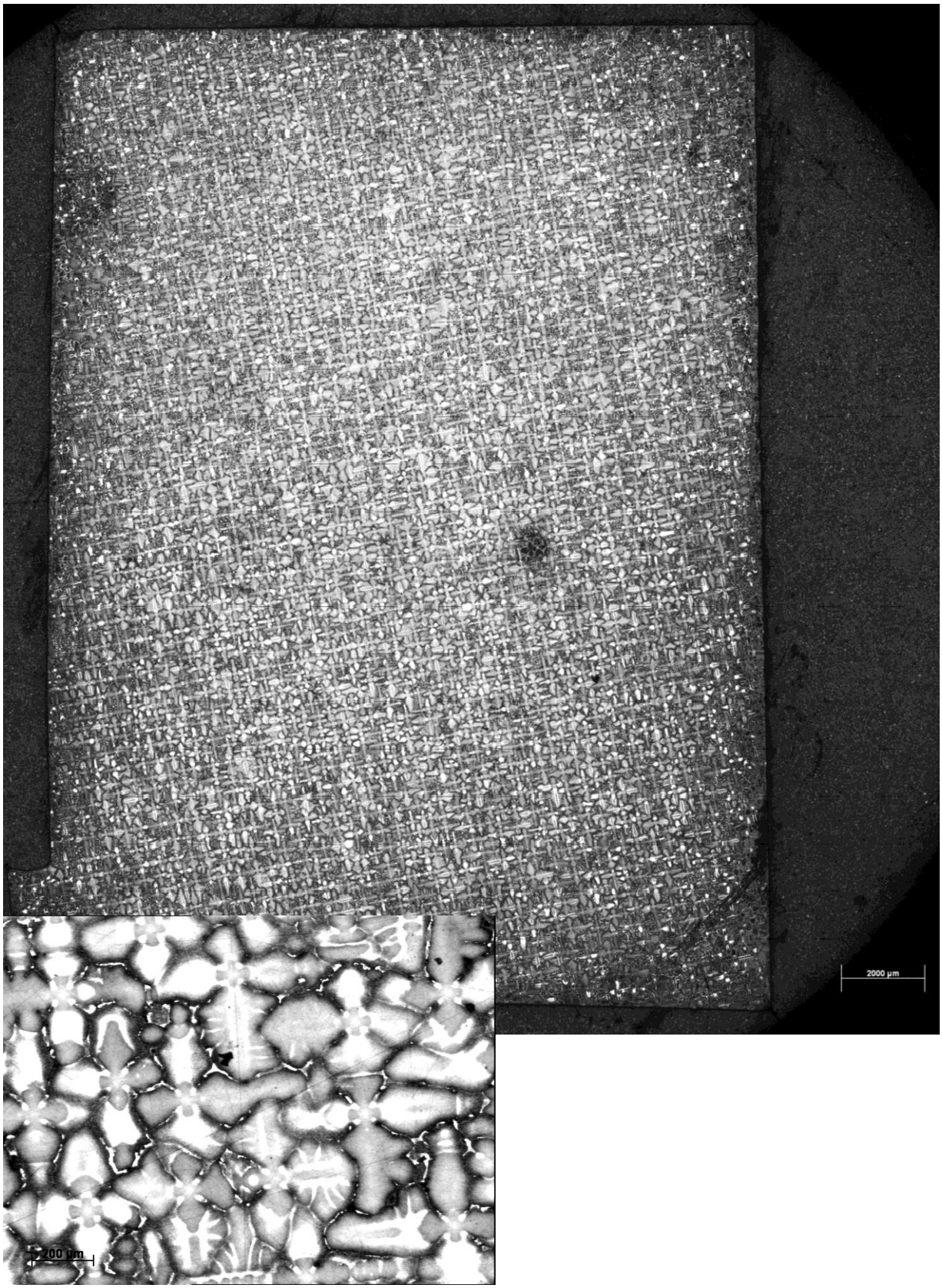


Figure 6-33: Section B_B which coincides with section B from (Jennings, 1996) and TC positions 5 & 6 from (Newell, 2009).

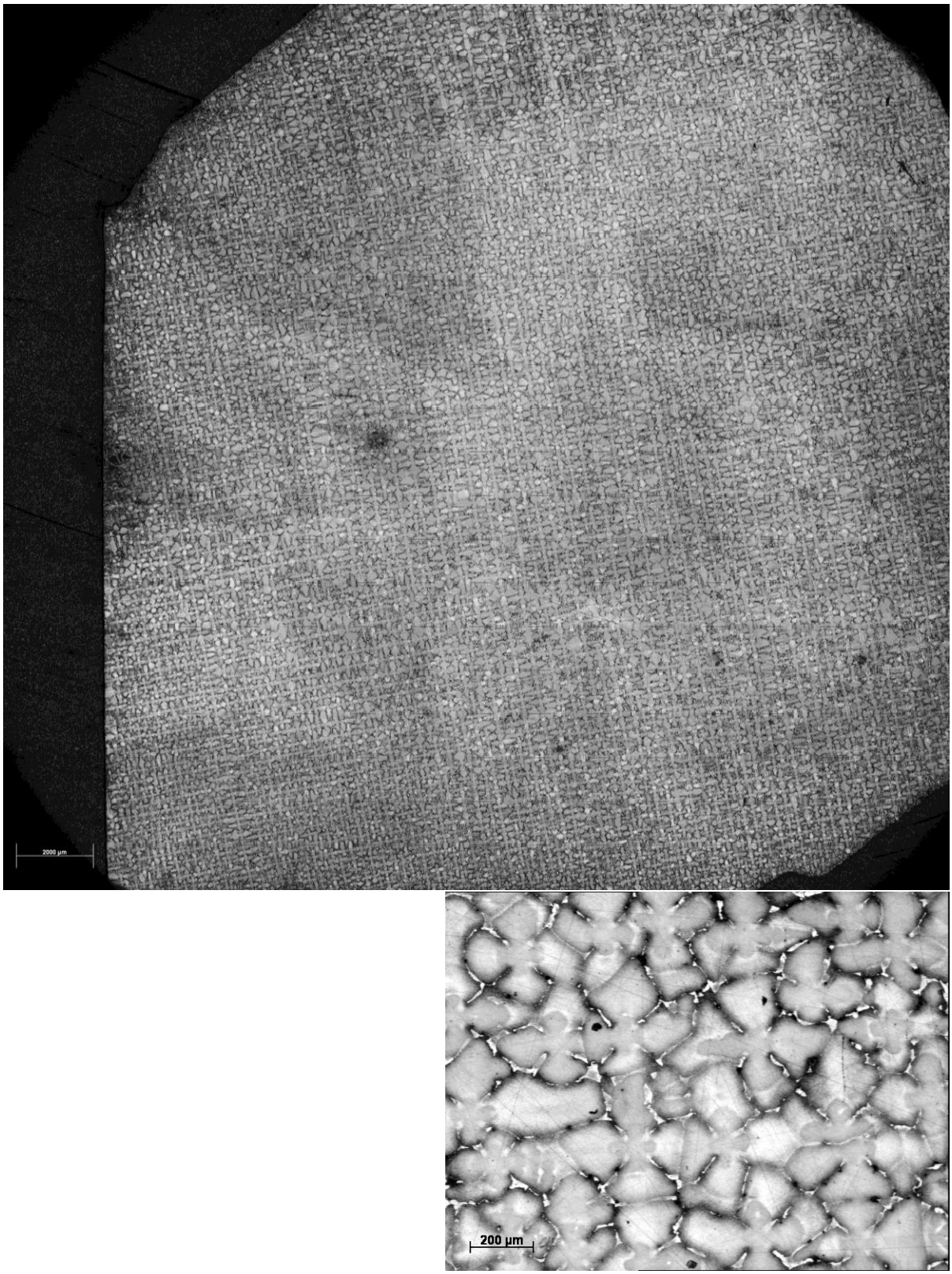


Figure 6-34: Section C_C which coincides with section G from (Jennings, 1996) and TC positions 1 & 2 from (Newell, 2009).

PDAS values measured during this study at discrete locations specified in the VeriCAST geometry are shown in Table 6-8.

Table 6-8: PDAS values measured during this study at discrete locations in the VeriCAST test geometry.

Section / Distance from chill x 10^{-6} m	**Mean PDAS ± standard error / x 10^{-6} m**	**Dendrite count**	**95% confidence limits for mean / x 10^{-6} m**
A_A / 87	352.19 ± 4.07	204	344.19 – 360.18
B_B / 96.5	333.77± 2.37	506	329.12– 338.42
Bottom / 110	268.79 ± 3.27	199	262.38 – 275.20
Middle / 135	287.64 ± 3.87	204	280.06 – 295.23
Top / 164.8	273.69 ± 4.14	168	265.58 – 281.80
C_C / 176	324.18 ± 2.41	422	319.46 – 328.90

Results presented by (Jennings, 1996) alongside those presented by (Newell, 2009) can now be plotted in comparison with PDAS values determined during this study using the experimental heating element and are shown in Figure 6-35.

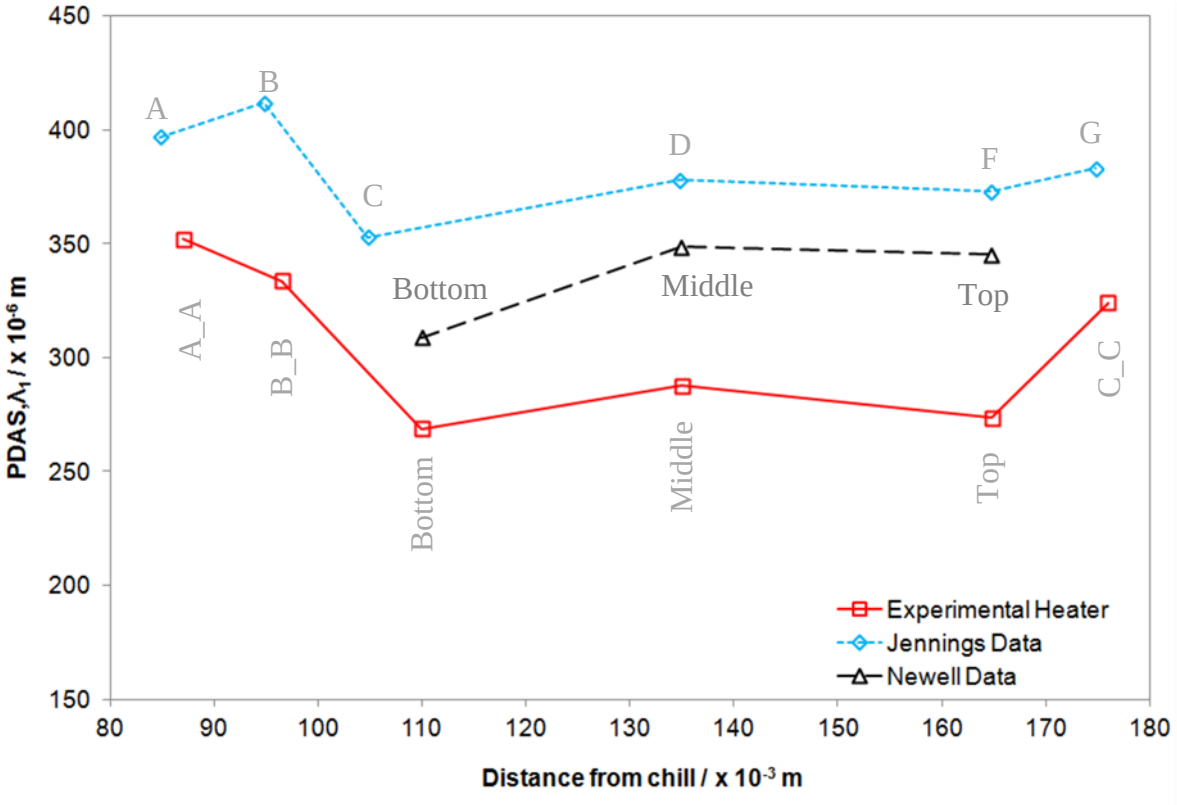


Figure 6-35: Experimentally measured PDAS for six sections of the VeriCAST test geometry. Data presented by (Jennings, 1996) was cast using an assembly of four VeriCAST moulds with a hot zone reference temperature of 1798.15 K (1525°C) and a withdrawal velocity of 9"hr^{-1} (6.35 x 10^{-5} ms^{-1}). Data from (Newell, 2009) and this work was cast with a hot zone reference temperature of 1803.15 K (1530°C) and a withdrawal velocity of 6.36 x 10^{-5} ms^{-1}. All casts used the largest aperture 'standard' baffle, 110 x 10^{-3} m ID for the single shot Bridgman furnace.

During validation work of the ProCAST model by (Newell, 2009), in-situ thermocouple measurements were taken at discrete locations within the VeriCAST geometry shown in Figure 6-26.

Given that the VeriCAST test pieces produced using the experimental heating element have been sectioned in planes corresponding with the historical thermocouple positions, the PDAS can subsequently be measured at the relevant locations. Referring back to Figure 6-26 the local microstructure at each point is shown in Figure 6-36 and PDAS values given in Table 6-9. The area measured corresponded to that displaced by an in-situ thermocouple in alumina sheath; approximately 4000 x 10^{-6} m by 4000 x 10^{-6} m.

Table 6-9: Measured PDAS values at various points in a cast using the VeriCAST using the experimental heater with a hot zone reference temperature of 1803.15 K, a withdrawal velocity of 6.36 x 10^{-5} ms^{-1} and a 110 x 10^{-3} m ID baffle. Positions reflect in-situ thermocouple measurements made by (Newell, 2009).

Thermocouple position	**Mean PDAS ± standard error / x 10^{-6} m**	**Dendrite count**	**95% confidence limits for mean / x 10^{-6} m**
1	307.82 ± 3.24	199	301.47 – 314.16
2	340.54 ± 3.57	223	333.55 – 347.53
3	287.64 ± 3.87	204	280.06 – 295.22
4	268.79 ± 3.27	199	262.38 – 275.20
5	329.68 ± 2.86	322	324.08 – 335.28
6	337.85 ± 4.09	184	329.84 – 345.86
7	352.19 ± 4.14	204	344.19 – 360.18

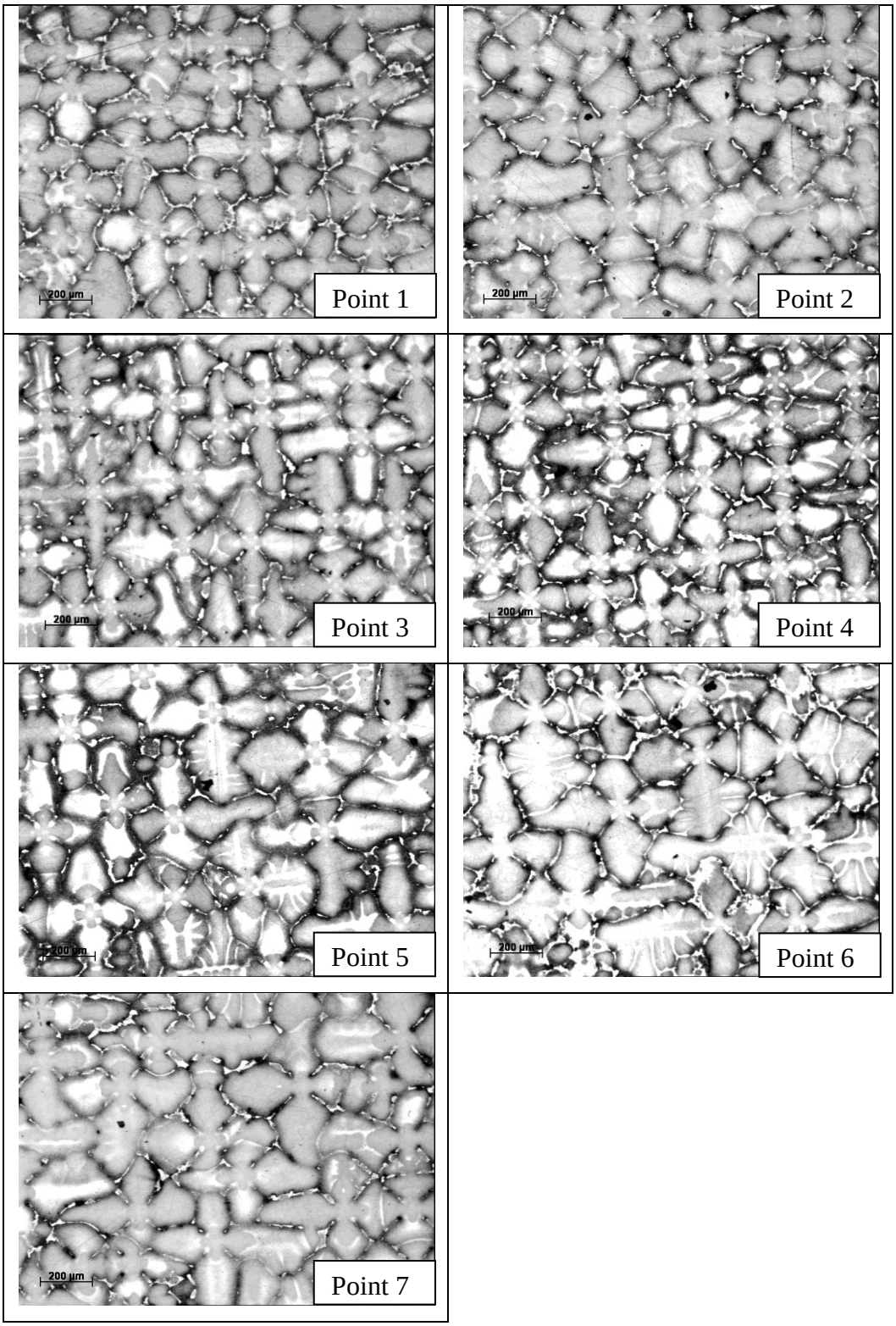


Figure 6-36: Micrographs showing structure of CMSX-4 at discrete locations corresponding to thermocouple locations used in ProCAST validation work by (Newell, 2009). The cast was produced using the experimental heating element with a hot zone reference temperature of 1803.15 K, a withdrawal velocity of 6.36 x 10^{-5} ms^{-1} and a 110 x 10^{-3} m ID baffle.

Under normal circumstances the thermal gradient can be derived by knowing the PDAS and withdrawal velocity, which is assumed to be equal to the solidification front velocity. However in the case of the VeriCAST mould with varying geometry it is expected the solidification front velocity will not remain constant and would vary depending on the cross sectional area of the mould at a given position.

The candidate position at which the solidification front velocity would be expected to be reasonably steady state is point 3, which is at the centre of the aerofoil section, equidistant between the root and shroud sections.

An estimate of the thermal gradient at this position can therefore be made and is shown in Figure 6-37. The difference in thermal gradient at thermocouple position 3 between the experimentally measured value captured during the ProCAST model validation and that derived from PDAS measurements taken from a cast using the experimental heating element represent an increase in the region of 32%. It is expected that the increase in thermal gradient would be consistent in all sections of the VeriCAST geometry using the improved single shot Bridgman furnace.

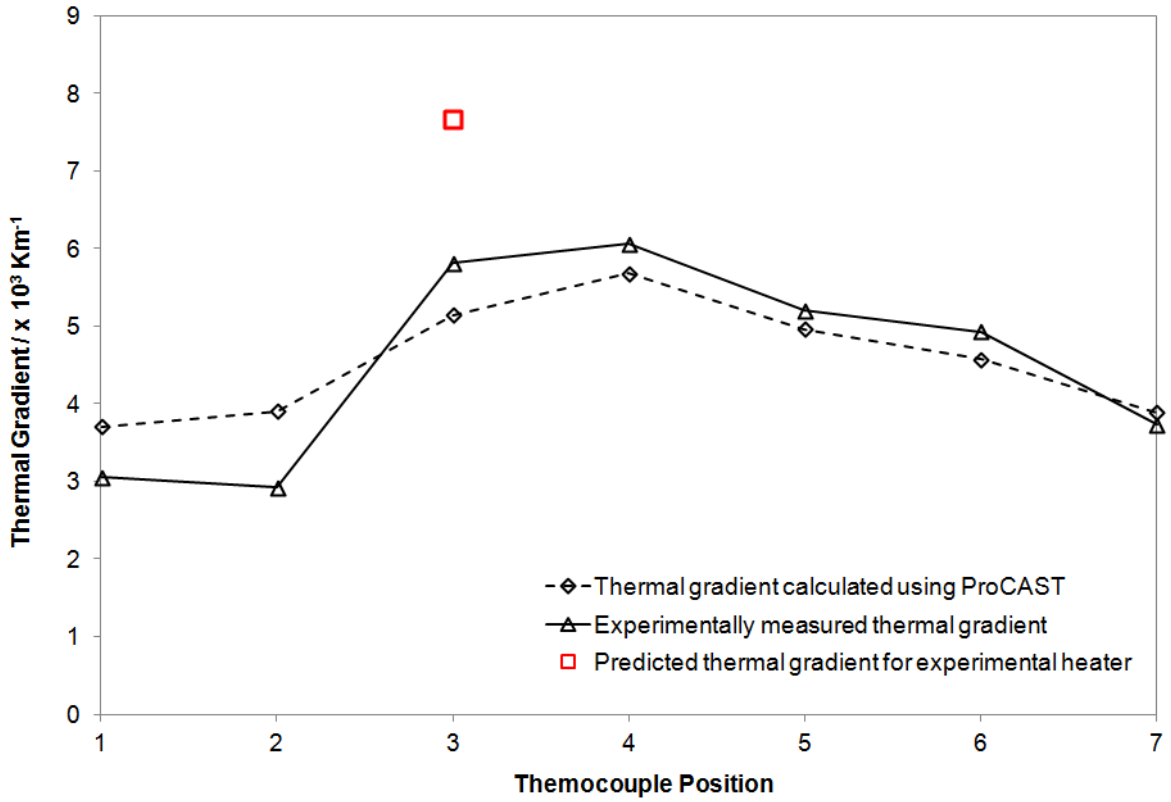


Figure 6-37: Estimated thermal gradient achieved when casting VeriCAST geometry using experimental heater, plotted against thermal gradient calculated by ProCAST model for identical conditions and those measured during validation work by (Newell, 2009). The furnace parameters were a hot zone reference temperature of 1803.15 K, a withdrawal velocity of 6.36 x 10^{-5} ms-1 and a 110 x 10^{-3} m ID baffle.

6.3 Conclusions

6.3.1 PDAS modification

Casts of the single crystal alloy CMSX-4 were carried out during this study using the standard and experimental heating elements with different baffle configurations; 20 x 10^{-3} m ID and 110 x 10^{-3} m ID.

When using a 20 x 10^{-3} m ID baffle at a hot zone temperature of 1823.15 K there was marginal PDAS reduction when using the experimental heating element in comparison to the standard. With the same baffle geometry at a hot zone temperature of 1923.15 K there was a slight reduction in PDS however the standard heating element produced the cast with smallest PDAS overall.

This suggests that in this baffle configuration, enhanced heat optimisation within the hot zone has little impact on the thermal gradient and the maximum cooling capacity within the cold zone has been reached.

Under these conditions the only method of increasing the thermal gradient further would be to use enhanced cooling methods within the cold zone. That said, under such conditions there is a tendency for the solidification front to be driven up towards the hot zone and the experimental heating element may find further use under such circumstances.

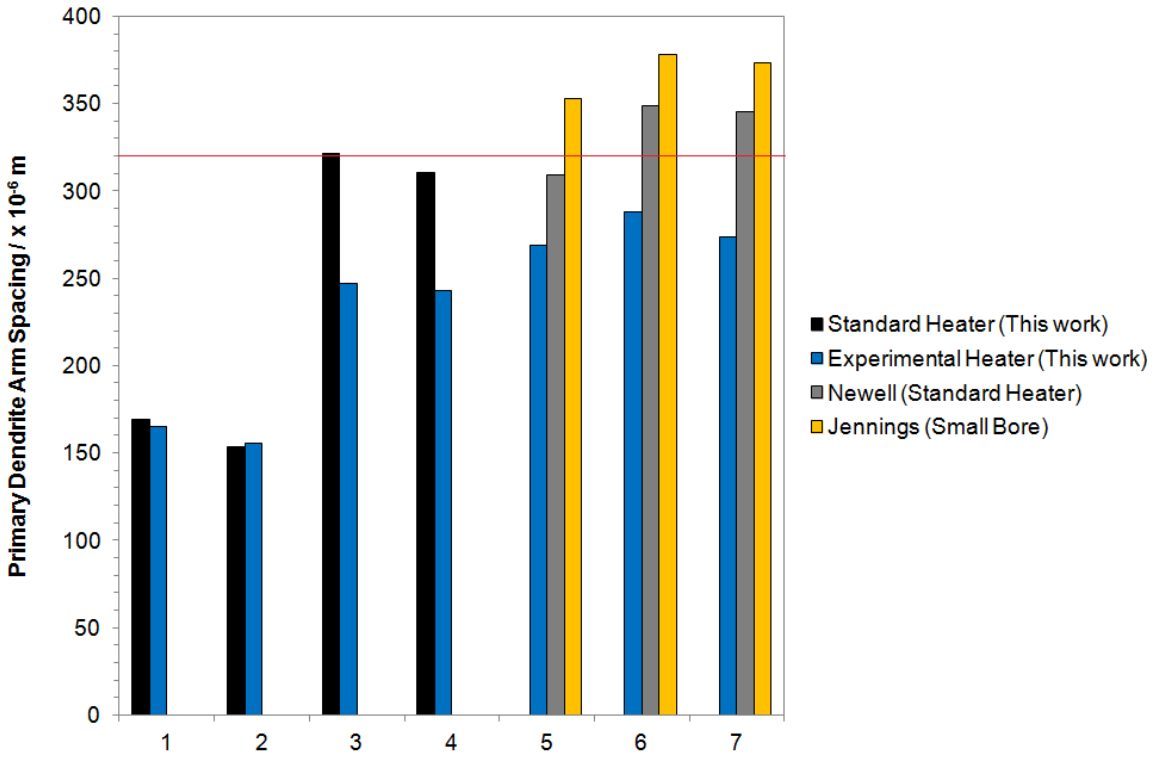
Test bar clusters were also cast using both heating element designs using a 110 x 10^{-3} m baffle and under such conditions the only parameter that can be modified is the hot zone thermal profile. Observation of the PDAS in single crystal test bars showed a significant reduction when comparing casts produced using the experimental and standard heating elements.

PDAS was reduced by between 27 – 30% which indicated that the thermal gradient had been increased by between 38 – 40%. This improvement is attributed to the enhanced heating at the base of the heating element which acts to stabilise and constrain the solidification front within the hot/cold zone interface.

VeriCAST geometry was also cast using the experimental heating element and compared with PDAS measurements taken by (Jennings, 1996) and (Newell, 2009). The microstructure within the aerofoil section of the VeriCAST mould cast using the experimental heating element showed the lowest PDAS.

A comparison of PDAS measurements for all experimental conditions obtained using the standard and experimental heating elements are shown in Figure 6-38 alongside data obtained from (Newell, 2009) and (Jennings, 1996). The horizontal line on the graph represents the minimum PDAS value below which freckling is not thought to occur (Pollock et al., 1992).

With exception of the configuration with intimate baffle, the experimental heating element has been shown to effectively reduce PDAS in the single crystal alloy CMSX-4 and hence increase the thermal gradient; the most pronounced effect being when using a 110×10^{-3} m ID ‘standard’ baffle.



1. *Single test bar. Hot zone reference temperature 1823.15 K, 20 x 10^{-3} m ID baffle, 10.67 x 10^{-5} ms^{-1} withdrawal rate.*
2. *Single test bar. Hot zone reference temperature 1923.15 K, 20 x 10^{-3} m ID baffle, 10.67 x 10^{-5} ms^{-1} withdrawal rate.*
3. *Multiple test bars. Hot zone reference temperature 1823.15 K, 110 x 10^{-3} m ID baffle, 6.36 x 10^{-5} ms^{-1} withdrawal rate.*
4. *Multiple test bars. Hot zone reference temperature 1823.15 K, 110 x 10^{-3} m ID baffle, 10.67 x 10^{-5} ms^{-1} withdrawal rate.*
5. *VeriCAST lower aerofoil. Hot zone reference temperature 1803.15 K, 110 x 10^{-3} m ID baffle, 6.36 x 10^{-5} ms^{-1} withdrawal rate.*
6. *VeriCAST middle aerofoil. Hot zone reference temperature 1803.15 K, 110 x 10^{-3} m ID baffle, 6.36 x 10^{-5} ms^{-1} withdrawal rate.*
7. *VeriCAST top aerofoil. Hot zone reference temperature 1803.15 K, 110 x 10^{-3} m ID baffle, 6.36 x 10^{-5} ms^{-1} withdrawal rate.*

Figure 6-38: Comparison of PDAS values measured during this study for a number number of experimental conditions and heater configurations. Data obtained from work by (Jennings, 1996, Newell, 2009) also shown for comparison. Red horizontal line on graph shows minimum PDAS value below which freckling was not observed (Pollock et al., 1992).

6.3.2 Eutectic alloys

A comprehensive comparison of the capabilities of eutectic alloys systems with respect to creep potential has been combined from literature. Two eutectic alloys have been cast using the single shot furnace to assess the furnace capability. The maximum withdrawal rate in order to achieve an aligned microstructure is in the region of 12 x 10^{-3} m hr^{-1} however there was no discernible improvement offered by the experimental heating element with only a moderate increase in thermal gradient.

Methods to increase the achievable withdrawal rate further would need to consider additional cooling techniques such as LMC or GCC.

A prevalent point with regard to the development of the CFD model in this work is the ability to calculate heat generation and transfer within the hot zone from first principles i.e. from the input of electrical energy.

The casting of eutectic alloy will undoubtedly require significantly more furnace time than current single crystal alloys, at which point the energy requirements for processing will become increasingly important. Using the CFD based approach described in this work will allow the process to be evaluated, not only on raw material costs, but also process costs.

CHAPTER 7 CONCLUSIONS

The single shot Bridgman furnace owned by Rolls-Royce Plc and located at the University of Birmingham is a furnace capable of high thermal gradient during solidification and was selected as a candidate furnace for continued process development. This chapter will summarise the main findings of this work.

7.1 Furnace model development

1. A computer model has been developed that has the capability of calculating the thermal field within a Bridgman furnace by means of energy input to the heating element and takes into account factors such as baffle geometry which affect the heat flux distribution.

2. Results from the CFX model have been compared with the experimentally measured thermocouple data obtained from the furnace centreline, encompassing the furnace hot zone, baffle region and cold zone with a good degree of accuracy. Previously obtained experimental data has also been compared with the CFX model with good results.

3. The CFX model has been qualitatively compared with the current ProCAST model and is believed to offer improved flexibility and accuracy when considering any number of configurations.

4. The results indicated that the magnitude of temperature difference between the heating element temperature and that of the hot zone reference temperature was not only a function of electrical current density but also baffle geometry.

5. This understanding was extended, and it was proposed that the heating element surface temperature will also vary depending on the geometry being cast.

6. The CFX model has been used as a tool in order to design optimised furnace heater geometry with the intention of imposing a positive thermal gradient towards the baffle region and maximising superheat.

7. The objective of designing the experimental heating element with respect to existing furnace architecture was that the experimental heating element should be easily retrofitted into the single shot furnace with no modification to power or control methods necessary.

8. This goal has been achieved, and no compatibility issues were ever experienced during use.

7.2 Experimental heater design and PDAS modification

9. An experimental heating element has been developed that has the ability to function in a similar way to a twin zone furnace, although in this case the temperature profile can be thought of as three distinct zones; a pre-heating zone in the upper section, a hot zone in the lower section and an additional intensified hot zone at the

base of the element.

10. When casting multiple single crystal components using a ‘standard’ open baffle configuration, which has an analogy with the industrial process, the resulting PDAS was reduced by between 27 – 30% in comparison to results obtained using the standard heating element. In the same instance the thermal gradient has been estimated to have increased by 38 – 40% when using the experimental heater.

11. When casting 13 x 10^{-3} m ID single crystal test bars using restrictive baffles the results were somewhat different. The maximum estimated thermal gradient achieved was in the region of 13.3 – 13.6 x 103 Km^{-1} using both heating elements and resulted in a PDAS in the region of 153 – 154 x 10^{-6} m. The results suggested that in this configuration the maximum cooling potential of the furnace cold zone was exhausted, suggesting any further gain in thermal gradient could only be achieved by accelerated cooling methods.

12. The VeriCAST test geometry has been cast using the experimental heater with encouraging results. The PDAS values measured were in the region of 15 – 26% lower than data presented by (Newell, 2009) for the same experimental setup and in the region of 11 – 26% lower than data presented by (Jennings, 1996), although in this case, furnace setup was not identical.

7.3 Eutectic alloys

13. When casting eutectic alloys using the same configuration described above, the maximum expected solidification velocity achievable would be in the region of 12×10^{-3} m hr^{-1}, again this appears to be irrespective of furnace configuration. Accelerated cooling techniques would be required to improve this further. The prospect of solidifying aerofoil sections separately for eutectic alloys has been discussed (McLean, 1983) however further work would be need in this area.

14. The creep potential of eutectic alloy systems has been reviewed and is presented in this work; however the creep potential with respect to spacing of the strengthening phase is sparse. Phase spacing with respect to solidification conditions has been quantified experimentally for the COTAC 744 alloy in this work but further creep testing would be required should this be considered a candidate turbine blade material.

CHAPTER 8 FUTURE WORK

The next stage of development of the single shot furnace should be the investigation of additional cooling techniques in conjunction with the experimental heating element developed during this work.

LMC is arguably the most established cooling technique for directionally solidified articles however initial investment and alteration to furnace architecture is high.

GCC is an attractive method due to the limited alterations that would be required for implementation; however the introduction of a cooling medium in the form of a gas could be problematic for furnace vacuum levels. The issue of gas impingement through the mould walls is also an area of ambiguity as modern shell systems often specify a final seal coat to be applied to the exterior before wax removal and subsequent firing.

If eutectic alloy systems are to be seriously considered as candidate HP turbine materials then additional creep data would be required. Creep data obtained thus far from literature makes no mention of the strengthening phase spacing used when measuring strain, however it has been shown in literature and this work that the solidification velocity has a strong effect on the morphology of the microstructure.

A comprehensive assessment of the realistic creep potential of the eutectic alloys would need to be determined using phase spacing which would be achievable on an industrial scale.

The methodology behind the experimental heating element developed in this work would be equally applicable to furnaces of a larger scale, such as the small bore furnace. It is recommended that the same methodology be used to assess larger furnaces, capable of

casting multiple component geometry, in order to assess the possible benefits.

Should alternative alloy development not be pursued, the methods developed in this work would be equally as applicable to the casting of current generation single crystal alloys; the emphasis being on optimisation of the microstructure in order to minimise heat treatment times and reduce cost.

REFERENCES

AL-JARBA, K. & FUCHS, G. 2004. Carbon-containing single-crystal nickel-based superalloys: Segregation behavior and carbide formation. *JOM,* 56**,** 50-55.

ANSYS, C. 2010. Release 13.0. CFX-Solver modeling guide. Technical report, Ansys.

ATKINSON, A. W. & WALSH, M. J. 1995. *Thermal Radiation Baffle For Use In Directional Solidification*. US patent application.US 5,429,176

AUBURTIN, P., WANG, T., COCKCROFT, S. L. & MITCHELL, A. 2000. Freckle formation and freckle criterion in superalloy castings. *Metallurgical and Materials Transactions B,* 31**,** 801-811.

BECKERMANN, C., GU, J. P. & BOETTINGER, W. J. 2000. Development of a freckle predictor via rayleigh number method for single-crystal nickel-base superalloy castings. *Metallurgical and Materials Transactions A,* 31**,** 2545-2557.

BIBRING, H., KHAN, T., RABINOVITCH, M. & STOHR, J. Year. Development And Evaluation Of New Industrial DS Monocarbide Reinforced Composites For Turbine Blades. *In:* KEAR, B. H., ed. Superalloys, 1976 Seven Springs, Pennsylvania. TMS, 331-340.

BRINEGAR, J. R. 2003. *Directional solidification method and apparatus*. US patent application B22D027/04.US 2003/0234092 A1

BRINEGAR, J. R., MUSKEGON, M., THOMPSON, D. & WHITEHALL, M. 2000. *Directional Solidification Method And Apparatus*.EP 1,946,868 A1

BROKLOFF, J. E., KERR, R. C. & BETZ, L. 1990. *Method And Apparatus For Use During Casting*. US patent application.US 4,969,501

BROOMFIELD, R. W., FORD, D. A., BHANGU, J. K., THOMAS, M. C., FRASIER, D. J., BURKHOLDER, P. S., HARRIS, K., ERICKSON, G. L. & WAHL, J. B. 1998. Development and turbine engine performance of three advanced rhenium containing superalloys for single crystal and directionally solidified blades and vanes. *Journal Name: Journal of Engineering for Gas Turbines and Power; Journal Volume: 120; Journal Issue: 3; Conference: 42. international gas turbine and aeroengine congress and exhibition, Orlando, FL (United States), 2-5 Jun 1997; Other Information: PBD: Jul 1998***,** Medium: X; Size: pp. 595-600.

BROWN, P. 2012. *RE: Method of furnace temperature measurement.* Type to DALE, S.

BROWN, P. 2013. Unpublished Data. Rolls-Royce plc.

BRUNO, G. & PINTO, H. C. 2004. The kinetics of the gamma ' phase and its strain in the nickel base superalloy SC16 studied by in-situ neutron and synchrotron radiation diffraction. *Superalloys 2004***,** 837-846.

BSI 1977. Methods for determination of the viscosity of liquids, BSI 188:1977.

BUTLAND, A. T. D. & MADDISON, R. J. 1973. The specific heat of graphite: An evaluation of measurements. *Journal of Nuclear Materials,* 49**,** 45-56.

CARTER, P., COX, D. C., GANDIN, C. A. & REED, R. C. 2000. Process modelling of grain selection during the solidification of single crystal superalloy castings. *Materials Science and Engineering a-Structural Materials Properties Microstructure and Processing,* 280**,** 233-246.

CHEUNG, Y. K., LO, S. H. & LEUNG, A. Y. T. 1996. *Finite element implementation,* Oxford, Blackwell Science.

CLOUGH, R. W. Year. The finite element method in plane stress analysis. *In:* Conference Papers [of The] Conference on Electronic Computation, 1960. American Society of Civil Engineers, 345-377.

COELHO, P. J., GONÇALVES, J. M., CARVALHO, M. G. & TRIVIC, D. N. 1998. Modelling of radiative heat transfer in enclosures with obstacles. *International Journal of Heat and Mass Transfer,* 41**,** 745-756.

COPLEY, S., GIAMEI, A. F., JOHNSON, S. & HORNBECKER, M. 1970. The origin of freckles in unidirectionally solidified castings. *Metallurgical Transactions,* 1**,** 2193-2204.

COURANT, R. 1943. Variational methods for the solution of problems of equilibrium and vibrations. *Bull. Amer. Math. Soc,* 49**,** 23.

CROSS, M., MCBRIDE, D., CROFT, T. N., WILLIAMS, A. J., PERICLEOUS, K. & LAWRENCE, J. A. 2006. Computational modeling of mold filling and related free-surface flows in shape casting: An overview of the challenges involved. *Metallurgical and Materials Transactions B,* 37**,** 879-885.

CUMBER, P. S. 1995. Improvements to the Discrete Transfer Method of Calculating Radiative Heat-Transfer. *International Journal of Heat and Mass Transfer,* 38**,** 2251-2258.

CUMPSTY, N. A. 1997. *Jet propulsion : a simple guide to the aerodynamic and thermodynamic design of jet engines,* Cambridge, Cambridge University Press.

D'SOUZA, N. & DONG, H. B. 2007. Solidification path in third-generation Ni-based superalloys, with an emphasis on last stage solidification. *Scripta Materialia,* 56**,** 41-44.

D'SOUZA, N. & DONG, H. B. 2008. An analysis of solidification path in the Ni-base superalloy, CMSX10K. *Superalloys 2008***,** 261-269.

DAMERVAL, C. 1987. Contributions to the investigation of the mechanical behaviour of y/y'-NbC cotac composites at medium and high temperatures.

DAVIES, J. R. 1997. *Heat-resistant materials,* ASM International.

DAVIS, J. R. 1996. *Cast Irons,* ASM.

DING, G. L., HUANG, W. D., HUANG, X., LIN, X. & ZHOU, Y. H. 1996. On primary dendritic spacing during unidirectional solidification. *Acta Materialia,* 44**,** 3705-3709.

ELECTROCHEMICAL SOCIETY, I., CAMPBELL, I. E. & SHERWOOD, E. M. 1967. *High-temperature materials and technology,* New York ; London, Wiley.

ELLIOTT, A., KARNEY, G., GIGLIOTTI, M. & POLLOCK, T. 2004a. Issues in processing by the liquid-Sn assisted directional solidification technique. *Green KA, Pollock TM, Harada H, et al. Superalloys***,** 421-430.

ELLIOTT, A. J. & POLLOCK, T. M. 2007. Thermal analysis of the Bridgman and liquid-metal-cooled directional solidification investment casting processes. *Metallurgical and Materials Transactions a-Physical Metallurgy and Materials Science,* 38A**,** 871-882.

ELLIOTT, A. J., TIN, S., KING, W. T., HUANG, S. C., GIGLIOTTI, M. F. X. & POLLOCK, T. M. 2004b. Directional solidification of large superalloy castings with radiation and liquid-metal cooling: A comparative assessment. *Metallurgical and Materials Transactions a-Physical Metallurgy and Materials Science,* 35A**,** 3221-3231.

ERICKSON, G. 1996. The development and application of CMSX-10. *Superalloys,* 1996**,** 35-44.

ERICKSON, G. L. 1994. *Single crystal nickel-based superalloy*.United States Patent 5,366,695

FELDHEIM, V. & LYBAERT, P. 2004. Solution of radiative heat transfer problems with the discrete transfer method applied to triangular meshes. *Journal of Computational and Applied Mathematics,* 168**,** 179-190.

FLEMINGS, M. C. 1974. *Solidification processing,* New York ; London, McGraw-Hill.

FORD, D. & ARTHEY, R. 1986. Development of single crystal alloys for specific engine applications. Rolls-Royce.

FULLAGAR, K. P. L., BROOMFIELD, R. W., HULANDS, M., HARRIS, K., ERICKSON, G. L. & SIKKENGA, S. L. 1996. Aero engine test experience with CMSX-4(R) alloy single-crystal turbine blades. *Journal of Engineering for Gas Turbines and Power-Transactions of the Asme,* 118**,** 380-388.

GANGLOFF, R. & HERTZBERG, R. Year. Elevated Temperature Tensile and Creep Rupture Behavior of the Unidirectionally Solidified Ni-Ni^ Nb Eutectic Composite. *In:* Proceedings of the Conference on In-Situ Composites, 1973. 83.

GEORGE, F. D. Year. Directionally Solidified Eutectics as High Temperature Fasteners. *In:* DAYKIN, R. P. & DERIDDER, A. J., eds. Superalloys, 1972 Champion, Pennsylvania. U1-U21.

GIAMEI, A. F. & KEAR, B. H. 1970. On the nature of freckles in nickel base superalloys. *Metallurgical Transactions,* 1**,** 2185-2192.

GIANCOLI, D. C. 2009 [1984]. Electric Currents and Resistance. *In:* PHILLIPS, J. (ed.) *Physics for Scientists and Engineers with Modern Physics.* 4th ed. Upper Saddle River, New Jersey: Prentice Hall.

GIGLIOTTI, M. & SAWYER, T. 1980. *Directional solidification furnace*.US 4,202,400

GIGLIOTTI, M. F. & HENRY, M. F. Year. *In:* Conference on in-situ composites-II, 1976 Lexington, Ma. Xerox individualised publishing

GOULETTE, M. J., SPILLING, P. D. & ARTHEY, R. P. 1984. Cost Effective Single Crystals. *In:* R.H.BRICKNELL, W.B.KENT, M.GELL, C.S.KORTOVITCH & J.F.RADAVICH (eds.) *Superalloys.* Warrendale, PA: The Metallurgical Society.

GRAHAM, L. D. 2004. *Apparatus And Method For Casting A Metal Article*. US patent application.US 2004/016529

GU, J., BECKERMANN, C. & GIAMEI, A. 1997. Motion and remelting of dendrite fragments during directional solidification of a nickel-base superalloy. *Metallurgical and Materials Transactions A,* 28**,** 1533-1542.

HAGEDORN, F. B. & HALL, P. M. 1963. Right-Angle Bends in Thin Strip Conductors. *Journal of Applied Physics,* 34**,** 128-133.

HAN, S. H. & TRIVEDI, R. 1994. Primary spacing selection in directionally solidified alloys. *Acta Metallurgica et Materialia,* 42**,** 25-41.

HARLOW, F. H. & FROMM, J. E. 1965. Computer experiments in fluid dynamics. *Scientific American,* 212**,** 104-110.

HARRIS, K., ERICKSON, G., SIKKENGA, S., BRENTNALL, W., AURRECOECHEA, J. & KUBARYCH, K. 1992. Development of the rhenium containing superalloys CMSX-4 and CM186 LC for single crystal blade and directionally solidified vane applications in advanced turbine engines. *Superalloys 1992,* 297.

HARRIS, K. & ERICKSON, G. L. 1987. *Single crystal alloy technology*.United States Patent 4,643,782

HARRIS, K. & WAHL, J. B. 2004. Improved single crystal superalloys, CMSX-4 (R)(SLS)[La+Y] and CMSX-486 (R). *Superalloys 2004***,** 45-52.

HENRY, M. F., JACKSON, M. R., ZHAO, J.-C. & GIGLIOTTI, M. F. 2005. *Directionally solidified eutectic superalloys for elevated temperature applications*. US patent application C22C019/05.US 2005/0135962 A1

HILL, V. L. & HUMPHREYS, V. E. 1977. Thermal fatigue and oxidation data of superalloys including directionally solidified eutectics. National Aeronautics And Space Administration.

HOBBS, R. A., TIN, S. & RAE, C. M. F. 2005. A castability model based on elemental solid-liquid partitioning in advanced nickel-base single-crystal superalloys. *Metallurgical and Materials Transactions A,* 36**,** 2761-2773.

HOGAN, L. M., KRAFT, R. W. & LEMKEY, F. D. 1971. Eutectic Grains. *Advances in material research,* 5**,** 83-216.

HOOPER, P. R. 2001. Thermal analysis of CMSX-4 (MSRR7248) - The effect of heating and cooling rates on apparent solidus, liquidus and phase transformation responses.: Rolls-Royce, CRDF/R01/09.

HOOPER, P. R. 2002. Thermal analysis of RR3000. Rolls-Royce, CRDF/R02/01.

HORROCKS, F. J. 1990a). The Calculation of Temperature Gradients from Dendrite Spacing in RB199 IP Single Crystal Turbine Blades cast in Modified RR Directional Solidification Furnaces and by Thyssen AG. Rolls-Royce. MTL26346.

HORROCKS, F. J. 1990b). The Measurement of Primary Dendrite Arm Spacing in Directionally Solidified and Single Crystal Materials.: Rolls-Royce plc. MTL26475.

HORVAY, G. & CAHN, J. W. 1961. Dendritic and spheroidal growth. *Acta Metallurgica,* 9**,** 695-705.

HRENNIKOFF, A. 1941. Solution of problems of elasticity by the framework method. *Journal of applied mechanics,* 8**,** 169-175.

HUGO, F. & BETZ, U. 1997. *Casting And Directional Solidification Using a Heat Sink*. GB patent application.GB 2,309,405

HUNT, J. D. 1979. *Solidification and Casting of Metals,* The Metals Society.

IVANTSOV, G. 1947. Temperature field around a spheriodal, cylindrical and acicular crystal growing in a supercooled melt. *Doklady Akademii Nauk SSSR,* 58**,** 567.

IVANTSOV, G. 1985. Temperature field around a spherical, cylindrical, and needle-shaped crystal, growing in a pre-cooled melt. *Temperature field around a spherical, cylindrical, and needle-shaped crystal, growing in a pre-cooled melt Transl. into ENGLISH of,* 1**,** 567-569.

JACKSON, K. A. & HUNT, J. D. 1966. Lamellar and Rod Eutectic Growth. *Transaction of the Metallurgical Society of AIME,* 236**,** 1129-1142.

JACKSON, M. R., RAIRDEN, J. R. & HAMPTON, L. V. 1974. Coatings for directional eutectics.

JENNINGS, P. A. 1996. Foundries satelite project - Vericast phase 1 simple blade casting trials and thermal history data generation - Final report.: Rolls-Royce, CRDF/R96/1.

JONES, S. & YUAN, C. 2003. Advances in shell moulding for investment casting. *Journal of Materials Processing Technology,* 135**,** 258-265.

KARUNARATNE, M. S. A., RAE, C. M. F. & REED, R. C. 2001. On the microstructural instability of an experimental nickel-based single-crystal superalloy. *Metallurgical and Materials Transactions A,* 32**,** 2409-2421.

KEAR, B. H. & PIEARCEY, B. J. 1967. Tensile and Creep Properties of Single Crystals of Nickel-Base Superalloy Mar-M200. *Transactions of the Metallurgical Society of Aime,* 239**,** 1209-&.

KERMANPUR, A., VARAHRAAM, N., ENGILEHEI, E., MOHAMMADZADEH, M. & DAVAMI, P. 2000. Directional solidification of Ni base superalloy IN738LC to improve creep properties. *Materials Science and Technology,* 16**,** 579-586.

KHAN, T. & STOHR, J. F. Year. COTAC 744: An Optimised D.S Composite For Turbine Blades. *In:* Superalloys, 1980. TMS.

KIRCHHOFF, G. 1868. Ueber den Einfluss der Wärmeleitung in einem Gase auf die Schallbewegung. *Annalen der Physik,* 210**,** 177-193.

KLUG, F. J. 2002. *Floating insulating baffle for high gradient casting.*US 6,446,700 B1

KNAUS, H., SCHNEIDER, R. & HAN, X. 1999. Comparison of Different Radiative Heat Transfer Models and their Applicability in Coal-Fired Utility Boiler Simulations. Stuttgart: Universitätsbibliothek der Universität Stuttgart.

KNOBEL, M., ALLIA, P., GOMEZPOLO, C., CHIRIAC, H. & VAZQUEZ, M. 1995. Joule heating in amorphous metallic wires. *Journal of Physics D-Applied Physics,* 28**,** 2398-2403.

KONTER, M., KATS, E. & HOFMANN, N. 2000. A novel casting process for single crystal gas turbune components. *Superalloys 2000***,** 189-200.

KRAFT, E. & THOMPSON, E. Year. Observations on the growth and tensile properties of Ni-rich and Ni--Al--Nb eutectic alloys. *In:* In Situ Composites, 1973 Lakeville, Connecticut. United Aircraft Research Labs., East Hartford, CT.

KRUG, P. 1998. *Einfluss einer Flüssigmetallkühlung auf die Mikrostruktur gerichtet erstarrter Superlegierungen.* Ph.D, Universität Erlangen-Nürnberg.

KUHN, H.-A., BIERMANN, H., MUGHRABI, H. & UNGAR, T. 1991. An X-ray study of creep-deformation induced changes of the lattice mismatch in the gamma-prime-hardened monocrystalline nickel-base superalloy SRR 99. *Journal Name: Acta Metallurgica et Materialia; (United States); Journal Volume: 39***,** Medium: X; Size: Pages: 2783-2794.

KURZ, W. & FISHER, D. J. 1989. *Fundamentals of solidification,* Trans Tech Publications.

LALLEMENT, B. L. 1989. *Heat Shield For Casting Furnace*. US patent application.US 4,819,709

LANGER, J. S. 1988. Existence of needle crystals in local models of solidification. *In:* PIERRE, P. & LIBCHABER, A. (eds.) *Dynamics of Curved Fronts.* San Diego: Academic Press.

LANGER, J. S. & MÜLLER-KRUMBHAAR, H. 1978a. Theory of dendritic growth—I. Elements of a stability analysis. *Acta Metallurgica,* 26**,** 1681-1687.

LANGER, J. S. & MÜLLER-KRUMBHAAR, H. 1978b. Theory of dendritic growth—II. Instabilities in the limit of vanishing surface tension. *Acta Metallurgica,* 26**,** 1689-1695.

LEMKEY, F. D. 1973. Eutectic Superalloys Stengthened by Ni3Cb lamellae and Ni3Al Precipitates. East Hartford: NASA Technical Publications.

LI, J. F. & ZHOU, Y. H. 2005. Eutectic Growth in Bulk Undercooled Melts. *Acta Materialia,* 53**,** 2351-2359.

LIU, L., HANG, T. W., ZOU, M. M., ZHANG, W. G., ZHANG, J. & FU, H. Z. 2008. The effects of withdrawal and melt overheating histories on the microstructure of a nicked-based single crystal superalloy. *Superalloys 2008***,** 287-293.

LIU, L., HUANG, T., QU, M., LIU, G., ZHANG, J. & FU, H. 2010. High thermal gradient directional solidification and its application in the processing of nickel-based superalloys. *Journal of Materials Processing Technology,* 210**,** 159-165.

LIVINGSTON, J. D., CLINE, H. E., KOCH, E. F. & RUSSELL, R. R. 1970. High-speed solidification of several eutectic alloys. *Acta Metallurgica,* 18**,** 399-404.

LOCKWOOD, F. C. & SHAH, N. G. 1981. A new radiation solution method for incorporation in general combustion prediction procedures. *Symposium (International) on Combustion,* 18**,** 1405-1414.

MA, D. & SAHM, P. 1998. Primary spacing in directional solidification. *Metallurgical and Materials Transactions A,* 29**,** 1113-1119.

MCLEAN, M. 1983. *Directionally solidified materials for high temperature service,* London, The Metals Society.

MENZIES, R. D., BRUCH, C. A., GIGLIOTTI, M. F., SMITH, J. A. & HAUBERT, R. C. 1988. The processing and testing of a hollow DS eutectic high pressure turbine blade. *Superalloys 1988***,** 355-364.

MERSEN 2009. Properties of Calcarb. MERSEN.

MERSEN. 2011. *RE: Calcarb specific heat values.* Type to DALE, S.

MILLER, R. A. 1987. Current status of thermal barrier coatings—an overview. *Surface and Coatings Technology,* 30**,** 1-11.

MILLER, R. A. 1997. Thermal barrier coatings for aircraft engines: history and directions. *Journal of Thermal Spray Technology,* 6**,** 35-42.

MULTI-LAB. 2011. *RE: Thermal conductivity of Alsint ceramic material.* Type to DALE, S.

MURAKUMO, T., KOBAYASHI, T., KOIZUMI, Y. & HARADA, H. 2004. Creep behaviour of Ni-base single-crystal superalloys with various γ′ volume fraction. *Acta Materialia,* 52**,** 3737-3744.

NEWELL, M. 2009. *Aspects of a novel casting process for the production of nickel-based superalloy high pressure turbine blades.* EngD, University of Birmingham.

NIELSEN, P. V., MURAKAMI, S., KATO, S., TOPP, C. & YANG, J.-H. 2003. Benchmark tests for a computer simulated person. *Aalborg University, Indoor Environmental Engineering*.

OAKLEY, B. 2011. *RE: Graphite material data.* Type to DALE, S.

OHM, G. S. 1827. *Die galvanische Kette, mathematisch bearbeitet,* Berlin.

PACE-TECHNOLOGIES Abrasive Grinding Paper. Pace Technologies.

PANWISAWAS, C., GEBELIN, J. C., WARNKEN, N., BROOMFIELD, R. W. & REED, R. C. 2011. Numerical Modelling of Stress and Strain Evolution during Solidification of a Single Crystal Superalloy. *Advanced Materials Research,* 278**,** 204-209.

PANWISAWAS, C., MATHUR, H., GEBELIN, J.-C., PUTMAN, D., RAE, C. M. & REED, R. C. 2012. Prediction of recrystallization in investment cast single-crystal superalloys. *Acta Materialia*.

PATTNAIK, S., KARUNAKAR, D. B. & JHA, P. K. 2012. Developments in investment casting process—A review. *Journal of Materials Processing Technology,* 212**,** 2332-2348.

PIWONKA, T. S. 1974. *Method For Directional Solidification*. US patent application.3,810,504

POLLOCK, T. & MURPHY, W. 1996. The breakdown of single-crystal solidification in high refractory nickel-base alloys. *Metallurgical and Materials Transactions A,* 27**,** 1081-1094.

POLLOCK, T., MURPHY, W., GOLDMAN, E., URAM, D. & TU, J. 1992. Grain defect formation during directional solidification of nickel base single crystals. General Electric Co. Cincinnati Ohio Aircraft Engine Technical Division.

POLLOCK, T. M. & TIN, S. 2006. Nickel-based superalloys for advanced turbine engines: chemistry, microstructure and properties. *Journal of propulsion and power,* 22**,** 361-374.

POLYAK, D. E. 2011. 2011 Minerals Yearbook. USGS.

POLYAK, D. E. 2013. Rhenium.

POPE, J. E. 1996. *Rules of Thumb for Mechanical Engineers*, Elsevier Science and Technology.

PORTER, D. A., EASTERLING, K. E. & SHERIF, M. Y. 2009. *Phase transformations in metals and alloys,* Boca Raton, Fla. ; London, CRC.

POWELL, R. W. & SCHOFIELD, F. H. 1939. The thermal and electrical conductivities of carbon and graphite to high temperatures. *Proceedings of the Physical Society,* 51**,** 153-172.

PRATT, D. C. 1986. Industrial Casting of Superalloys. *Materials Science and Technology,* 2**,** 426-435.

PYCZAK, F., DEVRIENT, B. & MUGHRABI, H. 2004. The effects of different alloying elements on the thermal expansion coefficients, lattice constants and misfit of nickel-based superalloys investigated by X-ray diffraction. *Superalloys 2004***,** 827-836.

QUESTED, P. & MCLEAN, M. 1984. Solidification morphologies in directionally solidified superalloys. *Materials Science and Engineering,* 65**,** 171-180.

QUESTED, P. N. & NORTHWOOD, J. E. 1980. *Directional solidification process*.GB 2066098A

RABINOVITCH, M., STOHR, J. F., KHAN, T. & BIBRING, H. 1983. Directionally Solidified Composites for Application at High Temperature. *In:* KELLY, A. & MILEIKO, S. T. (eds.) *Fabrication Of Composites.* Elsevier Science Publishers.

REED, R. C. 2006. *The superalloys : fundamentals and applications,* Cambridge, Cambridge University Press.

RICHARDSON, L. F. 1911. The Approximate Arithmetical Solution by Finite Differences of Physical Problems Involving Differential Equations, with an Application to the Stresses in a Masonry Dam. *Philosophical Transactions of the Royal Society of London. Series A, Containing Papers of a Mathematical or Physical Character,* 210**,** 307-357.

RIZZONI, G. 2003. *Principles and Applications of Electrical Engineering,* McGraw-Hill.

ROLLS-ROYCE, P. 1986. *The jet engine,* Rolls-Royce plc.

SCHLIENGER & FRENCH. 2008. *Heating to control solidification of cast structure*.EP1579018

SCHNEIDER, M. C., GU, J. P., BECKERMANN, C., BOETTINGER, W. J. & KATTNER, U. R. 1997. Modeling of micro- and macrosegregation and freckle formation in single-crystal nickel-base superalloy directional solidification. *Metallurgical and Materials Transactions A,* 28**,** 1517-1531.

SGL-GROUP 2007. RINGSDORFF - Speciality Graphite Grades for Continuous Casting. *SGL Group - The Carbon Company.*

SGL-GROUP 2008. SIGRAFLEX-Graphite Foils. SGL GROUP - The Carbon Company.

SIMS, C. T. 1984. A history of superalloy metallurgy for superalloy metallurgists. *Superalloys 1984***,** 399-419.

SINK, L. W. 1965. *Method of Casting Directionally Solidified Articles*. US patent application.(US3417809)

SMYTHE, W. R. 1950. *Static and Dynamic Electricity ... Second edition,* New York, McGraw-Hill Book Co.

SODERSTROM, M. J., DONALDSON, B. & BRINEGAR, J. R. 2005. *Directional Solidification Method And Apparatus*. US patent application.US 6,896,030

STOHR, J. F. & KHAN, T. 1980. Metallurgical Problems Encountered In The Conception And Development Of D.S Composites For Turbine Blade Applications. *Research Aerospaciale,* 6**,** 29-57.

TAMARIN, Y. 2002. *Protective coatings for turbine blades,* Materials Park, Ohio, ASM International.

TAYLOR, K. 1983a. *Induction furnace having improved thermal profile*.US 4,409,451

TAYLOR, P. Year. An illustrated history of lost wax casting. *In:* Proceedings of the 17th Annual BICTA Conference, Washington, DC, 1983b.

TERKELSEN, B. E. 1973. *Method And Apparatus For The Production Of Directionally Solidified Castings*. US patent application.US 3,714,977

THOMAS, F., SAWYER. 1976. *Method and apparatus for casting directionally solidified articles*.US3942581

THOMPSON, E., GEORGE, F. & BREINAN, E. 1972. The Influence of Interlamellar Spacing on the Strength of the Ni3Al-Ni3Cb Eutectic. DTIC Document.

TILLER, W. A., JACKSON, K. A., RUTTER, J. W. & CHALMERS, B. 1953. The redistribution of solute atoms during the solidification of metals. *Acta Metallurgica,* 1**,** 428-437.

TIN, S., POLLOCK, T. & KING, W. 2000. Carbon additions and grain defect formation in high refractory nickel-base single crystal superalloys. *Ann Arbor,* 1001**,** 48109.

TIN, S., POLLOCK, T. & MURPHY, W. 2001. Stabilization of thermosolutal convective instabilities in Ni-based single-crystal superalloys: Carbon additions and freckle formation. *Metallurgical and Materials Transactions A,* 32**,** 1743-1753.

TINGQUIST, S. C. & LAUX, E. G. 1974. *Method and Apparatus for Melting and Casting Metal*. US patent application.US3841384

TRIVEDI, R., P.MAGNIN & W.KURZ 1987. Theory of Eutectic Growth under Rapid Solidification Conditions. *Acta Metallurgica,* 35**,** 971-980.

TYLER, W. W. & WILSON, A. C. 1953. Thermal Conductivity, Electrical Resistivity, and Thermoelectric Power of Graphite. *Physical Review,* 89**,** 870-875.

VERNSNYDE, F. L. & GUARD, R. W. 1960. Directional grain structures for high temperature strength. *Transactions of the American Society of Metals***,** 485-493.

VORT, G. F. V., MANILOVA, E. P., MICHAEL, J. R. & LUCAS, G. M. Study of selective etching of carbides in steel.

WALSTON, S., CETEL, A., MACKAY, R., O'HARA, K., DUHL, D. & DRESHFIELD, R. 2004. Joint development of a fourth generation single crystal superalloy. *Superalloys 2004***,** 15-24.

WALTER, C., HALLSTEDT, B. & WARNKEN, N. 2005. Simulation of the solidification of CMSX-4. *Materials Science and Engineering a-Structural Materials Properties Microstructure and Processing,* 397**,** 385-390.

WANG, W., LEE, P. D. & MCLEAN, M. 2003. A model of solidification microstructures in nickel-based superalloys: predicting primary dendrite spacing selection. *Acta Materialia,* 51**,** 2971-2987.

WARNKEN, N. & REED, R. 2011. On the Characterization of Directionally Solidified Dendritic Microstructures. *Metallurgical and Materials Transactions A,* 42**,** 1675-1683.

WARNKEN, N. & REED, R. Year. A novel method for the characterisation of directionally solidified dendritic arrays. *In:* IOP Conference Series: Materials Science and Engineering, 2012. IOP Publishing.

WEIDONG, H., XINGGUO, G. & YAOHE, Z. 1993. Primary spacing selection of constrained dendritic growth. *Journal of Crystal Growth,* 134**,** 105-115.

WHITTENBERGER, J. D. & WIRTH, G. 1982. Structure and creep rupture properies of directionally solidified eutectic γ-γ'-α alloy. *Metal Science,* 16**,** 383-388.

WILLIAMS, J. C. & STARKE, E. A. 2003. Progress in structural materials for aerospace systems. *Acta Materialia,* 51**,** 5775-5799.

WOODFORD, D. A. 1977. Creep and rupture of an advanced fiber strengthened eutectic composite superalloy. *Metallurgical Transactions A,* 8A**,** 639-650.

WORSTER, M. G. 1992. Instabilities of the liquid and mushy regions during solidification of alloys. *Journal of Fluid Mechanics,* 237**,** 649-669.

YOUNG, H. D. 1992. *University physics,* Reading, Mass., Addison-Wesley.

ZAMBALDI, C., ROTERS, F., RAABE, D. & GLATZEL, U. 2007. Modeling and experiments on the indentation deformation and recrystallization of a single-crystal nickel-base superalloy. *Materials Science and Engineering a-Structural Materials Properties Microstructure and Processing,* 454**,** 433-440.

APPENDIX

Material Data

The following material property data has been used during this work. Sources of data are discussed in Chapter 5.

Alumina (Alsint)

Constant density – 3800 $Kg.m^{-3}$

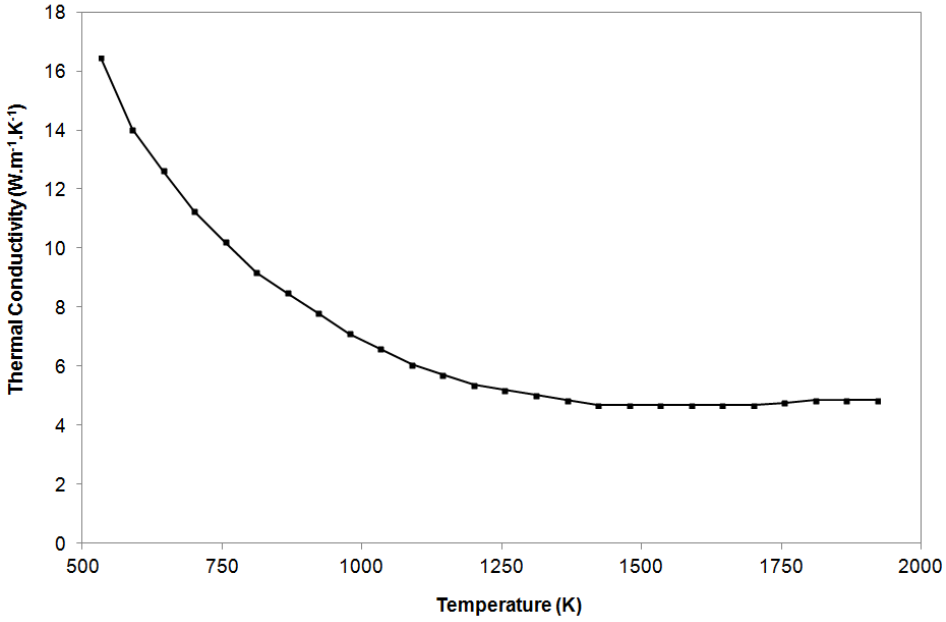


Figure A-1: Alumina thermal conductivity.

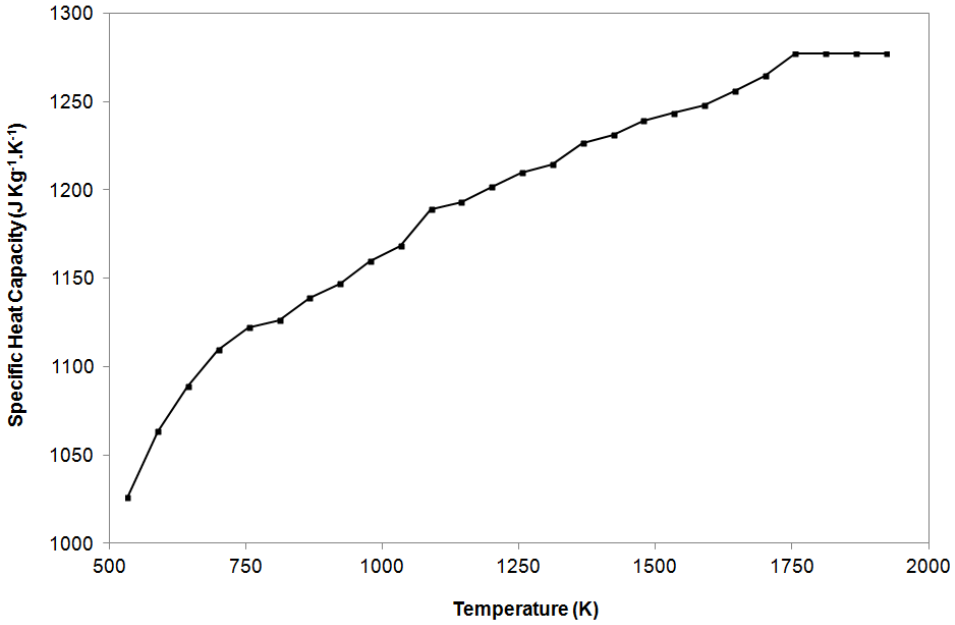


Figure A-2: Alumina specific heat capacity.

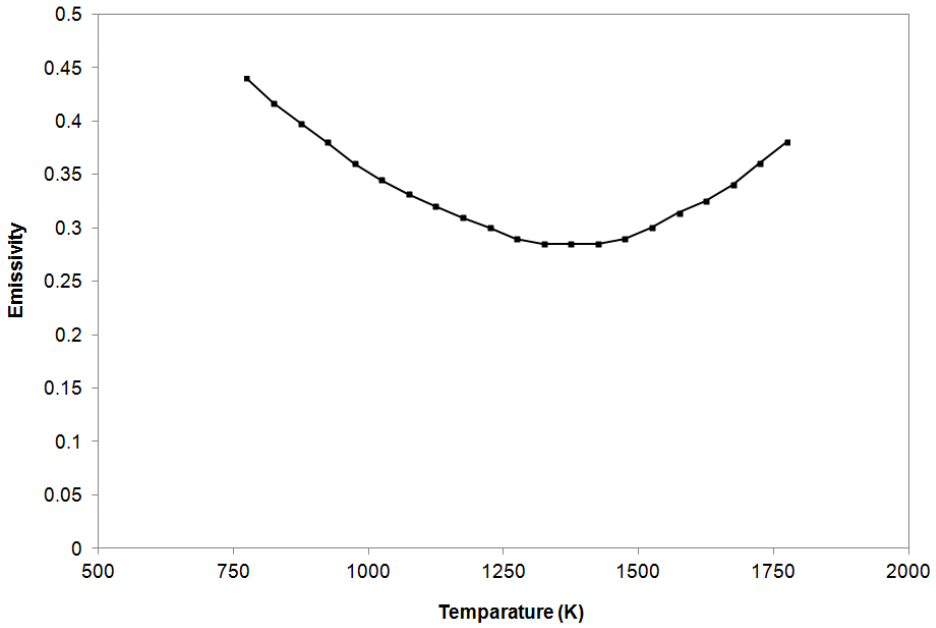


Figure A-3: Alumina emissivity.

Calcarb

Constant density – 150 $Kg.m^{-3}$

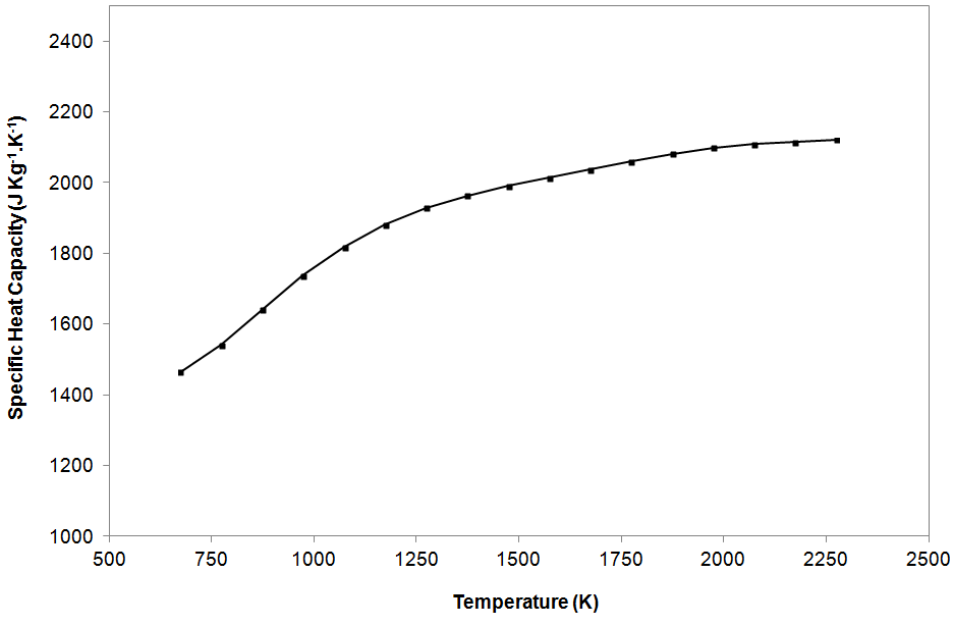


Figure A-4: Calcarb specific heat capacity.

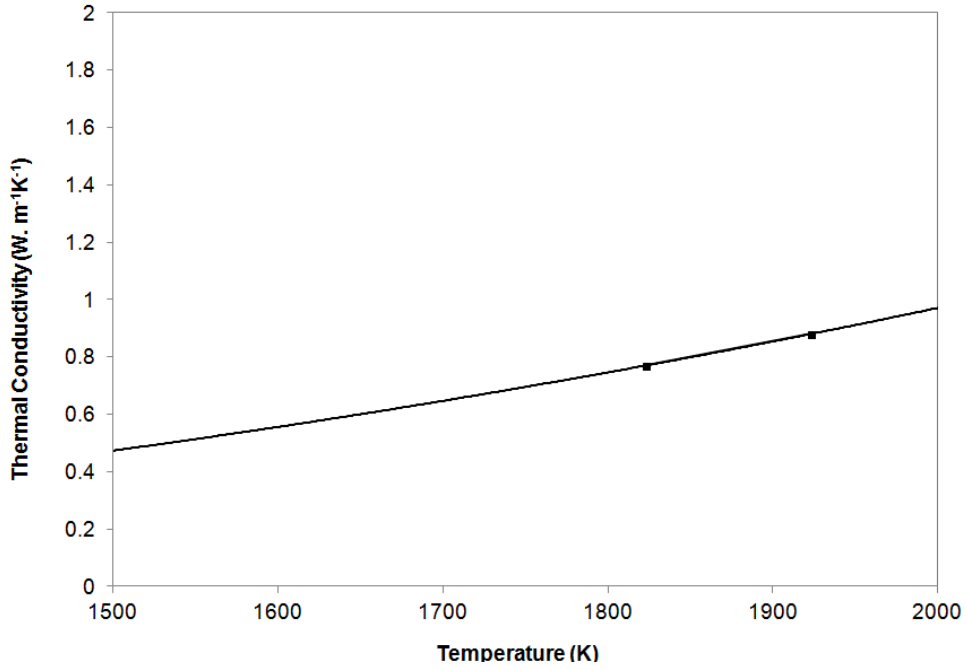


Figure A-5: Calcarb thermal conductivity.

COTAC 744

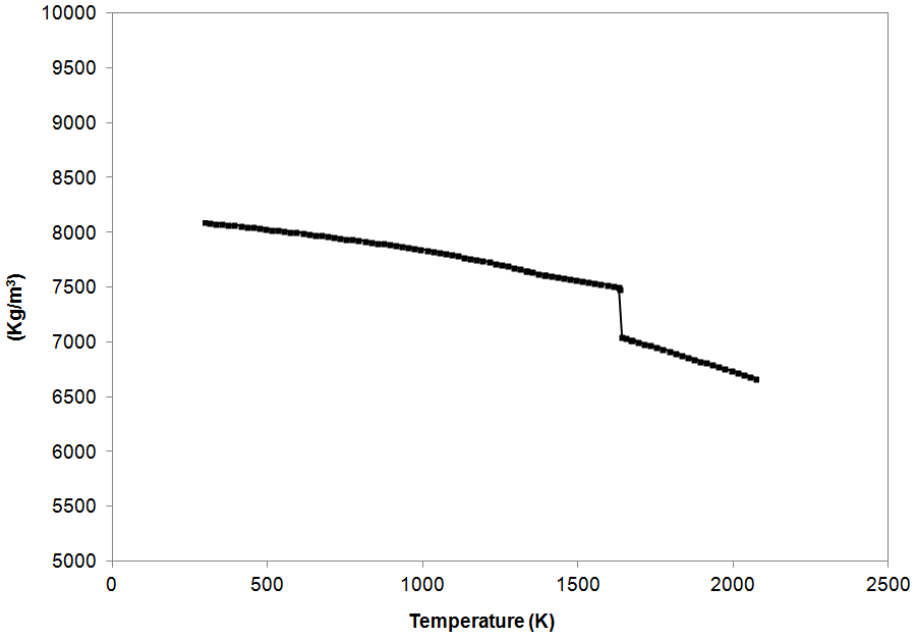


Figure A-6: COTAC 744 density

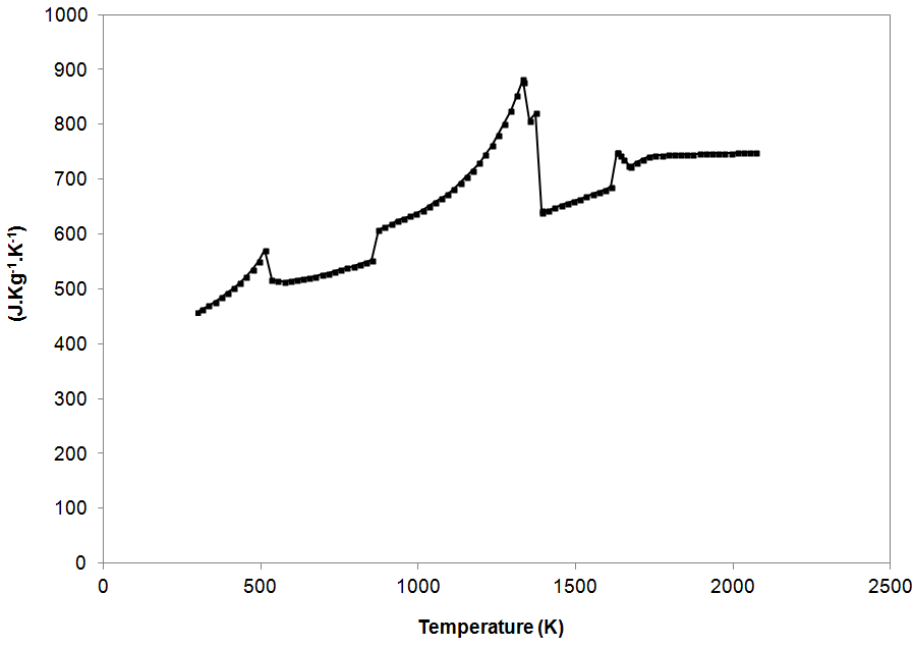


Figure A-7:COTAC 744 specific heat capacity.

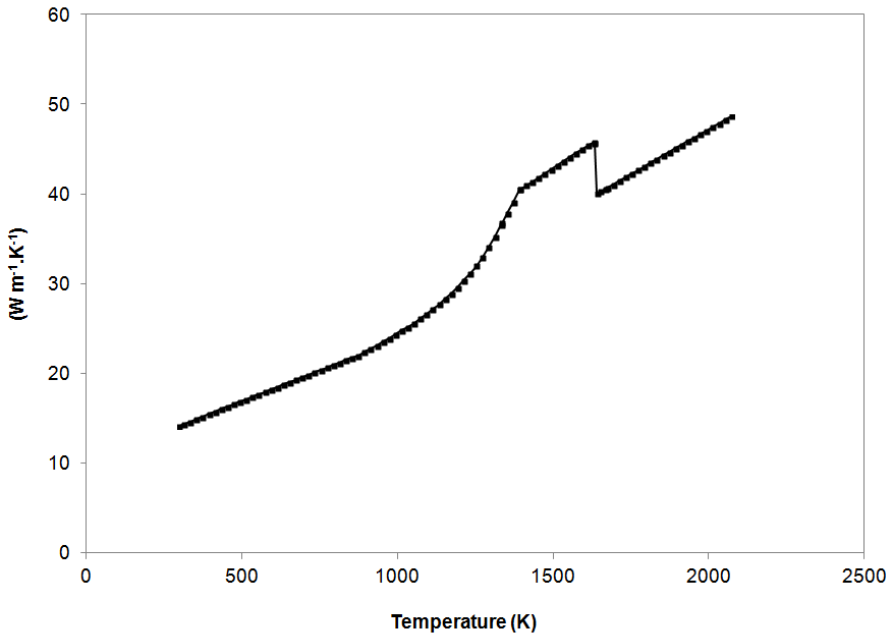


Figure A-8: COTAC 744 Thermal conductivity.

γ-γ'-δ

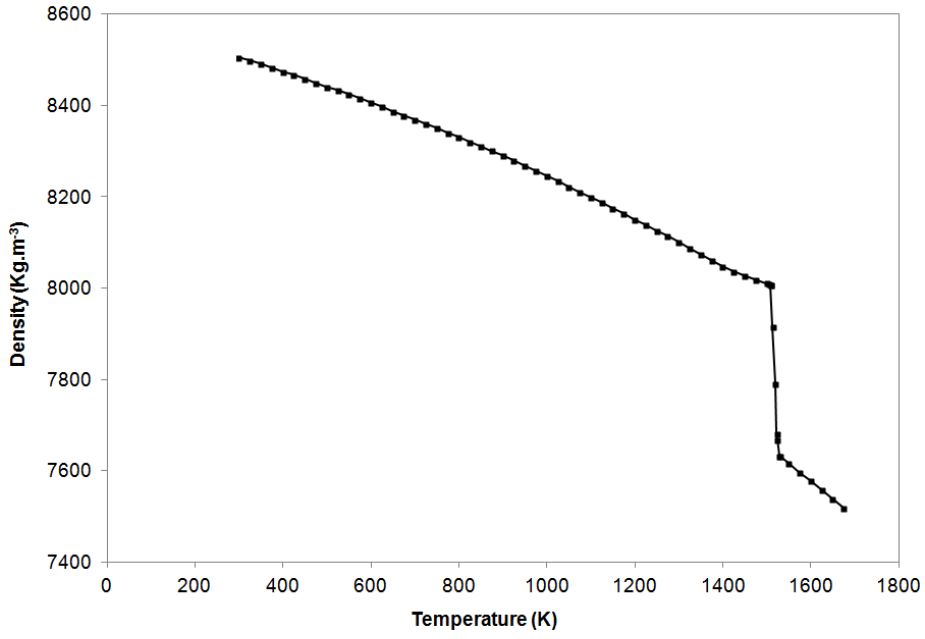


Figure A-9: γ-γ'-δ density.

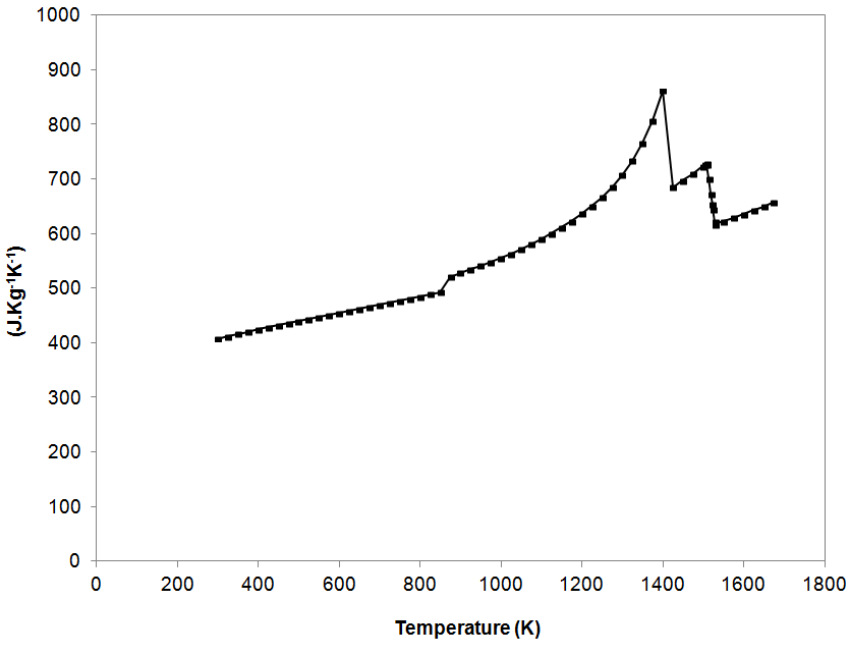


Figure A-10: γ-γ'-δ specific heat capacity.

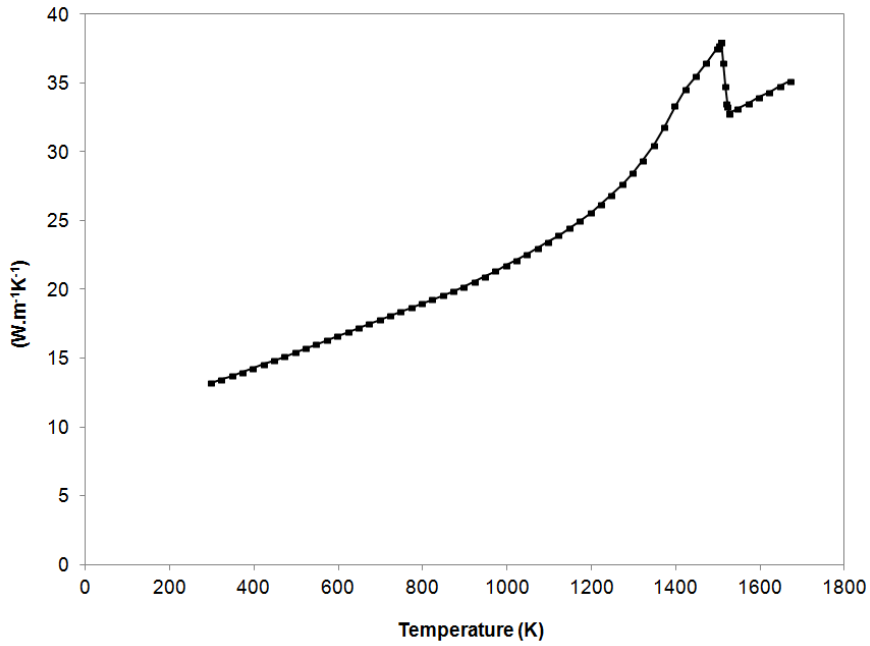


Figure A-11: γ-γ'-δ thermal conductivity.

Graphite

Constant density – 1720 $Kg.m^{-3}$
Constant electrical conductivity – 83333.33 $S.m^{-1}$

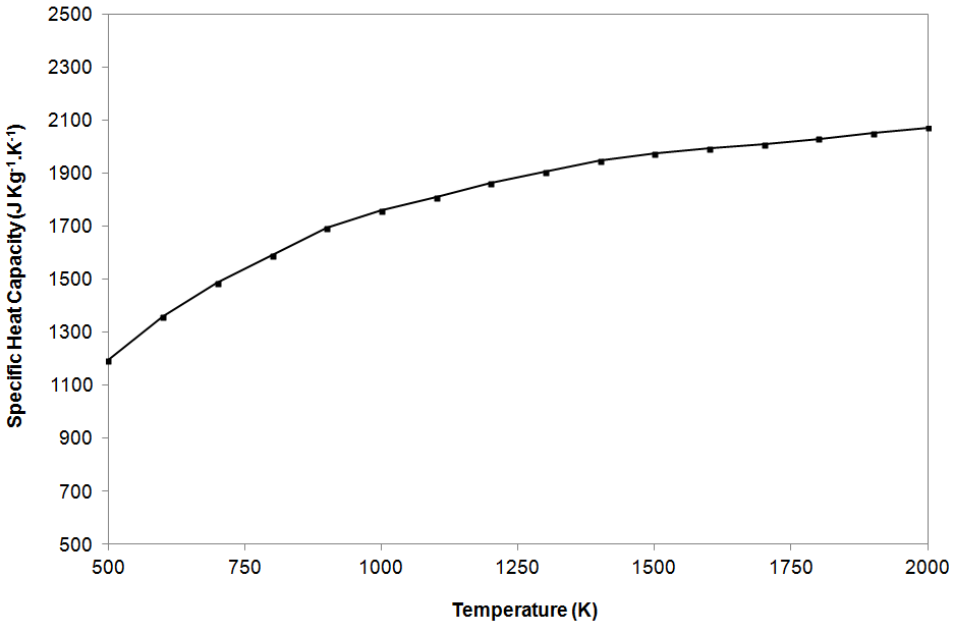


Figure A-12: Graphite specific heat capacity.

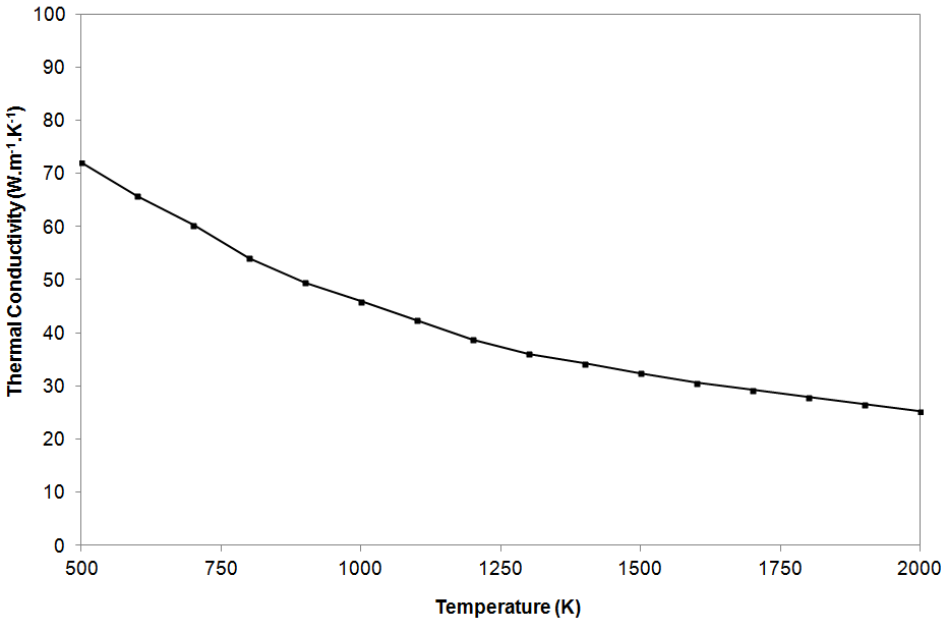


Figure A-13: Graphite thermal conductivity.

Copper

Constant density – 8920 $Kg.m^{-3}$

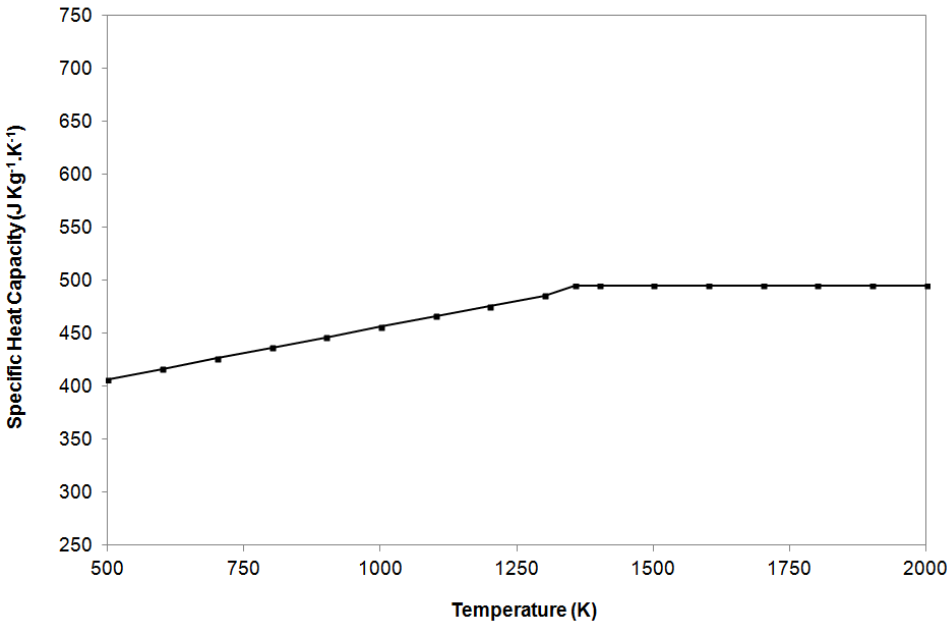


Figure A-14: Copper specific heat capacity.

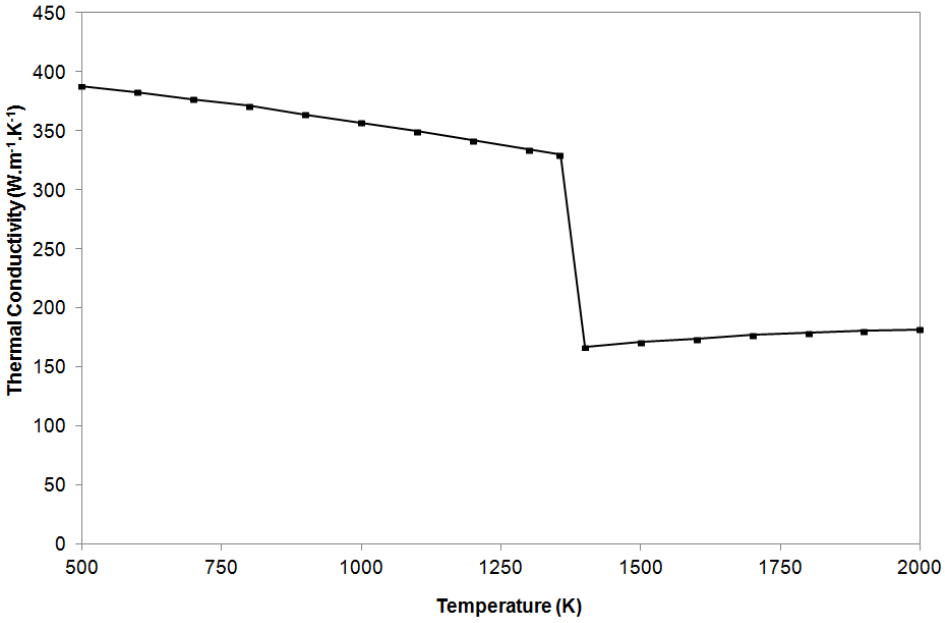


Figure A-15: Copper thermal conductivity.

Sigraflex

Constant density – 1020 Kg.m^{-3}

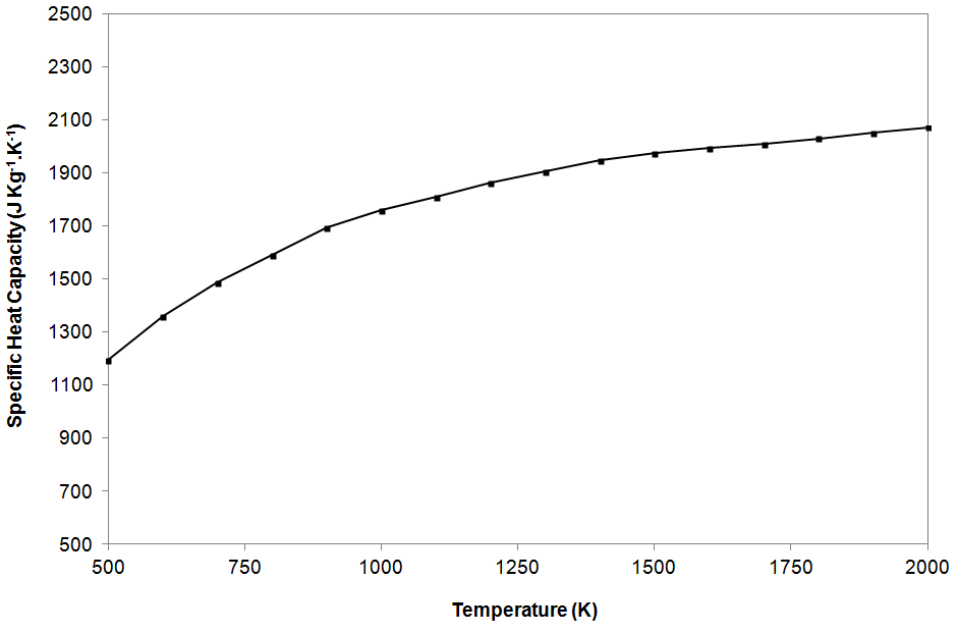


Figure A-16: Sigraflex specific heat capacity.

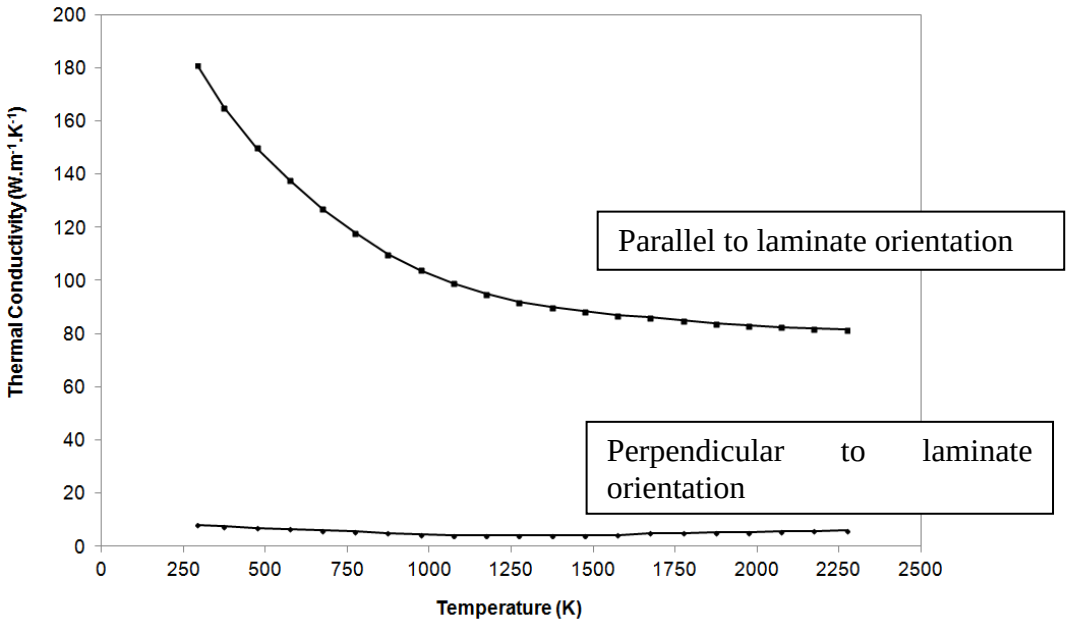


Figure A-17: Sigraflex thermal conductivity.

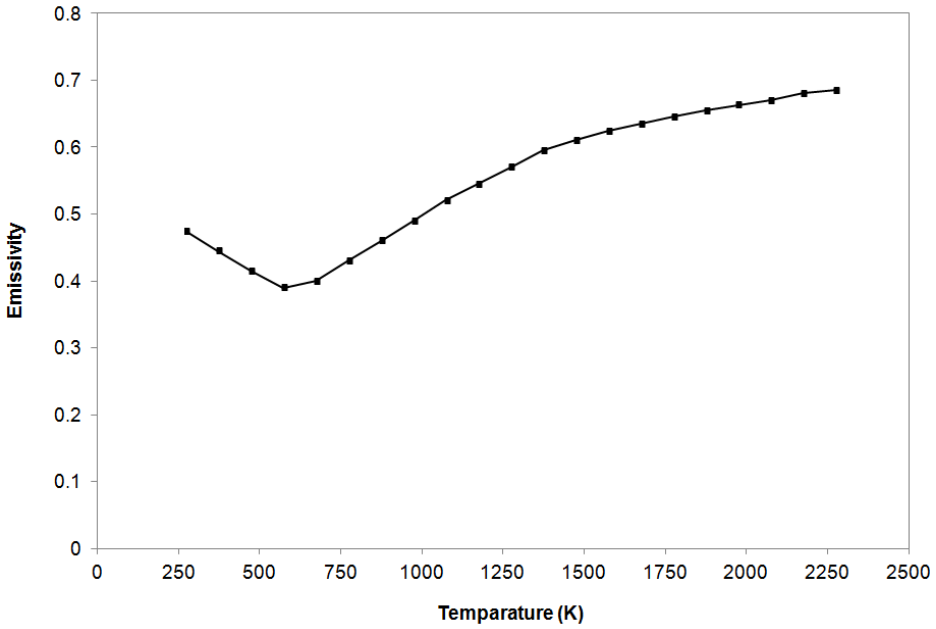


Figure A-18: Sigraflex emissivity.

Stainless Steel

Constant density – 8000 Kg.m^{-3}

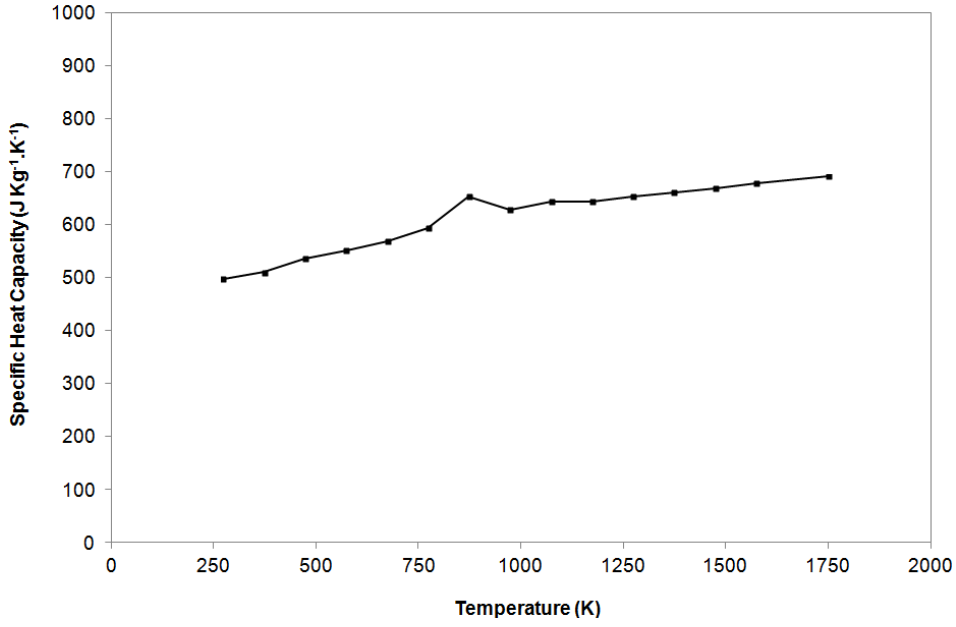


Figure A-19: Stainless steel specific heat capacity.

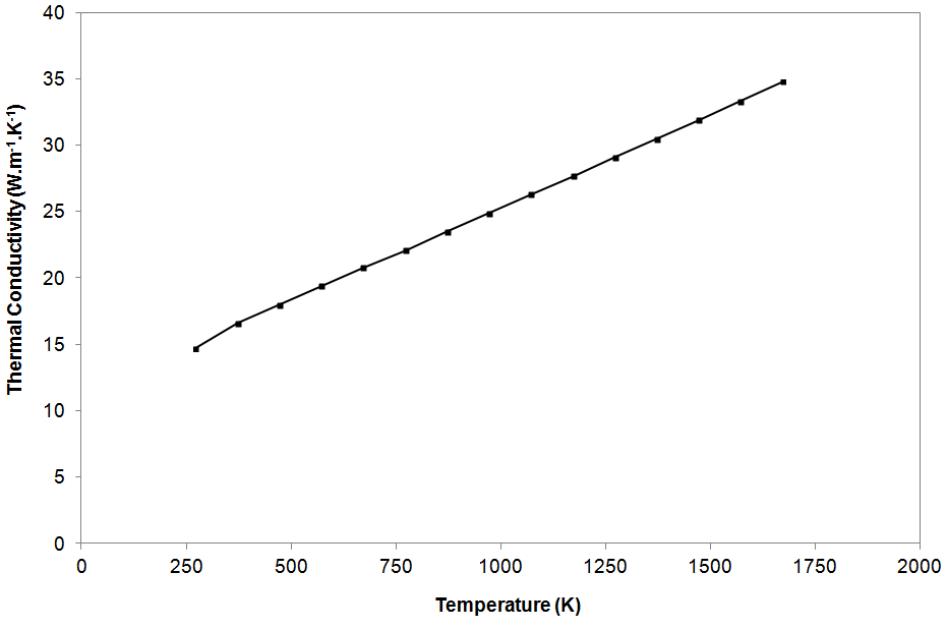


Figure A-20: Stainless steel thermal conductivity.

Zircar

Constant density – 365.416 $Kg.m^{-3}$

Constant specific heat capacity – 1047 $J.Kg^{-1}.K^{-1}$

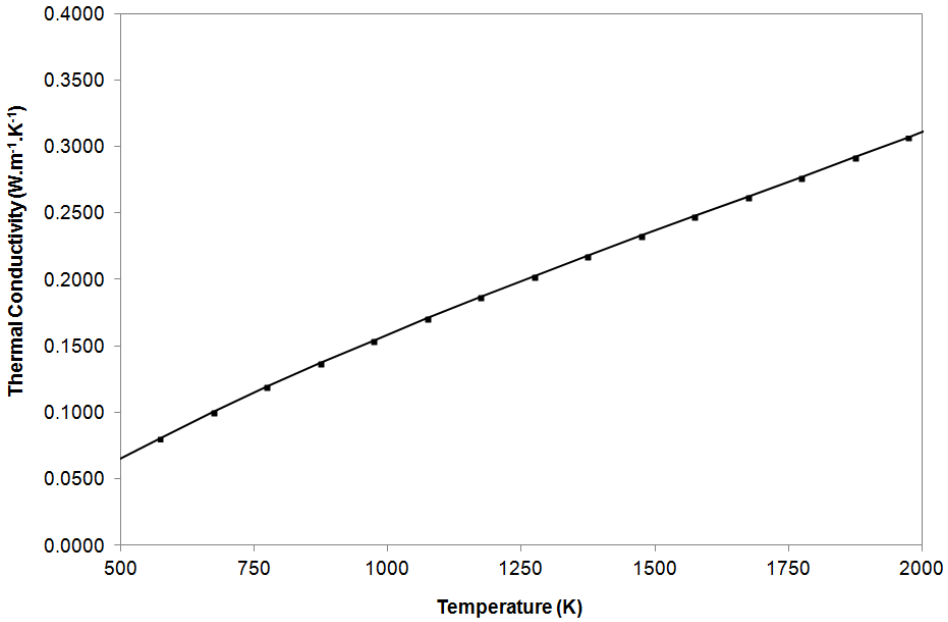


Figure A-21: Zircar thermal conductivity.

Experimental heater manufacturing drawing

